Evolution of Local Coordination of Zn Ions in Aqueous Electrolytes: Chemical, Thermal and Confinement Effects

Diwash Dhakal

A dissertation
submitted in partial fulfillment of the
requirements for the degree of

Doctor of Philosophy

University of Washington
2023

Reading Committee:
Gerald T. Seidler, Chair
Guozhong Cao
Arthur Barnard

Program Authorized to Offer Degree:
Materials Science and Engineering

University of Washington

Abstract

Evolution of Local Coordination of Zn Ions in Aqueous Electrolytes: Chemical, Thermal and Confinement Effects

Diwash Dhakal

Chair of the Supervisory Committee:
Gerald T. Seidler
Physics

The accelerating global transition towards renewable energy sources necessitates innovative and sustainable energy storage solutions to effectively manage the intermittent nature of renewable power generation. A key facet of this transition is the adoption of grid-scale energy storage technologies capable of accommodating the variability in renewable energy production.

Aqueous batteries, distinguished by their water-based electrolytes, have emerged as promising candidates for grid storage due to their inherent safety, cost-effectiveness, and environmental compatibility. However, the limited electrochemical voltage window (EVW) of aqueous electrolytes, attributed to hydrogen and oxygen evolution reactions at the electrodes, presents a significant hurdle for achieving energy-dense aqueous batteries. To that end, controlling the solvation structure of active ions in the electrolyte, for example by increasing the salt concentration of the electrolyte, has been shown to be an effective way of expanding the EVW of

aqueous electrolytes. Consequently, the ability to detect and study the solvation structure of active ions in aqueous electrolytes from dilute to concentrated state is central to further research and development on such electrolyte systems.

This research focuses on Zn-halide solutions for aqueous Zn-ion battery (ZIB) electrolytes. The study demonstrates that valence-to-core X-ray emission spectroscopy (VTC-XES) serves as a valuable tool for investigating the local structure of Zn^{2+} ions in aqueous solutions from dilute to extreme concentrations, quantifying coordination numbers without relying on thermodynamic formation constants. The developed methods contribute to the fundamental understanding of the solvation behavior of Zn^{2+} ions in aqueous solutions under varying conditions.

The investigation reveals that, under ambient conditions, higher ion activity leads to increased desolvation and contact ion pairing. This behavior is further observed with elevated solution temperatures. Additionally, aqueous $ZnCl_2$ electrolytes under nanoconfinement exhibit enhanced contact ion pairing, correlating with their increased EVW under nanoconfinement. These findings establish VTC-XES as a robust tool for studying local structures in aqueous Zn-halide solutions in general and contribute to the fundamental understanding of the physical chemistry of these specific systems.

Hence, first, this work establishes a new methodology for studying ion complexation in aqueous electrolytes. Second, it gives new inquiry into the connection between ion pairing and the electrochemical voltage window, especially for nanoconfined conditions immediately relevant for metal ion batteries. Third, the observed temperature dependence of ion pairing in the system under study directly challenges theoretical approaches used to predict ion complexation in geophysical brines under environmentally-relevant conditions, and also has relevance for higher-temperature operation of ZIB.

Dedicated to my parents:

Kishor P. Dhakal and Nirmala Dhakal

Acknowledgements

Thank you to my advisor, Professor Gerald Seidler, for helping me in many ways throughout my PhD journey. I learned so many valuable skills and lessons from you and am grateful to have you as my mentor. Many thanks to the awesome people in Seidler Lab, specifically Jared Abramson, Samantha Tetef, Anthony Gironda, Charles Cardot, and Helen Chen, for your support and helping make work enjoyable.

Thank you to Professor Guozhong Cao for the valuable insights and for always being there when I needed advice; Dr. Tim Fister for the insightful discussions and for the continuous support towards my professional development; Dr. Niri Govind and Dr. John Fulton for the helpful suggestions during my research; and all my collaborators for working with me and supporting my research.

I would like to acknowledge Joint Center for Energy Storage Research (JCESR), UW Clean Energy Institute (CEI) and National Science Foundation (NSF) for the funding support for my research, and the Department of Materials Science and Engineering at UW for supporting me through teaching assistantships.

Finally, many thanks to my family and friends for all your support, especially to my wife Dr. Seema Prasai, who sacrificed a lot for me, was always there to support me and gave me the best gift – Jianna. Also, thank you to Jianna, my little girl, who has made my life a lot more interesting and challenging at the same time. I love you all and could not have achieved this without you!

Table of Contents

List of Figures

Chapter 1

Chapter 2

Chapter 3

Chapter 4

Chapter 5

Chapter 6

Chapter 7

Chapter 8

List of Tables

Chapter 2

Chapter 6

Chapter 1: Brief Overview of Energy Sector

1.1: Introduction

Global energy usage has increased drastically over the course of the development of human civilization, most notably during the last two hundred years. (*1*, *2*) Historically, various scientific and technological advancements have initiated drastic changes in the way we use energy. (*2*) The development of steam engines as primary power generators led to a considerable rise in energy usage during the 19th century and the subsequent development of internal combustion engines and grid-level electricity generation led to an explosion in global energy usage as reflected by the steep incline in global energy usage during the 20th century in Figure 1.

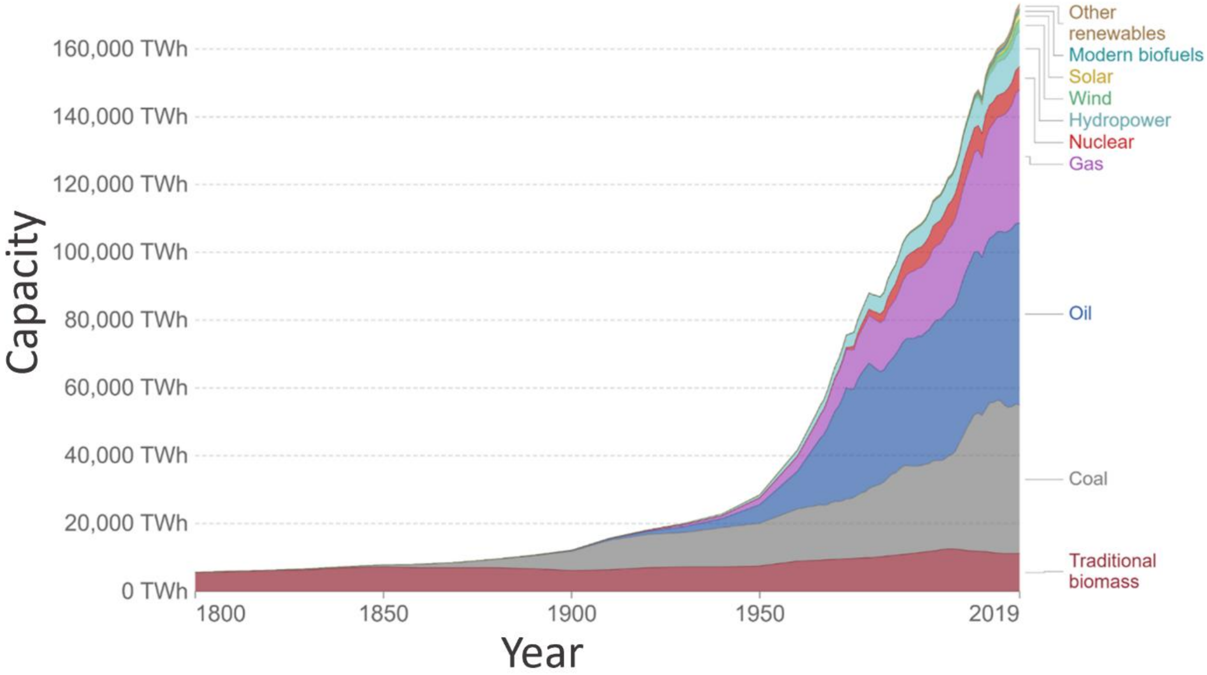

Figure 1: Global energy usage in TWh by source for the last 200 years. Figure used from Ritchie, *et al*. (*1*)

The energy consumption values in Figure 1 are for global total consumption. When converted to global per capita consumption, the average human alive today is assigned about 21 MWh energy compared to their predecessors in 1965 who consumed about 13 MWh. (*1*) In practice, energy consumption is very non-evenly distributed across different countries. In the United States, which is among the highest consumers, per capita energy consumption has been steadily high, fluctuating between 80-100 MWh since 1965. (*1*)

Energy consumption and gross domestic product (GDP) are closely related. Energy availability is prerequisite for most large improvements in GDP and consequent improvements in human welfare in poorer countries. (*3*) In wealthier, developed countries, energy consumption both buttresses common commercial effort but is also more actively, and sometimes conspicuously consumed. These trends are closely tied to the sustained technological progress that has been instrumental in the consistent rise in energy utilization. (*2*) For example, the widespread availability of the internet and the enterprises reliant on it has brought about a profound transformation across various commercial sectors and government services. (*4*) This has not only contributed to the overall growth of the global economy but has also consequently driven a substantial increase in the demand for energy to support this economic expansion. (*2*)

With the above background in mind, we address several core issues in the next few sections. First, we discuss the issue of global warming and its relationship with energy usage. Second, we summarize the steps needed to meet the energy requirements of the modern world in a sustainable way. Finally, we consider the grid requirements and possible storage technologies that are the key enabling factors in realizing a clean and sustainable energy future.

1.2: Global Warming and Energy Usage

Among the most used sources of energy are the fossil fuels coal, oil and natural gas, as shown in Figure 1. Although these sources have supplied us with the needed energy to run our civilization until now, they have also added huge amounts of CO_2 into the atmosphere. The resulting change in atmospheric chemistry has now resulted in the steady increase in global temperature causing adverse climatic effects like melting polar ice caps and rising sea level. (*5*) The increased atmospheric CO_2 has also triggered a less obvious but equally serious issue, ocean acidification, which threatens the health of our oceans and also the future availability of healthy fisheries for human use and consumption. (*5*)

The global march towards prosperity via energy consumption therefore comes with a truly global caveat: we have the ability to cause adverse consequences, including possibly permanently adverse consequences, on the scale of the planetary ecosystem.

In terms of usage, electricity generation, heating (including industrial-scale heating), and transportation combined are responsible for more than half of the total global greenhouse gas emission, as shown in figure 2. Such a trend in energy usage has already pushed us on the trajectory towards a permanent change in the planetary climate. Furthermore, as these sectors are bound to keep growing with both population increase and continuing attempts to lift developing countries out of poverty, the full effects of global warming are inevitable in the near future if we do not soon correct our course.

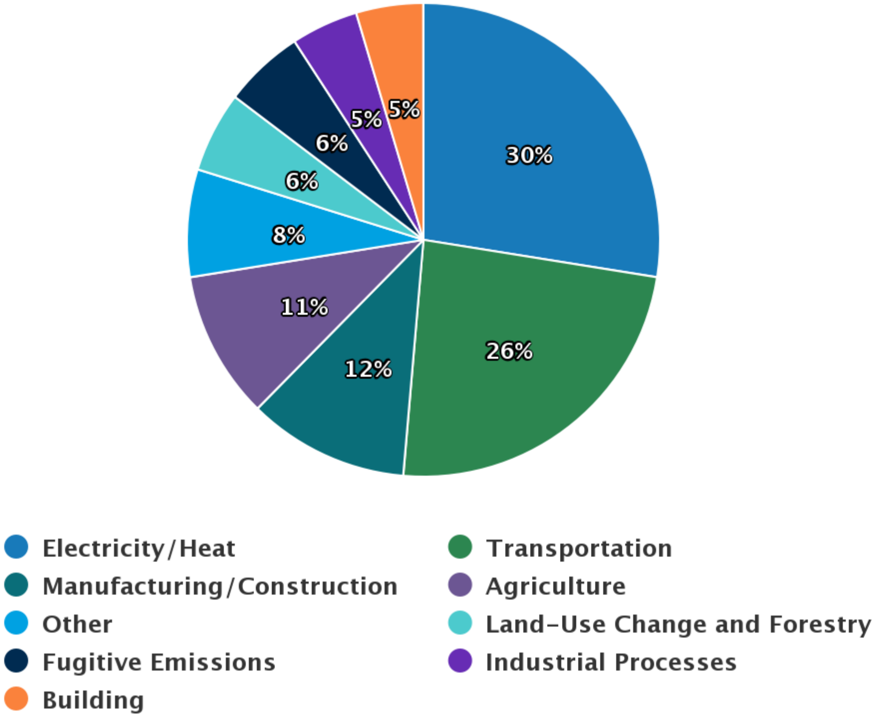

Figure 2: Greenhouse gas emissions by sector for the year 2018. Total global CO_2 emission for that year was about 49 billion metric tons. Figure reproduced from reference (*6*).

Several steps are seen as the most important to avert the worst consequences of climate change. First, the transportation sector needs to decarbonize and greatly reduce the emission of greenhouse gases. (*6*) One alternative for the internal combustion engine is the emissionless electric variant, which is already being implemented and has the potential for widespread market penetration in the next decade. (*7*) Such a transition to electric vehicles on a global scale requires advances in storage technology (i.e., batteries), and this especially includes the need for storage suited for the energy and power requirements of vehicles of different sizes and uses. (*8*)

Second, the electricity generation and distribution infrastructure need to be reformed to integrate clean and renewable sources as a central component. This is necessary to replace fossil-fuel based generation of electricity at the present scale and is also necessary to address growing electricity demand in the transportation sector. This poses energy storage challenges at the grid level, a challenge that has grossly different requirements than for vehicle electrification, and that consequently sees different solutions spanning from pumped storage to redox flow batteries. (*10*)

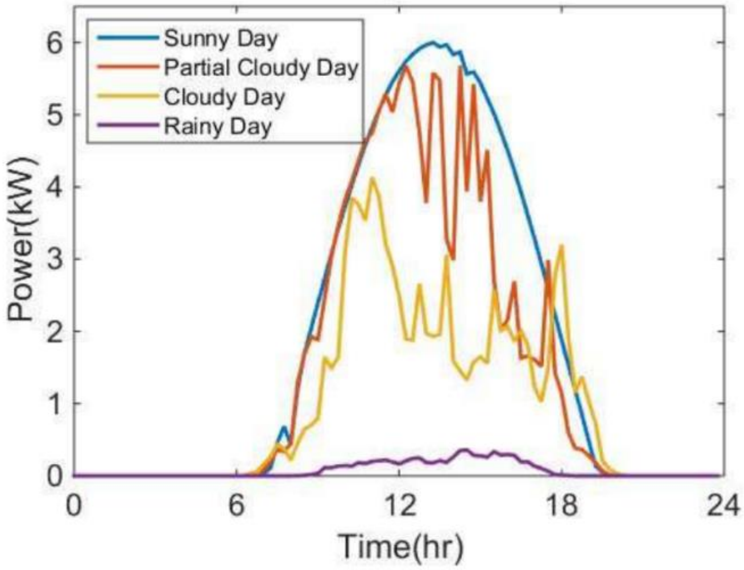

Figure 3: Power generated by a 6-kW solar panel for days with different weather conditions during the same season. Figure reproduced from Zhu, *et al.* (*9*)

1.3: Meeting the Modern Needs

That being said, remodeling the electric grid to accommodate renewable sources is not an easy feat. In the modern world, there are copious energy applications with a wide range of energy and power requirements. The annual usage of energy is a cumulative sum of various sectors using energy in different ways and for different purposes and more importantly with varying rates. Consequently, within a given year the overall energy demand is not uniform - both on a seasonal (long) and daily (short) basis.

Taking an example of residential electric energy use, the demand is usually higher in winters compared to summers and, within a single day, higher in mornings and evenings than at night. On the other hand, electricity generation by renewable sources like wind and solar is intermittent on scales ranging from hours to entire seasons. Figure 3 shows the power output of a typical 6-kW peak capacity solar panel for days with different weather conditions in the same season. First, it is obvious that solar power generation is limited to the daytime. Second, the power generation varies drastically during a season depending on the daily cloud cover. Moreover, there are seasonal variations in the amount of available sunshine influencing the power generation in longer time scales. The combination of short-term and seasonal variation in solar and wind generation of electricity presents an inherent problem: the electric grids in most countries are best-suited only for on-demand electricity generation and distribution.

With the system of electric energy generation and distribution in use, it is required that the energy production be also varied to match the demand. Our present electricity distribution grids are only designed for supplying energy from the production site to the consumption site and, except for purposes of some phase regulation, lack any storage buffer. This is not a problem for energy production schemes that use oil and coal where the amount of energy produced can be varied by varying the amount of fuel being used and the fuel can be stored and distributed as needed. However, in the case of renewable energy sources like solar or wind the amount of available fuel at any moment is not in our control and cannot be stored and distributed as needed. Rather, energy will have to be generated and then stored and distributed as needed.

Figure 4 compares the global energy generation as of 2018 to the projected shares of different sources for energy generation following the stated policies by 2040. (*11*) As compared to 2018, a substantially greater fraction of the energy would be generated from renewable resources by 2040. This necessitates an inevitable transition to a modern grid with an ability to incorporate renewable sources of electricity at different levels of the grid.

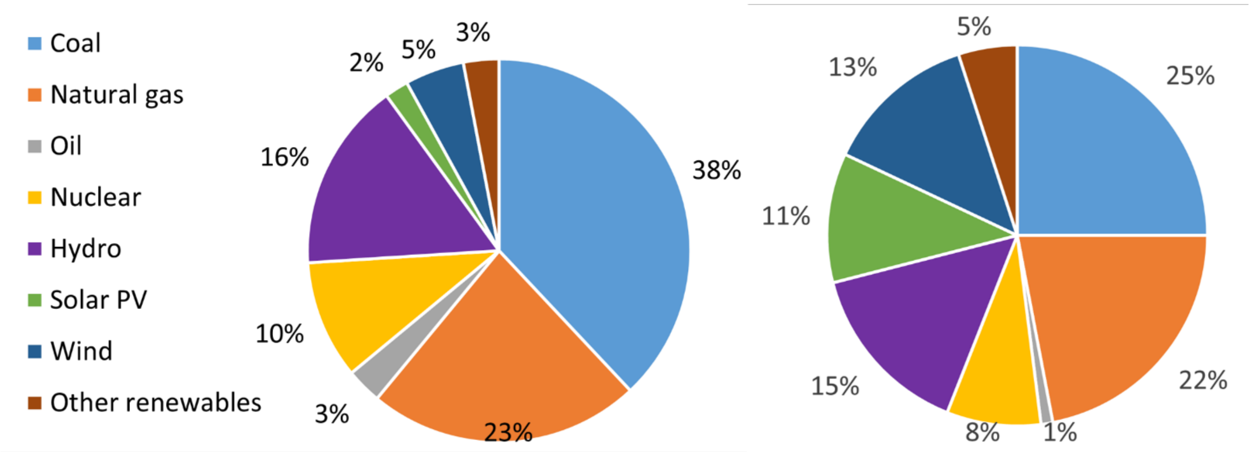

Figure 4: A comparison of global energy generation as of 2018 and the outcome of stated national policies in 2040, from the International Energy Agency's World Energy Outlook 2019. (*11*)

One of the main components of the modified grid, and the one that needs significant technological advancement, is the electrical energy storage system that serves as the buffer between renewable generation and consumption. Of the many proposed solutions for electrical energy storage at the grid level, a few have shown potential for practical implementation. Figure 5 compares various energy storage systems that are suited for different purposes in the grid in terms of their power rating and the discharge time needed. On the large scale, pumped hydropower shows promise because of its good efficiency and maturity of technology, but its use is limited to large scale and remote locations. Other types of energy storage technologies that are being explored for large-scale use include compressed air systems, flywheels, thermal storage systems, etc.

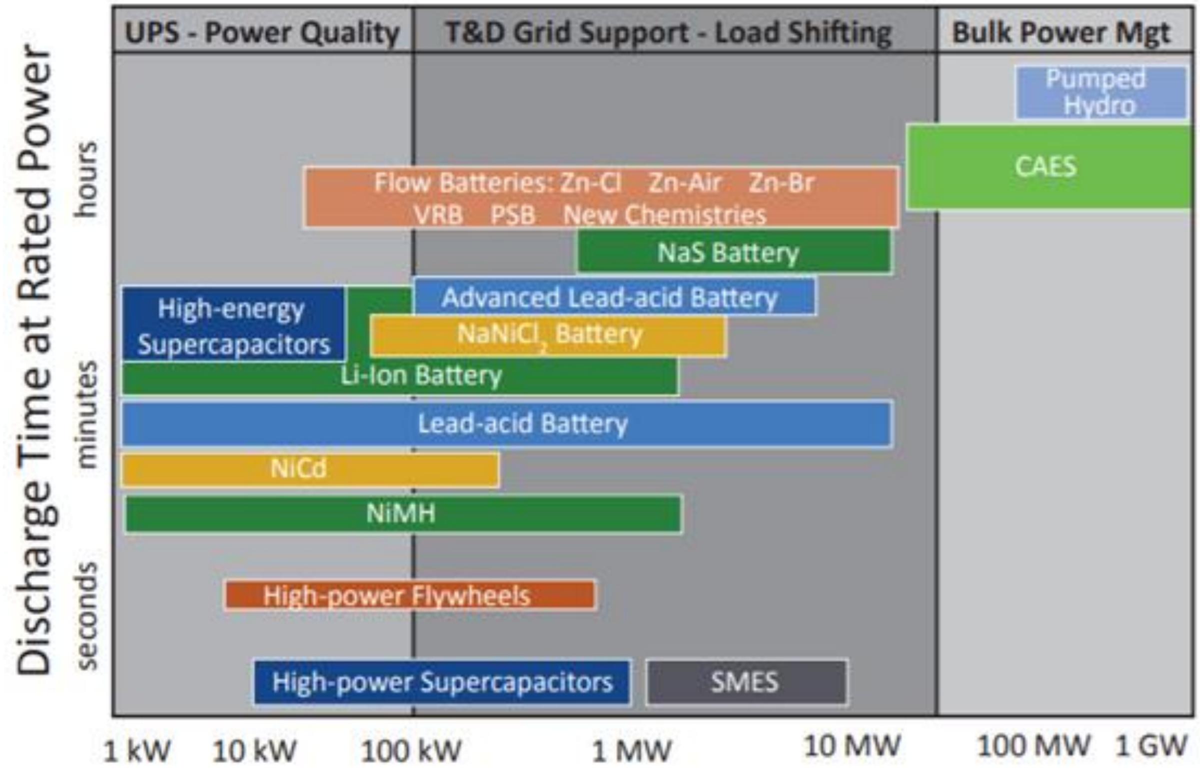

Figure 5: Comparison of different electricity storage systems in terms of stored power and the required discharge time from reference (*12*).

On the other hand, electrochemical storage schemes, rechargeable batteries in particular, have shown promise to provide a wide range of options suiting the needs from small scale storage with fast discharge time to regulate the power quality of electricity to the large-scale bulk energy management needs in the electric grid.

For instance, Li-ion battery (LIB) chemistry with its high energy/power density shows promise for load offsetting and power quality regulation in the grid. This chemistry is also suitable for use at small to intermediate scales serving consumers at homes and at locally established power regulation facilities. As such it has already seen use in many pilot projects in the grid and at homes in combination with roof-top solar panels. (*13*) Nonetheless, LIB usage on a larger scale is problematic because of cost issues and safety concerns associated with highly reactive lithium and flammable organic electrolytes. Moreover, there are long-term supply chain and sustainability issues associated with lithium and cobalt that are essential for the technology. (*14*)

By comparison, although toxic, lead-acid batteries are more favorable for larger scale establishments because they come at lower cost per kWh stored, have easier supply chain issues, and have much lower concerns for flammability. The maturity of lead-acid battery technology also presents additional advantages in reliability and fundamental understanding. (*15*)

Moreover, new redox battery chemistries based on abundant elements like Zn and Na are being researched for grid applications. (*16-18*) Such batteries could potentially provide better capacity, rate and cycling capabilities while still being cost effective as they use cheaper, safer and earth abundant raw materials. (*16*, *17*) In addition, flow batteries, which are yet another type of electrochemical energy storage devices, are also being researched for applications in the grid. (*19-21*) Flow batteries are different than conventional batteries mainly in terms of the component in which the energy is stored. Unlike conventional batteries which store energy in the electrodes, flow batteries store energy in the electrolyte - anolyte and catholyte – placed in separate tanks. As such they have the potential to be scaled for applications in the grid at different levels. (*20*)

To summarize, the global energy landscape is changing rapidly towards the accommodation of clean and renewable sources which inherently require storage systems to be embedded in the grid. Compared to other solutions, rechargeable batteries present the greatest potential especially by being able to provide solutions at different scales with different output power requirements while still being cost effective and sustainable in the long run.

1.4: References

1. H. Ritchie, M. Roser, P. Rosado. (Our World in Data, 2022).
2. R. Fouquet, A brief history of energy. *International handbook on the economics of energy*, 1-19 (2009).
3. D. I. Stern, in *Routledge handbook of Energy economics*. (Routledge, 2019), pp. 28-46.
4. M. Graham, W. H. Dutton, *Society and the internet: How networks of information and communication are changing our lives*. (Oxford University Press, 2019).
5. S. Kaplan, World is on brink of catastrophic warming, UN climate change report says. *The Washington Post* **20**, 2-4 (2023).
6. Climate Watch. (World Resources Institute, Washington, D.C., 2022).
7. US: Plug-in Cars Sales Approached 5% Market Share (Q4 2021). (InsideEVs, https://insideevs.com/news/566900/us-plugin-car-sales-2021q4/, 2023).
8. H. Ibrahim, A. Ilinca, J. Perron, Energy storage systems—Characteristics and comparisons. *Renewable and sustainable energy reviews* **12**, 1221-1250 (2008).
9. X. Q. Zhu, J. H. Yan, N. Lu, A Graphical Performance-Based Energy Storage Capacity Sizing Method for High Solar Penetration Residential Feeders. *Ieee Transactions on Smart Grid* **8**, 3-12 (2017).
10. Energy Storage Installations by Year. (DOE Global Energy Storage Database, https://sandia.gov/ess-ssl/gesdb/public/statistics.html, 2023).
11. World Energy Outlook. (International Energy Agency, Paris, 2019).
12. Quadrennial Technology Review. (Energy.gov, 2015).
13. G. Zubi, R. Dufo-López, M. Carvalho, G. Pasaoglu, The lithium-ion battery: State of the art and future perspectives. *Renewable and Sustainable Energy Reviews* **89**, 292-308 (2018).
14. N. Nitta, F. Wu, J. T. Lee, G. Yushin, Li-ion battery materials: present and future. *Materials today* **18**, 252-264 (2015).
15. G. J. May, A. Davidson, B. Monahov, Lead batteries for utility energy storage: A review. *Journal of energy storage* **15**, 145-157 (2018).
16. K. Kubota, M. Dahbi, T. Hosaka, S. Kumakura, S. Komaba, Towards K-ion and Na-ion batteries as “beyond Li-ion”. *The chemical record* **18**, 459-479 (2018).
17. J. O. G. Posada *et al.*, Aqueous batteries as grid scale energy storage solutions. *Renewable and Sustainable Energy Reviews* **68**, 1174-1182 (2017).
18. D. Kundu, B. D. Adams, V. Duffort, S. H. Vajargah, L. F. Nazar, A high-capacity and long-life aqueous rechargeable zinc battery using a metal oxide intercalation cathode. *Nature Energy* **1**, 16119 (2016).
19. B. Hu *et al.*, Redox-active inorganic materials for redox flow batteries. *Encyclopedia of Inorganic and Bioinorganic Chemistry* **3**, 211-235 (2019).
20. E. Sánchez-Díez *et al.*, Redox flow batteries: Status and perspective towards sustainable stationary energy storage. *Journal of Power Sources* **481**, 228804 (2021).
21. N. Xu, X. Li, X. Zhao, J. B. Goodenough, K. Huang, A novel solid oxide redox flow battery for grid energy storage. *Energy & Environmental Science* **4**, 4942-4946 (2011).

Chapter 2: Background on Batteries

2.1: Historical development

In this section, we review the historical development of batteries at a basic level. We start with the invention of the first very basic battery and briefly review each of the important developments in chronological order leading to the present day commercially available rechargeable batteries.

Batteries have come far since the invention of the first electrical battery by Italian scientist Alessandro Volta in 1800. (*1*) His battery, known as voltaic pile, used zinc and copper electrodes separated by paper soaked in brine solution as electrolyte, and it was the first device that could provide continuous electrical current to a circuit. Figure 1 shows the original drawings of the voltaic pile.

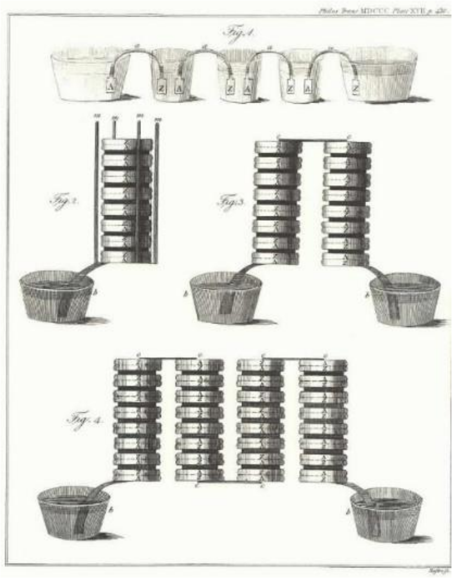

Figure 1: Original drawing of voltaic piles. Reproduced from Volta. (*1*)

About 40 years later, British chemist John Frederic Daniell invented a new cell that solved the "hydrogen bubble" problem of the Voltaic pile. This problem, in which bubbles collected on the bottom of the zinc electrodes, limited the pile's lifespan and uses. The Daniell cell used a copper pot filled with copper sulfate solution, which was further immersed in an earthenware container filled with sulfuric acid and a zinc electrode. (*2*)

The lead-acid battery was the first rechargeable battery, invented in 1859 by French physicist Gaston Planté. (*3*) Figure 2 shows the schematic of a Lead-acid battery at fully charged state. Lead-acid batteries excel in two areas: they are very low cost, and they can also supply high surge currents. In the modern era, this makes them suitable for use in vehicles even with today's technology, and it's part of the reason why billions of dollars of lead-acid batteries are sold globally. (*2*)

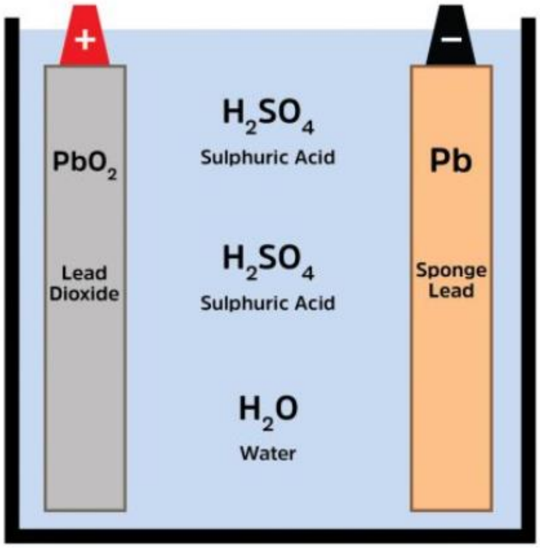

Figure 2: Schematic of a Lead-acid battery in fully charged state. During discharge, both electrodes (Pb and PbO_2) react with the electrolyte (aqueous H_2SO_4) to form $PbSO_4$. Reproduced from reference (*5*).

NiCd batteries were invented in 1899 by Waldemar Jungner in Sweden. (*4*) The first were "wet-cells" similar to lead-acid batteries, using a liquid electrolyte. NiCd batteries helped pave the way for the modern technology of handheld consumer electronics such as the transistor radio.

Popularized by brands like Duracell and Energizer, alkaline batteries are used in numerous regular household devices from remote controls to flashlights. They are inexpensive and typically non-rechargeable. The modern alkaline battery was invented by Canadian engineer Lewis Urry in the 1950s. (*6*) Using Zn and MnO_2 in the electrodes, the battery type gets its name from the alkaline electrolyte used: KOH.

Next came the nickel metal hydride (NiMH) formulation, which is similar to the rechargeable NiCd battery, but uses a hydrogen-absorbing alloy instead of Cd to reduce toxicity concerns. This makes it environmentally safer and also helps to increase the energy density. NiMH batteries are used in power tools, digital cameras, and some other electronic devices. They also were used in early hybrid vehicles such as the Toyota Prius. (*7*) The development of the NiMH spanned two decades and was sponsored by Daimler-Benz and Volkswagen AG. The first commercially available cells were in 1989. (*8*)

The emergence of the first Li ion battery in the 1970s can be attributed to the pioneering work of Michael Stanley Whittingham. With a combination of Li metal and TiS_2 as electrodes, Whittingham (*9*) laid the foundation for further exploration in this field. Successively, John Goodenough replaced the cathode with $LiCoO_2$ which gave the battery higher voltage and resulted in higher-capacity batteries. (*10*) During this era, Samar Basu demonstrated the electrochemical intercalation of lithium in graphite. (*11*) Unfortunately, the battery cells developed from it suffered from rapid deterioration of the graphite with each recharge. Akira Yoshino then used petroleum coke instead of graphite as anode along with the $LiCoO_2$ cathode developed by Goodenough to develop the first commercially viable battery. (*12*) This battery employed Li-ion intercalation in both the electrodes eliminating the fire hazard associated with the use of metallic Li as anode. The first Li-ion battery was released by Sony later in 1991. Since then, intensive developments and technological diversification have taken place with an expanding range of applications. Owing to the part Li-ion battery has played in our modern world, the main contributors in the successful implementation of the Li-ion battery technology – J. B. Goodenough, M. S. Whittingham, and A. Yoshino – were awarded with the prestigious Nobel Prize in Chemistry in the year 2019. (*13*)

Li-ion batteries have high energy density and now have a number of specific cathode formulations for different applications. For example, $LiCoO_2$ cathodes are used in laptops and smartphones, while $LiNiCoAlO_2$ cathodes, also known as NCAs, are used in the batteries of vehicles such as the Tesla Model S. Graphite is a common material for use in the anode, and the electrolyte is most often a type of lithium salt suspended in an organic solvent. A more detailed discussion of the Li-ion battery chemistry will be included in the coming sections.

While Li-ion batteries are often used for stationary storage (especially for grid regulation), the emphasis of stationary storage on price per unit capacity rather than power or energy density has opened a new and growing market for other battery chemistries, discussed later in the chapter.

2.2: Batteries in the modern world

2.2.1: Modern relevance

In the present day, the need to transition from fossil fuels to renewable energy sources has resulted in a considerable increase in research and commercialization of application-specific modes for electrical energy storage (EES). The applications that require EES are diverse, including power supply systems, transportation systems, etc. Each application has different segments, for instance, power supply systems could refer to grid-connected or off-grid systems. As such the EES solutions also need to be diverse in terms of the key properties including energy density, specific energy, specific power, round-trip efficiency, self-discharge rate, calendar and cycle lives, full charge and discharge times, initial cost, and safety. It should be highlighted that while some EES systems are strictly stationary, others are adaptable to mobile applications. Furthermore, some technologies can be produced as small size units, while others have limited adaptability to that. As the need for sustainable energy solutions intensifies, the market for EES technologies will continue to grow, and the most suitable technology for each application will evolve accordingly.

Batteries offer the widest range of EES technologies. These include lead-acid, lithium-ion, nickel-cadmium, nickel metal hydride, sodium-sulfur, vanadium redox, zinc-bromine, nickel-hydrogen, nickel-zinc, molten salt, and metal-air batteries, among others. Some batteries operate at ambient temperature, while others, such as molten salt operate at high temperatures.

Li-ion batteries are widely recognized as the power source for portable electronic devices such as smartphones, tablets, and laptops. However, their potential goes far beyond that, as they can play a significant role in the development of energy sustainability. With the integration of high shares of photovoltaic (PV) and wind energy in the power mix, batteries, combined with the electricity grid, can provide storage capacity and ancillary services. This can lead to an electricity mix with a small carbon footprint, which is essential for the widespread implementation of electric vehicles (EVs), where Li-ion batteries are the present technology of choice. (*14*)

Batteries also hold enormous potential for off-grid power supply systems, particularly in combination with solar home systems (SHS), to provide reliable access to electricity in developing regions. Despite numerous applications, the most relevant ones, in terms of present and projected market share, are portable electronic devices, road transport and electrical grid. It is estimated that by 2030, we will have over 1 TWh of globally installed storage capacity in batteries. This level of expansion poses additional challenges beyond those already stated, such as energy density and fast charging. (*15*)

One of the critical challenges is sustainability, which means ensuring that the resources used in battery production are renewable and not depleted over time. Additionally, it is essential to consider the recyclability of the components and the lifecycle of the system, which affects the battery's durability and overall sustainability. Furthermore, safety is of utmost importance to ensure that the batteries do not pose any risks to users and the environment. Finally, the cost of battery production must remain reasonable to ensure that the technology remains viable and accessible to the majority.

The need for viable solutions is intensifying rather than diminishing as we seek to reduce CO_2 emissions to mitigate the effects of global warming and shift from fossil fuels. According to the International Energy Agency, we can expect fossil fuel resources to dwindle from the mid-2020s onward, warranting the need for the development and implementation of renewable energy infrastructures in the present. (*16*)

2.2.2: Vehicle electrification

Hybrid electric vehicles (HEVs) represent a fusion of conventional internal combustion engines and electric propulsion systems, featuring both a battery and an electric engine. This ingenious combination leads to enhanced performance and improved fuel economy. What sets HEVs apart is their energy recovery system, which deftly captures deceleration power and stores it in the battery, ready for later acceleration. These vehicles can thrive with a small battery, typically just a few kWh in capacity. Given this modest capacity, there's little practical rationale for incorporating an external electric plug-in option to recharge the battery. In contrast, the plug-in hybrid electric vehicle (PHEV) boasts a larger battery, typically exceeding 8 kWh, justifying the need for external recharging. PHEV batteries offer ample capacity, allowing for an all-electric driving range of over 30 km. (*17*) Figure 3 shows a photo of a Toyota Prius car (a PHEV) and the general schematic of its mechanical and electrical connections.

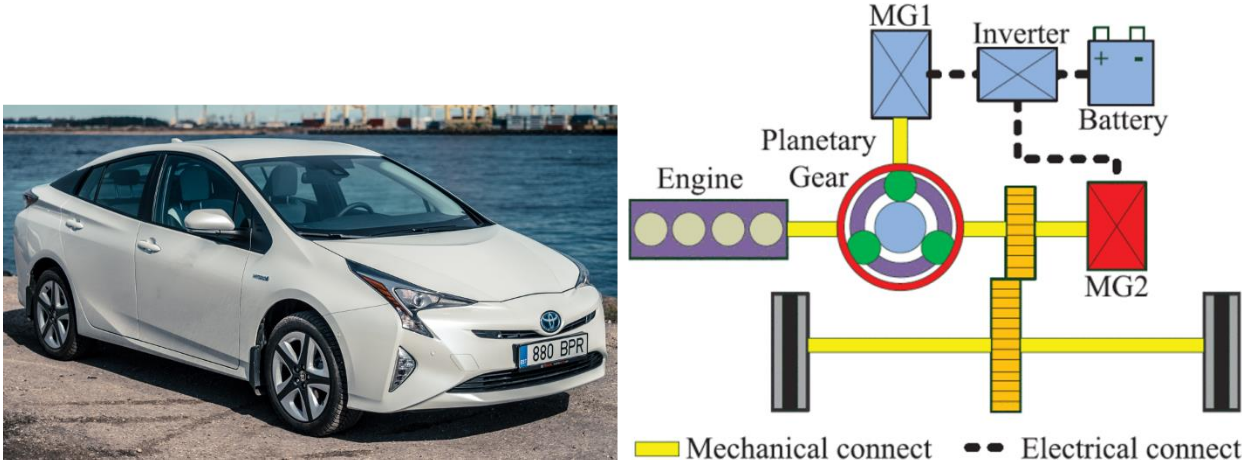

Figure 3: (left) Photo of a Toyota Prius car, (right) schematic of the electrical and mechanical connections for the same car. Figure (right) reproduced from Chen *et al*. (*18*)

For the electric vehicle (EV), the situation is very different. EVs bid farewell to the internal combustion engine and all its associated components, fully embracing electric driving. The battery capacity for EVs typically starts at around 18 kWh, enabling them to achieve impressive driving ranges, usually exceeding 120 km on a single charge. (*18*) Figure 4 shows the plot of HEV, PHEV and EV sales in USA and it is clear that the sales of each of these categories are rising rapidly, especially in the last couple years.

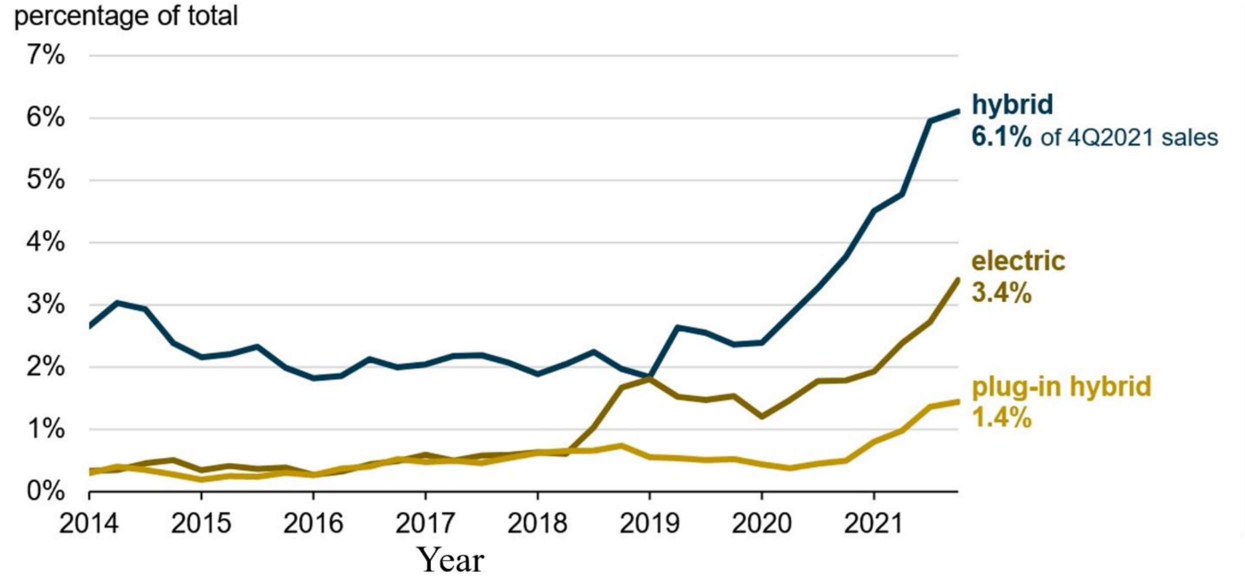

Figure 4: A plot of the quarterly sales of light-duty electric vehicles in USA by powertrain from 2014 to 2021. Y-axis is the percentage of total light-duty vehicle sales in that quarter. Figure reproduced from reference (*19*).

The lithium iron phosphate (LFP) battery, introduced commercialized in 1999, quickly earned a reputation as a promising technology thanks to its robustness, inherent safety features, and its reliance on abundant, eco-friendly materials. Impressively, these batteries can withstand up to 2000 full cycles and operate smoothly across a wide state of charge (SOC) window, ranging from 15% to 100%, maintaining a constant voltage within this range and thereby ensuring consistent performance. No doubt, these advantages initially positioned the LFP battery as an exciting candidate for EVs. However, its specific energy, falling in the 90–140 Wh/kg range, falls short when compared to other Li-ion chemistries. (*14*) As a result, the LFP battery has not played a major role in the EV industry, but it has found better success in e-bikes, which have been an unexpected success, with a global market size valued at around USD 50 billion in 2023. (*20*)

We now address another Li-ion battery type – the nickel cobalt aluminum (NCA) battery. The oxide cathode of this battery is crafted from a blend of 80% nickel, 15% cobalt, and 5% aluminum, making its reliance on cobalt relatively moderate compared to lithium cobalt oxide (LCO) batteries. NCA batteries stand out with their remarkable specific energy, ranging between 200–250 Wh/kg, as well as their high specific power, enduring around 1000–1500 full cycles. (*14*) These features have made NCA batteries highly sought-after for EV applications, and there are even plans for grid-connected use, such as for backup and load shifting. Notably, Tesla, a prominent player in the EV market, uses NCA batteries in its vehicles. With Tesla's ambitious manufacturing projections, their Gigafactory in Nevada, which boasts an impressive annual manufacturing output of 35 GWh, is capable of producing enough batteries for 500,000 EVs per year. Such manufacturing at extreme scale is expected to lead to cost advantages for the NCA cell, making it a formidable choice.

Another contender for EV use is the nickel manganese cobalt (NMC) battery, consisting of a $Li(Ni_{1-x-y}Mn_xCo_y)O_2$ cathode and a graphite anode. Compared to NCA, the NMC battery has lower energy density, typically falling within the 140–200 Wh/kg range, but it compensates with a longer cycle life, ranging from 1000–2000 cycles. (*21*) The proportions of nickel, manganese, and cobalt in the NMC battery can be varied to influence its characteristics, offering tailored solutions for specific applications. By increasing the mole fraction of Ni, specific energy is increased while increasing the share of manganese enhances specific power.

Although the LFP batteries initially showed promise for EV applications due to their safety and durability, a lower specific energy limited its widespread adoption in the EV industry, finding a more fitting role in e-bikes. On the other hand, NCA and NMC batteries have emerged as powerhouses for EVs, with NCA batteries being the choice for Tesla's electric vehicles and NMC batteries dominating the rest of the EV and PHEV markets.

A few years back, some car manufacturers were still exploring alternative battery technologies, like NiMH, as evidenced by Mitsubishi's focus. However, the landscape has undergone a transformative shift, and today the road-transport sector is unequivocally dominated by Li-ion batteries, with little likelihood of this changing in the near future. (*22*) The supremacy of Li-ion lies in its specific energy, and within the realm of Li-ion technologies, two chemistries stand out for their excellence in this aspect: NMC and NCA, which have become the primary contenders for automotive applications. (*14*) Until recently, some manufacturers experimented with combinations of NMC and LMO cells to harness the strengths of both. Yet, a paradigm shift has occurred, leading to battery packs exclusively featuring NMC cells. This strategic move allows for an extended electric driving range without adding unnecessary weight to the battery pack.

In this competitive arena, the LCO battery finds itself marginalized within the car industry. LCO cells suffer from a shorter cycle life, present safety concerns, and heavily rely on the use of critical cobalt, rendering them less favorable when compared to NMC and NCA alternatives. Interestingly, only one – the Chinese company BYD – chooses to adopt a different chemistry, namely LFP cells. This unique choice springs from the inherent safety, reliance on abundant and eco-friendly materials, and commendable cycle life offered by LFP batteries. BYD aims to bridge the gap in specific energy through battery cell innovation, as the current model, the EV BYD E6, while modestly powered, carries a rather hefty curb weight and still lags behind in this crucial aspect. (*14*)

In summary, the current electric vehicle landscape highlights the dominance of Li-ion technology, particularly NMC and NCA chemistries, while other contenders like NiMH and LCO have retreated from the limelight. BYD stands as a lone pioneer with its LFP cells, striving to bolster its position through advancements in specific energy, a critical factor in the competitive world of electric vehicles. In any case, as battery technology continues to advance, we can expect even more exciting developments in the field of electrochemical energy storage for electric vehicles.

2.2.3: Electrical grid modernization

As pointed out in Chapter 1, the steady increase in global energy needs and the progressive transformation towards renewable energy generation points towards the inevitable integration of the renewable energy sources to the electric grid and its eventual modernization. The present electric grid can be understood as a one-way delivery system with minimal flexibility where the load and generation are always matched. Now that the integration of renewable sources is reaching the scale of tens of percent of total energy production in many countries, the whole electric grid system needs to be revised and modernized. This entails the adoption of the so-called ‘smart grid’ with distributed generation and two-way energy flows enabling the large-scale integration of renewables and the ability to manage diverse generation mix and intermittency of the sources like wind and solar. Among other technologies that are required for such transformation, EES assumes the leading role and essentially drives the entire transformation. Besides allowing the efficient integration of renewables to the electric grid, energy storage at the grid level can enable significant cost savings while improving the infrastructure reliability and efficiency. As such it has seen consistent growth in the last decade as seen in Figure 5, where we show the global energy storage projects installed over time.

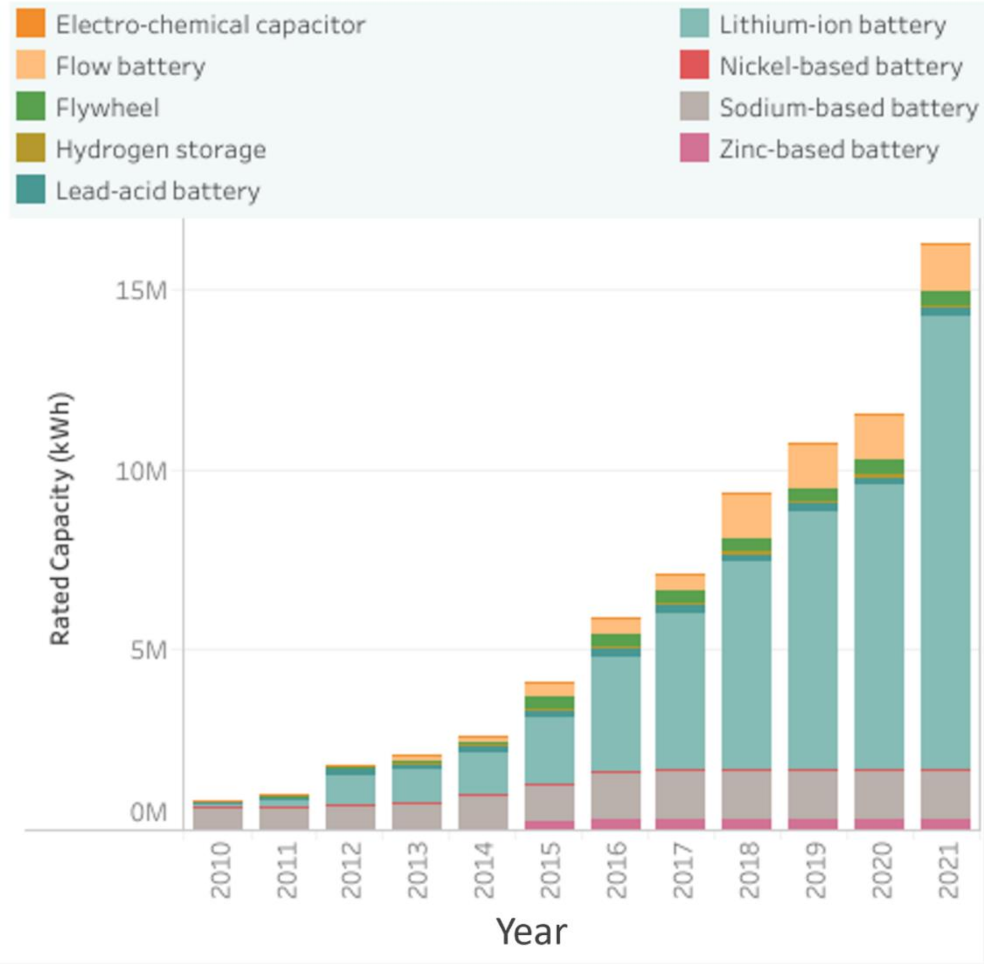

Figure 5: Global energy storage project installations over time. Figure adapted from DOE's Global Energy Storage Database. (*23*)

Electrical energy storage is essential at various stages of the electric grid for different purposes requiring a wide range of capability in terms of energy, power and discharge time. The choice of electric energy storage device depends on its application in the grid. Table 1 shows the three categories of grid-level energy storage applications, primarily driven by the discharge time required. Applications like frequency regulation and stabilization pertaining to the power quality of supplied electricity require discharge times of seconds to minutes at the most, while functions like ramping and supplying power during switching sources require discharge times up to an hour in general. These applications need higher power density output from the storage system although the total amount of energy required is relatively smaller. On the other hand, discharge times needed in the case of energy management applications extend to several hours at a time and require higher total stored capacity.

Table 1: Different classes of energy storage applications for the grid.

Common Name	**Example Applications**	**Discharge Time Required**
Power Quality	Transient Stability, Frequency Regulation	Seconds to Minutes
Bridging Power	Contingency Reserves, Ramping	Minutes to ≈1 hour
Energy Management	Load Leveling, Firm Capacity	Hours

As presented in Figure 6, electrochemical energy storage, batteries in particular, have the widest range of capabilities and serve as the most versatile and practical solution towards achieving a full integration of renewable energy into the electricity mix and realizing the ultimate transition to a smart grid. Some batteries can be scaled to store large amounts of electrical energy to aid in bulk energy management, while others are able to provide high power density making batteries the best candidate to be used to fulfill the requirements of the electric grid at different levels. Furthermore, different chemistries with their respective characteristic metrics match the requirements of different applications in the grid-level storage scheme. In that regard, various battery chemistries have already been adopted to some level with ongoing development of the field. The most used batteries for grid-level storage are Li-ion, Na-metal, Pb-acid and redox flow batteries in the order of percentage deployment, of which the most used Li-ion battery covers 3/4th of the total share. (*23*) Large projects are being installed at competitive costs even with current technology. For example, in 2017, Kauai Island Utility Cooperative installed a solar-plus-storage at \$0.11/kWh with a 100MWh battery capacity. (*23*) The total installed capacity of battery storage in the U.S. reached 10.8 GWh in 2023 and is continuing to grow with an ambitious goal of adding 75 GWh more by the end of 2027. (*15*) For reference, the total electricity generation in U.S. in the year 2022 was about 4000 TWh with renewable energy generation of about 900 TWh. (*15*)

For such goals to be fulfilled there are many issues to be addressed including the energy density, cost, cycle life, sustainability and safety of batteries. Up to the present, Li-ion batteries, the industry standard, have been researched the most and with promising results in terms of energy density, cycle life and also cost to some extent. But, because of resource limitations for Li and Co, there is great reason for concern that this chemistry cannot keep up with the growing need for vehicle electrification and grid storage. Furthermore, the safety concerns of fire in a battery that uses a very active Li in concert with flammable organic electrolytes are high and this only exacerbates the situation when the batteries are stacked to scale the storage system to large sizes to suit for the grid level storage scheme. In that regard, research and development has grown for alternative battery chemistries, especially those that employ abundant materials like Na and Zn and have inherently superior safety, such as by using aqueous electrolytes instead of flammable organic electrolytes. Using water as the electrolyte solvent also decreases battery cost. Among the most studied alternative chemistries are Na-ion, Zn-ion and redox flow batteries. These have the advantage of using earth abundant and non-toxic raw materials that will help check the cost and are also more sustainable. Nonetheless, these still fall behind the mature Li-ion battery in terms of the energy stored: for example, depending on the electrode formulation, Li-ion batteries can have energy density in the range of 325 – 785 Wh/L compared to the energy density range of 250 – 375 Wh/L for state-of-the-art Na-ion batteries. (*25*) In comparison, Zn-ion batteries have been shown to have energy density as high as 450 Wh/L with a capacity retention of more than 80% over 1000 cycles. (*26*)

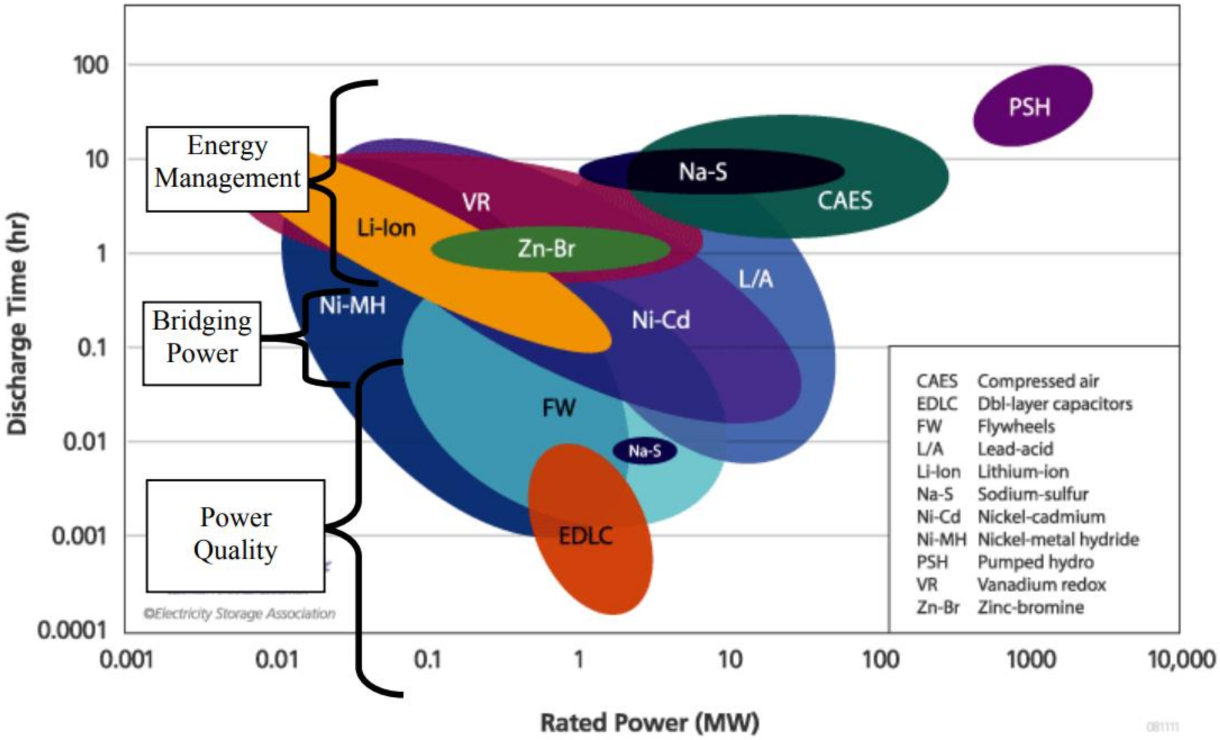

Figure 6: Various energy storage schemes suitable for different purposes in the electric grid in terms of their rated power in MW and discharge time in hour. Reproduced from Ibrahim *et al.* (*24*)

Another chemistry that is being considered for the purpose of grid level storage is the Pb-acid battery, which on itself is a matured and established battery technology. It has the advantage of having a long history and understanding of its working mechanisms along with durability and long cycle life. The main drawbacks of Pb-acid battery chemistry are the use of toxic Pb, the limited energy density that can be obtained from this chemistry and the slower response times compared to Li-ion batteries. Pb-acid batteries also suffer from shorter self-discharge time compared to Li-ion counterparts meaning that if left unused the Pb-acid battery loses its capacity faster than Li-ion battery. In a large-scale system this can amount to a large loss of usable energy, driving up the cost of operation.

Nevertheless, with more research and innovation these and other alternative chemistries have the potential to support the full integration of renewable energy sources to the grid and keep up with growing global energy needs. More efforts are needed, especially with regards to increasing energy capacity, cyclability and safety, and reducing the overall cost. In addition to the innovation in battery materials, the overall adoption of renewable energy and smart-grid also relies on the parallel innovation and development of supporting infrastructure like battery management systems and power electronics.

2.3: State-of-the-art

2.3.1: Li-ion Battery

Among the array of metals available for utilization in battery chemistry, Li stands out as the most promising because of its light weight and remarkable electropositive properties. These intrinsic advantages grant Li-based batteries an unparalleled potential for energy storage. However, the very reactivity that makes lithium so exceptional also presents a technological hurdle in constructing safe battery cells that contain this remarkable metal. Thus far, this challenge has been successfully confronted by sidestepping metallic lithium and instead employing compounds with the ability to liberate Li^+ ions. Figure 7 shows the important discoveries that helped to understand and pave the way for commercialization of modern Li-ion batteries.

A Li-ion battery cell has four essential components: the cathode, anode, electrolyte, and separator. During the charging process, the lithium ions embark on a journey from the cathode, traverse through the electrolyte and the separator, and reach their destination at the anode. When discharged, the ions make their return trip. Notably, the nomenclature of commercial batteries derives from the Li-ion donator housed in the cathode, as it wields significant influence over the cell's properties and distinguishes it from prior large-scale batteries, such as Pb-acid. A diverse range of lithium metal oxides assume this role, including lithium cobalt oxide (LCO), lithium manganese oxide (LMO), lithium iron phosphate (LFP), lithium nickel cobalt aluminum oxide (NCA), and lithium nickel manganese cobalt oxide (NMC). (*28*) These various materials yield markedly distinct battery characteristics. Graphite stands as the prevailing anode material, though some battery manufacturers have explored non-graphite alternatives like lithium titanate ($Li_4Ti_5O_{12}$). (*29*)

The electrolyte, based on lithium salts and organic solvents, assumes a pivotal role. Common lithium salts encompass lithium hexafluorophosphate ($LiPF_6$), lithium perchlorate ($LiClO_4$), and lithium hexafluoroarsenate ($LiAsF_6$). (*28*) Organic solvents play a crucial role in enhancing the mobility of lithium ions, thereby directly impacting battery performance. Prominent organic solvents include ethyl-methyl-carbonate, dimethyl-carbonate, diethyl carbonate, propylene carbonate, and ethylene carbonate. (*28*) In cases where cell casting lacks sufficient resilience, as is often true for polymer Li-ion batteries, a gel electrolyte is employed to prevent electrolyte leakage. To this end, a gel precursor, such as polyethylene-oxide, polyacrylonitrile, poly-vinylidene-fluoride, or polymethyl-methacrylate, is incorporated into the electrolyte. (*14*)

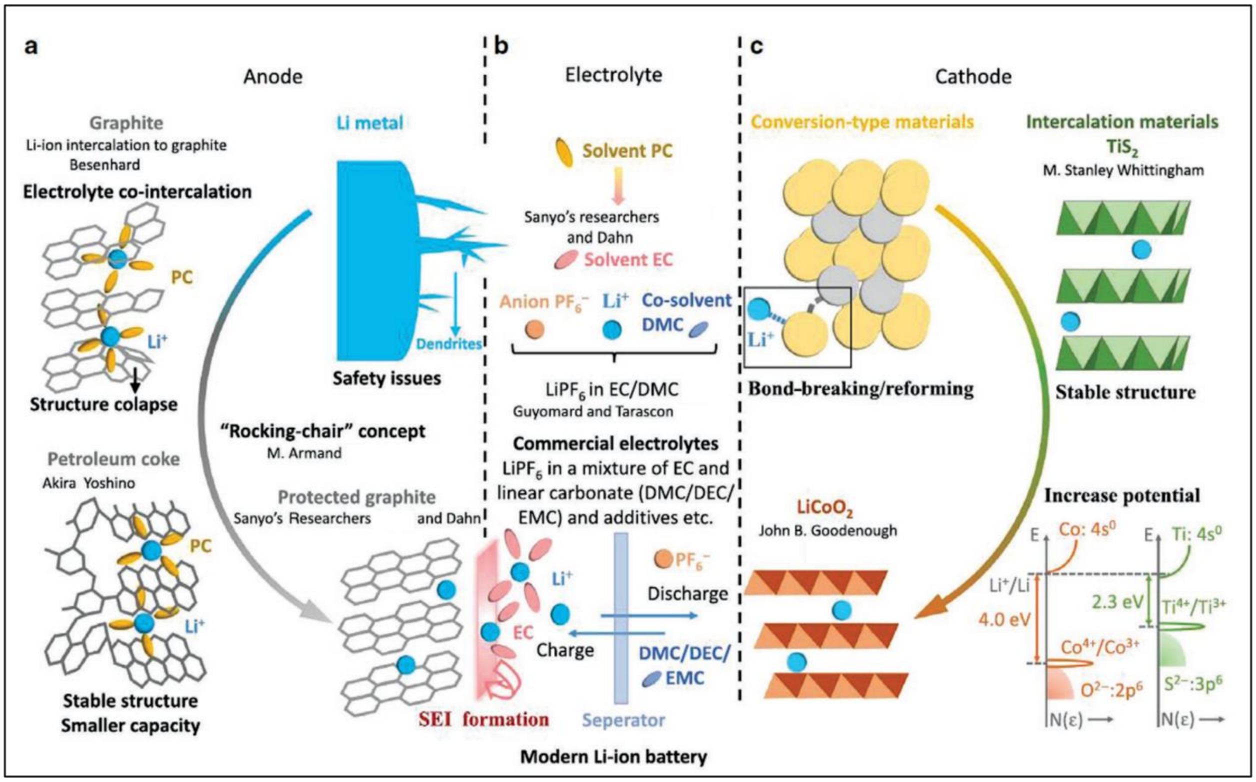

Figure 7: Milestone discoveries that shaped modern lithium-ion batteries. The development of (a) anode materials including lithium metal, petroleum coke and graphite, (b) electrolytes with the solvent propylene carbonate (PC), a mixture of ethylene carbonate (EC) and at least one linear carbonate selected from dimethyl carbonate (DMC), diethyl carbonate (DEC), ethyl methyl carbonate (EMC) and many additives, and (c) cathode materials including conversion-type materials, intercalation materials titanium disulfide (TiS_2) and lithium cobalt oxide ($LiCoO_2$). Reproduced from Xie *et al*. (*27*)

The separator, a safety component positioned between the cathode and anode, serves as a barrier, preventing direct contact and the potential for short-circuiting while permitting the passage of Li^+ ions. Polyethylene and polypropylene rank among the most commonly used separator materials. Li-ion cells can also incorporate additional safety features and elements, such as components that fortify the cell's mechanical integrity, insulators placed at the edges of the electrodes where short-circuit accidents are more likely to occur, and vents for relieving air pressure.

In terms of battery performance, the most important metrics are the specific energy, power, durability, and safety. Figure. 8 shows a semi-quantitative comparison of the properties of the different Li-ion battery chemistries in terms of the cathode used. The specific energy of a Li-ion battery hinges on the choice of cathode, anode materials, and their nano and micro-structures. (*14*) Additionally, cell design exerts a notable influence on this aspect, considering that the active materials merely occupy a fraction of the battery's overall weight. Existing commercial Li-ion batteries span a broad spectrum of specific energy, ranging approximately from 90 to 250 Wh/kg. (*27, 28*) Notably, NCA batteries reign supreme in this regard, while LFP batteries exhibit comparatively lower performance. Specific energy assumes a central role in the development of Li-ion batteries, particularly for mobile applications, resulting in a prevailing upward trajectory in this domain. (*14, 27, 28*)

On the other hand, the maximum power a Li-ion battery can deliver relies on factors such as voltage, density of lithium ions, solid electrolyte interphase (SEI), diffusion coefficient of the electrodes, and their conductivity. The specific power is often quantified through the power to energy (P/E) ratio, which measures the power in kW that a battery can furnish for every kWh of capacity. Power requirements vary depending on the specific application and play a decisive role in battery selection. For instance, PHEVs necessitate batteries with significantly higher P/E ratios compared to electric vehicles EVs. Consequently, PHEVs opt for batteries with a greater number of thinner cathodes and anodes to maximize SEI formation and the immediate availability of charge carriers. (*18*)

The durability of a battery is another important attribute that warrants careful consideration. Battery degradation is an inherent aspect, although its magnitude varies based on usage patterns. Harsh operating conditions, such as extreme temperatures, overcharging, deep discharging, and high amperage, expedite the degradation process. (*30*) This ageing phenomenon primarily arises from the loss of cyclable lithium and active electrode materials, resulting in noticeable capacity fade and reduced power output. A comprehensive exploration of ageing mechanisms and state-of-health (SOH) estimation methods can be found in Barre *et al*. (*30*) For users, the cycle life serves as the most pertinent indicator of durability. It signifies the number of full cycles a battery can sustain under standard operating conditions before crucial performance metrics, such as capacity and power, drop to 80% of their initial values. Nevertheless, depending on the application and considering capacity, power, and safety requirements, a battery might be deemed outdated at a value higher or lower than the conventional 80%. Gaining an in-depth understanding of the ageing mechanisms peculiar to specific battery chemistries paves the way for advanced battery designs with extended cycle lives. Consequently, improvements can be pursued at both the cell and the battery management system (BMS) levels.

Figure 8: Important characteristics of the state-of-the-art commercial Li-ion batteries. Reproduced from Zubi *et al*. (*14*)

2.3.2: Other chemistries – Zn-ion battery

With huge commercial success over the last few decades, Li-ion batteries have been the first choice in many applications ranging from consumer electronics to electric vehicles and now in applications relating to electric grid modernization. But the limited reserves of metals essential to the technology, like Li and Co, inherent safety concerns related to the active ion Li^+, and high costs still pose a significant challenge to the long-term continuous use of Li-ion battery technology. (*14, 22, 28*)

To that end, great efforts are now being diverted to the identification and development of alternative battery chemistries like Na-ion and K-ion, mainly because of their abundance in the earth crust and the low cost. (*25, 31*) But the inherent safety concerns are still there because of the high activity of Na and K, similar to Li. Additionally, the larger size of these ions make it difficult to find suitable electrode materials that can reversibly intercalate these cations.

Multivalent cations like Mg^{2+}, Ca^{2+}, and Zn^{2+}, on the other hand, have been shown to be more suitable in these regards because of their high abundance, better safety features and high energy density primarily because of their divalent character. (*32-35*) Nonetheless, finding compatible electrolytes for the efficient and reversible plating/stripping of Mg^{2+} and Ca^{2+} ions is still challenging because the current state-of-the-art electrolytes face problems like anode corrosion and side reactions to form inactive surface layers hindering the performance of these batteries. (*34, 35*) Furthermore, the very property that makes these multivalent ions desirable also limits the choice of cathodes owing to the stronger electrostatic interaction between multivalent ions and the cathode host material.

On the other hand, Zn-ion batteries (ZIBs) have been quietly gaining momentum because of their remarkable features and capturing the interest of numerous research groups. (*14, 32, 33, 36-40*) ZIBs offer an impressive variety of potential electrolytes, ranging from aqueous to non-aqueous solutions. (*14*) This versatility opens up exciting possibilities for the choice of cathode material and hence their application in various settings. One standout advantage is the higher redox potential of Zn, -0.763 V compared to a standard hydrogen electrode (SHE). This attribute grants

ZIBs the ability to function effectively in aqueous electrolytes, a feat that proves challenging for other mobile ion batteries. This sets them apart, enabling new opportunities for energy storage.

Safety and environmental considerations are also at the forefront. ZIBs demonstrate improved safety and reduced toxicity, making them a safer and more sustainable choice. An intriguing aspect of ZIBs lies in the reversibility of Zn plating/stripping. The use of near-neutral or slightly acidic electrolytes (e.g., pH = 3.6–6.0) helps reduce the formation of Zn dendrites and ZnO by-products, a notorious challenge faced by alkaline Zn-batteries. (*41*) This innovation significantly enhances the cycle life of ZIBs, promising durability and long-lasting performance. Moreover, ZIBs boast a higher volumetric energy density, an impressive 5855 mA h cm^{-3}, compared to 2061 mA h cm^{-3} for Li-ion batteries. (*21*) This is achieved due to the higher density of Zn and the involvement of two electrons in the redox reaction, making them a compelling choice for energy-intensive applications.

With these compelling advantages, it's no wonder that the spotlight is shifting towards Zn-ion batteries. Researchers are eager to explore the immense potential and versatility they offer, opening up new horizons for energy storage and beyond. As technology continues to evolve, we can expect ZIBs to play an increasingly vital role in shaping our energy landscape.

That said, there are still gaps in our understanding of the fundamentals of Zn metal anodes, intercalation in cathode material, involved reaction mechanisms and electrolyte performance. (*21, 33, 36-38, 40, 42-44*) Furthermore, the successful commercialization of these batteries also requires the understanding, development and scaling up of the associated manufacturing processes. For these reasons, we next consider the state-of-the-art of Zn-ion batteries with regards to cathodes, Zn metal anode and electrolytes.

Cathodes

Among the cathode materials for ZIBs, manganese oxide (MnO_2) with a wide variety of crystal structures is the most researched. (*44-50*) Specific capacities of MnO_2 cathodes with different crystal structures and different electrolytes are presented in figure 9. The stability and performance of the MnO_2 cathode depends strongly on the crystal structure. The theoretical capacity of MnO_2 cathodes for the redox $Mn^{4+/3+}$ is 308 mAh/g with an additional 308 mAh/g for the redox $Mn^{3+/2+}$ giving a cumulative capacity of 616 mAh/g for the whole reaction $Mn^{4+/2+}$. The actual capacity of the battery using this material varies significantly owing to the reaction mechanism, the amount of cathode material available for reaction, the reaction kinetics and the formation of byproducts.

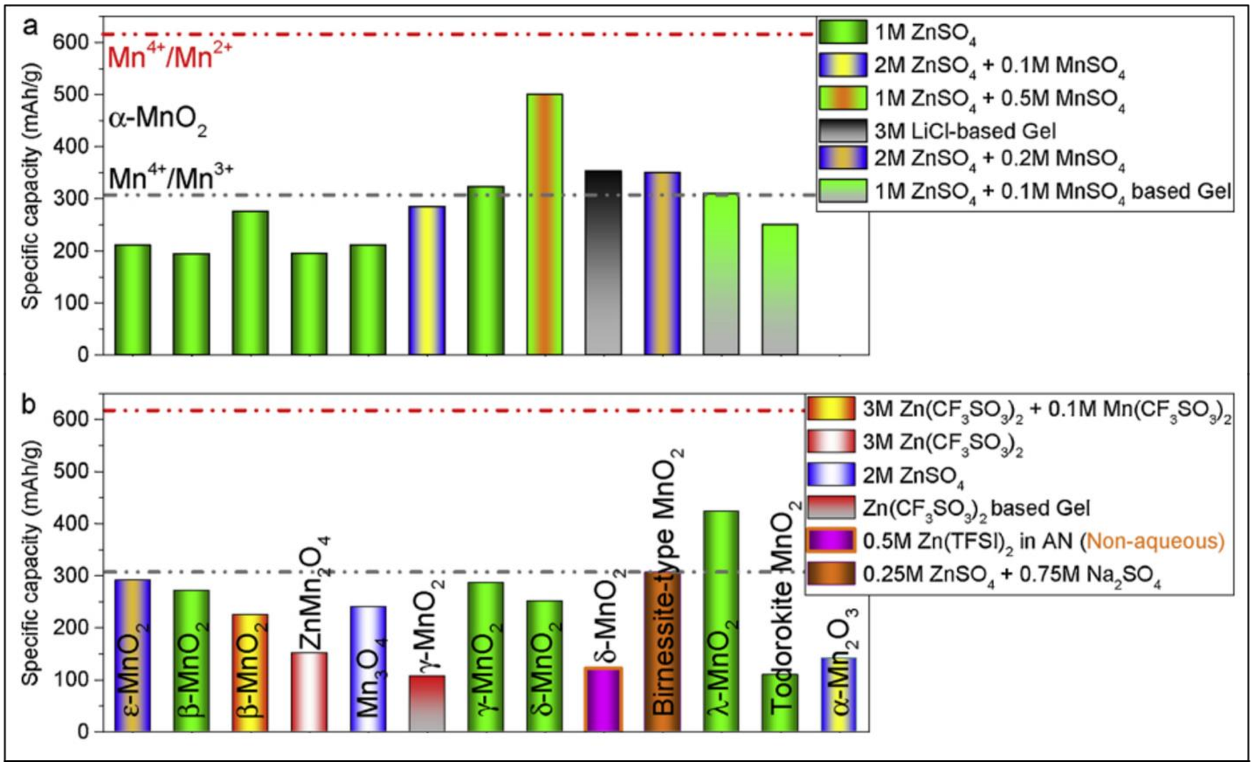

Figure 9: Specific capacity of Mn oxide cathodes with various crystal structures and various electrolytes as indicated in the legend: (a) α-MnO_2, (b) other MnO_2 crystal structures as indicated in figure. Adapted from Ming *et al*. (*42*)

Although it has been shown in different studies that the α-MnO_2 cathode with a 2 x 2 tunnel structure delivers around 200 mAh/g capacity, the actual reaction mechanism is still disputed. (*45, 46*) Some studies support the intercalation mechanism, (*45, 46*) whereas others lean more towards a phase transition mechanism. (*47, 48*) In addition, Pan *et al*. (*49*) demonstrated that a precipitation mechanism explains the so formed byproducts. In any case, the low realized capacity compared to the theoretical capacity puts doubt on the assumed $Mn^{4+/2+}$ as compared to the $Mn^{4+/3+}$ redox reaction. In fact, higher capacities over 300 mAh/g have been reported using α-MnO_2 cathodes with specific nanostructures, compositions and battery configurations, see figure 9 (a), in which case the dominant redox couple is more likely to be $Mn^{4+/2+}$. In addition, the co-intercalation of H^+ and Zn^{2+} is also a favored explanation for the reaction mechanisms in most of MnO_2 cathodes and it has been shown to be true for many phases. (*50, 51*)

Another family of cathodes that are the most used for ZIBs are the vanadium-based layered cathodes. These offer advantages of stability and diversity in terms of various coordination structures found in V-based cathodes. The theoretical capacity of V_2O_5 cathode based on the $V^{5+/3+}$ redox couple is 294.8 mAh/g. Nonetheless, actual capacities of over 300 mAh/g have been reported for the V-oxide based cathodes like $M_xV_2O_5.nH_2O$ where M = alkali, alkaline earth metal. (*26*) The structural stability of these cathodes can be improved by inserting other metals or water into the interlayer spacing making the frame sturdier and the intercalation easier at the same time. (*26, 52*)

Other candidates like Prussian blue analog-based (PBA) cathodes have also been studied for ZIBs with varying success. These refer to the transition-metal hexa-cyanoferrates (MHCFs) and different types of them can be prepared by varying the metal; examples are NiHCF, CuHCF

FeHCF and ZnHCF. These PBAs deliver relatively lower capacities in the range of up to 100 mAh/g. (*21, 42*)

In summary, the average capacity and voltage for the various ZIB cathodes follow this trend: MnO_2 (240 mAh/g, 1.3V) > V-based cathodes (245 mAh/g, 0.75V) > spinel oxides (170 mAh/g, 1.6V) > organic cathodes (335 mAh/g, 1V) > PBAs (70 mAh/g, 1.7V).

Anode

Zn metal is the most used anode in a ZIB because of its high theoretical capacity of 820 mAh/g and environmental friendliness. Zn metal anodes are especially relevant in aqueous ZIBs where the electrochemical voltage window of the battery using aqueous electrolyte is usually limited by the splitting of water via hydrogen evolution reaction (HER) and oxygen evolution reaction (OER). In this regard, Zn metal anode performs well because of the low plating/stripping potential of -0.76 V vs standard hydrogen electrode (SHE). A lot of effort has been recently put into optimizing the Zn metal anode for superior performance using techniques including mixing Zn powders, mixing with activated carbon, (*53*) electrodepositing Zn nanoparticles on carbon cloth, and using organic additives during electrodeposition of Zn. (*54*)

Nevertheless, issues like dendrite formation, corrosion, dead Zn and hydrogen evolution via HER still plague the performance of Zn metal anodes. Figure 10 shows a schematic diagram highlighting these issues. For a successful commercialization of ZIBs employing Zn metal anodes, these issues need to be understood and controlled or eliminated completely. I will now discuss briefly the causes and the strategies that have been explored to mitigate these issues.

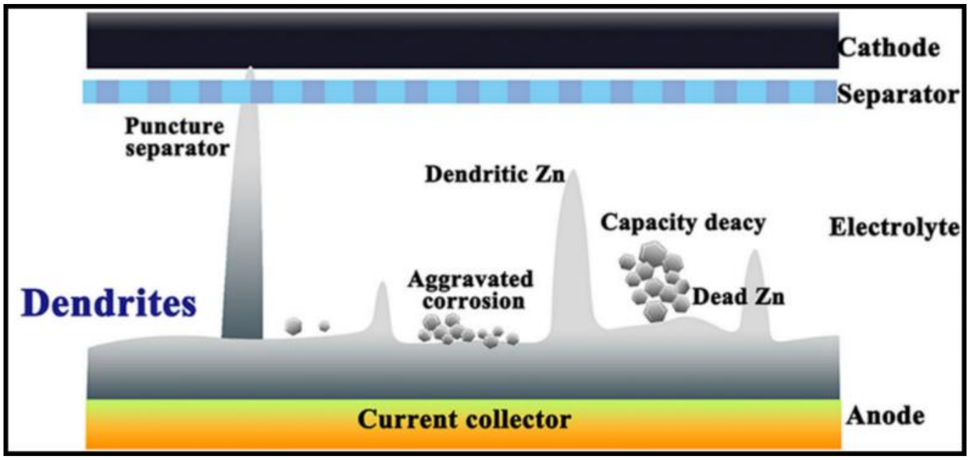

Figure 10: Schematic diagram depicting the issues in Zn metal anode. Reproduced from Xie *et al.* (*55*)

The issue of dendrite formation relates to the inability of the deposited Zn to form a smooth layer on the anode. This inability stems from both the Zn nucleation and growth processes. The nucleation process is generally driven by the electric field, ion concentration and surface energy. (*56*) As such, Zn dendrites can form mainly due to the partial nucleation caused by uneven distribution of electric field (via 'tip effect') and ions or a diminished number of nucleation sites due to high nucleation barriers at the interface. (*56*) In addition, Zn growth can also be affected by the degree of lattice mismatch and orientation of the substrate. (*4, 57*) To control the nucleation and growth of Zn, strategies like using 3D anodes, lattice-matched substrate and using zincophilic interface have been employed. (*56, 58*) Another key strategy used is to regulate the Zn-ion transmission by optimizing electrolytes, using special coatings and modifying separator to have superior mechanical strength. (*37, 40, 55, 59*)

Along with the dendrite formation, HER and corrosion are very detrimental to the performance of aqueous ZIBs. HER and corrosion would consume H^+ from the electrolyte and the excess OH^- will promote side reactions to generate inactive species like $Zn_4(OH)_6SO_4$ in a $ZnSO_4$ electrolyte. (*55*) The corrosion of active Zn in the anode can lead to serious battery capacity fading whereas HER can cause the Columbic efficiency to decline because the electrons will be used for HER besides electrodeposition of Zn.

Since both corrosion and HER are primarily related to the relative activity of water and Zn, various approaches from thermodynamic standpoint like reducing the activity of water and anode, to dynamic standpoint by constructing physical barriers to reduce water-anode contact have been used. (*42, 43, 55*)

Another avenue is to reduce the activity of water which has been tackled by adding additives and using highly concentrated electrolyte (so called 'water in salt electrolytes (WiSE)) where water is stabilized by breaking the hydrogen bond network and enhancing contact ion pairing. (*40, 43, 60, 61*) In addition, physical barriers including adsorption barriers, coating barriers and in-situ reduced barriers have been explored to suppress the corrosion and HER in Zn anodes to some extent. (*42, 55*)

Electrolyte

Electrolytes have a huge bearing on the overall performance of a battery. One of the most important characteristics of the electrolyte is its compatibility with the electrodes and its stability in the desired voltage window. ZIBs have been demonstrated with aqueous and non-aqueous electrolytes, but aqueous electrolytes have higher cost effectiveness, better stability for electrodes and inherent superior safety but suffer from the low voltage window due to water splitting via hydrogen (HER) and oxygen evolution reactions (OER). (*37, 40, 42, 61*)

Aqueous solutions of various zinc salts like $ZnSO_4$, $Zn(CF_3SO_3)_2$, $Zn(NO_3)_2$, $Zn(TFSI)_2$, $Zn(CH_3COO)_2$, $Zn(ClO_4)_2$ and $ZnCl_2$ have been investigated to serve as ZIB electrolytes. Among these, $ZnSO_4$ and $Zn(CF_3SO_3)_2$ are the most studied mainly because of their compatibility with the potential electrodes. In terms of commercialization, $ZnSO_4$ has the benefit of being cheap and readily available compared to $Zn(CF_3SO_3)_2$ which is relatively expensive.

The performance of an electrolyte depends on several factors: salt identity – different salts have different coordination behaviors; concentration effect – electrolyte concentration can alter the electrode performance; solvent effect – different solvation capabilities between aqueous and non-aqueous electrolytes; and additive effect – addition of additives can change the electrolyte performance by changing the dynamics of solvation. (*38, 42, 61*)

A comparison between aqueous $ZnSO_4$ and $Zn(CF_3SO_3)_2$ electrolytes using cation-deficient spinel $ZnMn_{1.86}Y_{0.14}O_4$ cathode suggested higher reversibility and faster kinetics of Zn plating/stripping in the latter. (*62*) This superior performance was attributed to the bulkiness of the $CF_3SO_3^-$ anions that decreased the number of water molecules in the vicinity of Zn^{2+} reducing the solvation effect and facilitating the charge transfer. Addition of $MnSO_4$ to the aqueous $ZnSO_4$ electrolyte significantly improves the stability and capacity of ZIBs, especially in case of Mn-based cathodes. It is believed that the addition of Mn^{2+} species in the electrolyte reduces the dissolution of cathode materials aiding to the enhanced stability and reduced capacity fading. (*42*)

Further, super-concentrated electrolytes or water in salt electrolytes (WiSE) have been demonstrated to be superior in terms of the reversibility of the Zn anode and reduction of dendrite formation. (*37, 40, 61*) These WiSE have been shown to displace water from the first solvation shell of the active ion and thus reduce HER and OER thereby improving the electrode stability and widening the electrochemical voltage window of the aqueous electrolyte. This topic will be discussed in greater detail in the following chapters.

2.4: References

1. A. Volta, XVII. On the electricity excited by the mere contact of conducting substances of different kinds. In a letter from Mr. Alexander Volta, F. R. S. Professor of Natural Philosophy in the University of Pavia, to the Rt. Hon. Sir Joseph Banks, Bart. K.B. P. R. S. *Philosophical Transactions of the Royal Society of London* **90**, 403-431 (1800).
2. J. Desjardins. (Visual Capitalist, https://www.visualcapitalist.com/evolution-of-battery-technology/, 2016).
3. P. Gaston, *Storage of Electrical Energy: And Researches in the Effects Created By Currents Combining Quantity With High Tension*. (Forgotten Books., 1901).
4. A. J. Bard, G. Inzelt, F. Scholz, *Electrochemical Dictionary*. (Springer Berlin Heidelberg, 2012).
5. Lead acid batteries. (ClubAssist, https://clubassist.com.au/Expert-Advice/News/Lead-acid-batteries, 2023).
6. C. Reed (The Guardian, https://www.theguardian.com/news/2004/dec/06/guardianobituaries, 2004).
7. B. Halvorson. (Green Car Reports, https://www.greencarreports.com/news/1120320_lithium-ion-vs-nickel-metal-hydride-toyota-still-likes-both-for-its-hybrids#:~:text=Starting%20with%20the%202015%20model,remain%20the%20case%2C%20Kaneko%20confirmed., 2018).
8. Nickel-Metal Hydride Battery. (Wikipedia, https://en.wikipedia.org/wiki/Nickel%E2%80%93metal_hydride_battery#cite_note-9, 2023).
9. M. S. Whittingham, Electrical energy storage and intercalation chemistry. *Science* **192**, 1126-1127 (1976).
10. K. Mizushima, P. Jones, P. Wiseman, J. B. Goodenough, LixCoO2 (0< x<-1): A new cathode material for batteries of high energy density. *Materials Research Bulletin* **15**, 783-789 (1980).
11. S. Basu *et al.*, Synthesis and properties of lithium-graphite intercalation compounds. *Materials Science and Engineering* **38**, 275-283 (1979).
12. A. Yoshino, K. Sanechika, T. Nakajima, Secondary battery Japanese patent no. 1989293. (1985).
13. P. V. Kamat, Lithium-Ion Batteries and Beyond: Celebrating the 2019 Nobel Prize in Chemistry - A Virtual Issue. *ACS Energy Letters* **4**, 2757-2759 (2019).
14. G. Zubi, R. Dufo-López, M. Carvalho, G. Pasaoglu, The lithium-ion battery: State of the art and future perspectives. *Renewable and Sustainable Energy Reviews* **89**, 292-308 (2018).
15. Short-Term Energy Outlook. (U.S. Energy Information Administration (EIA), https://www.eia.gov/outlooks/steo/report/index.php, 2023).
16. World Energy Outlook. (International Energy Agency, Paris, 2019).
17. L. McDonald. (evstatistics, https://evstatistics.com/2021/09/average-range-and-battery-size-of-phevs-currently-available-in-the-us/#:~:text=The%20mean%20(commonly%20referred%20to,65%20miles%20and%2034%20kWh., 2021).
18. Z. Chen, Y. Wu, N. Guo, J. Shen, R. Xiao, in *2018 IEEE Vehicle Power and Propulsion Conference (VPPC)*. (IEEE, 2018), pp. 1-6.
19. US: Plug-in Cars Sales Approached 5% Market Share (Q4 2021). (InsideEVs, https://insideevs.com/news/566900/us-plugin-car-sales-2021q4/, 2023).
20. E-bike Market. (MarketsAndMarkets, https://www.marketsandmarkets.com/Market-Reports/electric-bike-market-110827400.html, 2022).
21. M. Fichtner *et al.*, Rechargeable batteries of the future—the state of the art from a BATTERY 2030+ perspective. *Advanced Energy Materials* **12**, 2102904 (2022).
22. A. Opitz, P. Badami, L. Shen, K. Vignarooban, A. M. Kannan, Can Li-Ion batteries be the panacea for automotive applications? *Renewable and Sustainable Energy Reviews* **68**, 685-692 (2017).

23. Energy Storage Installations by Year. (DOE Global Energy Storage Database, https://sandia.gov/ess-ssl/gesdb/public/statistics.html, 2023).
24. H. Ibrahim, A. Ilinca, J. Perron, Energy storage systems—Characteristics and comparisons. *Renewable and sustainable energy reviews* **12**, 1221-1250 (2008).
25. K. Abraham, How comparable are sodium-ion batteries to lithium-ion counterparts? *ACS Energy Letters* **5**, 3544-3547 (2020).
26. D. Kundu, B. D. Adams, V. Duffort, S. H. Vajargah, L. F. Nazar, A high-capacity and long-life aqueous rechargeable zinc battery using a metal oxide intercalation cathode. *Nature Energy* **1**, 1-8 (2016).
27. J. Xie, Y.-C. Lu, A retrospective on lithium-ion batteries. *Nature communications* **11**, 2499 (2020).
28. N. Nitta, F. Wu, J. T. Lee, G. Yushin, Li-ion battery materials: present and future. *Materials today* **18**, 252-264 (2015).
29. M. Moorthi, Lithium titanate based batteries for high rate and high cycle life applications. *NEI corporation*, (1860).
30. A. Barré *et al.*, A review on lithium-ion battery ageing mechanisms and estimations for automotive applications. *Journal of Power Sources* **241**, 680-689 (2013).
31. L. Jiang *et al.*, Building aqueous K-ion batteries for energy storage. *Nature Energy* **4**, 495-503 (2019).
32. I. A. Rodríguez-Pérez *et al.*, Enabling Natural Graphite in High-Voltage Aqueous Graphite || Zn Metal Dual-Ion Batteries. *Advanced Energy Materials* **10**, 2001256 (2020).
33. Y. Zhang *et al.*, Pursuit of reversible Zn electrochemistry: a time-honored challenge towards low-cost and green energy storage. *NPG Asia Materials* **12**, 4 (2020).
34. S.-B. Son *et al.*, An artificial interphase enables reversible magnesium chemistry in carbonate electrolytes. *Nature Chemistry* **10**, 532-539 (2018).
35. D. Wang *et al.*, Plating and stripping calcium in an organic electrolyte. *Nature materials* **17**, 16-20 (2018).
36. H. Zhang, X. Liu, B. Qin, S. Passerini, Electrochemical intercalation of anions in graphite for high-voltage aqueous zinc battery. *Journal of Power Sources* **449**, 227594 (2020).
37. C. Zhang *et al.*, A ZnCl2 water-in-salt electrolyte for a reversible Zn metal anode. *Chemical Communications* **54**, 14097-14099 (2018).
38. L. Zhang *et al.*, ZnCl2 "Water-in-Salt" Electrolyte Transforms the Performance of Vanadium Oxide as a Zn Battery Cathode. *Advanced Functional Materials* **29**, 1902653 (2019).
39. H. Zhang, X. Liu, H. Li, I. Hasa, S. Passerini, Challenges and strategies for high-energy aqueous electrolyte rechargeable batteries. *Angewandte Chemie International Edition* **60**, 598-616 (2021).
40. C. Zhang *et al.*, The electrolyte comprising more robust water and superhalides transforms Zn-metal anode reversibly and dendrite-free. *Carbon Energy* **3**, 339-348 (2021).
41. K. Kordesh, M. Weissenbacher, Rechargeable alkaline manganese dioxide/zinc batteries. *Journal of power sources* **51**, 61-78 (1994).
42. J. Ming, J. Guo, C. Xia, W. Wang, H. N. Alshareef, Zinc-ion batteries: Materials, mechanisms, and applications. *Materials Science and Engineering: R: Reports* **135**, 58-84 (2019).
43. F. Wang *et al.*, Highly reversible zinc metal anode for aqueous batteries. *Nature Materials* **17**, 543-549 (2018).
44. X. Zeng, J. Hao, Z. Wang, J. Mao, Z. Guo, Recent progress and perspectives on aqueous Zn-based rechargeable batteries with mild aqueous electrolytes. *Energy Storage Materials* **20**, 410-437 (2019).
45. M. H. Alfaruqi *et al.*, Enhanced reversible divalent zinc storage in a structurally stable α-MnO2 nanorod electrode. *Journal of Power Sources* **288**, 320-327 (2015).
46. C. Xu, F. Kang, B. Li, H. Du, Recent progress on manganese dioxide based supercapacitors. *Journal of materials research* **25**, 1421-1432 (2010).
47. B. Lee *et al.*, Electrochemically-induced reversible transition from the tunneled to layered polymorphs of manganese dioxide. *Scientific reports* **4**, 6066 (2014).

48. B. Lee *et al.*, Elucidating the intercalation mechanism of zinc ions into α-MnO 2 for rechargeable zinc batteries. *Chemical communications* **51**, 9265-9268 (2015).
49. H. Pan *et al.*, Reversible aqueous zinc/manganese oxide energy storage from conversion reactions. *Nature Energy* **1**, 1-7 (2016).
50. N. Zhang *et al.*, Rechargeable aqueous zinc-manganese dioxide batteries with high energy and power densities. *Nature communications* **8**, 405 (2017).
51. J. Hao *et al.*, Electrochemically induced spinel-layered phase transition of Mn3O4 in high performance neutral aqueous rechargeable zinc battery. *Electrochimica Acta* **259**, 170-178 (2018).
52. C. Xia, J. Guo, P. Li, X. Zhang, H. N. Alshareef, Highly stable aqueous zinc-ion storage using a layered calcium vanadium oxide bronze cathode. *Angewandte Chemie* **130**, 4007-4012 (2018).
53. L. Zhang, L. Chen, X. Zhou, Z. Liu, Morphology-dependent electrochemical performance of zinc hexacyanoferrate cathode for zinc-ion battery. *Scientific reports* **5**, 18263 (2015).
54. W. Qiu *et al.*, High-performance flexible quasi-solid-state Zn–MnO 2 battery based on MnO 2 nanorod arrays coated 3D porous nitrogen-doped carbon cloth. *Journal of Materials Chemistry A* **5**, 14838-14846 (2017).
55. C. Xie *et al.*, Issues and solutions toward zinc anode in aqueous zinc-ion batteries: a mini review. *Carbon Energy* **2**, 540-560 (2020).
56. Q. Yang *et al.*, Do zinc dendrites exist in neutral zinc batteries: a developed electrohealing strategy to in situ rescue in-service batteries. *Advanced materials* **31**, 1903778 (2019).
57. A. J. Bard, L. R. Faulkner, H. S. White, *Electrochemical methods: fundamentals and applications*. (John Wiley & Sons, 2022).
58. Y. Yin *et al.*, Dendrite-free zinc deposition induced by tin-modified multifunctional 3D host for stable zinc-based flow battery. *Advanced Materials* **32**, 1906803 (2020).
59. M. Ghosh, V. Vijayakumar, S. Kurungot, Dendrite growth suppression by Zn2+-integrated nafion ionomer membranes: beyond porous separators toward aqueous Zn/V2O5 batteries with extended cycle life. *Energy Technology* **7**, 1900442 (2019).
60. L. M. Suo *et al.*, "Water-in-salt" electrolyte enables high-voltage aqueous lithium-ion chemistries. *Science* **350**, 938-943 (2015).
61. X. Ji, A perspective of ZnCl2 electrolytes: The physical and electrochemical properties. *eScience* **1**, 99-107 (2021).
62. N. Zhang *et al.*, Cation-deficient spinel ZnMn2O4 cathode in Zn (CF3SO3) 2 electrolyte for rechargeable aqueous Zn-ion battery. *Journal of the American Chemical Society* **138**, 12894-12901 (2016).

Chapter 3: Background on Electrolytes

3.1: General overview of electrolytes

Electrolyte is any substance that dissociates into positive and negative ions and consequently conducts electric current by the motion of ions rather than by electrons. The most common electrolytes are acids, bases and salts that dissociate into freely mobile ions when dissolved in a solvent, e.g., water or alcohol. Some salts, such as $ZnCl_2$, can function as electrolytes in the molten state without any solvent, (*1*) whereas some behave as electrolytes even in the solid state (for example AgI). (*2*) We encounter electrolytes in many sectors of the modern world ranging from biology and medicine to industrial processes and energy storage applications. (*3-7*)

Biologically, electrolytes are essential because they maintain the acid-base balance in the body and electrical neutrality in the living cells and are responsible for the generation of potentials in the nerves and muscles that are required for basic life function. (*3*) Furthermore, electrolytes are an integral part of the pharmaceutical industry as they are used as drugs to treat various disorders and play an important role in the processing of many other drugs. (*4*)

Industrially, electrolytes are important for a host of reasons. They are used in the electrolytic extraction of metals like Na and Al from their ores and in the refinement of metals like Cu. (*5*) They are also used for electroplating metals to give a decorative finish and protect from corrosion, and consequently, have found wide uses in the manufacture of jewelry, kitchen utensils, automobile parts and electrical components. (*6, 8, 9*) Furthermore, electrolytes are also used in the production of useful chemicals by various processes, including electrolysis. (*10*)

Electrolytes also have important implications in the geochemical sector. Many of the mineral ore deposits precipitate from the electrolytes (brine solutions), and thus the electrolytes play crucial roles in the transport and formation of these mineral ores in the geological repository. (*11, 12*) Understanding the properties of electrolyte solutions helps scientists to properly model the formation of mineral deposits which in turn aids in mining of important mineral resources for various applications.

Electrolytes also play a crucial role in the electrochemical energy storage sector, which is growing rapidly as a consequence of the need to transition to renewable energy sources. Here, electrolytes are crucial to the performance of the electrochemical devices, and they constitute the platform for the occurrence of the chemical reactions that are required for the working of such devices. For example, in a battery, the choice of electrolytes in combination with the electrodes determines the voltage at which the battery operates, hence dictating important properties like energy density. (*7, 13*)

Thus, electrolytes are important in various sectors of the modern technological world. For these different sectors, there are distinct expectations for an ideal electrolyte, and consequently electrolytes have been researched and studied in each of these contexts to a great extent. (*3-17*) For the purpose of this dissertation, we will briefly discuss the geochemical context and then focus on the application of electrolytes for electrochemical energy storage.

3.2: Electrolytes in Geochemistry

Electrolytes, specifically aqueous solutions, play a significant role in the geochemistry of hydrothermal brines which are the primary sources of metal ore deposits. (*11, 18*) Many important properties of the aqueous solutions rely heavily on the local structure and properties of water and that of the dissolved ions in the solution. Thus, the investigation of local structure and ion pairing of metal ions in aqueous solutions holds significant importance in the field of geochemistry, particularly concerning geothermal ore deposits. (*11, 16*) Understanding the behavior of metal ions in solution is crucial for unraveling geochemical processes and predicting the formation and distribution of mineral deposits in geothermal systems.

In geothermal brines the presence and mobility of metal ions play a pivotal role in mineral precipitation and dissolution. Studies of local structure provide insights into the coordination environments of metal ions, shedding light on their reactivity and potential for forming complexes with other species in the solution. This knowledge is instrumental in comprehending the thermodynamic and kinetic aspects of mineral formation and dissolution reactions. Ion pairing, or the association of metal ions with counter ions, significantly influences the solubility and transport of metals in aqueous solutions. (*19*) In the context of geochemistry, understanding ion pairing is essential for predicting the mobility of metals in natural systems. The interaction between metal ions and ligands in the solution affects their speciation, availability, and overall impact on the surrounding geological environment. Moreover, the study of local structure and ion pairing contributes to our understanding of the stability and reactivity of aqueous solutions under geothermal conditions. This knowledge is crucial for assessing the potential of geothermal fluids to transport, deposit, or leach minerals in the subsurface, influencing the formation of valuable ore deposits or contributing to environmental concerns related to metal contamination. (*11, 19, 20*)

Thus, investigating the local structure and ion pairing of metal ions in aqueous solutions is integral to advancing our understanding of geochemical processes, particularly in the context of geothermal ore deposits. This knowledge not only enhances our ability to predict the behavior of metal ions in natural systems but also has implications for mineral resource exploration, environmental management, and sustainable development practices in geologically active regions. (*11, 17, 21*) This context will be discussed in more detail in Chapter 8.

3.3: Battery electrolytes

3.3.1: Overview

The electrolyte holds a pivotal role in batteries by facilitating charge transfer and balance between electrodes. The electrode–electrolyte interaction significantly influences the interface between them and the internal structure of active materials. (*22*) Choosing an appropriate electrolyte is critical for achieving both safety and high performance in batteries. The rapid progress in electrode material development hinges on finding compatible electrolytes. (*13*) Thus, understanding the reaction mechanisms and designing better electrolytes are crucial for the advancement of safe and efficient batteries.

Figure 1 compares the key properties of various electrolyte types used in batteries in a semi-quantitative fashion. To summarize, aqueous electrolytes are environmentally benign and exhibit high conductivity and hence better rate capability, but they suffer from drawbacks like low energy density, cycling and thermal stability issues. Organic electrolytes and ionic liquids (ILs) on the other hand offer higher operating voltages with moderate ionic conductivity but present low thermal stability, safety issues and environmental risks. Polymer and solid-state electrolytes address concerns related to stability, but face challenges related to low ionic conductivity and hence rate capability issues. While each of these categories are developed and have their own merits, we will focus our discussion on aqueous electrolytes.

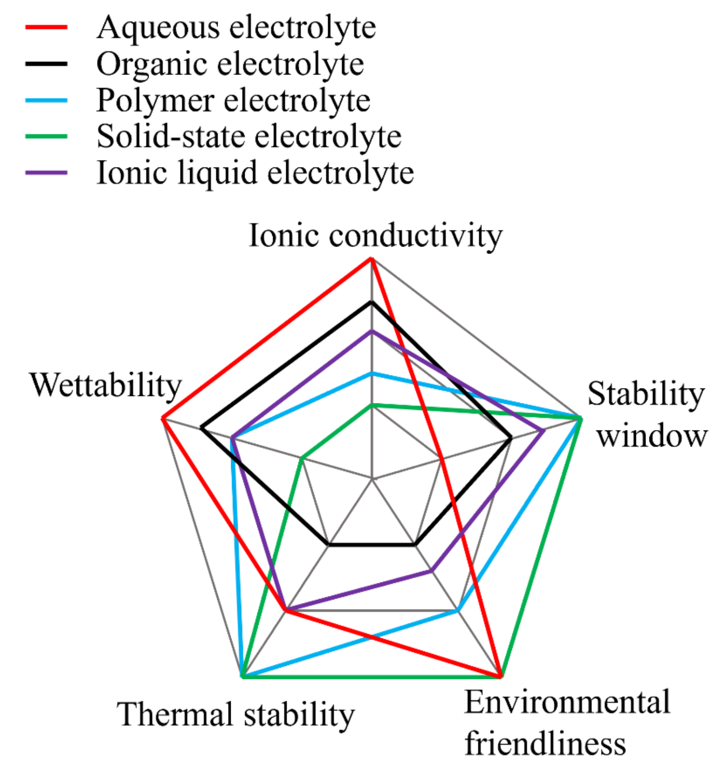

Figure 1: A semi-quantitative comparison of the key properties of various electrolyte types for batteries. Reproduced after Chen, *et al*. (*13*)

In the case of organic liquid electrolytes, the solid electrolyte interface (SEI) can function as a critical component to equip electrolytes with both electrochemical and thermal stability as well as excellent rate capability, which is absent in conventional aqueous electrolytes. (*13*) Thus, a reasonable design is necessary for aqueous electrolytes to enable good stability of the electrolyte/electrode interfaces.

In this context, it is useful to consider the schematic in Figure 2 which shows the open-circuit energy diagram of an aqueous electrolyte. The open circuit potential (V_{OC}) of a battery cell is:

$$eV_{OC} = \mu_A - \mu_C \qquad (1)$$

where 'e' is the magnitude of the electronic charge and μ_A and μ_C are the electrochemical potentials of the anode and cathode, respectively.

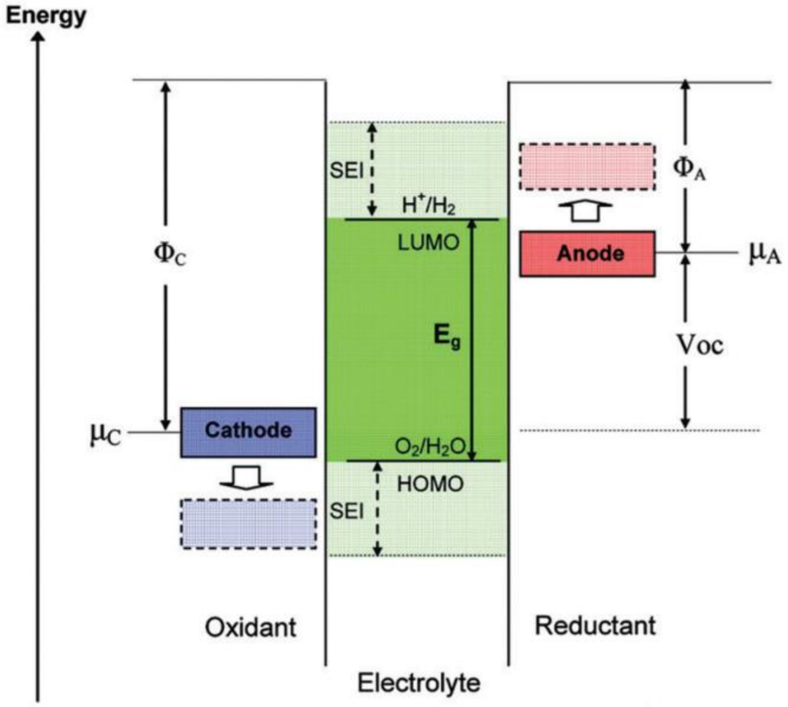

Figure 2: Schematic open-circuit energy diagram of an aqueous electrolyte. Reproduced from Goodenough and Kim (*23*).

The design of a wide electrochemical voltage window (EVW) electrolyte is based on the limiting μ_A and μ_C for the anode and cathode, respectively. (*23*) The EVW of the electrolyte originates from the energy gap (E_g) between the lowest unoccupied molecular orbital (LUMO) and highest occupied molecular orbital (HOMO) of the electrolyte. Thus, to achieve thermodynamic stability in a battery, μ_A and μ_C should be located inside the EVW of the electrolyte, as exhibited in the schematic illustration of the electron energies of the electrode and electrolyte in Figure 2. This is because an anode with μ_A above the LUMO can reduce the electrolyte unless a passivation layer generates a barrier to electron transfer from the anode to the electrolyte LUMO. Similarly, a cathode with μ_C below the HOMO will oxidize the electrolyte unless a passivation layer blocks electron transfer from the electrolyte HOMO to the cathode.

3.3.2: Aqueous electrolytes

Aqueous electrolytes offer numerous advantages compared to non-aqueous systems. (*13, 22*) They are cost-effective, inherently safe, and environmentally friendly. They exhibit high ionic conductivities, stemming from the low viscosity and high permittivity of water, and hence allow superior rate capability and power density in the battery. (*22, 24*) Unlike non-aqueous counterparts, batteries with aqueous electrolytes don't necessarily require tight sealing against water vapor ingress. (*13*) Water, as an electrolyte solvent, is advantageous because its decomposition products, hydrogen and oxygen, do not contaminate the electrolyte. In the event of overcharge, oxygen generated at the positive electrode diffuses through the separators and can be reduced to water at the negative electrode, a phenomenon known as the oxygen-cycle, making the battery tolerant to overcharge. (*22*) Further, it allows for the synthesis or dissolution of a metal oxide lattice in an electrode, involving oxygen from the solvent. (*24*)

However, the primary drawback of aqueous electrolytes is their low energy density primarily due to the relatively narrow EVW, theoretically limited to only 1.23 V. As indicated in Figure 2, the narrow EVW is particularly associated with oxygen evolution in high-potential and hydrogen evolution in low-potential aqueous electrolytes and represents a critical obstacle in augmenting the energy density of aqueous rechargeable batteries (ARBs). (*13, 25*) The same limitation associated with EVW also poses a challenge to achieving extended cyclic lifespan, thereby escalating the operational costs of energy storage stations reliant on ARBs. (*26*)

However, it has been demonstrated in many cases that by properly tailoring the properties of the battery components it is possible to expand the EVW of the aqueous electrolytes. For example, by utilizing electrode materials with high hydrogen and oxygen overvoltage, it is possible to achieve battery voltages up to 2 V, as observed in lead–acid batteries. Further, Wang, *et al*. (*27*) introduced a novel approach involving a sandwich polymer membrane and Li super ion conductor (LISICON) coating on a lithium metal anode. This technique, leveraging the 'cross-over' effect of lithium ions within the coated LISICON, resulted in an ARB achieving an output voltage of approximately 4.0 V — a dramatic step beyond the unmodified EVW of water. In this particular case, the gain in EVW came at a cost in of cyclic stability. (*27*)

Recently, there has been growing interest in highly concentrated aqueous electrolytes, particularly water-in-salt electrolytes (WiSE), due to their augmented EVW and the possibility of achieving higher energy density in batteries. (*13, 28-30*) Multiple mechanisms have been postulated for the improved EVW of these concentrated electrolytes. This issue deserves discussion and the resulting path, below, leads into a direct discussion of the $ZnCl_2$ system which has been a major focus of this dissertation work.

Highly concentrated aqueous electrolytes have seen more interest in recent years following the successful demonstration of wider EVW in Li-based WiSE system. (*13, 28-31*) WiSE are defined by the predominance of salt over the solvent in both weight and volume within a binary system, resulting in a cation solvation sheath that is deficient of water molecules. This WiSE concept has now been applied to various battery chemistries providing improvements like enhancing energy density, electrode and electrolyte stability, and even widening the working temperature windows of ARBs.

For energy density improvement, WiSE have been applied to Aqueous Rechargeable Lithium-ion Batteries (ARLiBs) with halogen conversion–intercalation chemistry in graphite, achieving a capacity of 243 mA h g^{-1} and creating a 4 V class ARLiB with an energy density of 460 W h kg^{-1}. (*27*) In Zinc-Air Battery (ZAB) chemistry, WiSE demonstrated an energy density of 1000 W h kg^{-1} in 200 cycles. (*32*) Additionally, WiSE facilitated aprotic $Li//O_2$ operations in Lithium-Air Batteries (LAB), showcasing their functionality in diverse systems. (*33*) In lithium-sulfur battery (LSB) systems, a solid–liquid two-phase reaction pathway induced excellent cyclic stability, where the liquid polysulfide phase in the sulfide electrode was thermodynamically separated from the WiSE. (*34*) In another study, concentration-controlled cathode dissolution in a $Na_3V_2(PO_4)_3$ cathode demonstrated a novel interface concentration confinement mechanism with WiSE, enhancing the cyclic stability of the $NaTi_2(PO_4)_3//Na_3V_2(PO_4)_3$ full cell. (*35*) WiSE systems, due to their properties like high viscosity and low ion diffusion, also decrease thermodynamics-controlled solvation or dissolution kinetics, providing stability and safety benefits. (*13*) Furthermore, WiSE can extend the working temperature range of ARBs, as demonstrated in a Potassium-ion Battery (PiB) with a wide temperature performance range (-20 °C to 60 °C). (*36*)

The challenges of WiSE at low temperatures, particularly salt crystallization, have been addressed by introducing asymmetric anions. (*37*) While expensive organic salts in WiSE systems increase overall cell costs, some studies explore cost-effective salt substitutions, notably with acetates, chlorates, and halides offering promising achievements. (*28, 38, 39*) Furthermore, ideas like addition of a different salt to make a hybrid WiSE for better electrochemical performance and also for lowering the cost are also being explored. (*40*).

Many of these enhancements brought about by WiSE in ARBs are attributed to the changing solvation structure which provides enhanced electrolyte stability by mitigating the hydrogen evolution reaction/oxygen evolution reaction (HER/OER) of water and limiting electrode dissolution in aqueous electrolytes. (*13, 22, 28, 31, 35, 39, 41*) Figure 3 shows a schematic explanation of the processes occurring at the electrolyte-electrode interface. As depicted in the figure, in a dilute aqueous electrolyte, the availability of water molecules in the vicinity of the electrode during charge transfer between the active ion and the electrode increases the possibility of water reduction which generates H_2 gas via HER and destabilizes the electrolyte. Furthermore, the reduced water then forms a non-passivating inorganic hydroxide layer on the electrode surface which allows the precipitation and dissolution of electrode materials into the electrolyte. In the case of a concentrated aqueous electrolyte, water molecules – especially the free water molecules – are quite depleted and thus anion reduction is favored more than water reduction. This produces inorganic carbonate, sulfate and fluoride-based layers which are effectively inert and thus passivate the electrode surface from dissolution and side reactions but allow the active ions to move in and out of the electrode. (*41*)

Unlike nonaqueous electrolyte systems where cathode and anode materials often surpass the thermodynamic stability limits of electrolyte components, (*42*) the prospect of kinetic safeguarding through a solid-electrolyte interphase (SEI) in aqueous environments had not been previously entertained until the pioneering work of Suo, *et al.* (*31*) These interphases, situated between electrode surfaces and the electrolyte, materialize through the sacrificial decomposition of electrolytes during initial charging, forming a barrier that facilitates ionic conduction while impeding electronic conduction. Their existence significantly broadens the EVW of electrolytes.

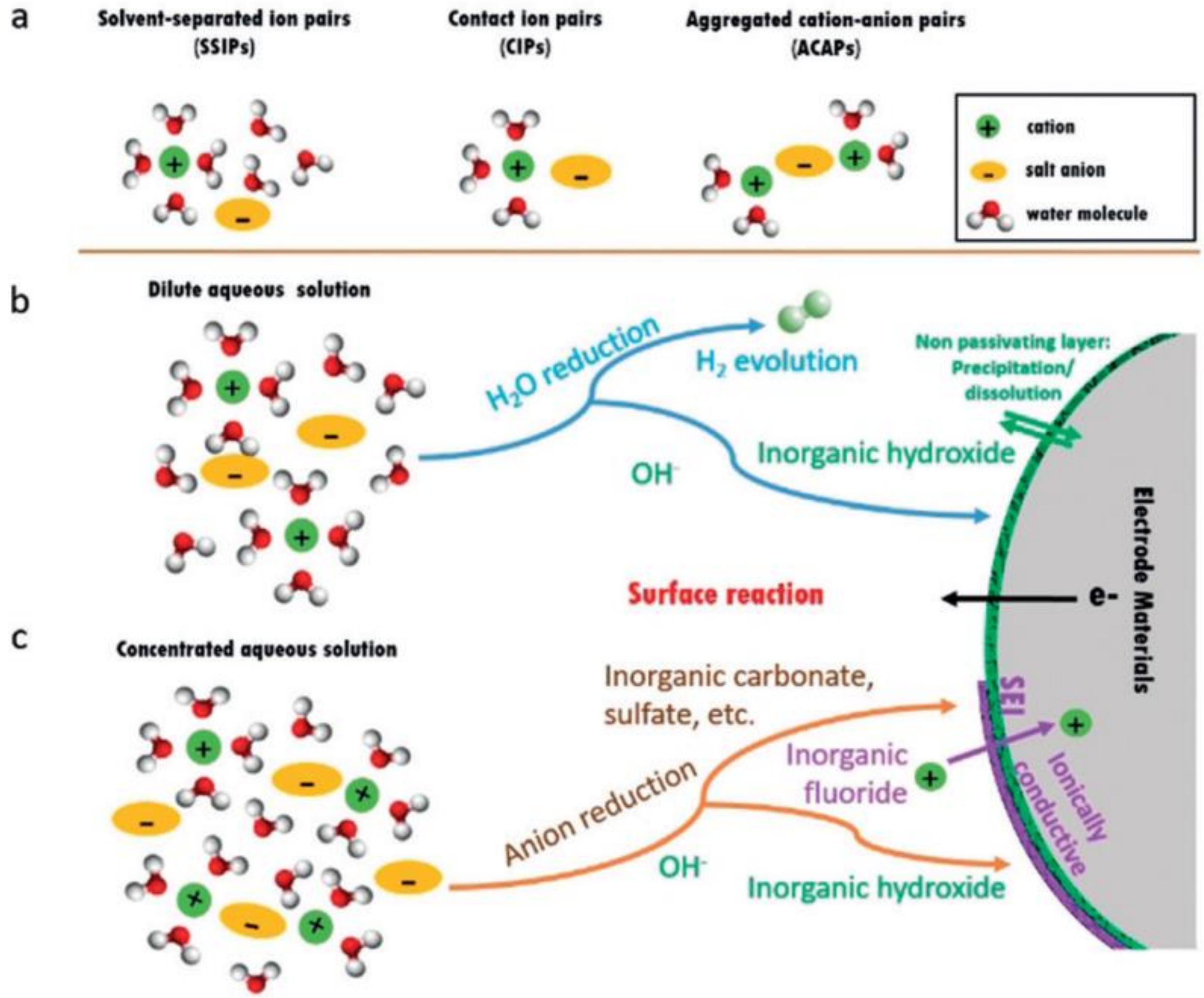

Figure 3: (a) Representative cation solvate species in aqueous solution, and schematic illustrations of the electrolyte reduction for the SEI formation in diluted (b) and concentrated (c) aqueous solutions for rechargeable metal-ion batteries. Reproduced from Zhang, *et al*. (*41*)

By contrast, conventional aqueous electrolytes lack a protective interphase since none of the decomposition by-products from water (H_2, O_2, or OH^-) can precipitate in a dense solid state. Thus, aqueous batteries, without interphases, are typically constrained to low voltage (<1.5 V) and low energy density (<70 Wh/kg), often exhibiting rapid capacity fading and low coulombic efficiency, particularly at low charging rates. (*7, 13, 41, 42*) Suo, *et al*. (*31*) demonstrated the development of interphases in an aqueous electrolyte by manipulating the electrolyte decomposition source during initial charging processes. Using a LiTFSI WiSE (> 20 m) with a Li-solvation sheath containing anions, those authors show a dense interphase formation primarily through anion reduction on the anode surface. Coupled with the significantly reduced electrochemical activity of water at such high concentrations, this WiSE established an expanded EVW of approximately 3.0 V. The expansion of the overall stability window, which resulted from the displacement of both oxygen and hydrogen evolution potentials considerably beyond the thermodynamic stability limits of pure water, was proportional to the increase in LiTFSI concentration. A full aqueous Li-ion battery, employing a model electrochemical couple ($LiMn_2O_4$ and Mo_6S_8), exhibited an open circuit voltage (V_{OC}) of 2.3 V and sustained nearly 100% coulombic efficiency over 1000 cycles at both low (0.15 C) and high (4.5 C) rates.

For aqueous zinc ion batteries (AZIBs), studies have shown that the concentration of the aqueous electrolytes influences the performance of battery in many ways, such as by alleviating dendrite formation, stabilizing the cathode material and improving the coulombic efficiency (CE). (*13, 28-30, 39, 43*) Again, it is believed that higher salt concentration alters the solvation and transport properties of the ions to enhance stability and kinetics and also reduces water activity and water-induced undesirable side reactions. According to Wang, *et al*., (*32*) a concentrated aqueous electrolyte (1 m $Zn(TFSI)_2$ + 20 m LiTFSI), enables dendrite-free Zn plating/stripping at nearly 100% CE, which those authors attribute to the optimization of the solvation structure of Zn^{2+} ions. Molecular dynamics simulations indicate that at such high concentrations the solvation shell is occupied primarily by $TFSI^-$, with six coordinating oxygens from $TFSI^-$ compared to those from water at lower concentrations, see Figure 4. Such findings encourage the accelerating adoption of AZIBs for grid-level electrochemical energy storage systems. (*43*)

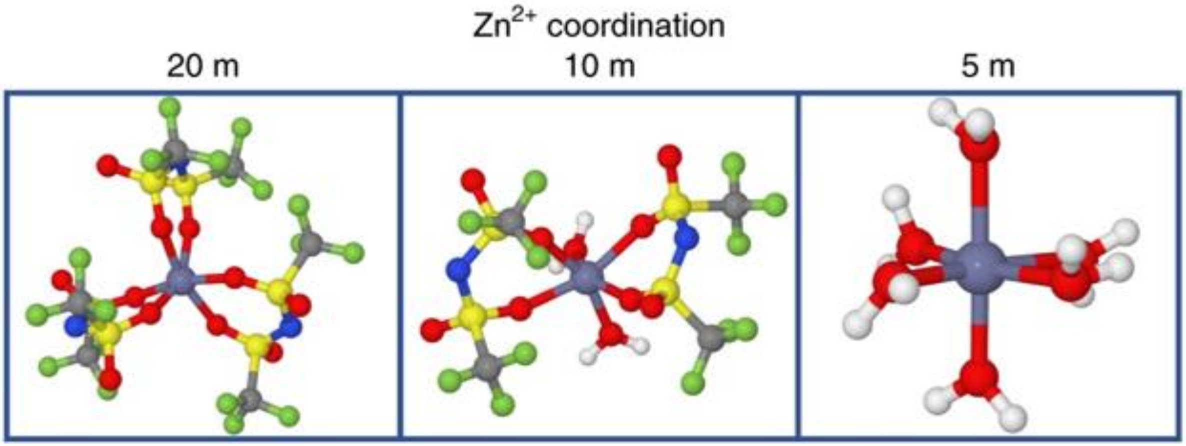

Figure 4: Zn^{2+} solvation structures in the electrolytes with 1 m $Zn(TFSI)_2$ and different concentrations of LiTFSI (20 m, 10 m and 5 m) as indicated above each panel in the figure. Figure reproduced from Wang, *et al*. (*32*)

Moreover, it has also been shown for the $ZnCl_2$ WiSE that the altered solvation structure of the active Zn^{2+} ion enhances the EVW and facilitates the dendrite free plating/stripping of Zn-metal anode. (*28*) Figure 5 shows the changing EVW of aqueous $ZnCl_2$ electrolyte with changing salt concentration. The EVW of $ZnCl_2$ solutions widened from 1.6 V to 2.3 V as the concentration was increased, impacting Zn plating potential and the onset potential of the hydrogen evolution reaction (HER). At lower concentrations, $ZnCl_2$ aqueous solution is believed to contain fully solvated Zn^{2+} ions.

However, in a 30 m $ZnCl_2$ solution, the stoichiometry of $ZnCl_2$ and H_2O in the solution prevents the formation of octahedral solvation shell for all Zn^{2+} ions, resulting in a WiSE essentially behaving as an ionic liquid. (*28*) Fourier transform infrared spectroscopy (FTIR) revealed a strong interaction between Zn^{2+} and water molecules, leading to increased viscosity and disrupted hydrogen bonding networks with increasing $ZnCl_2$ concentration. This interaction, along with incomplete hydration shells of Zn^{2+}, restrains water molecules from reacting with the Zn metal anode, explaining the enhanced Coulombic efficiency (CE) and the reduced formation of undesirable side reaction products like $Zn(OH)_2$ and ZnO in $ZnCl_2$ WiSE compared to dilute $ZnCl_2$ solutions.

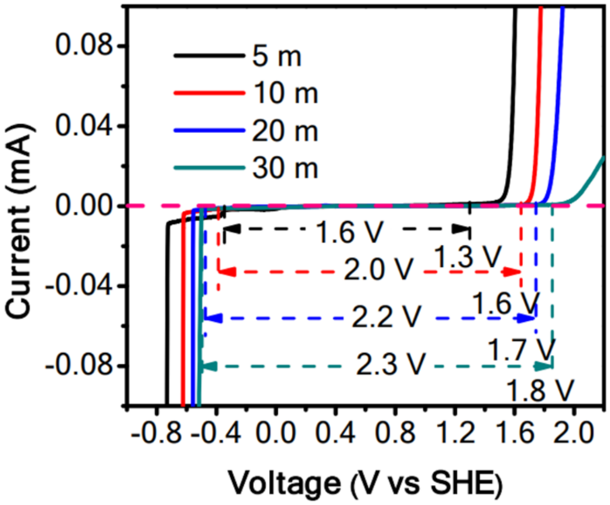

Figure 5: EVW of aqueous $ZnCl_2$ electrolyte with various concentrations as indicated in the legend. Figure reproduced from Zhang, *et al*. (*28*)

In summary, highly concentrated aqueous electrolytes exhibit better performance compared to their dilute counterparts in terms of many important parameters for aqueous rechargeable batteries. Overall, these improvements are believed to be due to factors like decreasing number of free water molecules for interaction, increased ion pairing, the disrupted hydrogen bonding network between water molecules in the electrolyte, and the formation of efficient SEIs due to the decomposition of anions rather than water during the charge transfer process – all related to the solvation structure of the active ion in the electrolyte. (*7, 13, 27, 28, 30-33, 36, 39, 41*)

As such the solvation structure of the active ions in the electrolyte needs to be understood in more detail and its relationship with the EVW and other associated phenomena needs to be quantified for the better understanding and wide use of such WiSE for aqueous batteries. In

Chapters 6 – 8, we seek to quantify the extent of ion pairing in the aqueous $ZnCl_2$ system under different conditions and in Chapter 7 we also study the influence of confinement on ion pairing and the relationship between ion pairing and the EVW.

3.4: References

1. X. Ji, A perspective of ZnCl2 electrolytes: The physical and electrochemical properties. *eScience* **1**, 99-107 (2021).
2. K. Funke, AgI-type solid electrolytes. *Progress in solid state chemistry* **11**, 345-402 (1976).
3. M. H. Weinberger, in *Handbook of research methods in cardiovascular behavioral medicine*. (Springer, 1989), pp. 133-143.
4. R. Latham, R. Linford, W. Schlindwein, Pharmaceutical and medical applications of polymer electrolytes. *Ionics* **9**, 41-46 (2003).
5. M. Li, C. Liu, A. Ding, C. Xiao, A review on the extraction and recovery of critical metals using molten salt electrolysis. *Journal of Environmental Chemical Engineering*, 109746 (2023).
6. W. Giurlani *et al.*, Electroplating for decorative applications: Recent trends in research and development. *Coatings* **8**, 260 (2018).
7. S. Khalid, N. Pianta, P. Mustarelli, R. Ruffo, Use of Water-In-Salt Concentrated Liquid Electrolytes in Electrochemical Energy Storage: State of the Art and Perspectives. *Batteries* **9**, 47 (2023).
8. A. Azmi, J. Jai, N. Zamanhuri, A. Yahya, in *IOP Conference Series: Materials Science and Engineering*. (IOP Publishing, 2018), vol. 358, pp. 012024.
9. A. A. Ojo, I. M. Dharmadasa, Electroplating of semiconductor materials for applications in large area electronics: A review. *Coatings* **8**, 262 (2018).
10. M. Li, C. Wang, Z. Chen, K. Xu, J. Lu, New concepts in electrolytes. *Chemical reviews* **120**, 6783-6819 (2020).
11. Y. Mei *et al.*, Zinc complexation in chloride-rich hydrothermal fluids (25–600°C): A thermodynamic model derived from ab initio molecular dynamics. *Geochimica et Cosmochimica Acta* **150**, 265-284 (2015).
12. W. Liu, B. Etschmann, G. Foran, M. Shelley, J. Brugger, Deriving formation constants for aqueous metal complexes from XANES spectra: Zn2+ and Fe2+ chloride complexes in hypersaline solutions. *American Mineralogist* **92**, 761-770 (2007).
13. S. Chen, M. Zhang, P. Zou, B. Sun, S. Tao, Historical development and novel concepts on electrolytes for aqueous rechargeable batteries. *Energy & Environmental Science* **15**, 1805-1839 (2022).
14. D. Dhakal *et al.*, The evolution of solvation symmetry and composition in Zn halide aqueous solutions from dilute to extreme concentrations. *Physical Chemistry Chemical Physics* **25**, 22650-22661 (2023).
15. J. L. Fulton, S. M. Heald, Y. S. Badyal, J. M. Simonson, Understanding the effects of concentration on the solvation structure of Ca2+ in aqueous solution. I: The perspective on local structure from EXAFS and XANES. *Journal of Physical Chemistry A* **107**, 4688-4696 (2003).
16. J. L. Fulton, Y. S. Chen, S. M. Heald, M. Balasubramanian, Hydration and contact ion pairing of Ca2+ with Cl- in supercritical aqueous solution. *Journal of Chemical Physics* **125**, 094507 (2006).

17. H. W. Wang, K. Yuan, N. Rampal, A. G. Stack, Solution and Interface Structure and Dynamics in Geochemistry: Gateway to Link Elementary Processes to Mineral Nucleation and Growth. *Crystal Growth & Design* **22**, 853-870 (2022).
18. W. Liu, S. Borg, B. Etschmann, Y. Mei, J. Brugger, An XAS study of speciation and thermodynamic properties of aqueous zinc bromide complexes at 25–150°C. *Chemical Geology* **298-299**, 57-69 (2012).
19. J. R. Ruaya, T. M. Seward, The stability of chlorozinc(II) complexes in hydrothermal solutions up to 350-degrees-C. *Geochimica Et Cosmochimica Acta* **50**, 651-661 (1986).
20. R. A. Mayanovic, A. J. Anderson, W. A. Bassett, I. M. Chou, XAFS measurements on zinc chloride aqueous solutions from ambient to supercritical conditions using the diamond anvil cell. *Journal of Synchrotron Radiation* **6**, 195-197 (1999).
21. Y. Nara *et al.*, Influences of electrolyte concentration on subcritical crack growth in sandstone in water. *Engineering Geology* **179**, 41-49 (2014).
22. W. Tang *et al.*, Aqueous rechargeable lithium batteries as an energy storage system of superfast charging. *Energy & Environmental Science* **6**, 2093-2104 (2013).
23. J. B. Goodenough, Y. Kim, Challenges for rechargeable Li batteries. *Chemistry of materials* **22**, 587-603 (2010).
24. Z. Liu *et al.*, Voltage issue of aqueous rechargeable metal-ion batteries. *Chemical Society Reviews* **49**, 180-232 (2020).
25. J.-Y. Luo, W.-J. Cui, P. He, Y.-Y. Xia, Raising the cycling stability of aqueous lithium-ion batteries by eliminating oxygen in the electrolyte. *Nature chemistry* **2**, 760-765 (2010).
26. J. O. G. Posada *et al.*, Aqueous batteries as grid scale energy storage solutions. *Renewable and Sustainable Energy Reviews* **68**, 1174-1182 (2017).
27. X. Wang, Y. Hou, Y. Zhu, Y. Wu, R. Holze, An aqueous rechargeable lithium battery using coated Li metal as anode. *Scientific reports* **3**, 1401 (2013).
28. C. Zhang *et al.*, A ZnCl2 water-in-salt electrolyte for a reversible Zn metal anode. *Chemical Communications* **54**, 14097-14099 (2018).
29. Y. Zhang *et al.*, Pursuit of reversible Zn electrochemistry: a time-honored challenge towards low-cost and green energy storage. *NPG Asia Materials* **12**, 4 (2020).
30. C. Zhang *et al.*, The electrolyte comprising more robust water and superhalides transforms Zn-metal anode reversibly and dendrite-free. *Carbon Energy* **3**, 339-348 (2021).
31. L. M. Suo *et al.*, "Water-in-salt" electrolyte enables high-voltage aqueous lithium-ion chemistries. *Science* **350**, 938-943 (2015).
32. F. Wang *et al.*, Highly reversible zinc metal anode for aqueous batteries. *Nature Materials* **17**, 543-549 (2018).
33. Q. Dong *et al.*, Cathodically stable Li-O2 battery operations using water-in-salt electrolyte. *Chem* **4**, 1345-1358 (2018).
34. C. Yang *et al.*, Unique aqueous Li-ion/sulfur chemistry with high energy density and reversibility. *Proceedings of the National Academy of Sciences* **114**, 6197-6202 (2017).
35. J. Yue *et al.*, Interface Concentrated-Confinement Suppressing Cathode Dissolution in Water-in-Salt Electrolyte. *Advanced Energy Materials* **10**, 2000665 (2020).
36. L. Jiang *et al.*, Building aqueous K-ion batteries for energy storage. *Nature Energy* **4**, 495-503 (2019).
37. D. Reber, R.-S. Kühnel, C. Battaglia, Suppressing crystallization of water-in-salt electrolytes by asymmetric anions enables low-temperature operation of high-voltage aqueous batteries. *ACS Materials Letters* **1**, 44-51 (2019).
38. D. P. Leonard, Z. Wei, G. Chen, F. Du, X. Ji, Water-in-salt electrolyte for potassium-ion batteries. *ACS Energy Letters* **3**, 373-374 (2018).
39. L. Zhang *et al.*, ZnCl2 "Water-in-Salt" Electrolyte Transforms the Performance of Vanadium Oxide as a Zn Battery Cathode. *Advanced Functional Materials* **29**, 1902653 (2019).

40. M. R. Lukatskaya *et al.*, Concentrated mixed cation acetate “water-in-salt” solutions as green and low-cost high voltage electrolytes for aqueous batteries. *Energy & Environmental Science* **11**, 2876-2883 (2018).
41. H. Zhang, X. Liu, H. Li, I. Hasa, S. Passerini, Challenges and strategies for high-energy aqueous electrolyte rechargeable batteries. *Angewandte Chemie International Edition* **60**, 598-616 (2021).
42. Y. Wang, J. Yi, Y. Xia, Recent progress in aqueous lithium-ion batteries. *Advanced Energy Materials* **2**, 830-840 (2012).
43. X. Zeng, J. Hao, Z. Wang, J. Mao, Z. Guo, Recent progress and perspectives on aqueous Zn-based rechargeable batteries with mild aqueous electrolytes. *Energy Storage Materials* **20**, 410-437 (2019).

Chapter 4: Background on X-ray Spectroscopy

4.1 Historical background

In work several years before the discovery of X-ray, Hertz (*1*) observed and recorded evidence for the photoelectric effect for the first time while doing experiments on radio waves; the discovery of the photoelectric effect would eventually be seen as a first step towards the understanding and development of the present-day X-ray spectroscopy methods. His apparatus, shown in Figure 1**,** consisted of a spark gap transmitter and a receiver for electromagnetic waves. During his experiment he noticed that when UV light was allowed to fall on the apparatus through a quartz panel, the detected spark length would be higher than when UV light was blocked using a glass panel that absorbs UV light. The UV light created photoelectrons which enhanced the sparks in Hertz's experiment. Later, Einstein developed the theory based on quantization of light energy to explain the observed effect – the theoretical perspective that was the official reason for his Nobel Prize in Physics in 1921. (*2*)

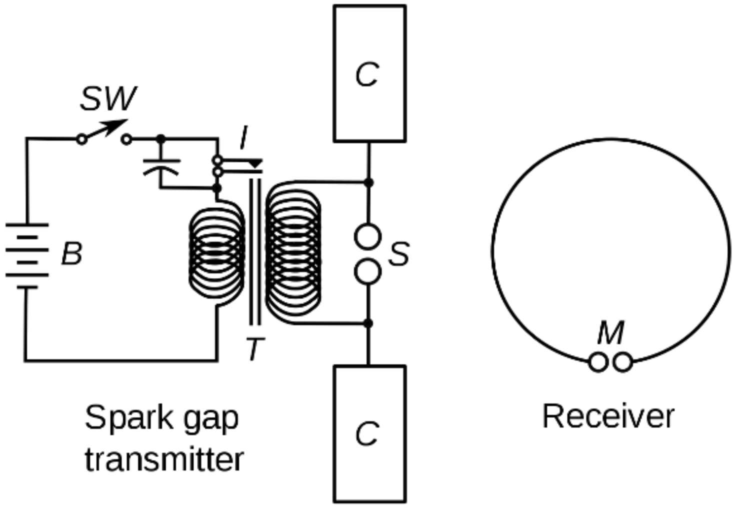

Figure 1: Schematic of the apparatus used by Heinrich Hertz in 1887. Reproduced from Mulligan. (*1*)

In 1895, while using a Crookes tube to study cathode rays (now known to be a beam of electrons), Roentgen found that some invisible ray, which he later termed an ‘X-ray’, coming from the tube that made a fluorescent screen far away from the tube glow. The fact that the X-rays penetrated matter with different strength depending on material properties enables Roentgen to take transmission images (later coined radiographs) of different objects which demonstrated the earliest possible uses of X-rays. Figure 2 shows a radiograph that Roentgen took of his wife’s hand, one of the first X-ray images ever taken. The discovery of X-rays was soon welcomed and saw widespread use in medicine and other sectors. (*3*) This launched numerous new directions in the scientific community and led to the development of new techniques and fields of research that are critical to today’s scientific advancement and understanding. (*3*)

Figure 2: An X-ray image of the hand of Roentgen’s wife, one of the first X-ray images. Reproduced from Mould. (3)

For example, in the present days X-ray photoelectron spectroscopy (XPS) is a widely used materials characterization technique. The principle of this technique is to measure simultaneously the current of photoelectrons escaping the sample and their kinetic energies. This technique can be used to learn about the binding energies of even the deepest electrons in an atom. A typical set of XPS spectra is shown in Figure 3. A survey spectrum is first collected to gain insight into the various elements and impurities present in the sample. Then a high-resolution spectrum is taken for a specific energy range of interest to learn the apparent binding energy of the chosen element and orbital, Si 2p in the case shown in figure 3, that is of importance to the scientific question to be answered. Such knowledge of the binding energies of electrons in materials can inform us about the electronic, chemical and structural properties of the material in question. However, because of the short mean free path of the ejected photoelectrons this technique is only suitable for characterizing the surface of a material, typically with a penetration less than 100 Å. (*5*)

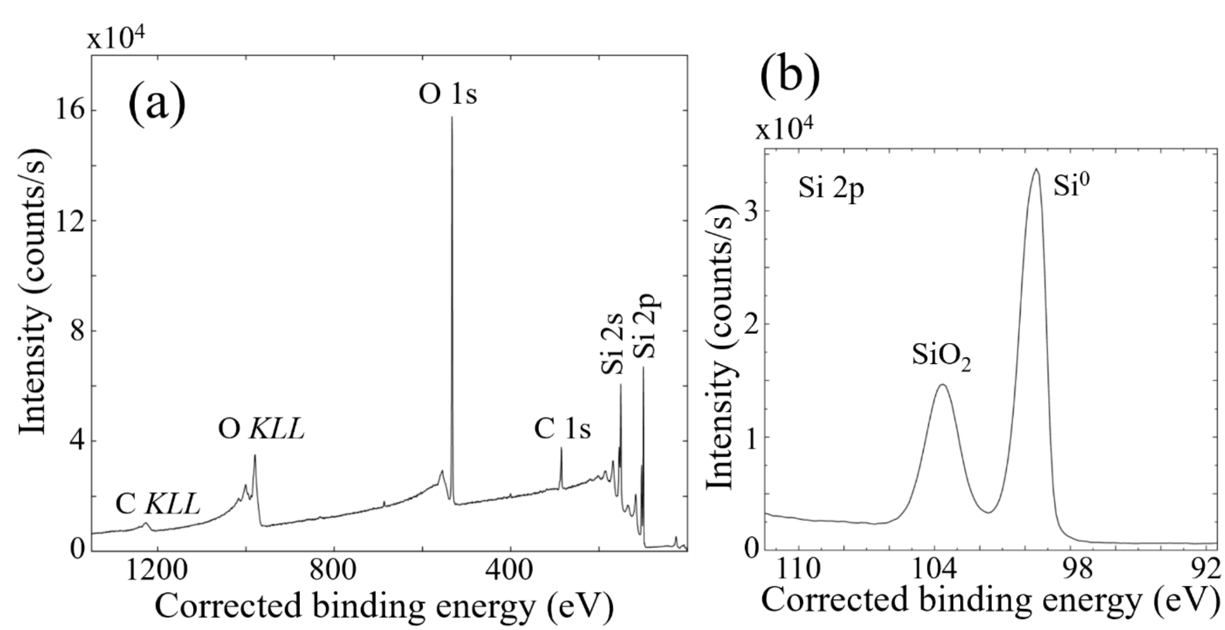

Figure 3: (a) A typical XPS survey spectrum from a Si/SiO$_2$ wafer and, (b) a high-resolution spectra of the Si 2p region. The x axis is the corrected binding energy of the electrons in respective orbitals. The additional peaks (C 1s, C *KLL*) seen in the survey spectrum are from the impurities and contamination. Figure reproduced from Jensen *et al*. (*4*).

4.2 X-Ray Absorption Spectroscopy (XAS)

In contrast to x-ray photoelectron spectroscopy, X-ray absorption spectroscopy (XAS) is a bulk measurement technique with rich information about local structure such as coordination symmetry, oxidation states, coordination numbers, and bond lengths. In XAS the absorption coefficient for the photoelectric effect as a function of photon energy directly interrogates the population of unoccupied states above the Fermi level. (*6*) Through the proper choice of the incident photon energy, such a measurement is inherently specific to a particular element and core level.

In a typical XAS experiment, the energy of a monochromatic incident beam is scanned through the absorption edge of the element of interest. The canonical example of a transmission-mode experiment at a synchrotron x-ray light source is shown schematically in figure 4. Monochromatic X-rays are generated from polychromatic beams by using a double-crystal monochromator. Subsequently, the X-ray beam passes successively through an incident flux monitor, the sample, and a transmitted flux monitor. This process is repeated at various energy points to assemble a complete spectral dataset. The intensity of the transmitted spectrum is governed by Beer's law, $A = ln\frac{I_o}{I_t} = \mu lc$, where A is the total absorbance from the sample, I_o is the incident intensity, I_t is the transmitted intensity, μ is the molar absorptivity, l is the path length and c is the concentration of the absorber in the sample. Hence, when X-ray transmission and the incident X-ray flux are known, the energy dependent absorption coefficient can be calculated.

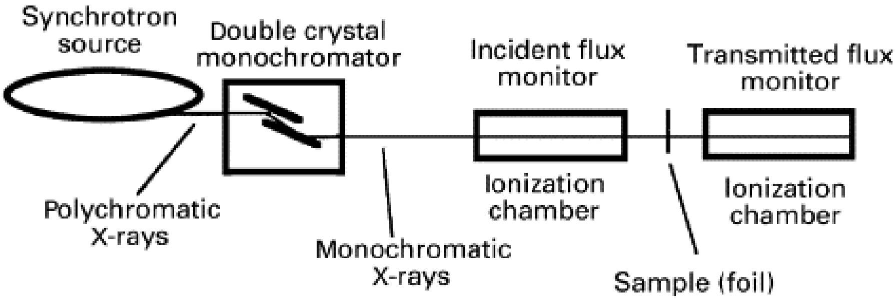

Figure 4: Schematic of a transmission mode XAS experiment. Reproduced from Lindon *et al*. (*7*).

In figure 5, we show in the left panel a K-edge XAS spectrum of a metal bonded with a light ligand and also show in the right panel a corresponding schematic for the origins of transitions corresponding to the characteristic features in the spectrum. Among these spectral features, some are better equipped than others to answer specific questions about material properties. It is useful to divide the spectrum into three regions: the pre-edge, the x-ray absorption near edge structure (XANES), and the extended x-ray absorption fine structure (EXAFS) as shown in the figure. We now discuss these three regimes in turn.

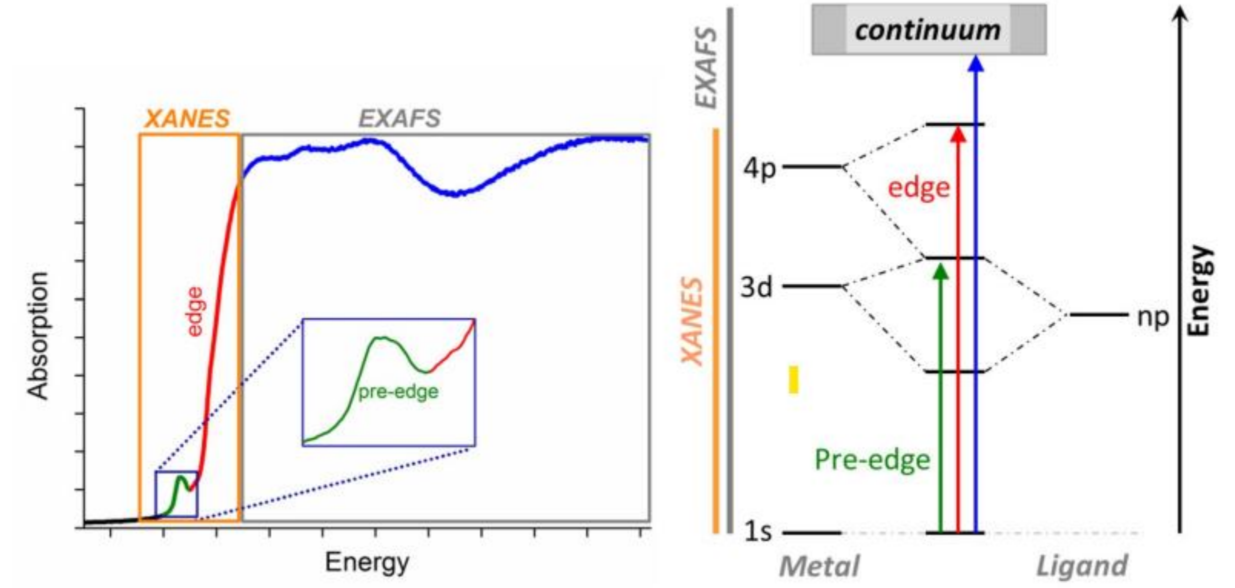

Figure 5: Left: X-ray absorption spectrum (XAS) with marked X-ray absorption near edge structure (XANES) and extended X-ray absorption fine structure (EXAFS) regions. The XANES region also includes the characteristic pre-edge and edge features. Right: Origin of the transitions corresponding to the characteristic features in the XAS spectrum on the left. Figure reproduced from Kowalska *et al*. (*8*).

4.2.1 Pre-edge Features

Pre-edge features refer to spectral information that is at lower energy than the onset of the electronic continuum. As a case in point, consider the K-edge XANES for Ti compounds shown in figure 6. In the figure, the K-edge XANES spectra of Ti with regular octahedral, distorted (irregular octahedral) and square-pyramidal symmetry are presented, showing changing pre-edge feature with coordination. Generally, for 3*d* transition metals, the strength of pre-edge features depends on the effect of the local environment on breaking the *d*-like character of the 3*d*-derived states; the key consideration is that x-ray photoabsorption is dominated by dipole transitions, and hence the initial 1*s* electron is predominantly sensitive to unoccupied final states having *p* character. For example, octahedral coordination results in pre-edge features with quite low intensity because *s* → *d* transitions are forbidden here, whereas tetrahedral coordination often generates very sharp, high-intensity pre-edge features, e.g., *s* → *p* transitions. (*9, 10*) In figure 6 the first two spectra ('regular' and 'irregular') have generally octahedral coordination of the Ti ion, and hence have weak pre-edge features. The final spectrum, which probes a square pyramidal local coordination instead shows a strong pre-edge feature because of the significant *p*-type character of the *d*-derived unoccupied states.

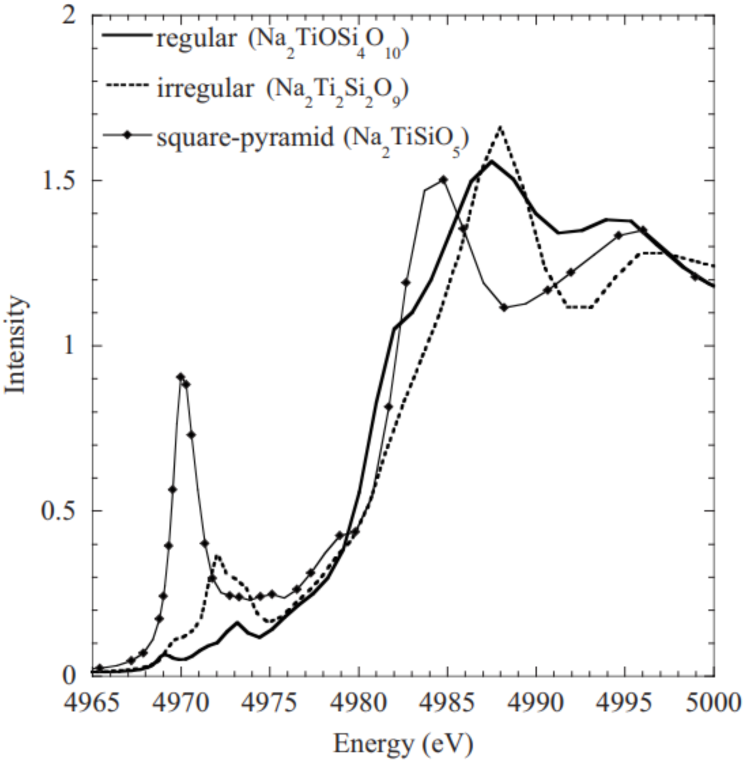

Figure 6: K-edge XANES spectra of Ti with regular octahedral, distorted (irregular octahedral) and square-pyramidal coordination symmetry in different compounds as indicated in legend, showing changing pre-edge features with coordination symmetry. Reproduced from Jiang *et al.* (*9*).

4.2.2 X-ray Absorption Near Edge Structure (XANES)

Many different inferences can be drawn from the XANES region, i.e., the XAS spectrum up to about 50 eV past the absorption edge. One common application of XANES is so-called 'fingerprint analysis' wherein one measures the XANES of known reference samples and subsequently compares the shape and structure of the spectrum with the XANES of an unknown system. (*12*) Using a more advanced analytic approach one can also perform a fit with a linear combination of known references or a principal component analysis to derive the relative contributions in mixed systems. (*13*) The reliability the analysis depends on the applicability of the available reference spectra set.

A second common XANES analysis is the determination of the oxidation state, or the change thereof, via shifts of the main absorption edge. (*11*) In a simple picture the edge position in K-edge XANES can be a direct measure of the analyte's valence state. This is illustrated in figure 7, where the edge position for Mn K-edge in different Mn-oxides having different oxidation states for Mn are compared. It is seen that the edge position smoothly shifts to higher energy values with the increase in oxidation number of the probed metal.

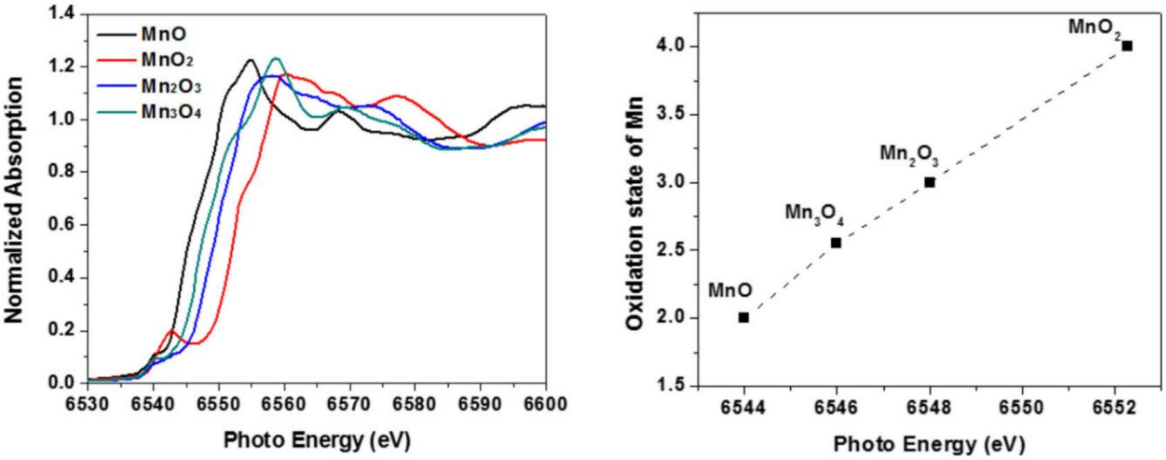

Figure 7: (left) Mn K-edge XANES spectra for different manganese oxides and, (right) Edge position plotted against oxidation state showing an almost linear correlation between the oxidation state and the edge position – the increase in oxidation number shifts the edge position to higher energy. Reproduced from Kuo *et al*. (*11*)

Another example is given in figure 8, where the absorption edge position is dependent on the oxidation state of the probed element (Cu) and shows a considerable shift to higher energy going from a monovalent Cu in Cu_2O to divalent Cu in CuTOTP (TOTP = tetraoxidotriphenylene) and $Cu(acac)_2$ (acac = acetylacetonate).

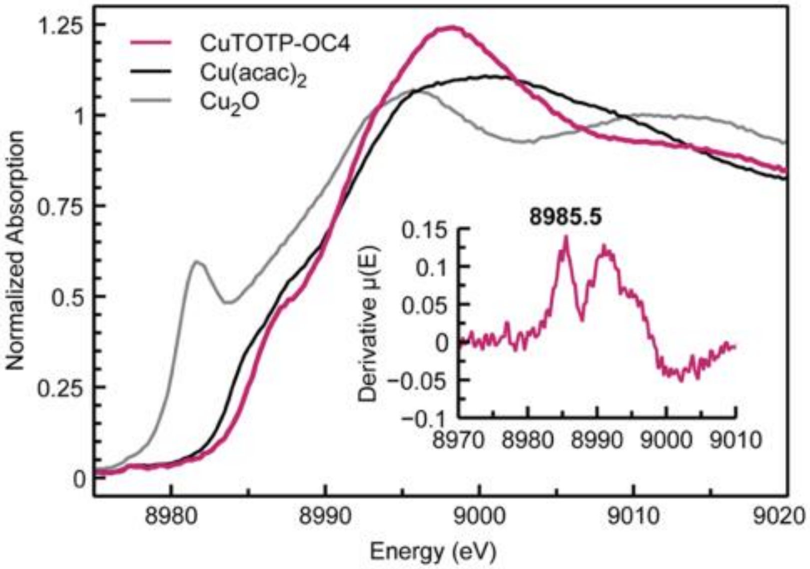

Figure 8: K-edge XANES spectra of Cu in CuTOTP (purple) compared to reference Cu_2O (gray) and $Cu(acac)_2$ (black) compounds. Figure reproduced from Zasada *et al*. (*14*).

One of the contributions to the absorption edge shift comes from the change in the oxidation state of the absorber. The change of oxidation state implies the addition (chemical reduction) or the removal (chemical oxidation) of an electron, which means that the local charge changes with respect to the neutral metal state. The shift of the absorption edge occurs due to the change of the effective charge of the nucleus. However, it should be noted that the absorption edge energy is not solely dependent on the oxidation state but is also affected by, e.g., coordination symmetry. For this reason, care must be taken while determining the oxidation state of the sample from XANES, especially if the reference compounds are not close to the sample in terms of ligand identity, coordination number and symmetry. Owing to its dependence on multiple observables, a more advanced analysis of the XANES spectra requires considerable theoretical support. Recently, machine learning is proving useful to extract various dependencies and information from XANES spectra, often with unexpected successes that are unobvious for unassisted human analysis. (*15*, *16*)

4.2.3 Extended X-ray Absorption Fine Structure (EXAFS)

Although XANES and EXAFS are part of the same experiment, their analysis provides complementary information. While XANES is sensitive to oxidation state and geometrical structure around the central atom, EXAFS provides quantitative information on the local structure defined by bond distances, coordination numbers, and disorder around the probed atom.

In a typical XAS spectra, the EXAFS starts from about 50 eV above the edge and is embedded in the overall absorption spectra as a set of small fluctuations diminishing in amplitude at higher energies as shown in figure 9 (top left). As depicted in figure 9 (bottom), this fine structure is caused by the constructive and destructive interference between the outgoing electron wave from the central excited atom (represented by solid circles) and the electron wave that is scattered from neighboring atoms (represented by dashed circles).

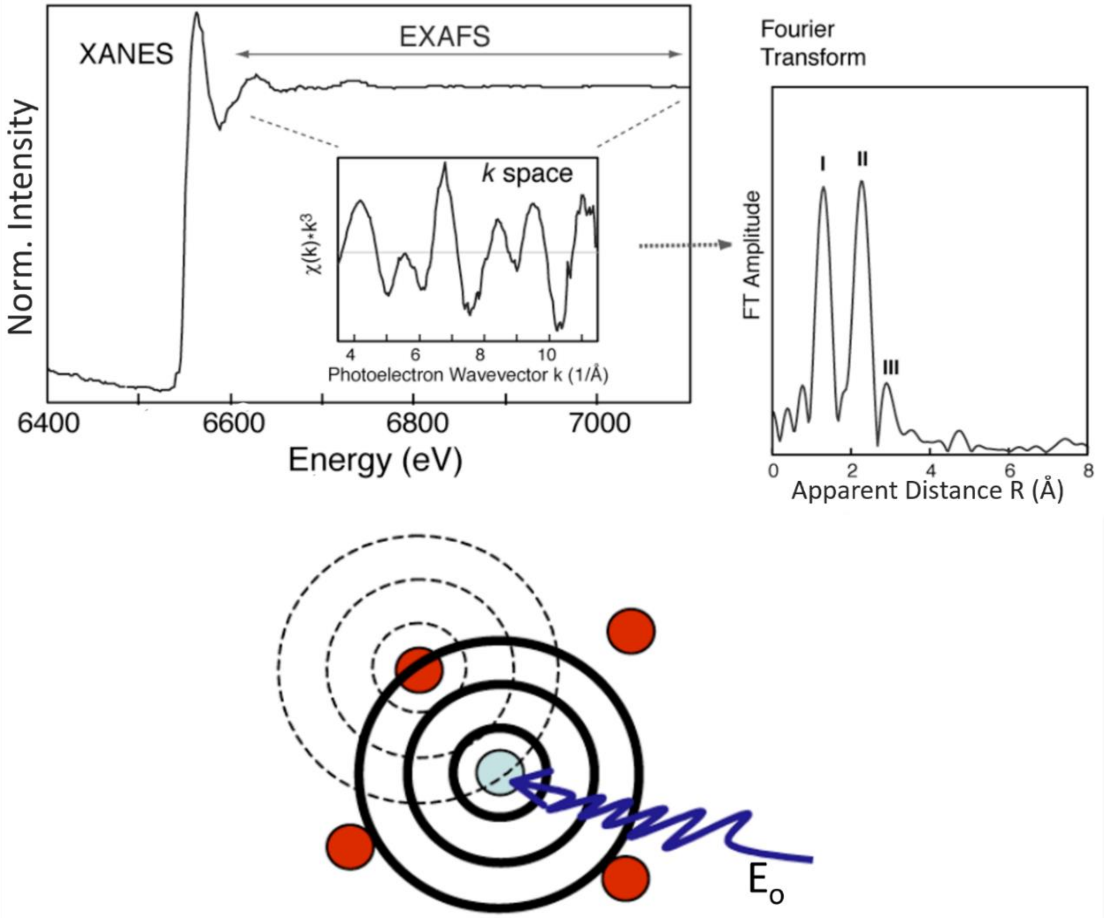

Figure 9: (top left) K-shell mass absorption coefficient of Mn in a photosystem II sample plotted versus the photon energy of the X-ray. Inset: The EXAFS spectrum $\chi(k)$ in k space. (top right) The Fourier transform of $\chi(k)$ in R space. (bottom) Schematic picture of the excited electron wave function. E_o is the incident X-ray photon energy. The excited electronic state is centered about the center atom (grey). The solid circles represent the crests of the outgoing part of the electron state. The surrounding atoms (red) diffract the outgoing part as shown by the dashed circles. Reproduced from Yano *et al*. (*17*).

For a given incident energy E_0, the emitted photoelectrons has kinetic energy $E_{kin} = E_0 - E_{ion} = p^2/2m_e$, where E_{ion} is the ionization energy, p is the momentum and m_e is the mass of electron. Hence, such photoelectrons also have a well-defined de Broglie wavelength $\lambda_B = h/p$, h being the Plank's constant. In a qualitative XAS scattering model, the photoelectron is then scattered by the atoms around the analyte, typically the first few coordination shells around the absorber. Depending on their kinetic energy, these coherently scattered photoelectron waves then constructively and destructively interfere and modulate the effective absorption cross section of the absorbing site at energy E_0. This energy-dependent modulation of the absorption cross section creates the fine structure, which then yields information on the local atomic structure around the absorbing site. (*18*)

The formal interpretation of the fine structure requires rigorous theoretical modelling and fitting to the experimental spectra, but can often yield useful information about the identity of ligand, coordination number, bond length and other observables of the system. (*19*) The XAS theory has been well developed and can be applied to complicated systems of which the structure is known. (*18, 20-25*) Briefly, the oscillatory part of the absorption coefficient, $\chi(k)$, is the difference between the observed absorption coefficient $\mu(k)$ and that of the free atom $\mu_o(k)$ normalized by the free atom coefficient:

$$\chi(k) = \frac{(\mu(k) - \mu_o(k))}{\mu_o(k)}. \qquad (1)$$

The Fourier transform of this modulation then gives the information about the scattering path lengths between the absorber and the neighboring atoms typically in the range of up to 5 Å. The so-called 'EXAFS equation' is used to fit the experimental spectra with N_j, R_{aj} and σ_{aj}^2 as variable parameters (*19*, *25*)

$$\chi(k) = S_o^2 \sum_j \frac{N_j|f_j(k)|}{kR_{aj}^2} e^{-2\sigma_{aj}^2 k^2} e^{-2R_{aj}/\lambda_j(k)} \sin\left(2kR_{aj} + \alpha_{aj}(k)\right). \qquad (2)$$

In Eq. 2, N_j is the number of equivalent backscattering atoms j at a distance R_{aj} from the absorber atom a, $f_j(k)$ is the backscattering amplitude and $e^{-2\sigma_{aj}^2 k^2}$ represents the disorder term or Debye-Waller factor with σ_{aj} as the root-mean-square deviation from the mean position, $e^{-2R_{aj}/\lambda_j(k)}$ reflects the losses due to inelastic scattering where $\lambda_j(k)$ is the electron mean free path, $\alpha_{aj}(k)$ is the phase shift introduced due to the atomic potentials of the absorber and scatterer and, S_o^2 serves as the amplitude reduction factor due to shake-up/shake-off processes at the absorber atom.

The variables are extracted by fitting the experimental spectra with theoretical modelling using any of the various software programs (such as FEFF, Athena, Artemis, Larch, etc.) that are available to facilitate the analysis and interpretation of the EXAFS data. This technique has helped answer many critical questions which are otherwise not accessible through other techniques. (*26-28*) For example, EXAFS has been extensively used in the field of photosynthesis to study the reaction mechanism via the structures of multi-nuclear metal clusters like Mn_4Ca related to the oxidation of water in the photosynthetic oxygen-evolving complex (OEC). Small changes in the structure associated with the transitions between intermediate states, S-states, in the water-oxidation reaction cycle can be detected with EXAFS. (*17*) In more rigorous studies, complementary EXAFS measurements of multiple elements, (*26, 27, 29*) Mn and Ca K-edges in case of the OEC cluster, (*30*) can be collected to greatly improve the information that can be extracted from EXAFS analysis.

4.3: X-ray Fluorescence (XRF)

The electronic transition between atomic energy levels is the origin for the characteristic X-ray fluorescence (XRF) and electron emission of atoms. When a previously created core hole is filled by the transition of an electron from a higher energy level, the extra energy of the transitioning electron can be dissipated by the emission of an X-ray photon or of an electron from a nearby shell. The process of emitting an X-ray photon to compensate for the energy difference between the energy levels is called XRF, whereas if the energy is compensated by ejecting a nearby electron, the process is called Auger emission. The relative yields between Auger and fluorescence are plotted against atomic number (Z) in figure 10. Generally, Auger emission is favored for transitions requiring lower energy compensation while fluorescence is favored for transitions corresponding to larger energy requirements. While Auger electron spectroscopy is a well-developed field onto itself, (*31*) we focus here on XRF.

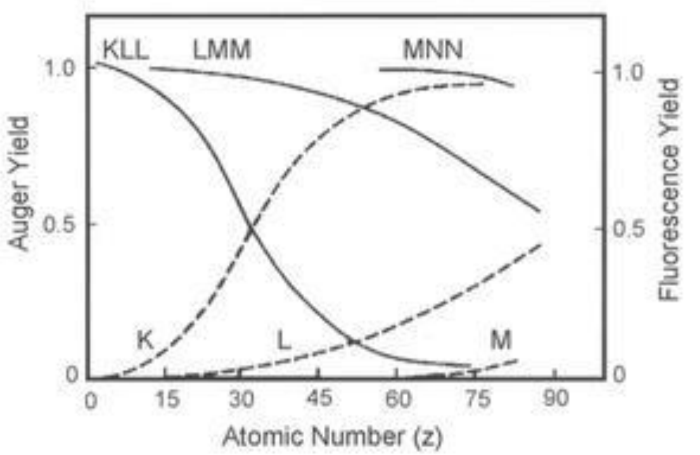

Figure 10: Auger and X-ray fluorescence (XRF) yields as a function of atomic number. Solid lines show Auger yield, and the dashed lines show fluorescence yield for different shells as labeled in the figure. Figure reproduced from Mogk (*32*).

Figure 11 shows the electronic transitions responsible for various XRF lines along with their nomenclature. Briefly, when an electron transitions from a higher energy level to fill a K-shell hole with the emission of X-ray the transition is called a K-line. These lines are termed Kα and Kβ for transitions arising from L and M-shells respectively, and so on. Each of these lines are then further divided; $K\alpha_1$, $K\alpha_2$, … for transitions arising from the sub-shells of L-shell, and so on.

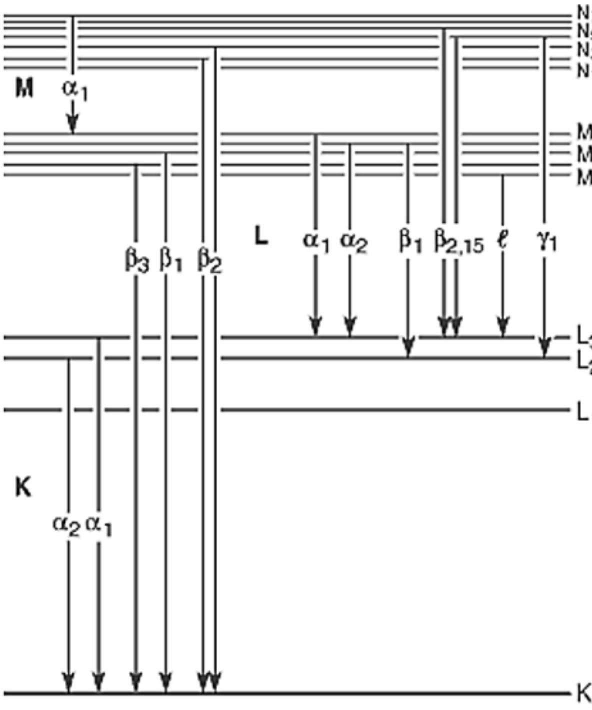

Figure 11: Electronic transitions that give rise to various X-ray fluorescence (XRF) lines. Figure reproduced from Thompson and Vaughan (*33*).

Figure 12 shows early photographic recordings of the Kα and Kβ fluorescence lines for a range of elements collected by Moseley, who discovered the relation between the energy (or frequency) of the emitted X-ray and the nature of the atom, especially the atomic number. This was the earliest application of x-ray fluorescence spectroscopy. Moseley's law is generally credited with regularizing the periodic table. (*35*) Moseley's law states that the square root of the frequency of emitted X-ray is proportional to the atomic number of the atom emitting it,

$$\upsilon = A(Z - b)^2 \qquad (3)$$

In Eq. 3, υ is the frequency of the emitted X-ray photon, A is the Rydberg frequency, Z is the atomic number of the emitting atom, and b is a constant depending on the type of line.

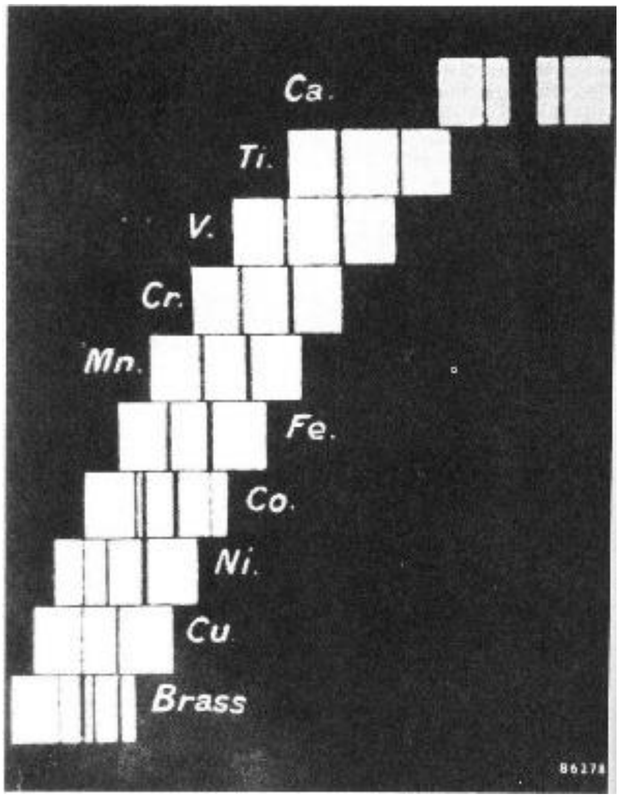

Figure 12: Photographic recording of Kα and Kβ XRF lines for a range of elements recorded by Moseley. Increasing energy is toward the left. Note: for the dispersive element used, the line position is proportional to the wavelength (not energy). Figure reproduced from Heilbron (*34*).

4.3.1: X-ray Fluorescence (XRF) Spectroscopy

The distinctions in energy levels among diverse atoms give rise to significant variations in the energy of fluorescence lines, resulting in infrequent overlap. This fact then ensures that, in most cases, the detection of fluorescence lines of a given element in the XRF spectra means the observation of the element itself. This idea is at the very core of XRF spectroscopy, widely used in the elemental analysis of materials.

A schematic diagram depicting a typical XRF experimental setup is shown in figure 13. The sample is illuminated by a powerful X-ray source that induces core holes in the sample, often creating fluorescence. The emitted X-rays are then detected by a suitably placed energy dispersive detector. The detected photons are analyzed, and the energy spectrum of the XRF is then available.

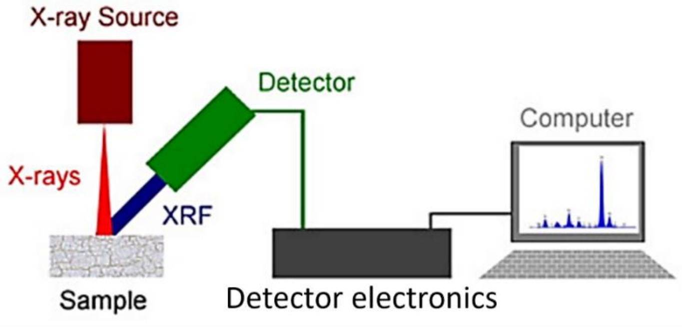

Figure 13: Schematic diagram for a typical XRF apparatus setup. From reference (*36*).

Generally, these experiments use lower resolution energy dispersive setups that cover larger energy range enabling shorter measurement times and rapid sampling. The typical energy resolution of an energy-dispersive XRF measurement is 100 – 200 eV, depending on photon energy, mainly attributed to the energy dispersive setup used for the measurements. Because the fluorescence lines of different elements are typically more separated than 200 eV, the resolution of the XRF measurements are good enough for elemental analysis. Moreover, this setup covers a wide range of energy making it possible to detect a wide range of elements (in terms of the atomic numbers) in the same experiment.

Figure 14 shows an XRF spectrum with the characteristic X-ray emission lines of different elements. The fact that the emission lines of different elements are separated enough to detect all of them in a mixture sample is clear in the figure, where even very close atomic number elements (e.g., C and O) can be resolved easily. Further, it is seen that a wide range of elements in terms of atomic number (C to Fe in this case) can be detected simultaneously in the same experiment. The intensity of the signal from different elements is proportional to the amount of those elements present in the sample, albeit with corrections needed for fluorescence yield and sample absorption. Elemental analysis can thus follow.

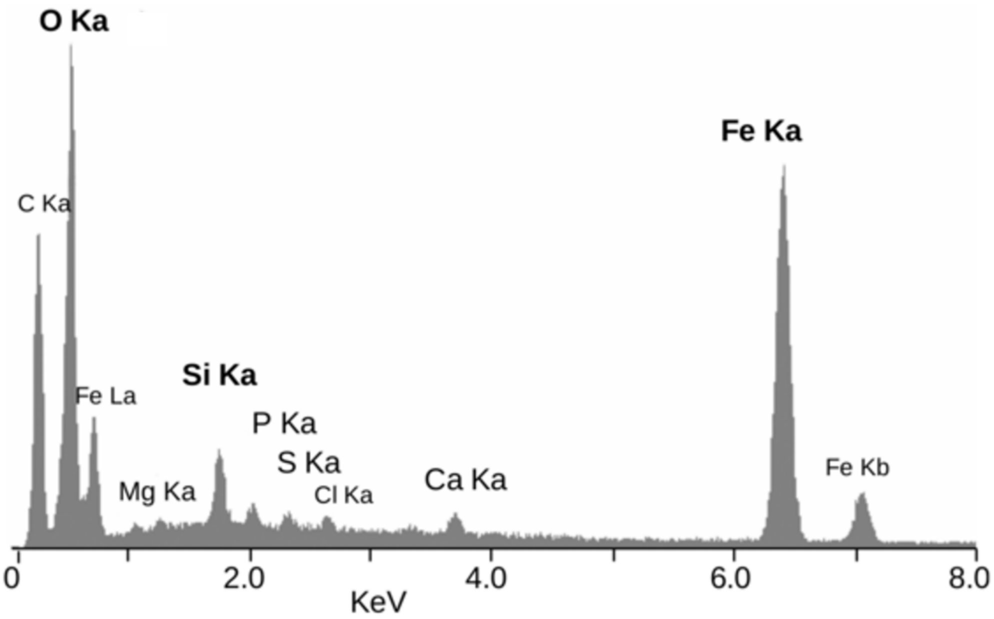

Figure 14: A typical XRF spectrum showing the characteristic X-ray emission lines for various elements. Figure reproduced from Corbari *et al*. (*37*).

4.3.2: X-ray Emission Spectroscopy (XES)

The prime technical differences between XRF spectroscopy and x-ray emission spectroscopy (XES) measurements are energy resolution, energy range covered, and the time needed for measurement, where XRF has lower resolution and generally covers larger energy range in a short time and XES typically has vastly superior resolution but covers smaller energy range and takes longer measurement times. The prime scientific difference, however, is that while XRF is concerned with the position and integral intensity of the fluorescence lines that gives enough information about the identity and the fractional contribution of various elements in a sample, XES seeks to investigate the changes in spectral shape and features to learn about the chemical nature and electronic structure of such elements in the sample. The higher resolution XES analysis is used to compare the fluorescence spectra from the absorbing atom in different chemical environments, and hence to relate spectral changes to the differences in local coordination, oxidation state, and electronic structure.

XES measurements involve analyzing the fluorescence X-rays with an energy resolution comparable to the core-hole broadening. For an instrument to work effectively, it needs to have a large angular acceptance while preserving good energy resolution. This can be achieved using wavelength dispersive approaches with Bragg optics operating close to backscattering conditions, where the ratio of accepted angle per energy increment is the largest. (*38*-*40*) The analyzer optics setup can be categorized into monochromators and polychromators, explained by the schematic in figure 15.

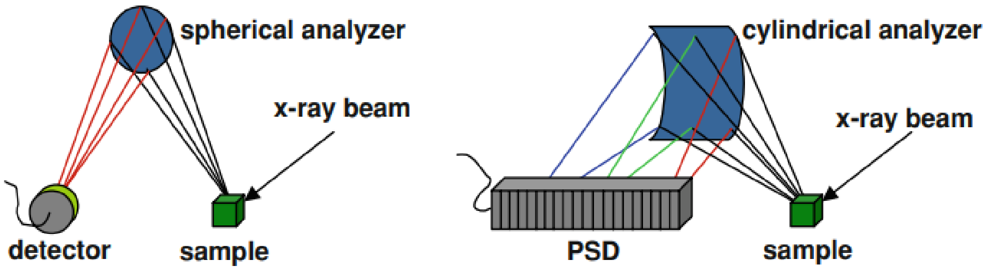

Figure 15: Schematics of XES experimental setup. (Left) Scanning monochromator in 1:1 focusing Rowland geometry with spherically curved Bragg crystal analyzer. XES spectrum is recorded by changing analyzer angle and detector position. (Right) Polychromator based on cylindrically curved Bragg crystal analyzer in von Hamos geometry. XES spectrum is recorded on a position sensitive detector (PSD). Figure reproduced from Bergmann and Glatzel (*40*).

In monochromators employing the Rowland circle geometry, energy is scanned point by point by changing the Bragg angle at the analyzer while keeping the source and detector on the Rowland circle defined by the analyzer curvature. These monochromators most often use spherically bent crystal analyzers to focus the analyzed X-rays at the detector, as shown in figure 15 (left).

On the other hand, polychromators disperse X-rays with different wavelengths (and hence energy) onto a position sensitive detector (PSD). This is commonly achieved in the von Hamos geometry, where a cylindrically bent Bragg crystal analyzer gives a line focus at the detector. Figure 15 (right) shows a schematic of a polychromator employing a cylindrically bent analyzer.

Having presented the differences between XRF and XES, consider the K-shell emission spectrum of Cr in Cr_2O_3 shown in figure 16. (*41*) In a typical K XES spectrum of a 3d transition metal, Cr in this case, there are three different regions of interest: the Kα, Kβ and VTC regions. These different spectral features are due to different transitions from higher orbitals to fill the K-shell core hole. The illustrations above each of these spectral regions in the Figure show a simple atomic orbital picture for the origin of respective spectral regions, where Kα comes from the transition 2p → 1s, Kβ from 3p → 1s, and VTC from the valence band (VB) to 1s transitions. As clearly seen in the spectrum, the Kα and Kβ spectral features are separated by several hundred electron volts. Also, the spectral intensities of the emission lines, which relates to the probability of the given transition, are quite different with the Kα integral intensity being around 10 times that for the Kβ and around 500 times the integral intensity in the VTC region. Moreover, each of these spectral regions show detailed structure, but for distinct reasons and with utility for different scientific questions. We now discuss these details, which are important background for much of the work in this dissertation.

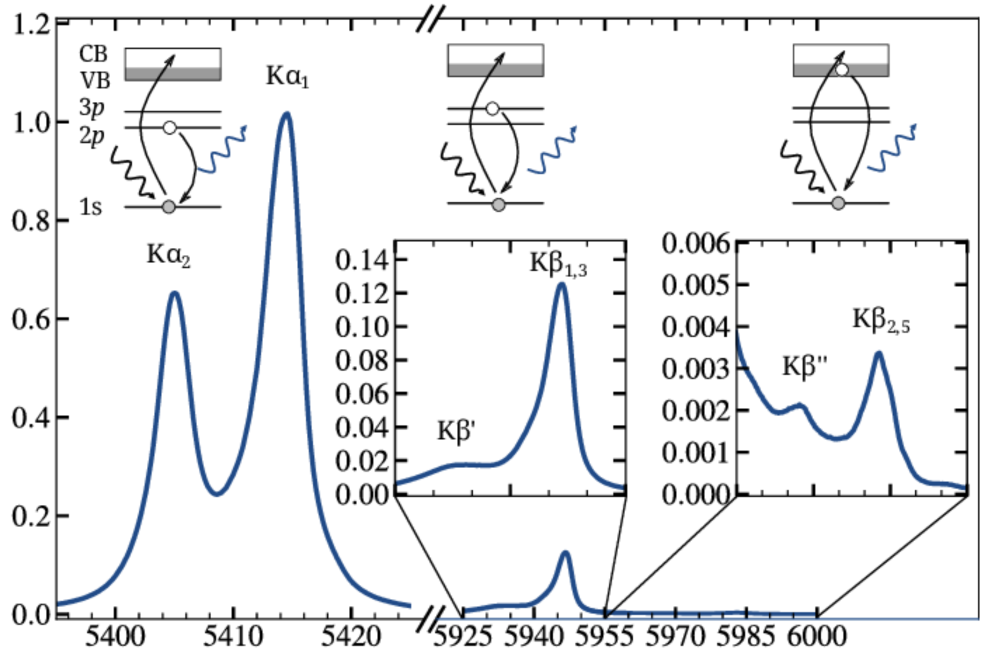

Figure 16: K-edge XES spectrum of Cr in Cr_2O_3 showing Kα, Kβ and VTC emission regions with relative amplitude and their origin in a simple atomic orbital picture. The insets show amplified views of the indicated portion of the spectrum. Figure reproduced from Rovezzi and Glatzel (*41*).

To begin, the Kα spectral feature, which arises from the 2p → 1s electronic transition, splits into $K\alpha_1$ and $K\alpha_2$ due to the spin-orbit splitting of the 2p orbital into $2p^{3/2}$ and $2p^{1/2}$, respectively. As such the $K\alpha_2$ line ($2p^{1/2}$ → 1s) is less intense and at a lower energy position compared to the $K\alpha_1$ line, ($2p^{3/2}$ → 1s), as seen in figure 17 for Cr Kα. On the other hand, the energy levels associated with the Kα spectral features are also affected by the valence level electronic structure (e.g., oxidation state) that can manifest as energy shifts in the Kα lines. (*40*)

For 3*d* transition metals the energy shifts in Kα lines can often be used to infer the change in oxidation state of the metal. The Jahrman (*42*) study made use of Kα energy shifts to differentiate and quantify Cr(VI), which is of interest because of its carcinogenic effect in humans, from Cr(III) in different commercially available plastics. The Figure shows the Kα emission lines for Cr in various plastics along with the reference spectra for trivalent and hexavalent Cr species on the top and bottom respectively. The fractional contributions of the trivalent and hexavalent Cr species in the samples were calculated from the results of the linear combination fits using the pure end-member species (trivalent, Cr_2O_3 and hexavalent, $BaCrO_4$).

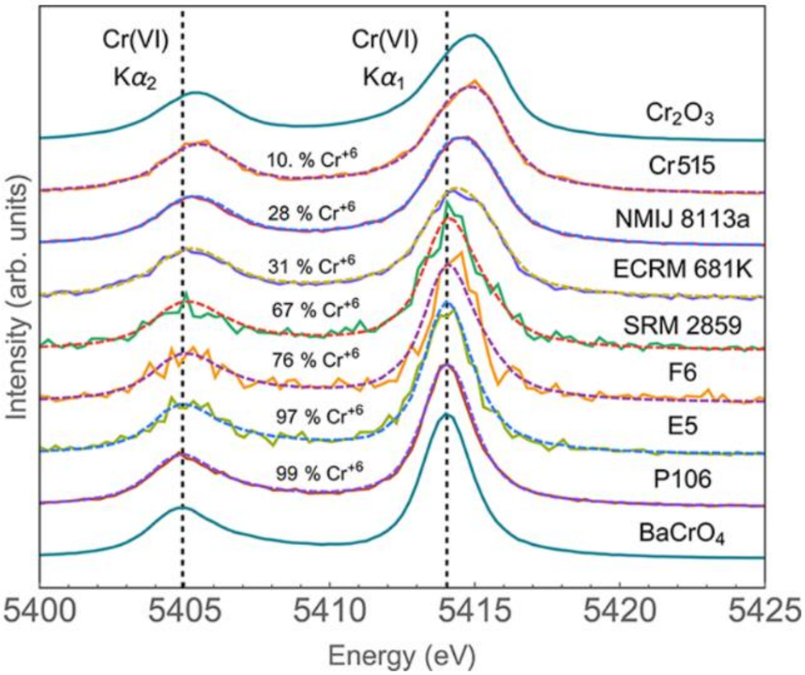

Figure 17: Vertically offset Cr Kα XES spectra of plastics bracketed by compounds of pure-end member species (trivalent Cr_2O_3, top; hexavalent $BaCrO_4$, bottom). The measured spectrum for each plastic is shown along with the fit (dashed) provided by a least-squares regression analysis and the percent Cr (VI) determined from the fit. The first 10 eV and last 15 eV, which were collected to properly correct for background, are omitted. Note that all spectra are background corrected and integral normalized. For ease of reference, vertical dashed lines pass through the center of the Cr $K\alpha_1$ and $K\alpha_2$ peaks in $BaCrO_4$. Figure reproduced from Jahrman *et al*. (*42*).

The Kβ spectral features are more strongly affected by the valence level electronic structure (e.g., oxidation state), which can manifest as energy shifts of the spectral features, similar to the case of Kα lines, but are also influenced by factors like ligand charge transfer effects and p-d exchange interactions and hence require very careful interpretation of the results. (*40*) For example, the Kβ spectral features also contain a satellite peak Kβ' on the lower energy side of the main $K\beta_{1,3}$ peak. This satellite peak is due to the 3p-3d exchange interaction and thus contains information about the total unpaired spin of the 3d electrons. (*28, 40*).

For example, Lin, *et al.*, (*28*) exploited the spin dependence of the Kβ' satellite peak to understand the spin transition of iron at high pressures corresponding to Earth's lower mantle conditions. Figure 18 shows the Fe-Kβ XES spectra from a single-crystal magnesiowustite, $(Mg_{0.75}Fe_{0.25})O$ as a function of applied pressure. In this case, the intensity of the Kβ' satellite peak is proportional to the unpaired 3d spin of the iron atoms, so that the change in the intensity of the satellite peak with pressure was used to understand the electronic spin transition of iron in magnesiowustite. The presence of the Kβ' satellite peak below 55 GPa is characteristic of the magnetic state of iron, whereas the absence of the satellite peak above 67 GPa indicates the collapse of magnetization. The authors were then able to relate this high-spin to low-spin transition to an abnormal compressional behavior between these two states which helped explain the seismic wave heterogeneity observed in Earth's lowermost mantle.

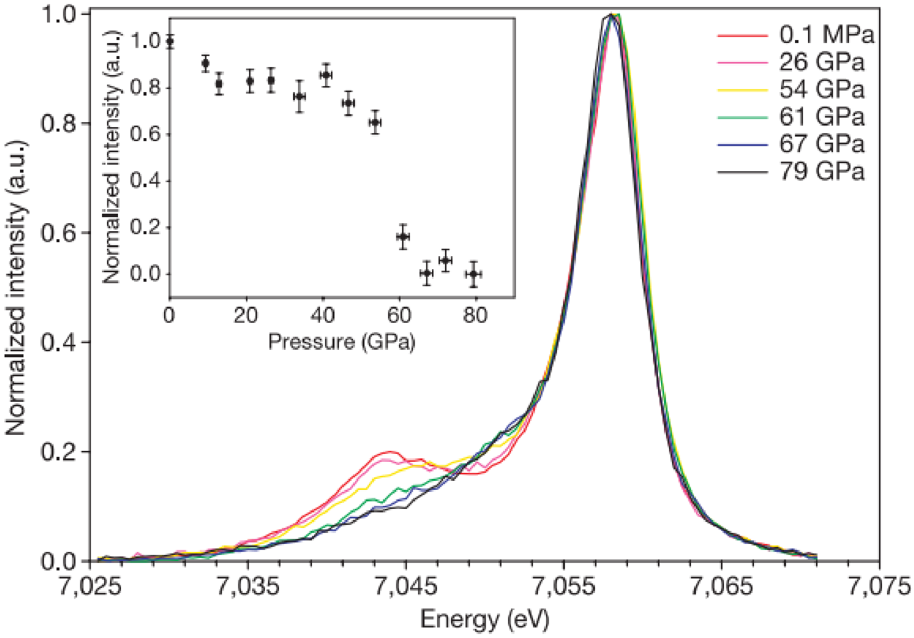

Figure 18: Representative Fe-Kβ XES spectra from a single-crystal magnesiowustite ($(Mg_{0.75}Fe_{0.25})O$) in <110> orientation as a function of applied pressure as indicated in the legend. Inset: Normalized intensity of the satellite Kβ' feature plotted against pressure. Figure reproduced from Lin *et al*. (*28*).

Finally, Figure 19 shows a schematic depiction of transitions related to different K-emission features in a molecular orbital picture. As seen in the figure, the valence-to-core (VTC) XES reflects the occupied orbitals directly involved in bonding, and consequently shows fine structure closely related to the coordination symmetry and other very local electronic effects.

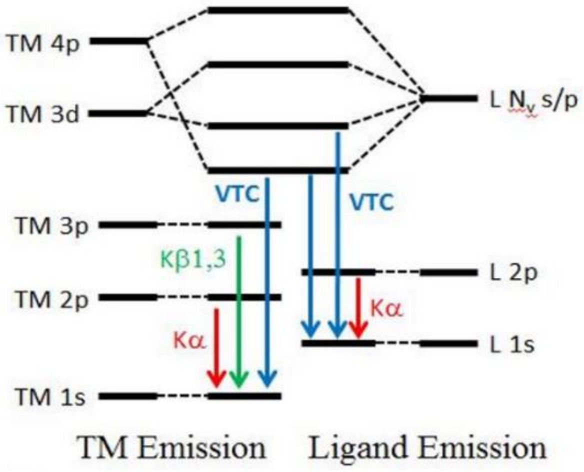

Figure 19: Schematic molecular orbital diagram showing the transitions related to transition metal K-emission features of a metal-ligand compound. Figure reproduced after Kowalska *et al*. (*8*).

The VTC emission is broadly divided into two pieces: the Kβ” region and the $K\beta_{2,5}$ region. The Kβ” region, which is on the lower energy side of the VTC, arises from hybridization of the transition metal 3*d* orbital and ligand semi-core orbitals. It has been demonstrated that the Kβ” feature is particularly sensitive to the ligand identity and can be used to distinguish even the light elements with close atomic numbers (e.g., C, N, O) bonded with the metal center. (*41*, *43*, *44*)

Figure 20 shows the experimental and simulated VTC spectra for a set of Cr-based compounds with different ligands. The ligand identity sensitivity of the energy position of the Kβ” peak arising from the ligand s-states is evident. In other studies, the polarization dependence of

XES has been used in conjunction with the VTC-Kβ” feature to learn about the orientation of specific ligands in a metal complex. (*41*, *46*)

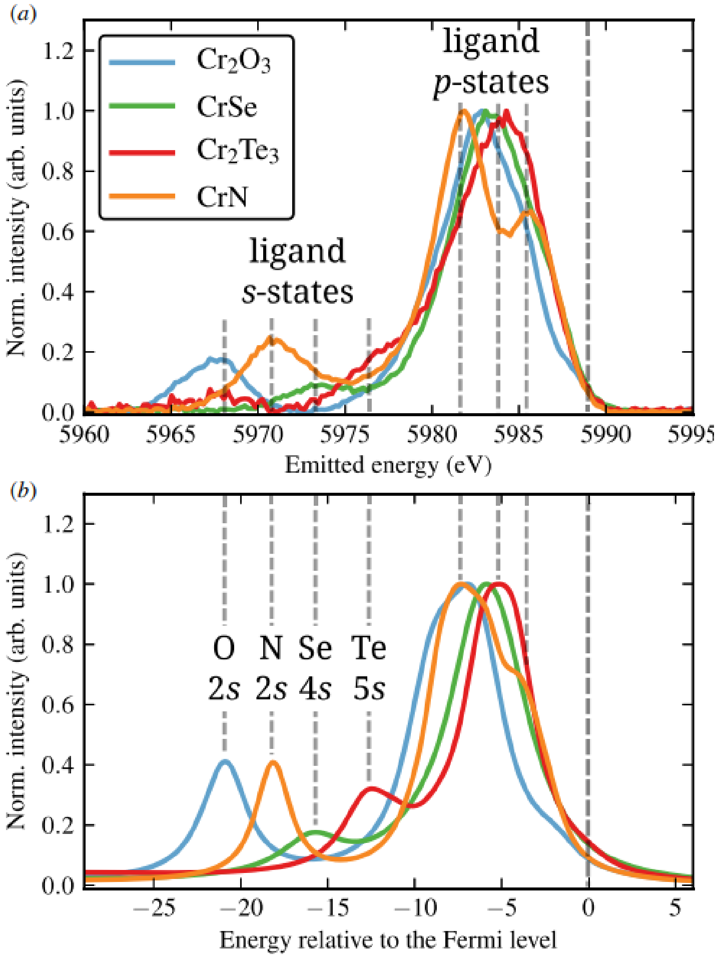

Figure 20: VTC XES spectra for various Cr-based compounds as indicated in the legend. (a) Experiment, (b) Ab initio simulations using FDMNES code. The Kβ” feature is related to the weak hybridization with weakly semicore ligand S – states. Figure reproduced from Rovezzi and Glatzel (*41*).

In contrast, the full interpretation of the $K\beta_{2,5}$ feature, which is on the higher energy side in the VTC, is more complicated. It arises from hybridized orbitals between the metal *3d* and ligand *p*-states. Thus, in addition to the nature and identity of the ligand it is also sensitive to coordination symmetry. (*47*) This was utilized by Gallo *et al*. to distinguish between octahedral and tetrahedral coordination of Ti atom. (*45*) As seen in figure 21, the experimental and theoretical data show clear distinction in the K$\beta_{2,5}$ feature between the octahedrally and tetrahedrally coordinated Ti atom with the same ligand O. Similar strong dependence of K$\beta_{2,5}$ on the metal's local symmetry is also presented in these studies. (*45, 48*)

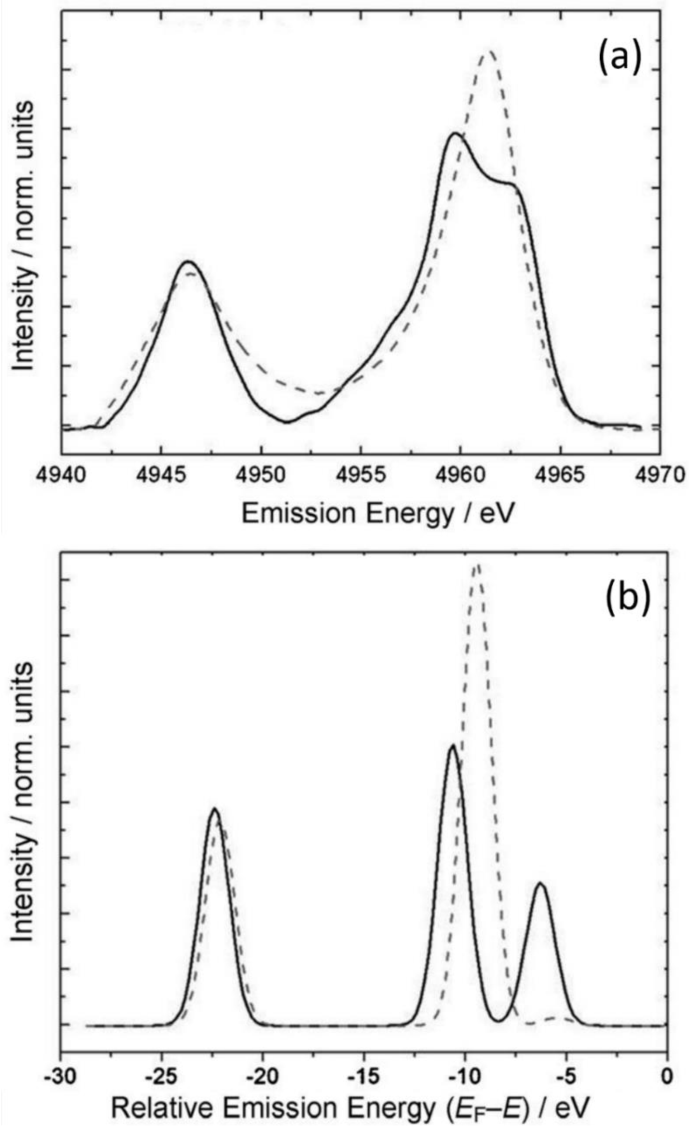

Figure 21: VTC XES spectra for Ti compounds in octahedral (dashed lines) and tetrahedral coordination (solid lines). (a) Experimental spectra of activated Titanium Silicate – 1 (TS-1/act) (solid line) and $CaTiO_3$ (dashed line), and (b) Calculated spectra of $Ti(OH)_4$ (solid line) and $Ti(OH)_6$ (dashed line). Reproduced from Gallo *et al*. (*45*).

Thus, VTC-XES has the potential to be a powerful tool to study the local structure of transition metals in a host of applications. Moreover, VTC-XES has the advantage of the possibility to relatively easily calculate the transitions with a molecular-orbital approach, for example using DFT methods. (*49-51*)

4.4: References

1. J. F. Mulligan, *Heinrich Rudolf Hertz (1857-1894): a collection of articles and addresses*. (Routledge, 2018).
2. E. B. Karlsson, in *The Nobel Prize: The First 100 Years*. (World Scientific Singapore, 2001), pp. 235.
3. R. F. Mould, The early history of x-ray diagnosis with emphasis on the contributions of physics 1895-1915. *Physics in Medicine & Biology* **40**, 1741 (1995).
4. D. S. Jensen *et al.*, Silicon (100)/SiO2 by XPS. *Surface Science Spectra* **20**, 36-42 (2013).
5. D. N. G. Krishna, J. Philip, Review on surface-characterization applications of X-ray photoelectron spectroscopy (XPS): Recent developments and challenges. *Applied Surface Science Advances* **12**, 100332 (2022).
6. P. Zimmermann *et al.*, Modern X-ray spectroscopy: XAS and XES in the laboratory. *Coordination Chemistry Reviews* **423**, 213466 (2020).
7. J. C. Lindon, G. E. Tranter, D. Koppenaal, *Encyclopedia of spectroscopy and spectrometry*. (Academic Press, 2016).
8. J. K. Kowalska, F. A. Lima, C. J. Pollock, J. A. Rees, S. DeBeer, A Practical Guide to High-resolution X-ray Spectroscopic Measurements and their Applications in Bioinorganic Chemistry. *Israel Journal of Chemistry* **56**, 803-815 (2016).
9. N. Jiang, D. Su, J. C. H. Spence, Determination of Ti coordination from pre-edge peaks in Ti K-edge XANES. *Physical Review B* **76**, 214117 (2007).
10. T. Yamamoto, Assignment of pre-edge peaks in K-edge x-ray absorption spectra of 3d transition metal compounds: electric dipole or quadrupole? *X-Ray Spectrometry* **37**, 572-584 (2008).
11. C. H. Kuo *et al.*, Facet-dependent catalytic activity of MnO electrocatalysts for oxygen reduction and oxygen evolution reactions. *Chemical Communications* **51**, 5951-5954 (2015).
12. N. Khare, J. D. Martin, D. Hesterberg, Phosphate bonding configuration on ferrihydrite based on molecular orbital calculations and XANES fingerprinting. *Geochimica et Cosmochimica Acta* **71**, 4405-4415 (2007).
13. S. Rojsatien *et al.*, Quantitative analysis of Cu XANES spectra using linear combination fitting of binary mixtures simulated by FEFF9. *Radiation Physics and Chemistry* **202**, 110548 (2023).

14. L. B. Zasada *et al.*, Conjugated Metal–Organic Macrocycles: Synthesis, Characterization, and Electrical Conductivity. *Journal of the American Chemical Society* **144**, 4515-4521 (2022).
15. S. Tetef, N. Govind, G. T. Seidler, Unsupervised machine learning for unbiased chemical classification in X-ray absorption spectroscopy and X-ray emission spectroscopy. *Physical Chemistry Chemical Physics* **23**, 23586-23601 (2021).
16. J. Timoshenko, D. Lu, Y. Lin, A. I. Frenkel, Supervised Machine-Learning-Based Determination of Three-Dimensional Structure of Metallic Nanoparticles. *The Journal of Physical Chemistry Letters* **8**, 5091-5098 (2017).
17. J. Yano, V. K. Yachandra, X-ray absorption spectroscopy. *Photosynthesis Research* **102**, 241-254 (2009).
18. E. A. Stern, Theory of the extended x-ray-absorption fine structure. *Physical Review B* **10**, 3027 (1974).
19. S. Gurman, Interpretation of EXAFS data. *Journal of synchrotron radiation* **2**, 56-63 (1995).
20. J. J. Rehr, R. C. Albers, Theoretical approaches to x-ray absorption fine structure. *Reviews of modern physics* **72**, 621 (2000).
21. P. Lee, J. Pendry, Theory of the extended x-ray absorption fine structure. *Physical Review B* **11**, 2795 (1975).
22. C. Ashley, S. Doniach, Theory of extended x-ray absorption edge fine structure (EXAFS) in crystalline solids. *Physical Review B* **11**, 1279 (1975).
23. J. J. Boland, S. E. Crane, J. D. Baldeschwieler, Theory of extended x-ray absorption fine structure: Single and multiple scattering formalisms. *The Journal of Chemical Physics* **77**, 142-153 (1982).
24. D. R. Sandstrom, F. W. Lytle, Developments in extended X-ray absorption fine structure applied to chemical systems. *Annual Review of Physical Chemistry* **30**, 215-238 (1979).
25. D. E. Sayers, E. A. Stern, F. W. Lytle, New technique for investigating noncrystalline structures: Fourier analysis of the extended x-ray—absorption fine structure. *Physical review letters* **27**, 1204 (1971).
26. Y. Pushkar, J. Yano, K. Sauer, A. Boussac, V. K. Yachandra, Structural changes in the Mn4Ca cluster and the mechanism of photosynthetic water splitting. *Proceedings of the National Academy of Sciences* **105**, 1879-1884 (2008).
27. M. J. Latimer *et al.*, Evidence for the proximity of calcium to the manganese cluster of photosystem II: determination by X-ray absorption spectroscopy. *Biochemistry* **34**, 10898-10909 (1995).
28. J.-F. Lin *et al.*, Spin transition of iron in magnesiowüstite in the Earth's lower mantle. *Nature* **436**, 377-380 (2005).
29. R. M. Cinco *et al.*, Strontium EXAFS reveals the proximity of calcium to the manganese cluster of oxygen-evolving photosystem II. *The Journal of Physical Chemistry B* **102**, 8248-8256 (1998).
30. R. M. Cinco *et al.*, Calcium EXAFS establishes the Mn-Ca cluster in the oxygen-evolving complex of photosystem II. *Biochemistry* **41**, 12928-12933 (2002).
31. R. P. Gunawardane, C. R. Arumainayagam, in *Handbook of applied solid state spectroscopy,* D. Vij, Ed. (Springer, Boston, MA, 2006), pp. 451-483.
32. D. Mogk. (Montana State University, https://serc.carleton.edu/msu_nanotech/methods/aes.html, 2023).

33. Albert C. Thompson, D. Vaughan, Eds., *X-ray Data Booklet*, (Lawerence Berkeley National Laboratory, Berkeley, CA, 2001).
34. J. L. Heilbron, The Work of H. G. J. Moseley. *Isis* **57**, 336-364 (1966).
35. G. Gorin, Mendeleev and Moseley: The principal discoverers of the periodic law. *Journal of chemical education* **73**, 490-493 (1996).
36. PhysicsOpenLab. (PhysicsOpenLab, https://physicsopenlab.org/2016/02/24/diy-xrf-spectrometry/, 2016).
37. L. Corbari *et al.*, Iron oxide deposits associated with the ectosymbiotic bacteria in the hydrothermal vent shrimp <i>Rimicaris exoculata</i>. *Biogeosciences* **5**, 1295-1310 (2008).
38. E. P. Jahrman *et al.*, An improved laboratory-based x-ray absorption fine structure and x-ray emission spectrometer for analytical applications in materials chemistry research. *Review of Scientific Instruments* **90**, 024106 (2019).
39. G. Seidler *et al.*, A laboratory-based hard x-ray monochromator for high-resolution x-ray emission spectroscopy and x-ray absorption near edge structure measurements. *Review of Scientific Instruments* **85**, 113906 (2014).
40. U. Bergmann, P. Glatzel, X-ray emission spectroscopy. *Photosynthesis Research* **102**, 255-266 (2009).
41. M. Rovezzi, P. Glatzel, Hard x-ray emission spectroscopy: a powerful tool for the characterization of magnetic semiconductors. *Semiconductor Science and Technology* **29**, 023002 (2014).
42. E. P. Jahrman, G. T. Seidler, J. R. Sieber, Determination of Hexavalent Chromium Fractions in Plastics Using Laboratory-Based, High-Resolution X-ray Emission Spectroscopy. *Analytical Chemistry* **90**, 6587-6593 (2018).
43. K. M. Lancaster *et al.*, X-ray emission spectroscopy evidences a central carbon in the nitrogenase iron-molybdenum cofactor. *Science* **334**, 974-977 (2011).
44. U. Bergmann, C. Horne, T. Collins, J. Workman, S. Cramer, Chemical dependence of interatomic X-ray transition energies and intensities–a study of Mn Kβ ″and Kβ2, 5 spectra. *Chemical physics letters* **302**, 119-124 (1999).
45. E. Gallo *et al.*, Preference towards Five-Coordination in Ti Silicalite-1 upon Molecular Adsorption. *Chemphyschem* **14**, 79-83 (2013).
46. U. Bergmann, J. Bendix, P. Glatzel, H. B. Gray, S. P. Cramer, Anisotropic valence→ core x-ray fluorescence from a [Rh (en) 3][Mn (N)(CN) 5]· H 2 O single crystal: Experimental results and density functional calculations. *The Journal of chemical physics* **116**, 2011-2015 (2002).
47. E. Gallo, P. Glatzel, Valence to core X-ray emission spectroscopy. *Advanced Materials* **26**, 7730-7746 (2014).
48. G. Smolentsev *et al.*, X-ray emission spectroscopy to study ligand valence orbitals in Mn coordination complexes. *Journal of the American Chemical Society* **131**, 13161-13167 (2009).
49. C. J. Pollock, S. DeBeer, Valence-to-core X-ray emission spectroscopy: a sensitive probe of the nature of a bound ligand. *Journal of the American Chemical Society* **133**, 5594-5601 (2011).
50. E. Gallo, C. Lamberti, P. Glatzel, Investigation of the valence electronic states of Ti (IV) in Ti silicalite-1 coupling X-ray emission spectroscopy and density functional calculations. *Physical Chemistry Chemical Physics* **13**, 19409-19419 (2011).

51. D. R. Mortensen *et al.*, Benchmark results and theoretical treatments for valence-to-core x-ray emission spectroscopy in transition metal compounds. *Physical Review B* **96**, 125136 (2017).

Chapter 5: Research Motivation

The complexation of the redox-active ion in a battery electrolyte influences the critical processes of battery performance, including ion conductivity, charge transfer resistance and the stability of different species. (*1*) This lattermost issue, species stability, in turn affects the stability and formation of the solid-electrolyte interface (SEI) and ultimately the electrode stability and related kinetics. (*2, 3*) It is known that the formation of contact ion pairs and the evolution of any solvation complexes are modulated by parameters such as size, charge, and nature of the active ion, and the concentration, dielectric constant and temperature of the host (modified) solvent. (*4*)

Despite renewed interest and ongoing research in the local dynamics and structure of electrolytes, many important questions remain to be answered concerning the complex relationship between composition, structure and dynamics in the electrolyte and the resulting effects on the performance of the battery. (*5*) These issues are not abstract, academic concerns: Better electrolytes for next-generation batteries to ensure the widespread use of renewable energy requires clear fundamental understanding of the solvation structure of the electrolyte solution and its impact on performance. Here, we investigate electrolytes for Zn-ion batteries, a representative example of novel rechargeable battery that is seeing extensive contemporary effort. (*6*) Using advanced x-ray spectroscopies in the lab and at synchrotron light sources, we characterize the degree of ion pairing as a function of concentration, anion activity, temperature, and nano-scale confinement. Our results serve as the basis for critical comparison to thermodynamic and atomic-scale modeling, serve as benchmark standards for future determination of the sensitivity of other methods to ion pairing, and establish the usefulness of lab-based x-ray spectroscopies for ion-pairing questions, thus defining a new direction that can accelerate research in this field.

With an eye toward the cleanest possible results for the underlying microscopics, we study aqueous $ZnCl_2$ (and, to a lesser extent $ZnBr_2$) electrolytes. $ZnCl_2$ electrolytes are among the simple and inexpensive alternatives that are seeing contemporary research interest for next-generation aqueous batteries, and they provide a straightforward platform to study the evolution of solvation complex in aqueous electrolytes. (*6-10*) Our results, and the methods that we develop for the study – quantification of ion pairing using valence-to-core X-ray emission spectroscopy (VTC-XES) – can later be used to understand the behavior of more complex electrolytes.

In Figure 1, we show the various potential Zn^{2+} coordination in aq. $ZnCl_2$ solution. Starting at (a), we see the octahedral aquo coordination of Zn^{2+} which is expected for low concentrations and ion activities – this is well known for other Zn-aqueous electrolytes, such as $Zn(NO_3)_2$. (*11*) At very high concentrations with anion activity enhanced with a second salt, there is strong reason to expect the tetrahedral coordination (g). The other structures are possible intermediates that may, or may not, exist under special compositions and thermodynamic conditions. That said, one generality is that tetrahedral coordination is generally expected due to steric constraints if there is coordination of even one Cl^- anion.

A calculated phase-coordination diagram for aq. $ZnCl_2$ is shown in Figure 2. The solid curves in the diagram indicate equilibrium contours from, e.g., the Nernst equation, and do not necessarily indicate strict phase boundaries rather than crossovers in populations having different Zn^{2+} coordination. Although all the three studies (*12-14*) used a similar solubility-based chemical equilibrium method to model the speciation, the results obtained are quite different. This points towards the underlying limitation in extrapolating dilute-limit models to higher concentrations and the need for robust experimental results to investigate such theoretical predictions and motivate new models suitable for higher concentrations.

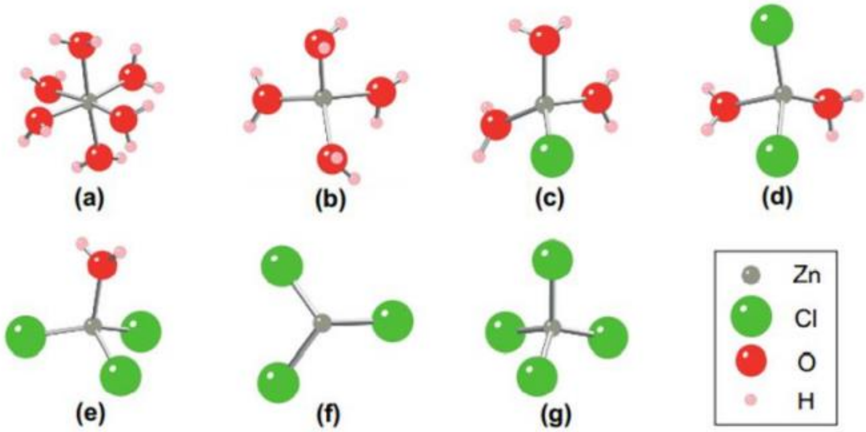

Figure 1: Snapshots of different Zn(II)-Cl complexes formed during molecular dynamics (MD) simulations. Note, in particular, (a) showing an octahedral coordination with six water molecules, and (g) exhibiting the endpoint of tetrahedral coordination with four Cl^- ions. Figure adapted from Mei *et al*. (*15*)

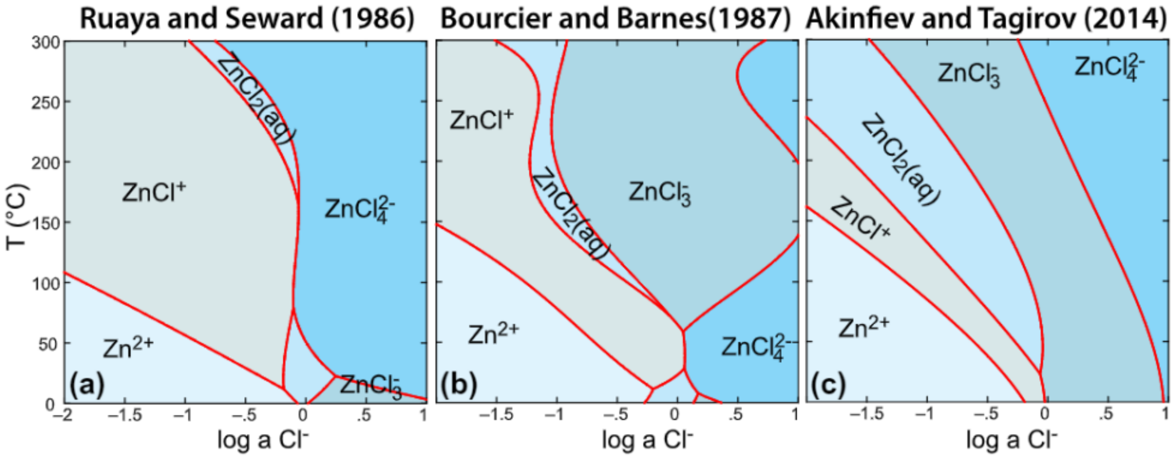

Figure 2: A summary of three phase-coordination diagrams for aq. $ZnCl_2$, calculated from the thermodynamic formation constants reported in different studies as indicated on the top of each panel. Figure reproduced from Mei *et al*. (*15*)

Thus, we seek to experimentally quantify the extent of ion pairing and understand the local coordination of Zn^{2+} ions in aqueous Zn-Cl system under different conditions. First, in Chapter 6, we investigate the solutions as a function of concentration. Because of the 1:2 mole ratio of Zn^{2+} and Cl^-, such solutions cannot reach full transition to $ZnCl_4^{2-}$ coordination without, e.g., gross polymerization, an outcome that is unlikely. Consequently, we also study the $ZnCl_2$ solutions augmented with an additional chloride salt, such as NaCl or LiCl, to increase the Cl^- ion activity and more fully access the fully ion-paired, tetrahedral coordination of $ZnCl_4^{2-}$. Then, in Chapter 7, using the methods developed in chapter 6, we investigate the effects of nanoconfinement on the ion pairing behavior in aqueous $ZnCl_2$ solutions and compare the extent of ion pairing to the electrochemical voltage window of these electrolytes. Finally, in Chapter 8, we explore the effects of elevated temperature on the evolution of ion pairing in Zn-Cl aqueous system. Each of these contexts will be discussed in more detail in the respective Chapters.

5.1: References

1. P. G. Bruce, M. T. Hardgrave, C. A. Vincent, Steady state current flow in solid binary electrolyte cells: part 2. The effect of ion association. *Journal of electroanalytical chemistry and interfacial electrochemistry* **271**, 27-34 (1989).
2. L. M. Suo *et al.*, "Water-in-salt" electrolyte enables high-voltage aqueous lithium-ion chemistries. *Science* **350**, 938-943 (2015).
3. L. Doucey, M. Revault, A. Lautié, A. Chaussé, R. Messina, A study of the Li/Li+ couple in DMC and PC solvents: part 1: characterization of LiAsF6/DMC and LiAsF6/PC solutions. *Electrochimica acta* **44**, 2371-2377 (1999).
4. M. R. Wright, *An introduction to aqueous electrolyte solutions*. (John Wiley & Sons, 2007).
5. N. N. Rajput, T. J. Seguin, B. M. Wood, X. Qu, K. A. Persson, in *Modeling Electrochemical Energy Storage at the Atomic Scale*. (Springer, 2018), pp. 79-124.
6. X. Zeng, J. Hao, Z. Wang, J. Mao, Z. Guo, Recent progress and perspectives on aqueous Zn-based rechargeable batteries with mild aqueous electrolytes. *Energy Storage Materials* **20**, 410-437 (2019).
7. F. Wang *et al.*, Highly reversible zinc metal anode for aqueous batteries. *Nature Materials* **17**, 543-549 (2018).
8. C. Zhang *et al.*, A ZnCl2 water-in-salt electrolyte for a reversible Zn metal anode. *Chemical Communications* **54**, 14097-14099 (2018).
9. L. Zhang *et al.*, ZnCl2 "Water-in-Salt" Electrolyte Transforms the Performance of Vanadium Oxide as a Zn Battery Cathode. *Advanced Functional Materials* **29**, 1902653 (2019).
10. C. Zhang *et al.*, The electrolyte comprising more robust water and superhalides transforms Zn-metal anode reversibly and dendrite-free. *Carbon Energy* **3**, 339-348 (2021).

11. S. P. Dagnall, D. N. Hague, A. D. Towl, X-ray diffraction study of aqueous zinc (II) nitrate. *Journal of the Chemical Society, Faraday Transactions 2: Molecular and Chemical Physics* **78**, 2161-2167 (1982).
12. J. R. Ruaya, T. M. Seward, The stability of chlorozinc(II) complexes in hydrothermal solutions up to 350-degrees-C. *Geochimica Et Cosmochimica Acta* **50**, 651-661 (1986).
13. W. L. Bourcier, H. L. Barnes, Ore solution chemistry; VII, stabilities of chloride and bisulfide complexes of Zinc to 350 degrees C. *Economic Geology* **82**, 1839 - 1863 (1987).
14. N. N. Akinfiev, B. R. Tagirov, Zn in hydrothermal systems: Thermodynamic description of hydroxide, chloride, and hydrosulfide complexes. *Geochemistry International* **52**, 197-214 (2014).
15. Y. Mei *et al.*, Zinc complexation in chloride-rich hydrothermal fluids (25–600°C): A thermodynamic model derived from ab initio molecular dynamics. *Geochimica et Cosmochimica Acta* **150**, 265-284 (2015).

Chapter 6: The Evolution of Solvation Symmetry and Composition in Zn Halide Aqueous Solutions from Dilute to Extreme Concentrations

This chapter is based on a manuscript that first appeared in the journal "Physical Chemistry Chemical Physics" of the Royal Society of Chemistry.

Diwash Dhakal, Darren M. Driscoll, Niranjan Govind, Andrew G. Stack, Nikhil Rampal, Gregory Schenter, Christopher J. Mundy, Timothy T. Fister, John L. Fulton, Mahalingam Balasubramanian, Gerald T. Seidler, "The evolution of solvation symmetry and composition in Zn halide aqueous solutions from dilute to extreme concentrations." *Physical Chemistry Chemical Physics* **25**, 22650-22661 (2023). (DOI: https://doi.org/10.1039/D3CP01559A)

6.1: Abstract

The emergence of cation-anion species, or contact ion pairs, is fundamental to understanding the physical properties of aqueous solutions when moving from the ideal, low-concentration limit to the manifestly non-ideal limits of very high solute concentration or constituent ion activity. We focus here on Zn halide solutions both as a model system and also as an exemplar of the applications spanning from (i) electrical energy storage via the paradigm of water in salt electrolyte (WiSE) to (ii) the physical chemistry of brines in geochemistry to (iii) the long-standing problem of nucleation. Using a combination of experimental and theoretical approaches we quantify the halide coordination number and changing coordination geometry without embedded use of theoretical equilibrium constants. These results and the associated methods, notably including the use of valence-to-core x-ray emission spectroscopy, provide new insights into the Zn halide system and new research directions in the physical chemistry of concentrated electrolytes.

6.2: Introduction

The structure and resulting chemical and electronic properties of aqueous solutions is central to the coupled experimental and theoretical development of physical chemistry. Specifically, any comprehensive understanding must address the classic progression from ideal dilute solutions with uncoordinated solute ions to, first, more concentrated cases requiring nontrivial activity coefficients and sophisticated thermodynamic modeling to, finally, more extreme cases with strong anion-cation coordination. (*1*-*3*) This sequence of conditions still bears contemporary relevance both as a testing ground of, e.g., *ab initio* molecular dynamics, and also for the accelerating importance of both traditional concentrated solutions and ionic liquids across numerous fields of research and technology. (*4*-*7*)

We report a combined experimental and theoretical investigation of ion pairing in Zn-halide aqueous solutions over their full accessible concentration range. This is, on one hand, undeniably a model system that is highly amenable to modern theoretical treatments and, on the other hand, is also deeply relevant for electrical energy storage, for geochemical processes, and for the fundamental understanding of the dynamics and influence of ion association on precipitation of solid phases. (*8*-*15*)

To begin, following the successful demonstration of rechargeable Zn-ion intercalation chemistry and the introduction of the highly concentrated electrolyte concept, there is growing interest in Zn-based multivalent aqueous chemistry (*16*-*18*) due to the higher energy density promised by a multivalent battery and the nontoxicity and earth-abundance of Zn. (*19, 20*) Significantly motivating the present work, recent studies (*16, 21*) of so-called ‘water-in-salt electrolytes’ (WiSE) for aqueous batteries have shown that the presence and extent of ion pairing in an aqueous electrolyte plays a vital role in enlarging the electrochemical window of the electrolyte, thus increasing stored energy density. This includes $ZnCl_2$ WiSE in Zn-ion batteries, which show enhanced performance at high salt concentrations, both in pure and mixed salt solutions. (*12-15*) The presence of ion-paired complexes, especially the tetrahedral $ZnCl_4^{2-}$ complex, at such high salt concentrations is believed to be essential to the improved performance. However, neither the extent of ion pairing nor its exact correlation with the resulting electrochemical properties are well understood.

In fact, the detailed occurrence of contact ion pairing in aqueous $ZnCl_2$ solutions remains uncertain despite extensive prior work for a completely different reason: the physical chemistry of geochemical brines. The solubilities of minerals are influenced by the type and concentration of ligands present in the brine. Metal complexes with different ligands contribute to the overall solubility in varying degrees and thus it is very important to understand the distribution of various complexes in an aqueous solution. (*9*) As chloride is considered to be the dominant anion in most natural hydrothermal solutions and furthermore as chloride complexes of Zn are considered the main species responsible for Zn transport in such systems, the evolution of ion pairing in aqueous $ZnCl_2$ is central to understanding the transport mechanisms for Zn in hydrothermal brines, (*9, 22, 23*) and its successful modeling can inform other geochemical processes.

Finally, the extent of ion association in complex aqueous solutions, particularly with respect to the mechanisms of precipitation of solid phases, is an even broader topic with strong and contentious contemporary interest. (*10, 24-28*) Linking the atomic-scale structure and dynamics of the solution to the elementary reaction mechanisms by which nucleation occurs is an inherently difficult problem due to the transient nature of nucleation reactions and intermediates involved in their formation and the range of different types of potential solutes in solutions (see e.g., Wang *et al*., 2022 (*29*)). There is growing evidence that the longer-range solution structure, i.e., outside the immediate first solvation shell, can induce changes in the reactivity of ion complexes and subsequent phase selection and rates during nucleation reactions. (*30, 31*) This is especially true at high concentrations, where classical notions about the nature of activity-concentration relationships of solutes become invalidated. $ZnCl_2$ is a good test case for ideas about extended networks of associated ions because it is known to have ion complexes and has a high solubility that is facile for solution structure measurements. That being said, there remains broad disagreement about the nature of the speciation and the degree and distribution of higher order complex formation. (*30*) Given the uncertainties here, considerable benefit would accrue from a firm characterization of the Zn^{+2} first-shell coordination across the relevant range of concentrations, ion activity, and even temperature. Such a result would serve as a powerful anchor for theoretical treatment in the difficult, highly concentrated (and hence highly correlated) domain, and also would be strong prior information for improved interpretation of extended x-ray absorption fine structure (EXAFS).

Hence, in all cases the central questions surround the relative domains of thermodynamic stability or coexistence for the variety of local coordinations of the Zn^{+2} ion, as shown in Figure 1 and Figure SI-1 and tabulated in Table SI-1. For temperatures near ambient, several studies of Zn-Cl solutions agree that (1) there is predominantly octahedrally-coordinated $Zn(H_2O)_6^{2+}$ at low Zn concentrations and low anion activity, and that (2) there is predominantly tetrahedrally-coordinated $ZnCl_4^{2-}$ at very high anion activity.(*8, 9*) However, these works disagree on the intermediate regime, in some cases suggesting that other moieties, such as partially-hydrated and partially chlorinated Zn^{+2} in a tetrahedral environment, can be thermodynamically favored. To this end, aqueous Zn-halide solutions have seen previous detailed study of the local and extended solvation structure by EXAFS (*9*, *11*, *32*), XANES (*22*), x-ray diffraction (*33*, *34*) and neutron diffraction (*35*).

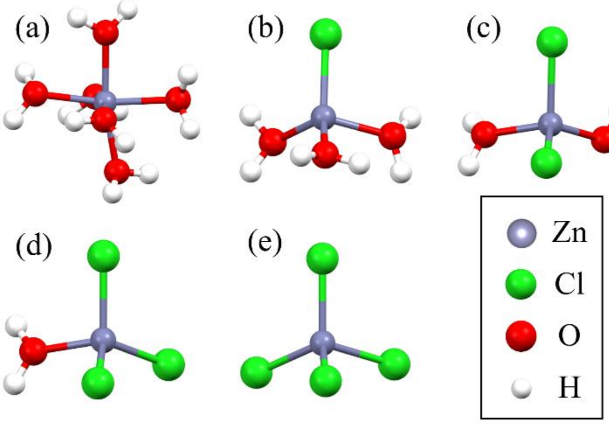

Figure 1. DFT-optimized Zn^{+2} coordination structures for (a) $Zn(H_2O)_6^{+2}$, (b) $ZnCl(H_2O)_3^{+}$, (c) $ZnCl_2(H_2O)_2$, (d) $ZnCl_3(H_2O)^{-}$, (e) $ZnCl_4^{-2}$. In all cases, hybrid DFT based optimizations using the PBE0 exchange-correlation functional was performed with 40 explicit water molecules, while the long-range solvation was treated implicitly. For clarity, the water molecules beyond the first shell are not shown.

In the present work on $ZnCl_2$ and $ZnBr_2$ aqueous solutions we employ two complementary experimental methods having direct sensitivity to the question of local coordination: XANES, where we extend prior work to higher concentrations, and valence-to-core x-ray emission spectroscopy (VTC-XES), being used here for the first time on this class of question. The VTC-XES results, which measure the occupied density of states near the Fermi level, show unambiguous, and quite significantly, an exclusive sensitivity to the first-shell coordination, unlike XANES, which is also sensitive to the overall environment up to higher shells. With support from time-dependent density functional theory (TDDFT), we find that the VTC-XES allows inference of the number of chloride ligands per Zn ion, henceforth N_{Cl}. The resulting proposed dependence of N_{Cl} on Zn salt concentration or on total Cl concentration when other salts are added is compared and contrasted with Classical Molecular Dynamics (CMD) and lattice Monte Carlo (MC) calculations. Our study provides a new benchmark for ion pairing in Zn halide systems while also presenting a new methodology for studying first-shell coordination in concentrated solutions.

6.3: Methods

6.3.1: Materials and Solutions

For both the XES and XANES studies, aqueous solution samples of $Zn(NO_3)_2$, $ZnCl_2$, and $ZnBr_2$, often with added chloride salts (LiCl or NaCl) or bromide salts (LiBr), were prepared in air by dissolving weighed amounts of respective salts in HPLC-grade water. For higher concentrations, a magnetic stirrer was used for ~30 minutes to generate clear samples without visual sign of undissolved solute. Aqueous solution samples of ZnO and $Zn(OH)_2$ with added KOH were similarly prepared in air. The anhydrous $ZnCl_2$ polycrystalline reference sample was prepared in a glovebox starting with anhydrous $ZnCl_2$. ZnO and $Zn(OH)_2$ polycrystalline samples were prepared in air. All reagents were purchased from standard vendors (Alfa-Aesar, Sigma Aldrich, Fisher Scientific) in 99.9% purity or higher. For XES experiments, the solution samples were then loaded into thin-walled quartz capillaries (Charles Supper Corp.) closed with sealing wax. A significant air space was included in the capillary to accommodate possible evolved gas during x-ray irradiation. For XAS experiments, solutions were placed within PEEK holders of varying thickness having polyimide windows and sealed with epoxy.

6.3.2: X-ray Emission Spectroscopy (XES)

The XES measurements were performed with a laboratory-based x-ray emission spectrometer, described in detail in Jahrman, *et al*. (*36*) The x-ray source has a Pd anode and was operated at ~100 W power (35 kV and 2.8 mA). A Ge (555) spherically bent crystal analyzer had favorable Bragg angles and energy resolution for the required energy range. The vertical capillary sample holders were placed ~5 mm away from the Be exit window of the x-ray tube. Optimal lateral placement with respect to the vertical entrance slit of the spectrometer was verified by the method of Mortensen, *et al*. (*37*)

Each Zn XES scan spanned both the main Kβ line and the valence-to-core (VTC) region. Specifically, the scans were collected over the energy range 9550 – 9700 eV in 0.25-eV steps. We use a 40 s integration time per point in a region spanning the VTC emission (9630 – 9680 eV) and a shorter 4 s integration time per point in a lower-energy region spanning the main Kβ peak (9550 – 9630 eV) and a higher-energy region (9680 – 9700 eV) taken to assist with background subtraction. Total measurement times for each solution sample were typically 24 h for the Cl-containing solutions and 36 h for the Br-containing solutions. Comparison of early and later scans shows no evidence of beam damage. The average sample temperature was ~42°C for Cl-containing solutions and ~25°C for Br-containing solutions. The higher temperature of the Cl-containing solutions was due to heating from the end of the x-ray tube and was avoided for the Br-containing studies by adding a fan blowing on the sample location. A few representative Cl-containing solutions, especially in the intermediate concentration range where the temperature dependence is expected to be the strongest and hence serve as the upper bound of the mismatch, were also measured at 25°C. As shown in Figure SI-2 there is only a small systematic difference between the spectra measured at the two temperatures, resulting in <5% change in the inferred octahedral contribution (discussed in detail below and in the results and discussion).

Frequent measurement of the Kβ emission for a metallic Zn reference served as a check against any monochromator drift and allowed correction for instrumental calibration across multiple experiments, often separated by other uses of the spectrometer. The final energy scale is consistent across all data sets to ~25 meV.

Processing of the XES data followed several steps. First, we subtracted a constant background with value typically <5% of the count rate in the VTC region; this was due to stray scatter of the primary x-ray radiation. We found the relative Zn Kβ line shape and energy within our measurements to be invariant across metallic Zn and all solutions studied, due to the filled 3d10 shells for Zn^{+2}. A common shift in Bragg angle was thus applied to all the spectra to align our measurements with the accepted absolute energy value of 9572 eV for the Kβ line in literature. (*38*) See Figure SI-3.

The invariance of the Zn Kβ spectra allows a unique approach to processing the VTC-XES results, wherein the spectra were brought to a consistent molar scale via integral normalization of the VTC-XES by the area under the Zn Kβ spectral feature (specifically from 9550 – 9600 eV). The success of this normalization is prerequisite for any inference of the relative population of different local coordinations of the Zn^{+2} ion. The dominant error in cross-sample normalization of the VTC-XES will be from differences in the energy dependence of penetration of excitation radiation and escape of fluorescence at the main Kβ compared to the VTC region, and we estimate this contributes less than 3% error to the relative normalization of the valence-level emission with respect to the Kβ.

Enabled by the spectral normalization to a common mole-Zn scaled basis, a linear combination analysis of the various solution concentration series was used to infer information about the average number of chloride (or bromide) ligands per Zn ion. These fits were performed in Python using the VTC-XES data between 9640 – 9660 eV. The analysis utilized two solution end-point standards: a dilute ZnX_2 ($X = Br^-$ or Cl^-) solution and a 1 m ZnX_2 solution with a very high concentration of added LiX salt to achieve the highest accessible anion activity.

6.3.3: X-ray Absorption Near Edge Structure (XANES)

X-ray absorption spectroscopy was performed at beamline 20-BM of the Advanced Photon Source. Aqueous solutions of $ZnCl_2$, $ZnBr_2$, LiCl, and LiBr of varying concentrations were placed in PEEK cells with polyimide windows and sealed with epoxy. XAS measurements were acquired in transmission mode by placing gas ionization chambers before (50% He, 50 % N_2) and after (100% N_2) each sample. The incident beam was reduced to a spot size of 1 mm horizontal by 0.5 mm vertical by a toroidal mirror. Harmonic rejection was performed using a Rh-coated flat mirror and detuning the incident beam by 15%. Spectra were acquired at the Zn K-edge and all spectra were energy aligned to that of the first derivate peak of a Zn reference foil (9660.76 eV).(*39*) Spectral background removal and normalization of the XAS spectra were performed within the Athena software program.(*40*)

The fact of background (per-atom or molar) normalization to the theoretical atomic background, in analogy with the discussion of normalization of the VTC-XES above, enables the attempt of a linear combination analysis of the different solution concentration series. The fits were performed in Athena using the XANES data between 9655 – 9675 eV. This analysis utilized two Zn K-edge solution standards: a dilute ZnX_2 (X = Br^- or Cl^-) solution and a highly concentrated 5 m LiX solution with 0.25 m ZnX_2.

6.3.4: Density Functional Theory (DFT) & Time-Dependent Density Functional Theory (TDDFT) Calculations

All ground-state (DFT) and excited-state (TDDFT) calculations were performed with the NWChem quantum chemistry program.(*41*, *42*). DFT-based optimizations of the Zn^{+2} coordination structures ($Zn(H_2O)_6^{+2}$, $ZnCl(H_2O)_3^+$, $ZnCl_2(H_2O)_2$, $ZnCl_3(H_2O)^-$, and $ZnCl_4^{-2}$) were performed with Zn represented with the Stuttgart relativistic small core (RSC) effective core potential (ECP) (*43*) and basis set, Cl represented with the Stuttgart relativistic large core (RLC) ECP (*44*) and basis and O and H atoms were represented with 6-31G* basis set.(*45*) All basis sets and ECPs were accessed from the EMSL Basis Set Exchange. (*45*) The exchange-correlation was treated with the global hybrid PBE0 functional. (*46*) In all cases a $ZnCl_x$ cluster with 40 waters was optimized while the long-range solvation was treated with implicit solvation (COSMO). (*47*) The resulting first-shell structures are shown in Figure 1. Similar process was followed for the Zn-Br system, the resulting first-shell structures are shown in Figure SI-1.

XANES and VTC-XES calculations were performed at the Zn K-edge for all optimized solvated $ZnCl_x$ clusters for comparison with the experimental spectra shown in Figure 2. These calculations were performed at the TDDFT level of theory. The XANES were computed with the TDDFT-based restricted excitation window approach, (*48*) which involves defining a model subspace of single excitations from the relevant core orbitals to the unoccupied orbitals. The VTC-XES were computed using the TDDFT-based protocol described in Reference (*49*). For these calculations, the Zn atom in all the clusters was represented with the Sapporo-TZP-2012 all-electron basis set(*50*) while the remaining atoms were represented as in the ground-state calculations. To describe excitations beyond the dipole approximation, higher-order contributions were included in the calculation of the oscillator strengths.

For comparison with experiment, all calculated XANES spectra were Lorentzian-broadened by 0.6 eV and shifted with a single common energy offset (+205 eV) across all spectra to align with the prominent XANES feature at 9670 eV for the $Zn(H_2O)_6^{+2}$ complex. Similarly, for comparison with experiment the TDDFT VTC-XES results were broadened by 1.5 eV and shifted with a single, common energy offset of 14.5 eV such that the tetrahedral spectral features aligned with the corresponding features on experimental spectra. The spectral intensities of the calculated VTC-XES were normalized using the area under the calculated main Kβ peak, the same process that was used for the experimental spectra (see section II.B. above).

6.3.5: Classical Molecular Dynamics Simulations and Models of Speciation

Classical Molecular Dynamics (CMD) simulations were performed using the LAMMPS (*51*) software package in the canonical (NVT) ensemble and the isothermal-isobaric (NPT) ensemble on a system containing zinc and/or lithium and chloride ions with SPC/E water. (*52*) The forcefield for $ZnCl_2$ was taken from previous work. (*30*) For LiCl, two sets of forcefields were utilized. (*53, 54*) Interactions in the solution were represented by combining the Lennard-Jones potential and Coulombic interactions shifted to zero at 12 Å, where the cross-terms were defined using the Lorentz-Berthelot mixing rules (if they aren’t explicitly defined in the forcefield). The particle-particle particle-mesh technique (*55*) was applied for long-range electrostatic force calculations.

Briefly, the initial configurations were generated using Packmol (*56*) with a tolerance of 2 Å. The equilibration of the system involved several steps. To begin, the system was equilibrated at 300 K in NVT ensemble for 2 ns, then to enhance the sampling, the temperature was ramped up to 1500 K and run for a further 5 ns. After the system was cooled down back to 300 K, the system was equilibrated in NPT ensemble for 5 ns. Finally, the trajectories were harvested during a 50 ns run in NVT ensemble.

To extend the results of the CMD simulations to a range of concentrations, the speciation was estimated using the geochemical speciation software PHREEQC, version 2.15. (*57*) The equilibrium constants for the formation of $ZnCl^+$, $ZnCl_2$, $ZnCl_3^-$, and $ZnCl_4^{-2}$ from aqueous Zn^{+2} and Cl^- were defined from the atomistic level simulation and the equilibrium concentration of each species calculated via mass balance and mass actions equations. For speciation in sodium chloride, aqueous Na^+ was added to the species considered but without interaction with zinc or zinc chloride species. No other species were considered (i.e., the default databases were not used, but a custom model chemistry was created to reflect only the reactions as defined in Rampal *et al.*, 2021 (*30*)). The average chloride per zinc was calculated by summing the concentrations of each individual chloride-bearing species, multiplied by the number of chlorines in the species, and divided by the total zinc concentration in the solution.

Several assumptions were tested to determine the sensitivity of the results. First, two different assumptions about activities were used, in the first, the activities for each species were estimated from the Davies equation, where at low ionic strengths it resembles the Debye-Hückel activity-concentration relationship but at high ionic strengths ($\gtrsim$ 1 molal) the activity coefficients start to increase by a factor twice the ionic strength. (*58*, *59*) Alternately, no difference between activity and concentration was considered. The different ways to treat the activities changed the speciation differently at high and low ionic strengths, but did not substantively affect the maximum number of chlorines per zinc atom predicted. Additional tests included using equilibrium constants measured in 4.5 m versus 0.01 m solutions. Here, the equilibrium constants measured at 4.5 m predicted a more rapid rise in the number of chorines per zinc with concentration than those measured in 0.01 m solution, but both sets converged on the same number of chlorines per zinc at high concentrations.

Lastly, the role of dimer formation was considered. These were found previously to represent 5% of the ionic clusters in solution at 4.5 m $ZnCl_2$, comprised dominantly of $Zn_2Cl_5^-$ and Zn_2Cl_4 moieties (each contain a bridging chloride separating the two zincs). (*30*) Adding these species to speciation lowered the estimate of the maximum average number of chlorines per zinc by ~10%, or 0.2 chlorines per zinc for pure $ZnCl_2$. Based on the sum total of sensitivity analysis, the predicted speciation from the CMD simulations is thought to be fairly robust using this method.

6.3.6: Monte Carlo Simulations

In an effort to efficiently treat the collective correlation of ions with increasing concentration, a coarse-grained lattice Monte Carlo (MC) model was constructed that used intermolecular potentials derived from the CMD simulations. At high concentrations (e.g. > 4.5 m) the increasingly glass-like behavior of most electrolyte solutions results in equilibrium timescales that are well beyond the reach of classical molecular dynamics. For this reason, MC is one of the few methods that can be used to realistically model the speciation at these extreme concentrations. For the CMD approach, the equilibrium constants derived from the MD trajectory at 4.5 m $ZnCl_2$ were used to predict speciation at extreme concentrations. The appropriateness of this assumption is unknown. Thus, MC potentially provides a significant improvement by directly calculating speciation at extreme concentrations using realistic representations of all ion-ion interactions that are increasingly important at short range.

The potential of mean force between all ion pairs in water were generated from an ensemble average using CMD simulations. From this, the long-range Coulomb interaction of the form $q_i q_j / \epsilon r_{ij}$ was removed to extract the short-range interaction of pairs, $u_{s,i,j}(r_{i,j})$, where the dielectric constant ϵ = 80 and q_a is the ionic charge. The influence of the water was approximated by its mean-field response to the ions. A periodic cubic lattice with lattice spacing 2 Å and with 20 lattice points in each Cartesian direction was constructed as the foundation of an approximate Monte Carlo scheme. We populate the lattice with an initial concentration of ions, n_a, a = Zn or Cl, randomly distributed with the full system charge neutral. Unoccupied sites represent a water background. Ions are constrained to be on lattice sites. The energy of the system, $U = \sum_{i<j} \left(u_{s,i,j}(r_{i,j}) + q_i q_j / \epsilon r_{ij} \right)$ where interaction between periodic images is taken into account using an Ewald technique. (*60, 61*)

Metropolis Monte Carlo relaxation of the system was performed at an effective temperature of 300 K. Two types of moves were considered: ion-ion pair swaps and ion-vacancy swaps. The system was propagated until fluctuations in energy reached a constant mean value. Configurations beyond this point were used as representative configurations of the ensemble to be used for evaluating averages. Figure SI-4 depicts the short-range potential and the location of lattice interaction distances. From an ensemble of configurations, we were then able to calculate the connectivity and population of coordinated ions, i.e., the relative occurrence of the different hydrated and/or chlorinated moieties.

6.4: Results and Discussion

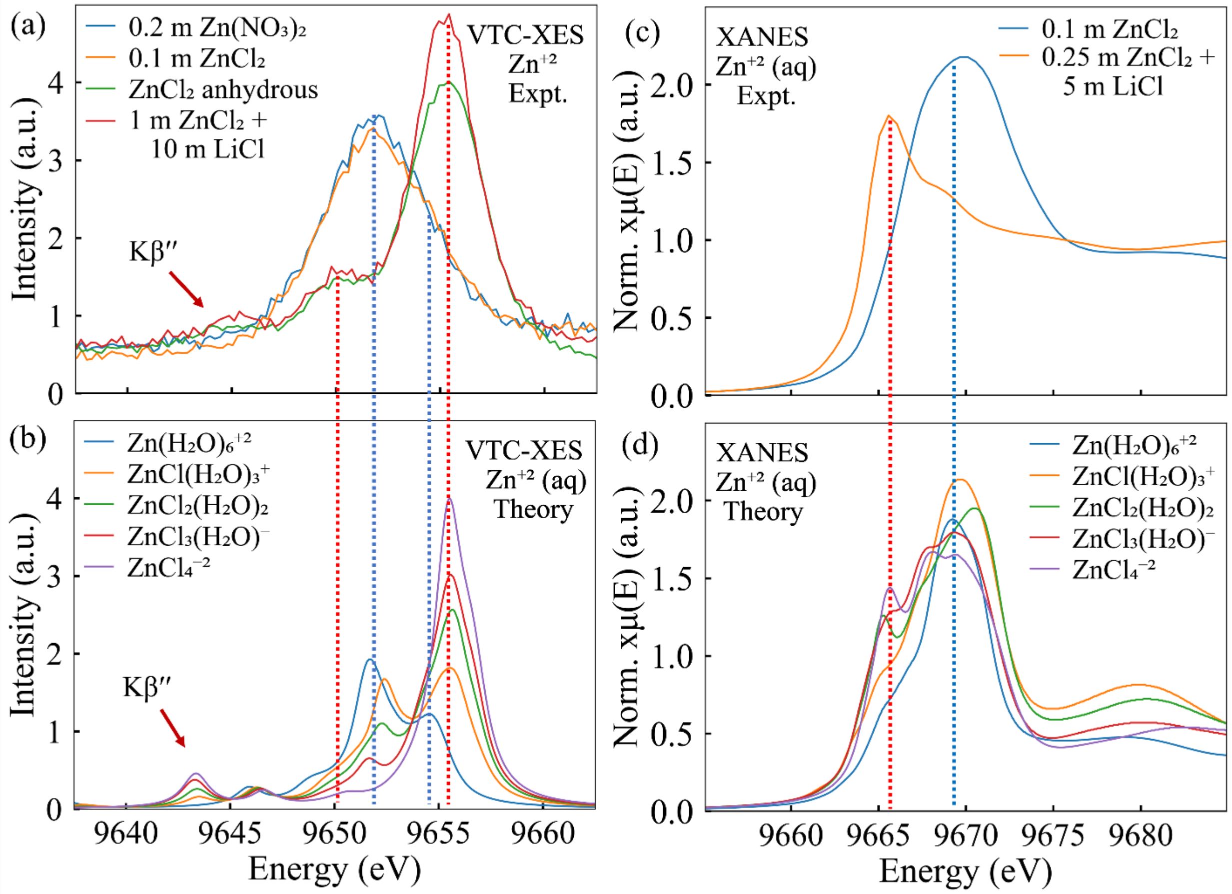

Figure 2. Comparison of VTC-XES (a) and (b) and XANES (c) and (d) between TDDFT theory and experimental results. The peak around 9645 eV in the VTC-XES spectra labeled as Kβ" in (a) and (b) is attributed to the transitions from Cl 3*s*-derived states to the Zn 1s orbital.

To begin, in Figure 2 we present the experimental and theoretical spectra for the endpoint species at the lowest and highest ion activities of this study. For both the VTC-XES and XANES spectra, the change from fully octahedrally coordinated $Zn(H_2O)_6^{+2}$ to nominally tetrahedrally coordinated $ZnCl_4^{-2}$ is apparent. For instance, similar spectral features in the XANES for $ZnCl_2$ solutions were reported in Liu *et al.*, (*22*) and again similar features were observed in studies of other metal-halide systems. (*62-64*) For VTC-XES, unique spectral features assigned to either octahedral or tetrahedral symmetries in crystalline solids have been previously reported for Ti-based crystalline compounds by Gallo *et al*. (*65*) We have further confirmed these distinct spectral assignments for a series of Zn standards with supplementary measurements of ZnO, $Zn(OH)_2$, 0.5 m ZnO + 6 m KOH solution and 0.1 m $Zn(OH)_2$ + 6 m KOH solution, all of which have tetrahedral coordination of the Zn^{+2} ion and all of which show the same features, see Figure SI-5. Again, the extreme locality of VTC-XES is particularly well-suited to the problem of first shell coordination and composition.

On the other hand, XANES theory only qualitatively matches the experimental spectra in that it does predict the emergence of the sharp feature at 9666 eV, but it fails to correctly predict the chemical evolution of the peak at 9669 eV. The VTC-XES predictions are stronger, with better matching of peaks and intensities and correct identification of the Cl ligand peak (K□’’ in the figures). The theoretical spectra in Figure 2 include not just the endpoint spectra, but also predictions for tetrahedral moieties with intermediate composition, e.g., that contain both some water and some chlorine. Note that the progression from $Zn(H_2O)_6^{+2}$ to $ZnCl_4^{-2}$ is quite smooth as a function of the number of Cl ions in the tetrahedral moiety for VTC-XES but is more bimodal for XANES. This difference can be attributed to the fact that XANES probes the more delocalized unoccupied valence states and hence is more sensitive to changes in higher order shells whereas, VTC-XES is only sensitive to the first coordination shell as it probes the occupied states that are less delocalized. This detail will play an important role in later discussion.

Next, in Figures 3 and 4 we present the experimental concentration series for the $ZnCl_2$ and $ZnBr_2$ systems, respectively. The spectral evolution follows Figure 2, with the added point that achieving apparently complete conversion to $ZnCl_4^{-2}$ requires very high anion activity, here by added chlorine salts, i.e., the 1:2 composition ratio of Zn to Cl in the pure solutions is not apparently abetted by widespread polymerization.

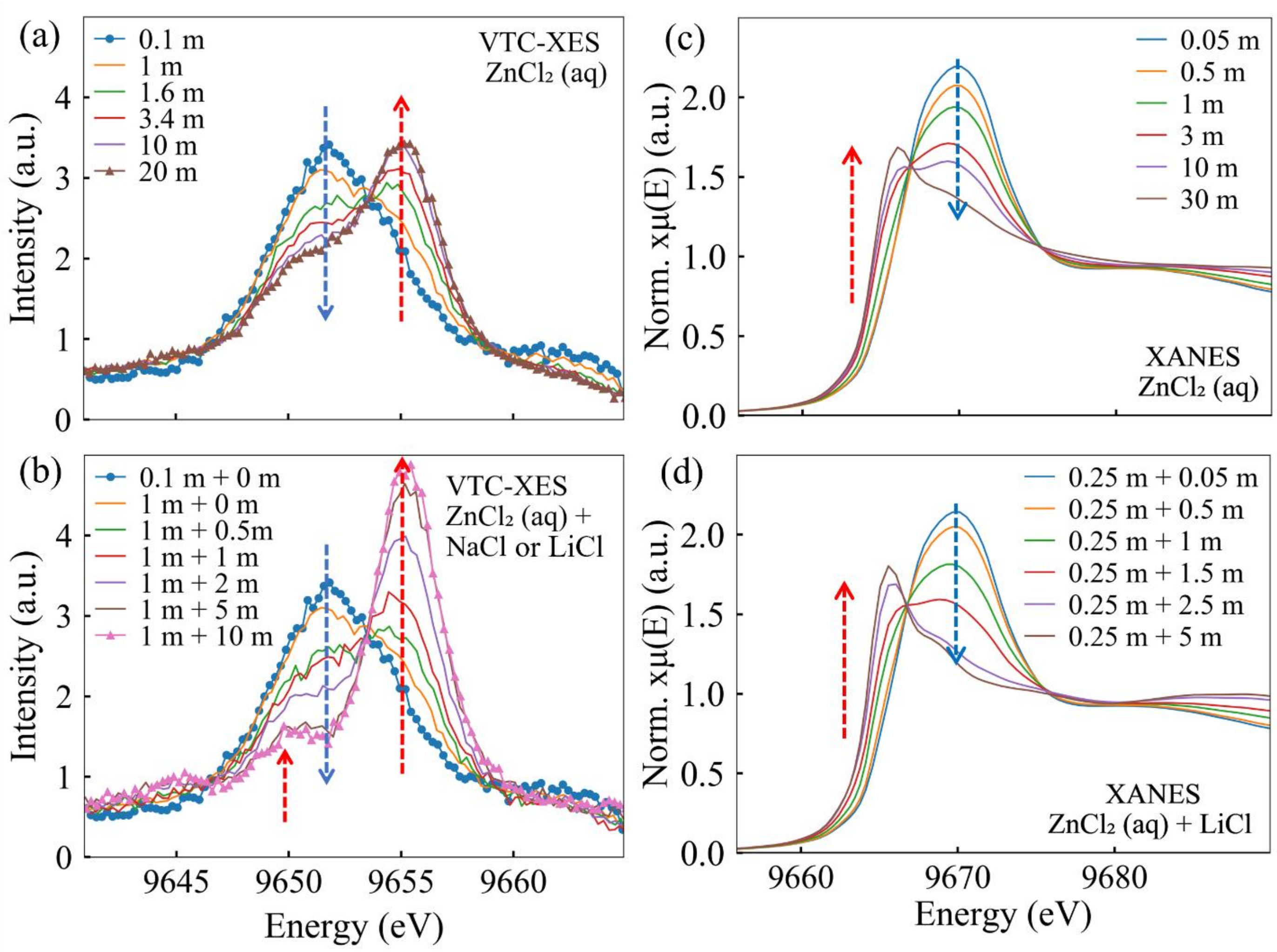

Figure 3. (a) and (c): VTC-XES and Zn K-edge XANES measurements of $ZnCl_2$ aqueous solution ranging from the dilute to the super-concentrated regime; (b) VTC-XES for 1 m $ZnCl_2$ with added Cl salt; (d) Zn K-edge XANES for 0.25 m $ZnCl_2$ solution with added Cl salt. The blue and red arrows annotate peaks that correspond to octahedral and tetrahedral coordinations, respectively.

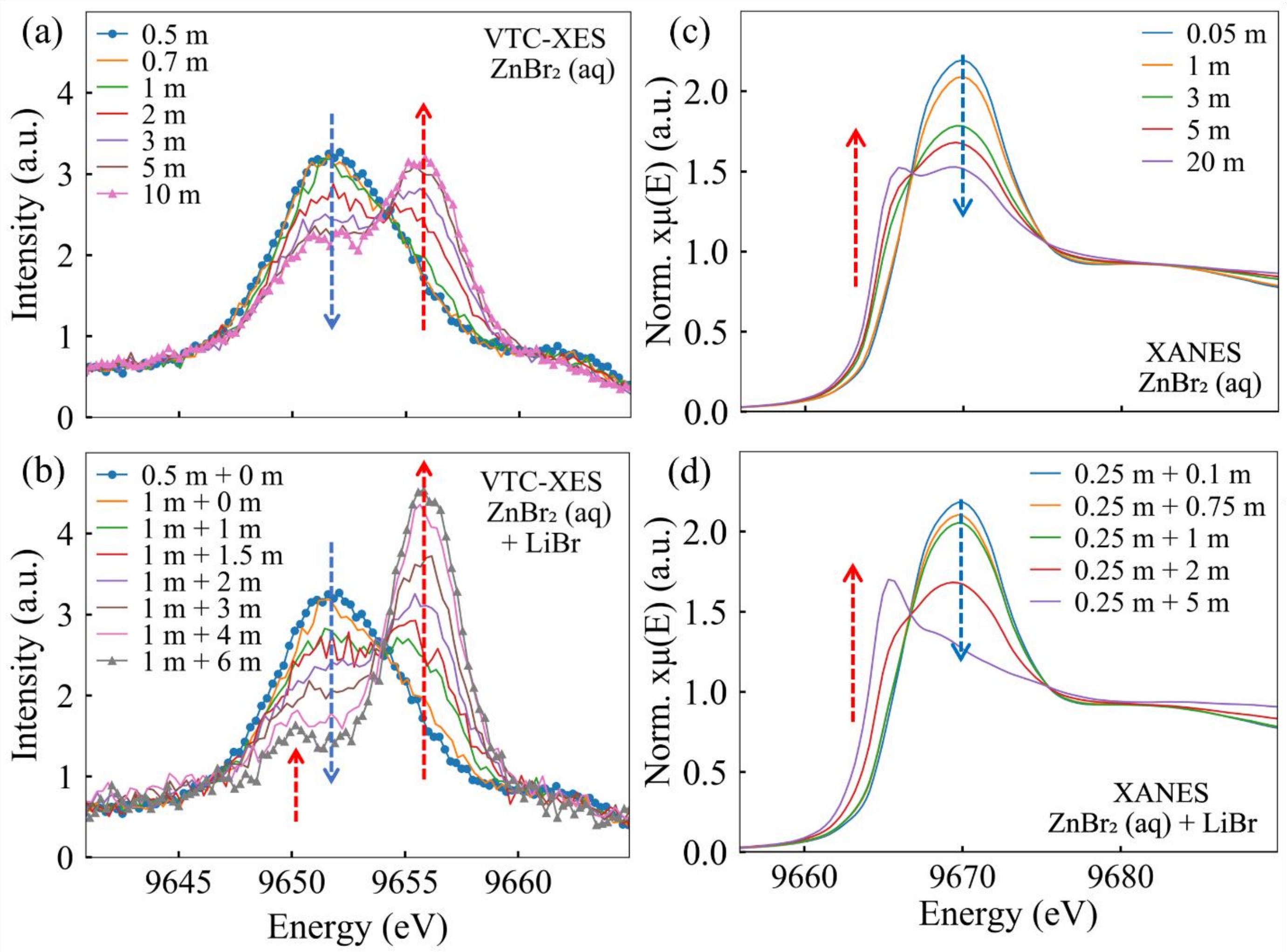

Figure 4. (a) and (c): VTC-XES and Zn K-edge XANES measurements of $ZnBr_2$ aqueous solution ranging from the dilute to the super-concentrated regime; (b) VTC-XES for 1 m $ZnBr_2$ with added Br salt; (d) Zn K-edge XANES for 0.25 m $ZnBr_2$ solution with added Br salt. The blue and red arrows annotate peaks that correspond to octahedral and tetrahedral coordinations, respectively.

An added detail in Figures 3 and 4 merits discussion. Recall that all $\mu(E)$ are on a common mole basis because of standard normalization by the atomic background, and that all VTC-XES are also on a common mole basis because of our normalization via the integral of the K□ diagram line intensity (see methods and Figure SI-3), an approach that is justified by the filled $3d^{10}$ electronic configuration of the Zn^{+2} ion. Consequently, the existence of isosbestic (or, at least, quasi-isosbestic) points in all panels of both figures is suggestive, but not conclusive, of a simple mixture of the two endpoint moieties. This observation opens our inquiry into what details of the local Zn^{+2} coordination can be inferred from our results, and especially from the progression of results as a function of anion activity. In this, we progress through systematically more complex models for the Zn ion local environment, moving from a two-component model of only octahedral $Zn(H_2O)_6^{+2}$ and tetrahedral $ZnCl_4^{-2}$, to a model that allows for an intermediate series of partially hydrated tetrahedral moieties, and finally to the question of possible polymerization.

Hence, in Figure 5, we show the result of decomposing the measured spectra for pure $ZnCl_2$ and pure $ZnBr_2$ solutions into a simple linear combination of the endpoint octahedral and fully chlorinated/brominated tetrahedral extremes. The relatively rapid onset of significant tetrahedral coordination with this conversion significantly saturating at ~3 – 5 m is obvious. The quality of these one-parameter fits are excellent for the VTC-XES (Figure SI-6 – Figure SI-9) which, again, is almost exclusively sensitive to the first coordination shell. By contrast, the fits are rather poor for the XANES spectra at high concentrations (Figure SI-10), where contributions from higher solvation shell should be expected to break the basis of the local two-component model. That being said, it is important to note that the measured octahedral fraction even for the VTC-XES appears to be at least slightly less than 0.5 (though within the estimated errors) at the highest concentration for both pure solution studies. This result is unintuitive because it corresponds to an average Zn-Cl coordination to be larger than two. It is worth noting that this equal segregation into octahedral Zn with six waters and tetrahedral Zn with four chlorides has been found to exist in crystals having a 3:2:1 composition ratio between water, chloride, and zinc. (*66*)

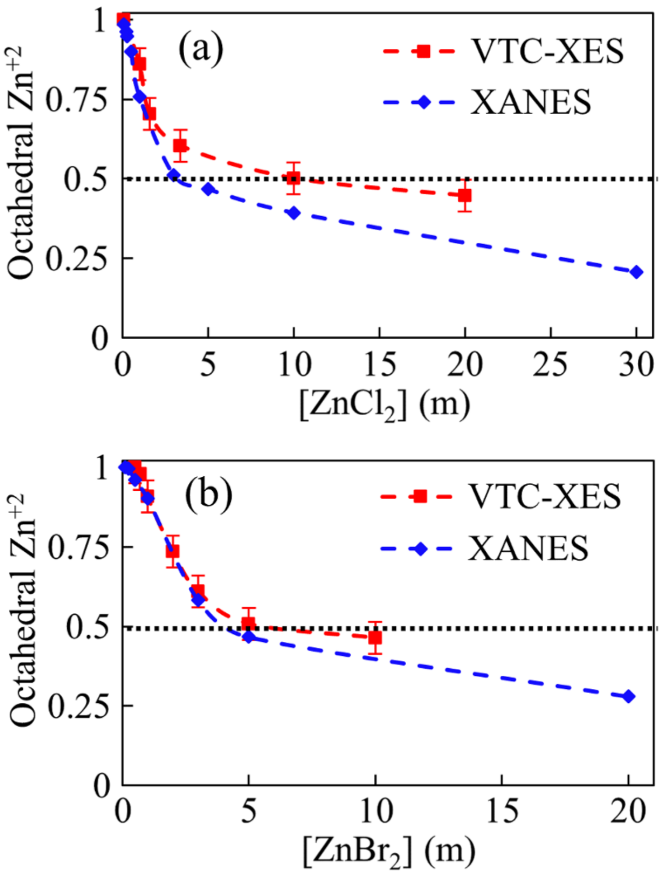

Figure 5. Linear combination analysis of XANES measurements and XES measurements for the $ZnCl_2$ (a) and $ZnBr_2$ (b) concentration series, based on a simple two-endpoint model. The vertical axis shows the *nominal* fraction of octahedral Zn^{+2} if there are no intermediate tetrahedral coordinations and if second-shell effects can be ignored.

While the occurrence of nominally isosbestic points in the mole-normalized spectra of Figures 3 and 4 suggests a simple two-component model, this is problematic. In fact, from a thermodynamic standpoint, several prior studies (*9*, *22*, *32*, *67*) of $ZnCl_2$ solutions as a function of anion activity instead conclude that there must be some rich admixture of intermediate tetrahedral moieties of the form $Zn(H_2O)_{4-x}Cl_x^{2-x}$.

This brings us to the closely linked questions of (1) how to address the likely occurrence of intermediate moieties in our interpretation of spectra and (2) the reason for the surprisingly good VTC-XES fits for the one-parameter, two-component model, as per above and Figure SI-6 – Figure

SI-9. Referring back to Figure 2, note the TDDFT predicted VTC-XES for the range of likely Zn^{+2} environments is quite smooth in the Cl coordination number, x. Furthermore, because of a near-degeneracy of the octahedral fingerprint and one of the peaks in the tetrahedral spectra, the spectra for intermediate moieties are not very linearly independent from the endpoint spectra. While this scenario prohibits determination of the relative concentrations of chlorinated moieties, it does allow inference of the average number of chloride ligand (N_{Cl}) coordinated per Zn^{+2} ion via peak fitting performed on the calculated VTC-XES spectra (Table SI-3) and the one parameter fit results, see section 19 in the SI for a detailed treatment of this problem.

We present the inferred N_{Cl} for both the pure solution study and the high Cl concentration study in Figure 6. The results for both systems are impressively physical: the pure solution study saturates at $N_{Cl} \approx 2$, the maximum value consistent with an absence of polymerization subject to the scale set when the high Cl concentration study reaches *the assumed value* $N_{Cl} = 4$, i.e., we have assumed the endpoint, highest-Cl-concentration sample itself is dominated by $ZnCl_4^{-2}$. We are comfortable with this assumption (i) because of the spectral similarities between the endpoint spectrum and the crystalline references, (ii) because of agreement with prior EXAFS study of D'Angelo *et al*. (*32*) and (iii) because of the intuitive consistency of the result $N_{Cl} \approx 2$ for the pure solution case. Very similar results occur for $ZnBr_2$, see Figure SI-11.

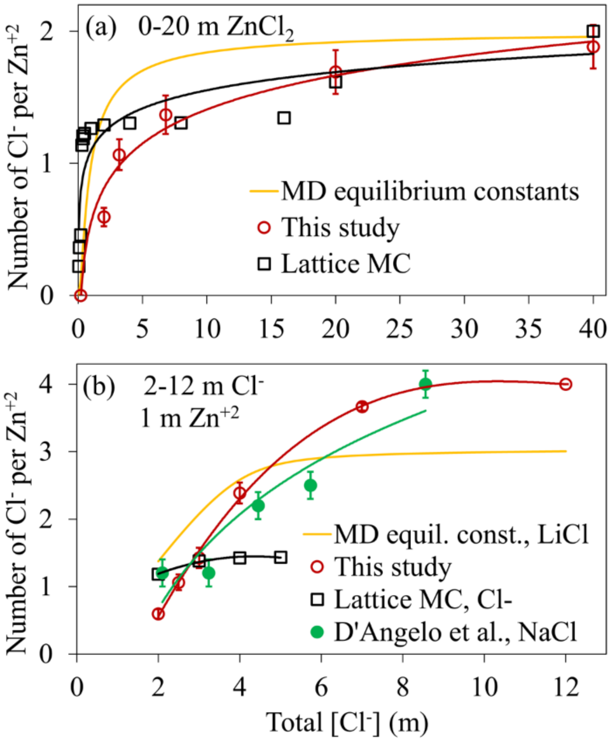

Figure 6: Average number of Cl coordinated with Zn in the solution as a function of the total Cl concentration for (a) pure $ZnCl_2$ concentration series and (b) added salt series. The data from D'Angelo *et al*. (*32*) used molarity scale with 1 M $ZnCl_2$ and added NaCl and hence have slightly different Zn^{+2} concentrations between data points in the molal scale in this figure. The lines in the figure serve only as guides to the eye, except for the one labeled as "MD equilibrium constants".

However, it is important to recognize that these results differ from inferences in some prior work, both experiment and theory, and therefore there is considerable value in seeking additional perspectives on the Zn coordination, especially in the limit of high anion activity. For example, D'Angelo *et al*. (*32*) agree with $N_{Cl} = 4$ at high Cl ion activity, where this result is based entirely on EXAFS data to infer coordination number, i.e., the conclusion drawn is purely from a structural point of view. On the other hand, Ruaya and Seward (*23*) disagree, finding a smaller estimate for N_{Cl} from an indirect analysis inferring of Zn complexes from the solubility of another salt (AgCl) and where the conclusion drawn is contingent on thermodynamic parameters.

This brings us to the classical molecular dynamics (CMD) simulations that we have performed on the same chemical systems. Qualitatively, a key, significant similarity between the CMD results and experiment is the observation of a relatively fast onset of substantial ion pairing with a tendency to saturation at intermediate concentrations. For a quantitative comparison of the CMD and experiment, in Figure 6 we have included the curves for the average number of Cl^- ligands that were derived from the equilibrium constants generated from the CMD 1D Potential of Mean Force (PMF) calculations. The agreement for pure solutions is impressive: although theory predicts an even faster onset of ion pairing, there is complete agreement about the occurrence of saturation with two Cl^- neighbors and an absence of any significant polymerization.

However, in Figure 6b, the agreement between the CMD and experimental results for the number of Cl^- is more problematic for the case with fixed Zn^{+2} concentration and high Cl^- activity, exactly where additional certainty about our experimentally motivated postulate that $N_{Cl} = 4$ would be most valuable. The CMD results do see, again, a quite strong drive toward ion pairing, but it almost entirely excludes the occurrence of $ZnCl_4^{-2}$. For more detail, in Figure 7 we show the predicted relative populations of different Zn^{+2} moieties as a function of $ZnCl_2$ concentration (Figure 7a) and as a function of total Cl^- concentration starting with 1 m $ZnCl_2$ and then adding supplemental Cl^- salts (Figure 7b).

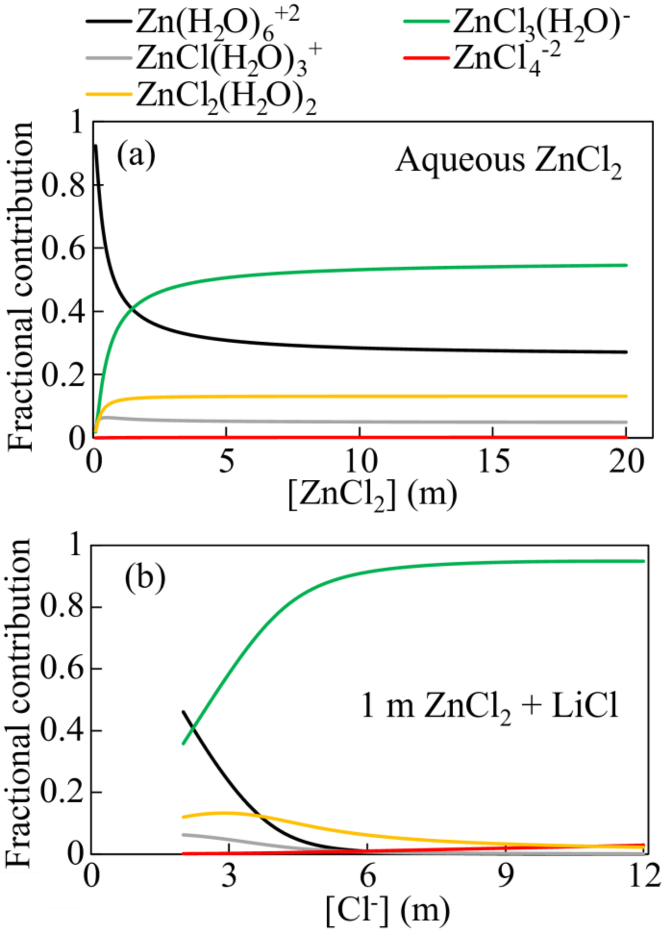

Figure. 7: Concentration dependent evolution of the concentrations of different moieties in pure $ZnCl_2$ solution (a) and 1 m $ZnCl_2$ + LiCl (b), calculated using CMD-derived equilibrium constants and assuming activities equal concentrations.

There are several potential sources for the discrepancy. First, it could be that the speciation predicted from CMD derived equilibrium constants are being extrapolated to conditions beyond their validity. As one test of this possibility, we ran explicit simulations of 1 m $ZnCl_2$ at multiple concentrations of LiCl using existing force fields for lithium. (*53*, *54*) These simulations, the results of which are included in the supporting information (Figure SI-13), are consistent with the results of the predicted speciation from the CMD in Figure 6, with a maximum of three chlorides per zinc atom and consistent with speciation in prior CMD simulations (see Table SI-2 for a list). This rules out any issues with the speciation calculations, or the specific parameterization of the

CMD force field. Second, there could be a systematic error in the speciation predicted by CMD. At this time however, we do not have a specific basis to understand the origin of this error, except to speculate that the extent of ion pairing is often overestimated in both formal charge and electronic continuum correction models. (*29, 68*) It is not difficult to envision that these types of errors could also result in a difficulty predicting correct stability of the zinc chloride tetramer. Third, there could be unforeseen issues with the interpretation of the experiments leading to an overestimation of the average number of chlorides surrounding the zinc. To get insight into this we compare the TDDFT calculated VTC-XES spectra of monomer $ZnCl_3^-$ complex with that of dimer $Zn_2Cl_5^-$ complex with one shared Cl. (Figure SI-14) It should be noted that in both cases considered there are 3 Cl-ions coordinated with each Zn-ion. Our due diligence here was to confirm that the VTC-XES spectra are not sufficiently sensitive to presence of dimers.

Lastly, and perhaps most tantalizingly, there could be an unforeseen effect of lithium and/or sodium that influences the speciation of zinc chloride monomers that stabilizes zinc tetrachloride. Such effects have been observed in complex, highly concentrated solutions before, especially in their roles in solution dynamics and nucleation mechanisms (*31*) as well as aggregation phenomena (*69*) in alkaline aluminate solutions. This would not necessarily be predicted using the explicit simulations of the mixed solutions described in the supporting information (Figure SI-13) since these are relying on mixing terms to provide the interaction between the sodium or lithium and the zinc chloride species. However, we find no difference between the experimental VTC-XES spectra recorded for 1 m $ZnCl_2$ + 5 m LiCl and 1 m $ZnCl_2$ + 5 m NaCl solutions (see Figure SI-15).

We turn briefly to the Monte Carlo (MC) simulation results in Figure 6a for the $ZnCl_2$ solution. In the dilute region, the onset of ion pairing is even more rapid than the CMD results while at higher concentrations there appears to be an incremental increase in the coordination just above 16 m Cl^- (8 m $ZnCl_2$). This apparent discontinuous nature of the Cl^- association is not unexpected for the coarse-grain lattice of MC that involves discrete ion-ion locations rather than a continuum of sites as in CMD. We recall that MC is expected to be a much more accurate representation of the equilibrium species at extreme concentrations since it provides a direct accounting for the strong, short-range inter-ionic interactions that are based upon realistic pair potentials while the CMD is an extrapolation of equilibrium constants derived from CMD 1D PMF calculations at 4.5 m $ZnCl_2$. In this regard, Figure 6a shows that the MC results are in somewhat better agreement with experiment than the CMD results at concentrations above 4.5 m $ZnCl_2$. MC also convincingly proves, in a way that is not possible via CMD, that the use of realistic ion-ion potentials yields at endpoint structure which saturates at $N_{Cl} = 2$. To some extent, the general agreement between MC and CMD at high concentrations, justifies the use of CMD as an approximation to this speciation. Finally, we note, for solutions with high Cl chloride concentrations in Figure 6b, the MC results are incomplete above 6 m C1- due to challenge of identifying coordination numbers on a lattice that are consistent with the continuum description.

Taken *en masse,* our combined experimental and theoretical results support several conclusions of strong contemporary interest. First, aqueous solutions of Zn halide salts show a quite rapid onset of ion pairing, and almost certainly exhibit a diverse population of partially chlorinated tetrahedral coordinations. Second, we have considerable evidence for the satisfying result that $N_{Cl} \approx 2$ for concentrated pure solutions, i.e., that there is full anion coordination without polymerization. That being said, this inference is dependent on the assumption, made reasonable by the observed spectra but at least partially disputed by the classical molecular dynamics calculations, that solutions with lower Zn concentration and high anion activity fully reach $N_{Cl} = 4$, i.e., are dominated by $ZnCl_4^{2-}$ species. Finally, the hyper-local sensitivity of VTC-XES in solution, where second-shell coordination effects are yet even weaker than in a molecule or compound, is greatly beneficial for the study of ion pairing on an element-specific basis and should see broader future use.

6.5: Conclusions

We report a combined experimental and theoretical treatment of ion pairing in Zn halide (ZnX_2, with X = Cl, Br) solutions over the full range of concentrations for pure solutions and over the full range of ion activities for 1 m solutions with added halide salts. Making particular use of the extreme local sensitivity of valence to core x-ray emission spectroscopy (VTC-XES) for this problem, we provide a new method to infer the average number of halide atoms coordinated to Zn^{+2}. This finds a strong onset to ion pairing and saturation at two halide atoms in the first shell for pure solutions but saturation at four halides, i.e., the ZnX_4^{2-} complex, for added salt solutions. Comparison to classical molecular dynamics finds generally good agreement with these results, with the exception of a strong prediction against the formation of ZnX_4^{2-}. This work informs ongoing discussion of the thermodynamics of Zn halide brines, of the physical chemistry of electrolytes for Zn halide batteries and suggests a broader use of VTC-XES for ion pairing studies and other problems involving metal complex formation in solution.

6.6: Acknowledgements

This work was supported by the Joint Center for Energy Storage Research, an Energy Innovation Hub funded by the U.S. Department of Energy. A.G.S. and N.R. were supported by the

U.S. Department of Energy, Office of Science, Office of Basic Energy Sciences, Chemical Sciences, Geosciences, and Biosciences Division. This research used resources of the Advanced Photon Source, an Office of Science User Facility operated for the U.S. Department of Energy (DOE) Office of Science by Argonne National Laboratory and was supported by the U.S. DOE under contract no. DE-AC02-06CH11357. Work by N.G. was supported under project 72685, J.L.F. under project 16248, and G.K.S and C.J.M. under project 16249, funded by the U.S. Department of Energy (DOE), Office of Science, Office of Basic Energy Sciences, Division of Chemical Sciences, Geosciences, and Biosciences. This research benefited from computational resources provided by EMSL, a DOE Office of Science User Facility sponsored by the Office of Biological and Environmental Research and located at PNNL. PNNL is operated by Battelle Memorial Institute for the United States Department of Energy under DOE Contract No. DE-AC05-76RL1830. This research also used resources of the National Energy Research Scientific Computing Center (NERSC), a U.S. Department of Energy Office of Science User Facility operated under Contract No. DE-AC02-05CH11231.

6.7: References

1. Y. Marcus, G. Hefter, Ion pairing. *Chemical Reviews* **106**, 4585-4621 (2006).
2. E. W. Castner, J. F. Wishart, Spotlight on ionic liquids. *Journal of Chemical Physics* **132**, 120901 (2010).
3. P. G. Wolynes, Dynamics of electrolyte-solutions. *Annual Review of Physical Chemistry* **31**, 345-376 (1980).
4. F. Endres, S. Z. El Abedin, Air and water stable ionic liquids in physical chemistry. *Physical Chemistry Chemical Physics* **8**, 2101-2116 (2006).
5. Y. F. Hu, X. M. Peng, Effect of the Structures of Ionic Liquids on Their Physical Chemical Properties. *Structures and Interactions of Ionic Liquids* **151**, 141-174 (2014).
6. M. Kar, T. J. Simons, M. Forsyth, D. R. MacFarlane, Ionic liquid electrolytes as a platform for rechargeable metal-air batteries: a perspective. *Physical Chemistry Chemical Physics* **16**, 18658-18674 (2014).
7. S. K. Singh, A. W. Savoy, Ionic liquids synthesis and applications: An overview. *Journal of Molecular Liquids* **297**, 112038 (2020).
8. W. Liu, S. Borg, B. Etschmann, Y. Mei, J. Brugger, An XAS study of speciation and thermodynamic properties of aqueous zinc bromide complexes at 25–150°C. *Chemical Geology* **298-299**, 57-69 (2012).
9. Y. Mei *et al.*, Zinc complexation in chloride-rich hydrothermal fluids (25–600°C): A thermodynamic model derived from ab initio molecular dynamics. *Geochimica et Cosmochimica Acta* **150**, 265-284 (2015).
10. R. Demichelis, P. Raiteri, J. D. Gale, D. Quigley, D. Gebauer, Stable prenucleation mineral clusters are liquid-like ionic polymers. *Nat. Commun.* **2**, 590 (2011).
11. P. Dreier, P. Rabe, EXAFS-Study of the Zn2+ Coordination in Aqueous Halide Solutions. *J. Phys. Colloques* **47**, 809-812 (1986).
12. X. Ji, A perspective of ZnCl2 electrolytes: The physical and electrochemical properties. *eScience* **1**, 99-107 (2021).
13. C. Zhang *et al.*, A ZnCl2 water-in-salt electrolyte for a reversible Zn metal anode. *Chemical Communications* **54**, 14097-14099 (2018).
14. L. Zhang *et al.*, ZnCl2 "Water-in-Salt" Electrolyte Transforms the Performance of Vanadium Oxide as a Zn Battery Cathode. *Advanced Functional Materials* **29**, 1902653 (2019).
15. C. Zhang *et al.*, The electrolyte comprising more robust water and superhalides transforms Zn-metal anode reversibly and dendrite-free. *Carbon Energy* **3**, 339-348 (2021).
16. F. Wang *et al.*, Highly reversible zinc metal anode for aqueous batteries. *Nature Materials* **17**, 543-549 (2018).
17. H. Zhang, X. Liu, B. Qin, S. Passerini, Electrochemical intercalation of anions in graphite for high-voltage aqueous zinc battery. *Journal of Power Sources* **449**, 227594 (2020).
18. I. A. Rodríguez-Pérez *et al.*, Enabling Natural Graphite in High-Voltage Aqueous Graphite || Zn Metal Dual-Ion Batteries. *Advanced Energy Materials* **10**, 2001256 (2020).
19. J. Song, K. Xu, N. Liu, D. Reed, X. Li, Crossroads in the renaissance of rechargeable aqueous zinc batteries. *Materials Today* **45**, 191-212 (2021).
20. Y. Zhang *et al.*, Pursuit of reversible Zn electrochemistry: a time-honored challenge towards low-cost and green energy storage. *NPG Asia Materials* **12**, 4 (2020).
21. L. M. Suo *et al.*, "Water-in-salt" electrolyte enables high-voltage aqueous lithium-ion chemistries. *Science* **350**, 938-943 (2015).
22. W. Liu, B. Etschmann, G. Foran, M. Shelley, J. Brugger, Deriving formation constants for aqueous metal complexes from XANES spectra: Zn2+ and Fe2+ chloride complexes in hypersaline solutions. *American Mineralogist* **92**, 761-770 (2007).

23. J. R. Ruaya, T. M. Seward, The stability of chlorozinc(II) complexes in hydrothermal solutions up to 350-degrees-C. *Geochimica Et Cosmochimica Acta* **50**, 651-661 (1986).
24. D. Gebauer, M. Kellermeier, J. D. Gale, L. Bergström, H. Cölfen, Pre-nucleation clusters as solute precursors in crystal- lisation. . *Chem. Soc. Rev.* **43**, 2348 - 2371 (2014).
25. D. Gebauer, P. Raiteri, J. D. Gale, H. Colfen, On classical and non-classical views on nucleation. *American Journal of Science* **318**, 969-988 (2018).
26. K. Henzler *et al.*, Supersaturated calcium carbonate solutions are classical. *Sci. Adv.* **4**, eaao6283 (2018).
27. J. P. Larentzos, L. J. Criscenti, A Molecular Dynamics Study of Alkaline Earth Metal-Chloride Complexation in Aqueous Solution. *Journal of Physical Chemistry B* **112**, 14243-14250 (2008).
28. A. F. Wallace *et al.*, Microscopic Evidence for Liquid-Liquid Separation in Supersaturated CaCO3 Solutions. *Science* **341**, 885-889 (2013).
29. H. W. Wang, K. Yuan, N. Rampal, A. G. Stack, Solution and Interface Structure and Dynamics in Geochemistry: Gateway to Link Elementary Processes to Mineral Nucleation and Growth. *Crystal Growth & Design* **22**, 853-870 (2022).
30. N. Rampal *et al.*, Local molecular environment drives speciation and reactivity of ion complexes in concentrated salt solution. *Journal of Molecular Liquids* **340**, 116898 (2021).
31. H. W. Wang *et al.*, Countercations Control Local Specific Bonding Interactions and Nucleation Mechanisms in Concentrated Water-in-Salt Solutions. *Journal of Physical Chemistry Letters* **10**, 3318-3325 (2019).
32. P. D’Angelo, A. Zitolo, F. Ceccacci, R. Caminiti, G. Aquilanti, Structural characterization of zinc(II) chloride in aqueous solution and in the protic ionic liquid ethyl ammonium nitrate by x-ray absorption spectroscopy. *The Journal of Chemical Physics* **135**, 154509 (2011).
33. R. F. Kruh, C. L. Standley, An X-Ray Diffraction Study of Aqueous Zinc Chloride Solutions. *Inorganic Chemistry* **1**, 941-943 (1962).
34. R. J. Wilcox *et al.*, Crystalline and Liquid Structure of Zinc Chloride Trihydrate: A Unique Ionic Liquid. *Inorganic Chemistry* **54**, 1109-1119 (2015).
35. E. Duboue-Dijon, P. E. Mason, H. E. Fischer, P. Jungwirth, Hydration and Ion Pairing in Aqueous Mg2+ and Zn2+ Solutions: Force-Field Description Aided by Neutron Scattering Experiments and Ab Initio Molecular Dynamics Simulations. *Journal of Physical Chemistry B* **122**, 3296-3306 (2018).
36. E. P. Jahrman *et al.*, An improved laboratory-based x-ray absorption fine structure and x-ray emission spectrometer for analytical applications in materials chemistry research. *Review of Scientific Instruments* **90**, 024106 (2019).
37. D. R. Mortensen *et al.*, Benchmark results and theoretical treatments for valence-to-core x-ray emission spectroscopy in transition metal compounds. *Physical Review B* **96**, 125136 (2017).
38. J. A. Bearden, X-ray Wavelengths. *Reviews of Modern Physics* **39**, 78 (1967).
39. S. Kraft, J. Stümpel, P. Becker, U. Kuetgens, High resolution x-ray absorption spectroscopy with absolute energy calibration for the determination of absorption edge energies. *Review of Scientific Instruments* **67**, 681-687 (1996).
40. B. Ravel, M. Newville, ATHENA, ARTEMIS, HEPHAESTUS: data analysis for X-ray absorption spectroscopy using IFEFFIT. *Journal of Synchrotron Radiation* **12**, 537-541 (2005).
41. E. Apra *et al.*, NWChem: Past, present, and future. *Journal of Chemical Physics* **152**, 184102 (2020).
42. M. Valiev *et al.*, NWChem: A comprehensive and scalable open-source solution for large scale molecular simulations. *Computer Physics Communications* **181**, 1477-1489 (2010).
43. M. Dolg, U. Wedig, H. Stoll, H. Preuss, Energy-adjusted ab-initio pseudopotentials for the 1st-row transition-elements. *Journal of Chemical Physics* **86**, 866-872 (1987).
44. A. Bergner, M. Dolg, W. Kuchle, H. Stoll, H. Preuss, Ab-initio energy-adjusted pseudopotentials for elements of groups 13-17. *Molecular Physics* **80**, 1431-1441 (1993).

45. B. P. Pritchard, D. Altarawy, B. Didier, T. D. Gibson, T. L. Windus, New Basis Set Exchange: An Open, Up-to-Date Resource for the Molecular Sciences Community. *Journal of Chemical Information and Modeling* **59**, 4814-4820 (2019).
46. J. P. Perdew, M. Ernzerhof, K. Burke, Rationale for mixing exact exchange with density functional approximations. *The Journal of Chemical Physics* **105**, 9982-9985 (1996).
47. A. Klamt, G. Schuurmann, COSMO - A new approach to dielectric screening in solvents with explicit expressions for the screening energy and its gradient. *Journal of the Chemical Society-Perkin Transactions 2*, 799-805 (1993).
48. K. Lopata, B. E. Van Kuiken, M. Khalil, N. Govind, Linear-Response and Real-Time Time-Dependent Density Functional Theory Studies of Core-Level Near-Edge X-Ray Absorption. *Journal of Chemical Theory and Computation* **8**, 3284-3292 (2012).
49. Y. Zhang, S. Mukamel, M. Khalil, N. Govind, Simulating Valence-to-Core X-ray Emission Spectroscopy of Transition Metal Complexes with Time-Dependent Density Functional Theory. *Journal of Chemical Theory and Computation* **11**, 5804-5809 (2015).
50. T. Noro, M. Sekiya, T. Koga, Segmented contracted basis sets for atoms H through Xe: Sapporo-(DK)-nZP sets (n = D, T, Q). *Theoretical Chemistry Accounts* **131**, 1124 (2012).
51. S. Plimpton, Fast parallel algorithms for short-range molecular-dynamics. *Journal of Computational Physics* **117**, 1-19 (1995).
52. H. J. C. Berendsen, J. R. Grigera, T. P. Straatsma, The missing term in effective pair potentials. *Journal of Physical Chemistry* **91**, 6269-6271 (1987).
53. E. Pluharova, P. E. Mason, P. Jungwirth, Ion Pairing in Aqueous Lithium Salt Solutions with Monovalent and Divalent Counter-Anions. *Journal of Physical Chemistry A* **117**, 11766-11773 (2013).
54. M. T. H. Nguyen, O. Tichacek, H. Martinez-Seara, P. E. Mason, P. Jungwirth, Resolving the Equal Number Density Puzzle: Molecular Picture from Simulations of LiCl(aq) and NaCl(aq). *Journal of Physical Chemistry B* **125**, 3153-3162 (2021).
55. W. M. Brown, A. Kohlmeyer, S. J. Plimpton, A. N. Tharrington, Implementing molecular dynamics on hybrid high performance computers - Particle-particle particle-mesh. *Computer Physics Communications* **183**, 449-459 (2012).
56. L. Martinez, R. Andrade, E. G. Birgin, J. M. Martinez, PACKMOL: A Package for Building Initial Configurations for Molecular Dynamics Simulations. *Journal of Computational Chemistry* **30**, 2157-2164 (2009).
57. D. L. Parkhurst, C. A. J. Appelo, "User’s Guide to PHREEQC (Version 2): A Computer Program for Speciation, Batch-Reaction, One-Dimensional Transport, and Inverse Geochemical Calculations.," *Water-Resources Investigations Report* (1999).
58. C. W. Davies, Ion Association. *London: Butterworths*, 37-53 (1962).
59. J. I. Drever, *The Geochemistry of Natural Waters: Surface and Groundwater Environments*. (Prentice-Hall Inc., Upper Saddle River, New Jersey, 1997).
60. P. P. Ewald, Die Berechnung optischer und elektrostatischer Gitterpotentiale. *Annalen der Physik* **369**, 253-287 (1921).
61. D. Frenkel, B. Smit, *Understanding Molecular Simulation: From Algorithms to Applications*. (Academic Press, ed. 2, 2001).
62. Y. S. Chen, J. L. Fulton, W. Partenheimer, A XANES and EXAFS study of hydration and ion pairing in ambient aqueous MnBr2 solutions. *Journal of Solution Chemistry* **34**, 993-1007 (2005).
63. J. L. Fulton, S. M. Heald, Y. S. Badyal, J. M. Simonson, Understanding the effects of concentration on the solvation structure of Ca2+ in aqueous solution. I: The perspective on local structure from EXAFS and XANES. *Journal of Physical Chemistry A* **107**, 4688-4696 (2003).
64. M. M. Hoffmann, J. G. Darab, B. J. Palmer, J. L. Fulton, A transition in the Ni2+ complex structure from six- to four-coordinate upon formation of ion pair species in supercritical water: An X-ray absorption fine structure, near-infrared, and molecular dynamics study. *Journal of Physical Chemistry A* **103**, 8471-8482 (1999).

65. E. Gallo *et al.*, Preference towards Five-Coordination in Ti Silicalite-1 upon Molecular Adsorption. *Chemphyschem* **14**, 79-83 (2013).
66. E. Hennings, H. Schmidt, W. Voigt, Crystal structures of ZnCl2.2.5H2O, ZnCl2.3H2O and ZnCl2.4.5H2O. *Acta Crystallographica Section E* **70**, 515-518 (2014).
67. M. Maeda, T. Ito, M. Hori, G. Johansson, The structure of zinc chloride complexes in aqueous solution. *Zeitschrift Fur Naturforschung Section a-a Journal of Physical Sciences* **51**, 63-70 (1996).
68. D. Biriukov *et al.*, The "good," the "bad," and the "hidden" in neutron scattering and molecular dynamics of ionic aqueous solutions. *Journal of Chemical Physics* **156**, 194505 (2022).
69. L. M. Anovitz *et al.*, Frustrated Coulombic and Cation Size Effects on Nanoscale Boehmite Aggregation: A Tumbler Small- and Ultra-Small-Angle Neutron Scattering Study. *Journal of Physical Chemistry C* **126**, 4391-4414 (2022).

6.8: Supplementary Information

Table SI-1: DFT optimized structures used for TDDFT calculations with average bond length and standard deviation.

Coordination Complex (Symmetry)	Zn first shell ligand	Bond length (Å)	Standard Deviation (Å)		Coordination Complex (Symmetry)	Zn first shell ligand	Bond length (Å)	Standard Deviation (Å)
$Zn(H_2O)_6^{+2}$ (Octahedral)	O	2.11	0.03		$Zn(H_2O)_6^{+2}$ (Octahedral)	O	2.11	0.03
$ZnCl(H_2O)_3^{+}$ (Tetrahedral)	O	1.97	0.02		$ZnBr(H_2O)_3^{+}$ (Tetrahedral)	O	1.97	0.02
	Cl	2.28	0.00			Br	2.37	0.00
$ZnCl_2(H_2O)_2$ (Tetrahedral)	O	1.96	0.02		$ZnBr_2(H_2O)_2$ (Tetrahedral)	O	1.97	0.00
	Cl	2.30	0.02			Br	2.40	0.02
$ZnCl_3H_2O^{-}$ (Tetrahedral)	O	1.98	0.00		$ZnBr_3H_2O^{-}$ (Tetrahedral)	O	1.98	0.00
	Cl	2.28	0.01			Br	2.40	0.00
$ZnCl_4^{-2}$ (Tetrahedral)	Cl	2.30	0.02		$ZnBr_4^{-2}$ (Tetrahedral)	Br	2.42	0.02

Table SI-2: Zn – Cl coordination numbers for 1 m $ZnCl_2$ with added LiCl extracted from references 53 and 54 in the manuscript.

Zn – Cl Coordination numbers for: 1 m $ZnCl_2$ + (*x*) LiCl			
x	**2.5 m**	**5 m**	**10 m**
Pluharova *et al*.[53]	2.92	3.08	3.14
Nguyen *et al*.[54]	2.71	2.80	2.99

Table SI-3: Linear decomposition of intermediate moiety spectra onto the endpoint spectra from TDDFT.

Moiety	**Octahedral contribution**	**Tetrahedral contribution**
$Zn(H_2O)_6^{+2}$	1	0
$ZnCl(H_2O)_3^{+}$	0.55	0.45
$ZnCl_2(H_2O)_2$	0.31	0.69
$ZnCl_3(H_2O)^{-}$	0.16	0.84
$ZnCl_4^{-2}$	0	1

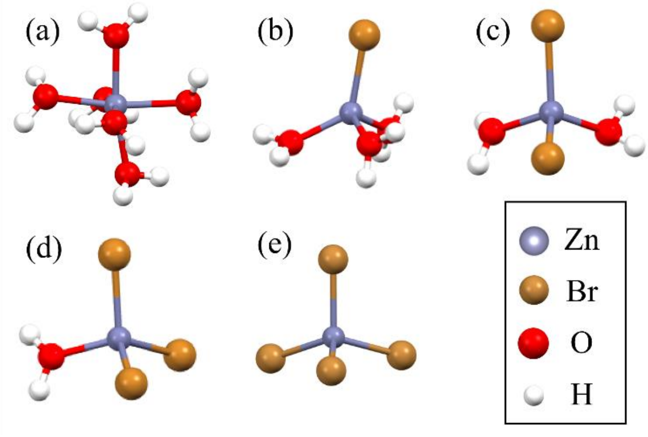

Figure SI-1. DFT optimized structures for Zn^{+2} complex with Br^- addition.

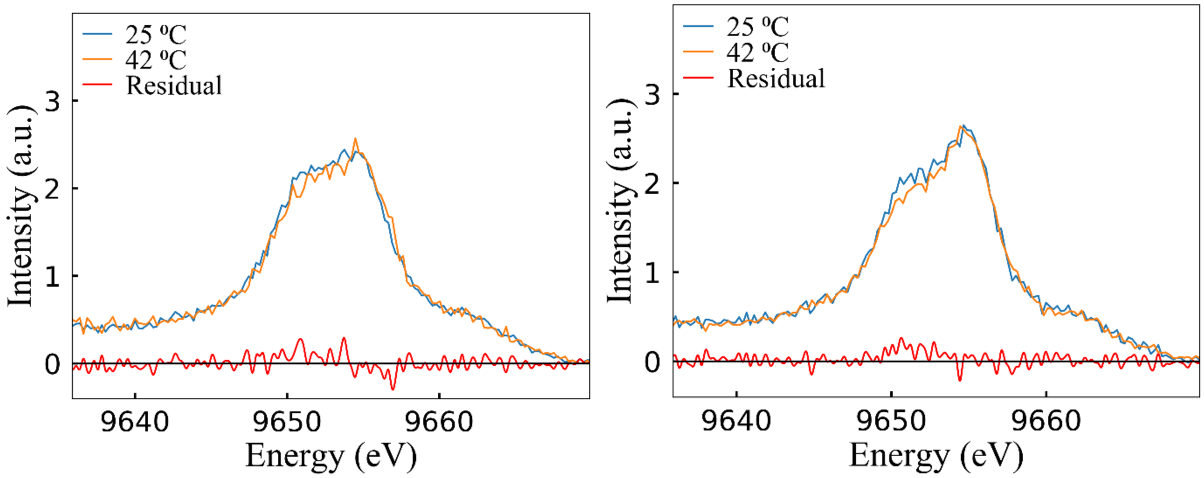

Figure SI-2: VTC-XES spectra at 25°C and 42°C for (a) 1 m ZnCl2 + 0.5 m NaCl and (b) 1 m ZnCl2 + 1 m NaCl, showing the small difference within permissible error (4% octahedral contribution change was noticed in the LCA).

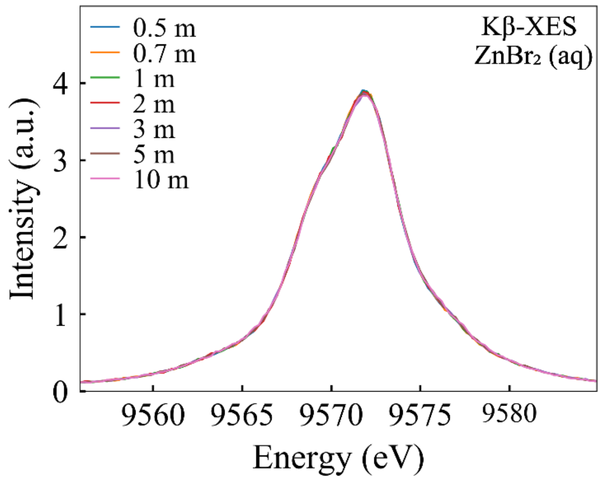

Figure SI-3: Representative Zn Kβ XES spectra for aqueous $ZnBr_2$ concentration series showing excellent alignment after normalization.

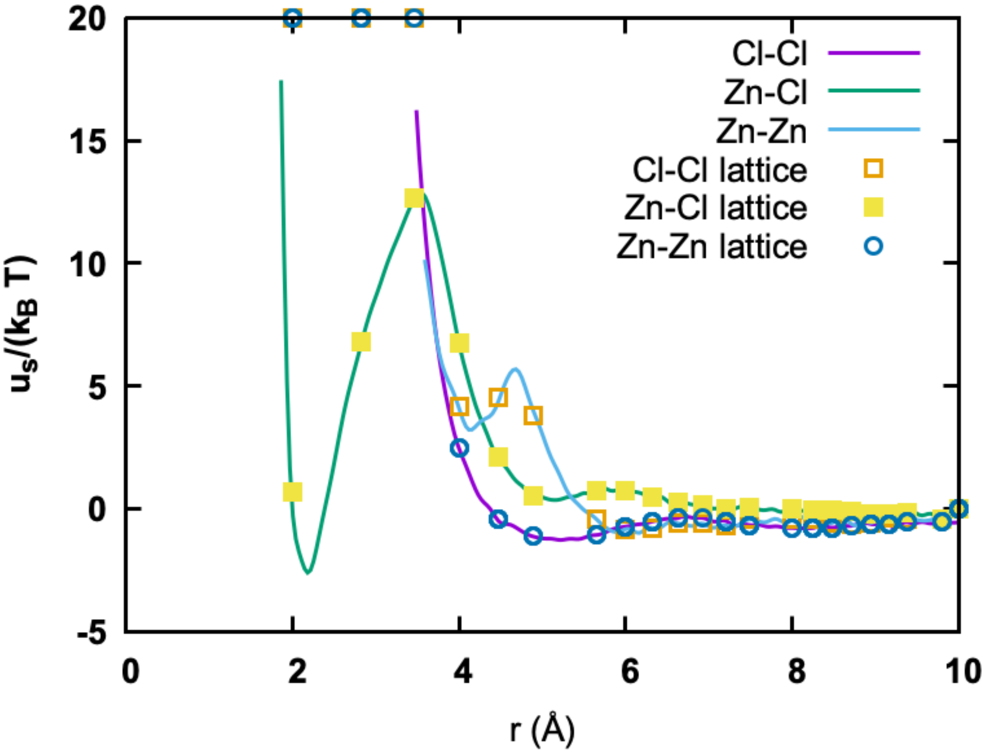

Figure SI-4: Short range potential and location of lattice interaction distances used for Monte Carlo simulations.

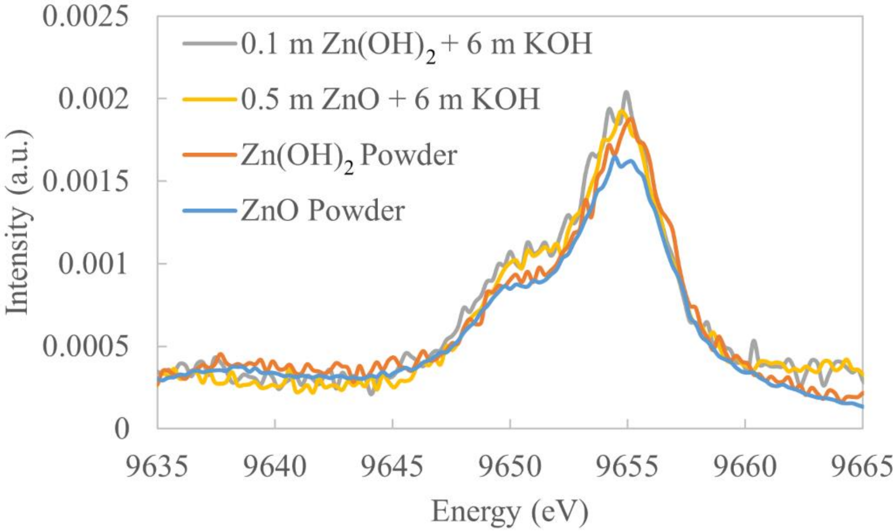

Figure SI-5: VTC-XES spectra of various Zn-species with O as the first neighbor.

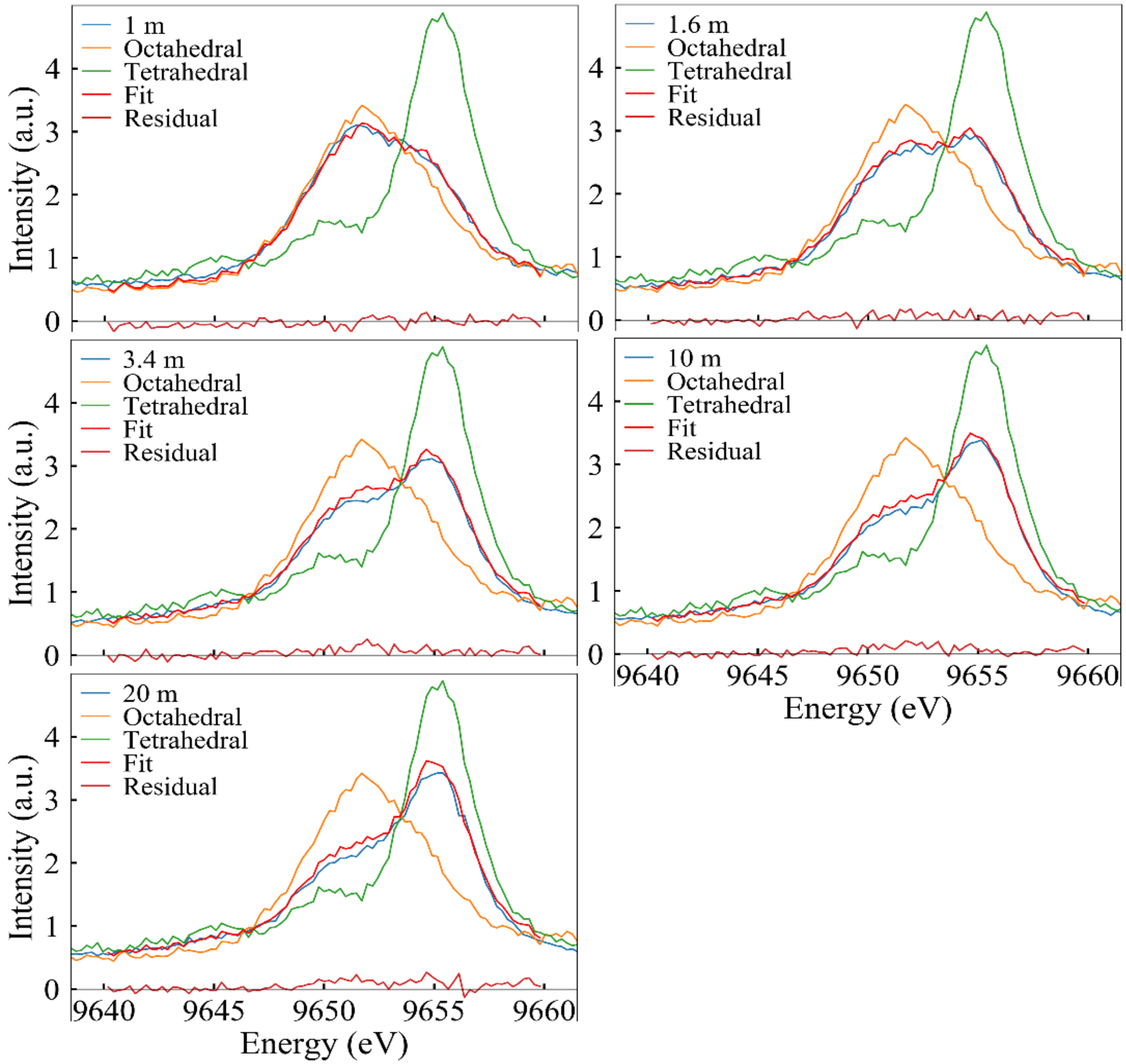

Figure SI-6: LCA fits along with residuals and end point spectra for the $ZnCl_2$ concentration series.

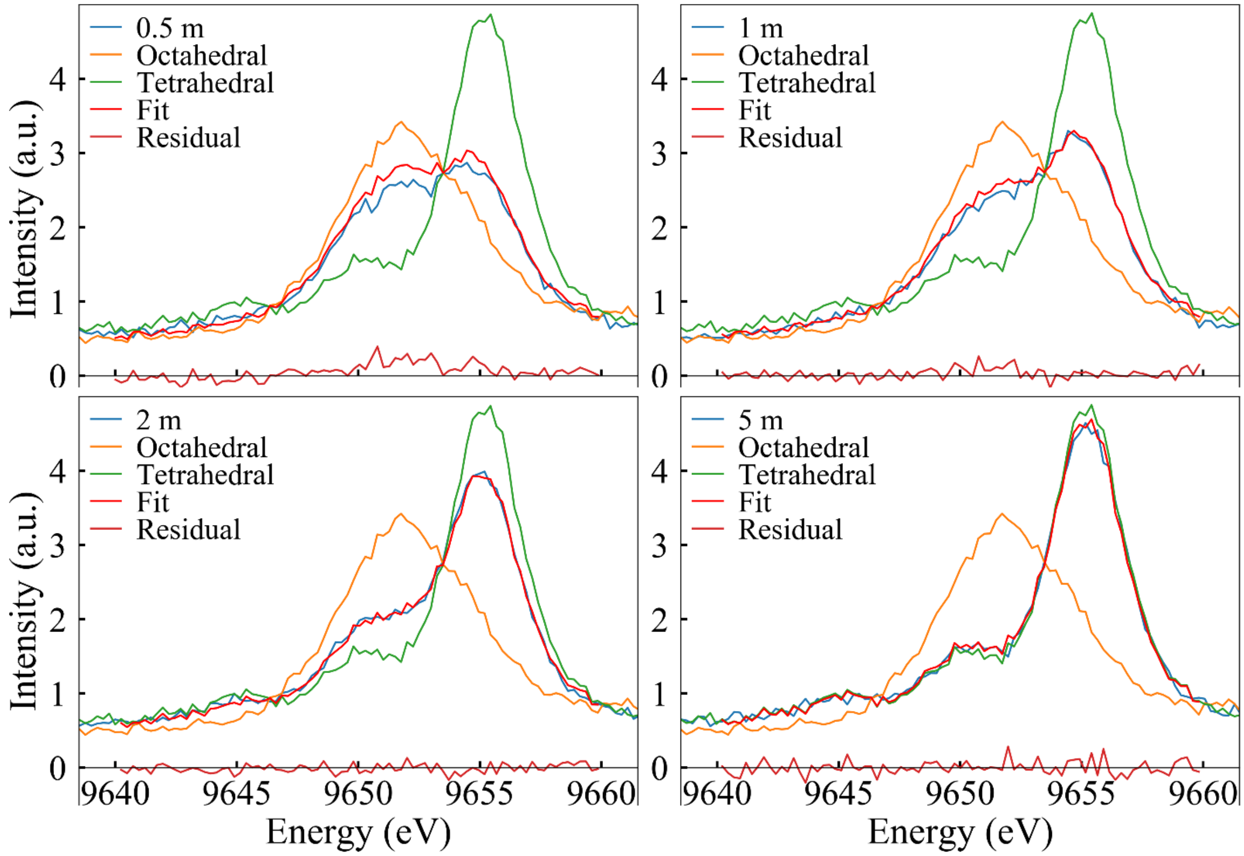

Figure SI-7: LCA fits along with residuals and end point spectra for the samples with composition 1 m $ZnCl_2$ + *x* m NaCl (*x* given in legend).

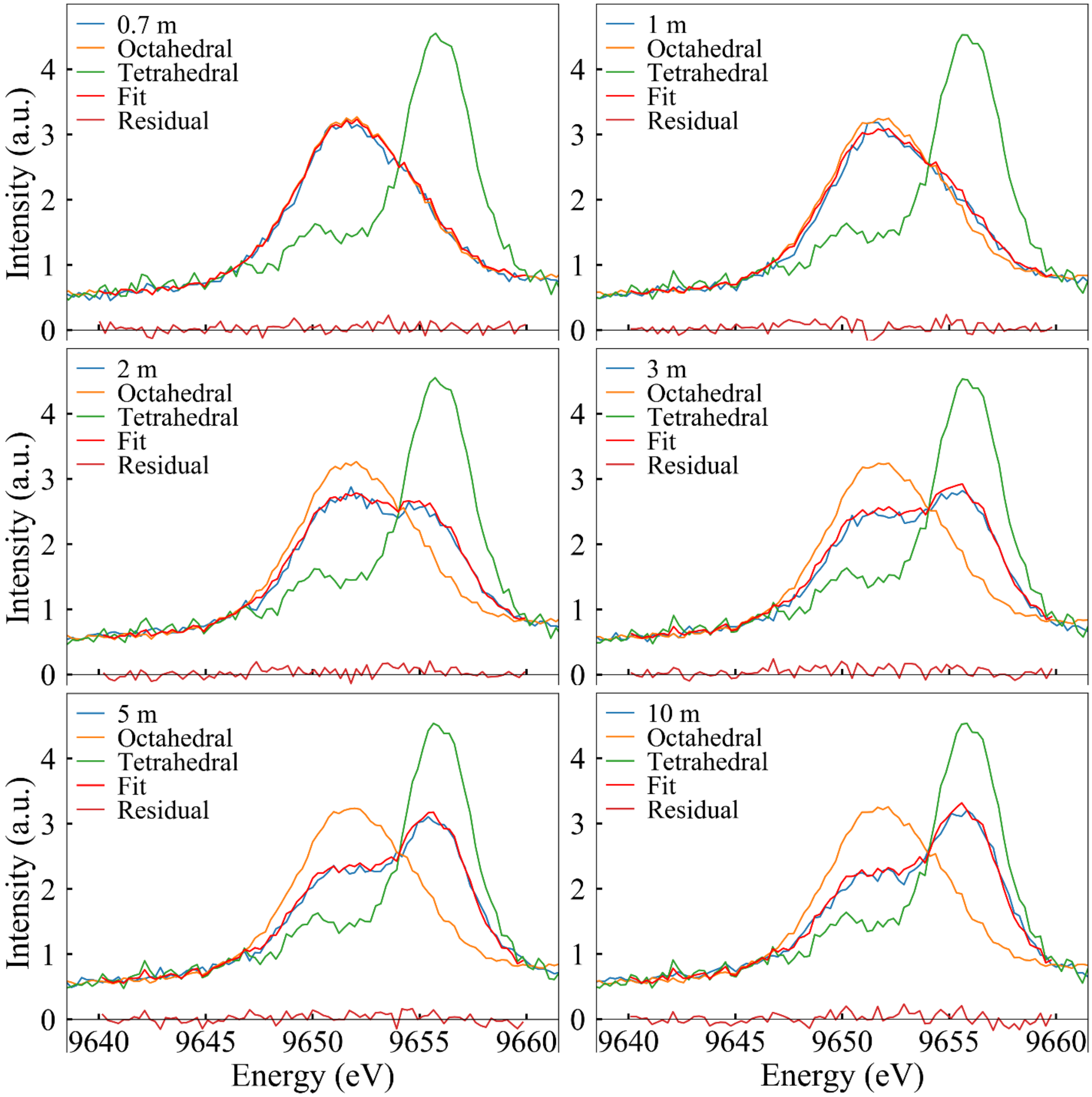

Figure SI-8: LCA fits along with residuals and end point spectra for the $ZnBr_2$ concentration series.

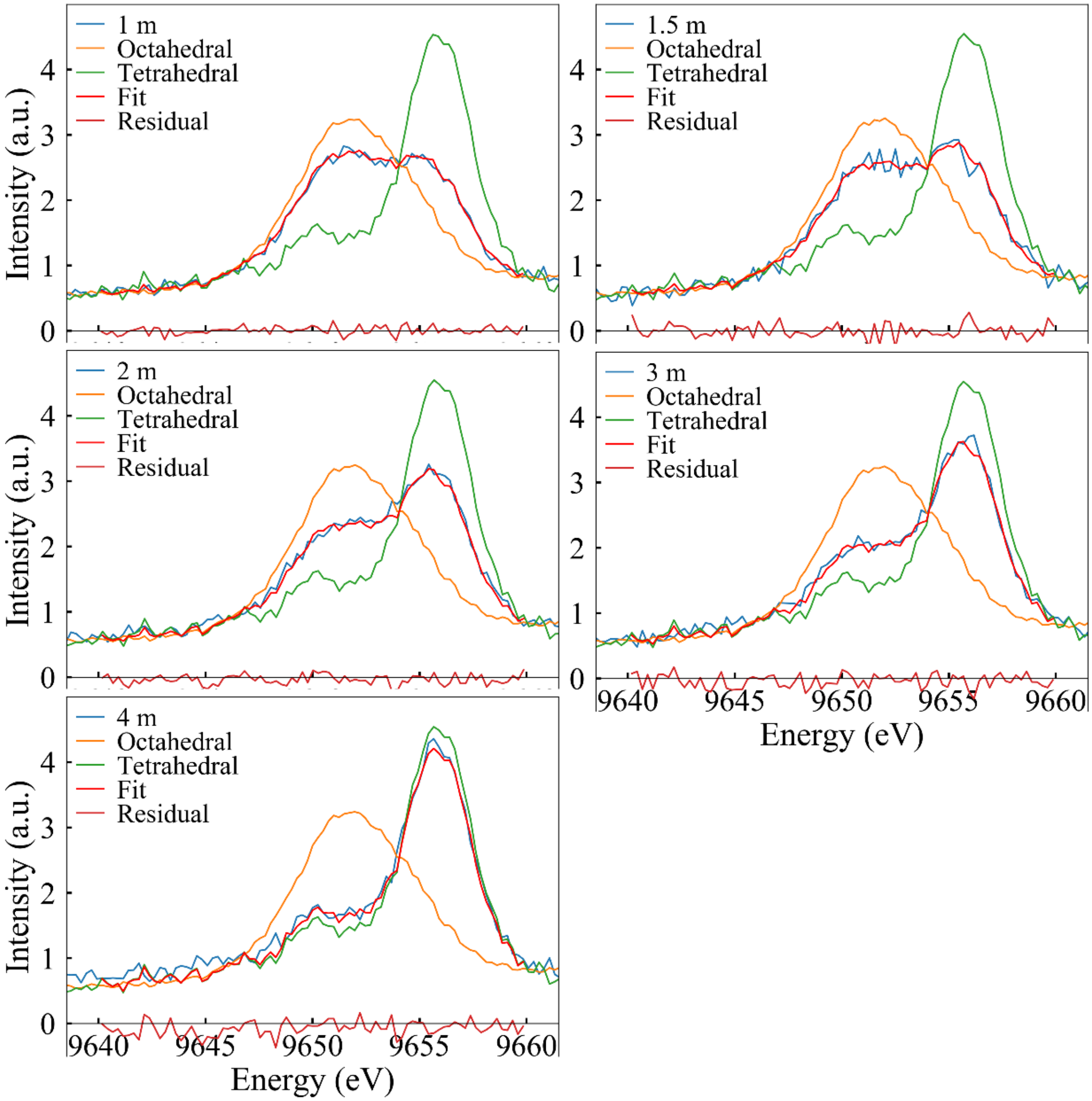

Figure SI-9: LCA fits along with residuals and end point spectra for the samples with composition 1 m $ZnBr_2$ + *x* m LiBr (*x* given in legend).

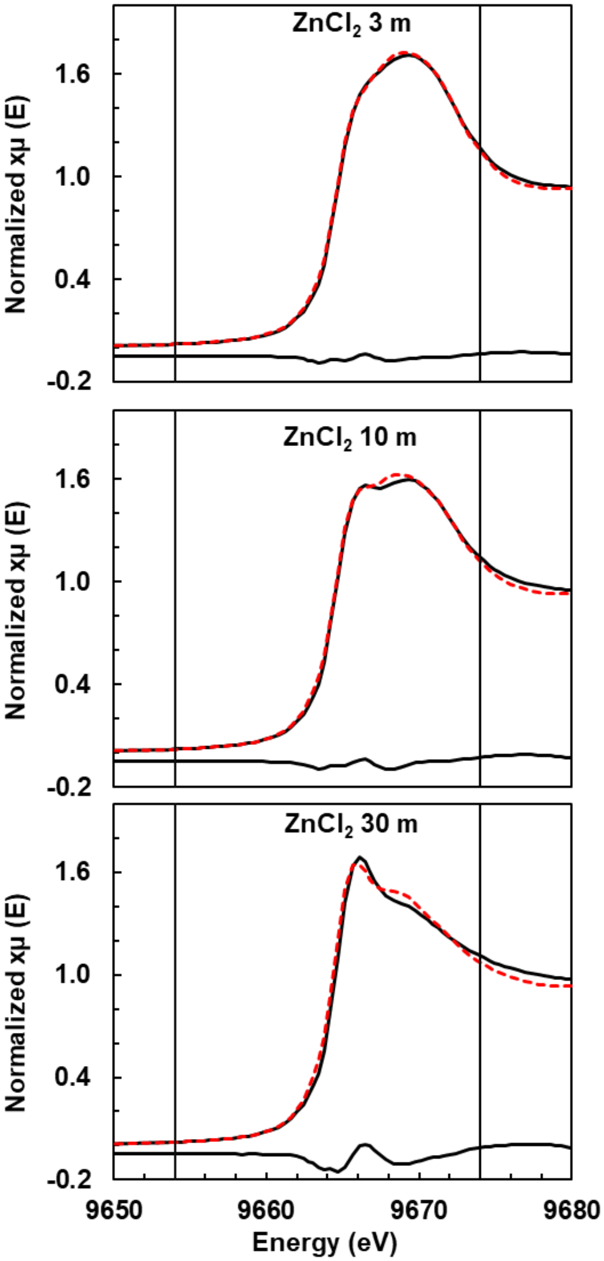

Figure SI-10: Selected LCA fits and experimental XANES data with residual for $ZnCl_2$ concentration series.

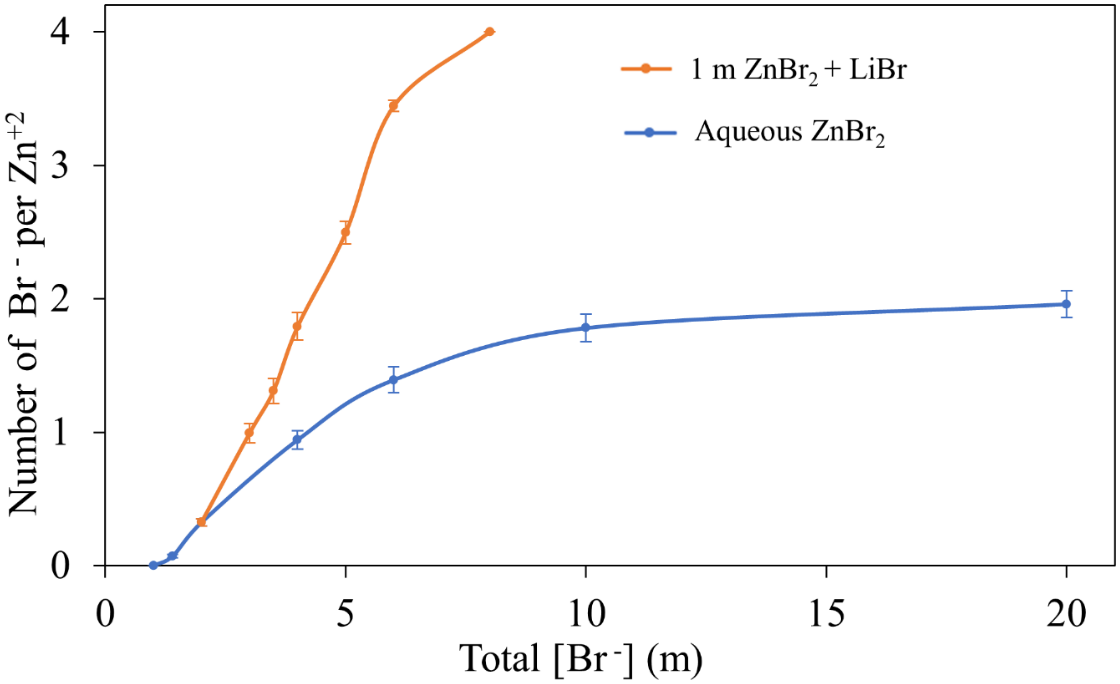

Figure SI-11: Average number of Br $^-$ coordinated with Zn^{+2} in the solution as a function of the total Br $^-$ concentration for pure $ZnBr_2$ concentration series and added salt series.

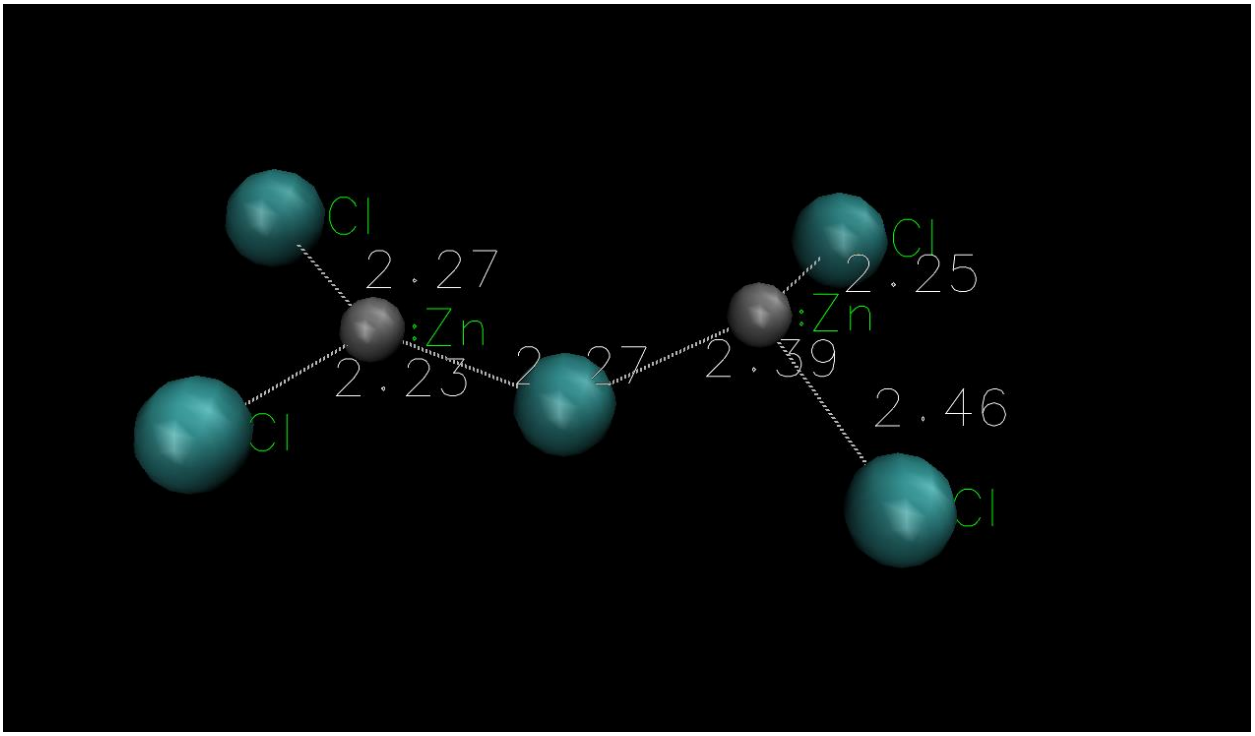

Figure SI-12: MC derived $Zn_2Cl_3^{1-}$ dimer (with bridging Cl) structure. The numerical values are bond lengths in Angstroms.

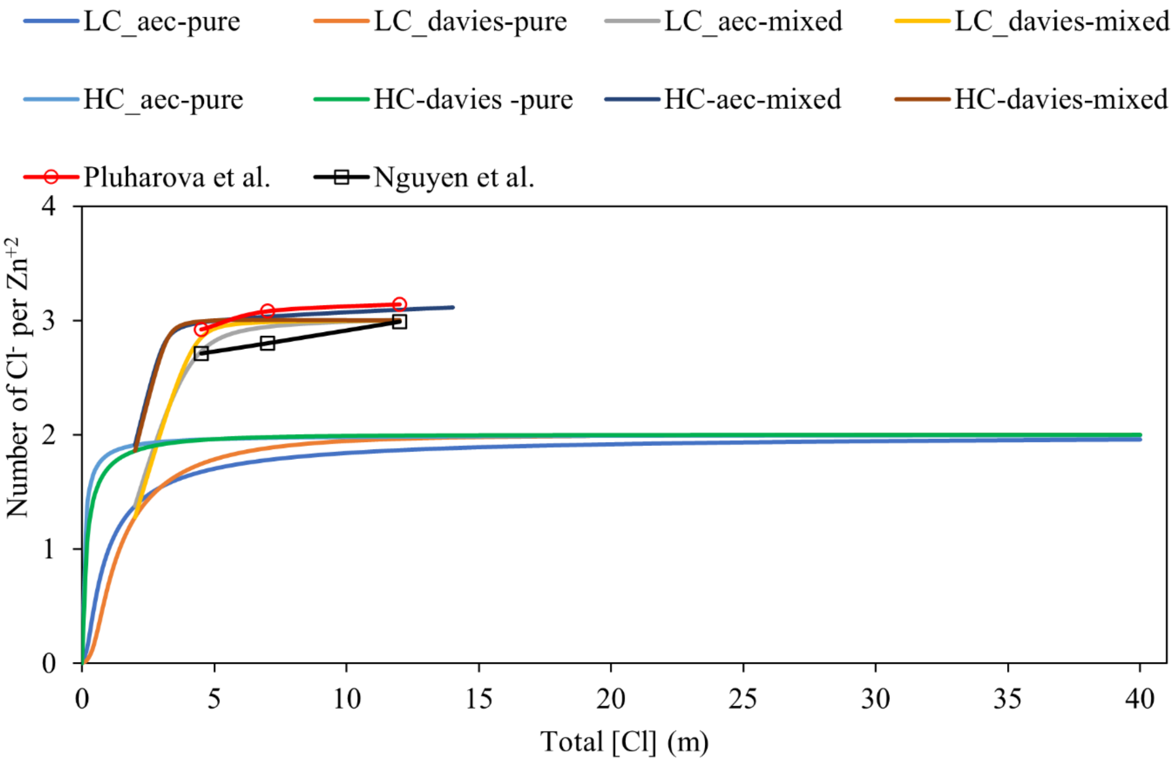

Figure SI-13: Average chloride coordination number per zinc as a function of total chloride concentration for pure and mixed salt solutions derived from various theoretical methods as indicated in the legend. In the legend: LC – low concentration, HC – high concentration, aec – activities are assumed to equal concentrations, Davies – indicates that activity corrections were calculated using the Davies equation, pure – is pure $ZnCl_2$ solutions and mixed - is 1 m $ZnCl_2$ + a variable amount of NaCl. Pluharova *et al*. is Ref. 53 and Nguyen *et al*. is Ref. 54 in the manuscript.

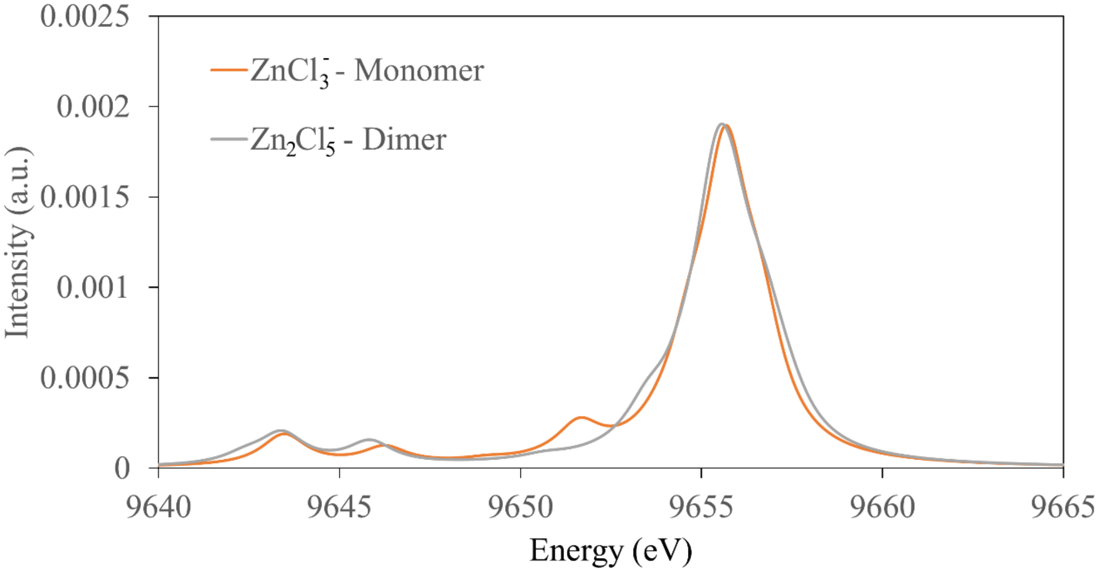

Figure SI-14: TDDFT calculated VTC-XES spectra of dimer $Zn_2Cl_5^-$ and monomer $ZnCl_3^-$.

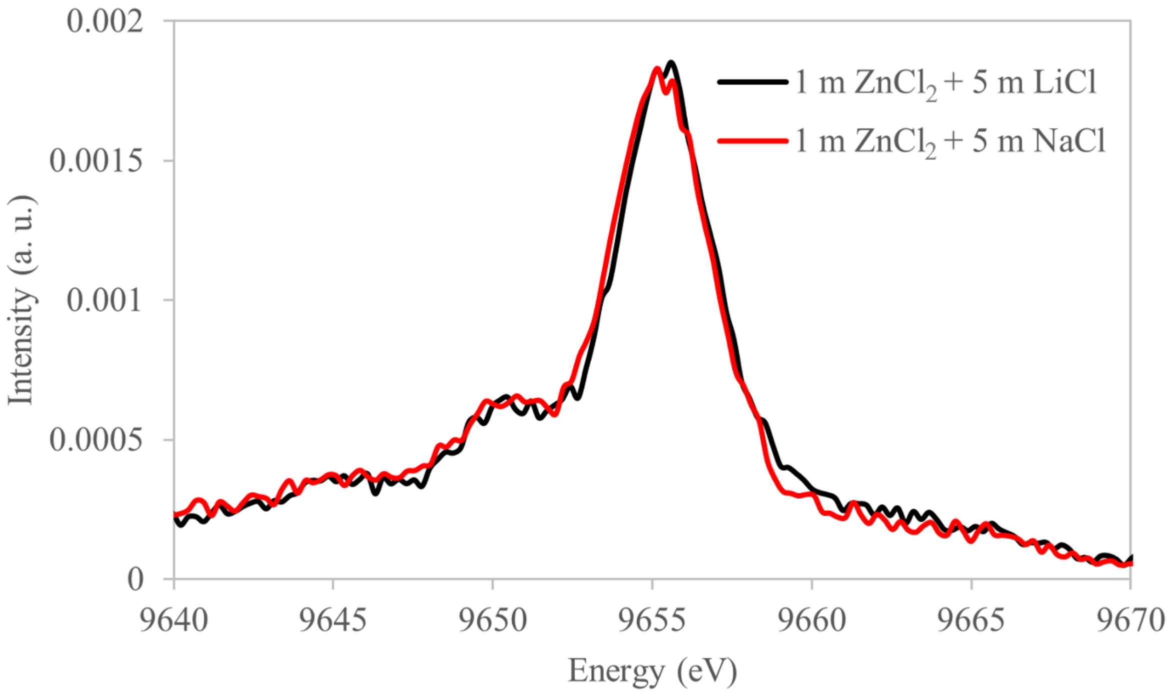

Figure SI-15: Identical experimental VTC-XES spectra for 1 molal $ZnCl_2$ aqueous solutions with added NaCl and LiCl confirming the null effects of the additional cation on the VTC-XES spectra of the Zn-complex.

Details of the N_{Cl} calculation

A physical admixture of local environments results in a similarly weighted VTC-XES spectrum:

$$I(E) = \sum_{x=0}^{4} n_x \, I_x(E). \qquad (1)$$

where n_x is the fractional contribution of the species with *x* Cl ligands ($\sum n_x = 1$) and $I_x(E)$ is the mole-normalized VTC-XES spectrum for, again, the species with *x* Cl ligands. If the spectra for intermediate moieties are (even approximately) linearly dependent on the endpoint spectra, we would have

$$I_x(E) = (1 - f_x) I_0(E) + f_x I_4(E). \qquad (2)$$

where f_x is the fraction of tetrahedral weight in $I_x(E)$. While we cannot prepare pure samples of the intermediate moieties to test the validity of Eq. 2, we do find that the TDDFT predicted spectra for the intermediate moieties are indeed very nearly linearly dependent on the endpoint octahedral and nominally tetrahedral fully chlorinated spectra, and furthermore that the linear dependence is quite smooth in *x* (see Table SI-3 for the linear decomposition of calculated intermediate moiety spectra onto the endpoint configurations). The latter detail has a subtle, but very useful consequence: In the idealized smoothly varying case where $f_x = x/4$, Eq. 1 simplifies to a one-parameter expression in terms of the average number of Cl ligands, N_{Cl}, without any ability to infer specific n_x, i.e.,

$$I(E) = \frac{4 - N_{Cl}}{4} I_0(E) + \frac{N_{Cl}}{4} I_4(E). \qquad (3)$$

If f_x deviates only modestly from $x/4$, as is the case here, then a numerical survey of Eq. 1, constrained by Eq. 2, over the physically allowed solutions to n_x will effectively correct Eq. 3 and find a physically allowed range of values for N_{Cl}.

For the calculation of N_{Cl}, the values for the fractional contribution of intermediate moieties (n_x in equation 1 above) were varied over the range of (+/-) 0.05 around the values obtained from the fitting of calculated VTC-XES spectra (see Table SI-3). The permissible fractions of all intermediate moieties present in each spectrum were allowed to fluctuate anywhere between 0 and 1, such that the mole fraction sum is conserved at unity. The average of all the values obtained for N_{Cl} was then reported with an error bar of one standard deviation (Figure 6 in the article).

Ancillary information about the CMD force field.

The force field was used without modification from some of our prior work (Rampal *et al.*, 2021, Ref. 30 in manuscript). The force field was refined to reproduce the neutron diffraction with isotopic substitution experiments on 4.5 m $ZnCl_2$ solutions. In this method, the differences in the structure factors is measured of two matched solutions in "null" water (with zero coherent scattering from hydrogen) that differ only in the isotope of chloride in the solutions. The Fourier transform of that difference structure factor reveals the atomic-scale Pair Distribution Function (PDF) with respect to chloride. After formal charge models were found to overestimate the extent of solution structuring, an electronic continuum correction method was applied, specifically the force field was adapted from prior work (Duboue-Dijon *et al.*, 2018, Ref. 35 in manuscript; itself developed from total scattering PDF of null water $ZnCl_2$ solutions) to reproduce measured NDIS data more precisely. The parameters to which this force field was tuned reflects the ion clustering of the solutions specifically, hence the excellent agreement with the XES data in pure $ZnCl_2$ solutions measured here. However, in review, the question was raised about how this force field reproduces other thermodynamic properties of the system, in particular the hydration free energies of the aqueous ions. To examine this, we calculated an average potential energy difference for the hydrated aqueous ions and water, and applied a correction for the ECC's model's lack of formal charges (Döpke *et al.*, 2020, (Ref. 1)). These give hydration free energies of zinc and chloride as -1904 and -374 kJ/mol, respectively. The experimental estimates are -1975 and -344 kJ/mol, for Zn^{2+} and Cl^-, respectively (Marcus, 2015, (Ref. 2)). Considering the force field was not tuned to reproduce the hydration free energy specifically, the agreement is acceptable. While improvement could be made for zinc especially, we stress that this force field is designed to reproduce the atomic-scale solution structure, especially the extent of ion clustering. Previous work has shown that for classical models, improving agreement with one set of calibration data often leads to a degradation in the agreement of others (Biriukov *et al.*, 2022, Ref. 68 in manuscript). Thus, a precise match for hydration free energy will likely lead to a degradation of the ability to model ion clustering.

References:

1. Döpke, M. F.; Moultos, O. A.; Hartkamp, R.; On the transferability of ion parameters to the TIP4P/2005 water model using molecular dynamics simulations. *J. Chem. Phys.* 152, 024501, 2020.
2. Marcus, Y.; Ions in Solution and their Solvation. *John Wiley & Sons, Incorp.* Hoboken, NJ, 2015

Chapter 7: Quantification of Enhanced Ion-Pairing in Nanoconfined Electrolytes Using Valence-to-Core X-ray Emission Spectroscopy

This chapter is based on a manuscript under preparation with the following authors:

Diwash Dhakal, Timothy T. Fister, Gerald T. Seidler.

7.1: Abstract

The increasing use of nanostructured materials in contact with aqueous solutions for various technological applications including energy storage requires an improved understanding of the effects of nanoconfinement. In this study, we use valence-to-core X-ray emission spectroscopy (VTC-XES) to quantify the effects of nanoconfinement on the evolution of local coordination structure of Zn complexes in aqueous zinc chloride systems. Recent work (Dhakal, *et al.*, 2023) establishes the ability to quantify the Zn–Cl first shell coordination number. We find that ion pairing is enhanced in solutions under nanoconfinement compared to their bulk counterparts, and we also find that the electrochemical voltage window (EVW) of such electrolyte solutions is correlated to the extent of ion pairing. Several possible explanations for both the enhancement in ion pairing and its correlation with the EVW are discussed, with significant connection to the broader concept of water-in-salt electrolytes (WiSE).

7.2: Introduction

Aqueous solutions are ubiquitous in many important systems, ranging from naturally occurring geological (*1*) and biological systems (*2*) to technological applications such as catalytic (*3*) and energy storage systems. (*4*) Consequently, such systems have been studied to understand their structural and thermodynamic properties, (*5-7*) in addition to the efforts to engineer technological solutions to problems including ore refinement, water purification, catalysis, energy storage, and materials synthesis. (*3-18*) The properties of such aqueous solutions depend greatly on the properties of water and the solvation structure of the ions in the solution. (*5, 6, 19*) Further, the solvation structure of hydrated ions itself is greatly influenced by the properties of solvating water.

With the increasing interest in nanostructured hosts for aqueous solutions for technological applications in catalysis, (*20*) water purification, (*17*) energy conversion and storage (*21, 22*) and other fields, (*23-26*) it has become essential to understand the behavior of aqueous electrolytes in nanoconfined environments. Under nanoconfinement, the molecular configuration and other properties of both water and the solvated species are considerably different than in the bulk. For nanoconfined aqueous solutions, the local density of water is no longer uniform, (*27*) the hydrogen bonding is weaker, (*28*) and the dipole orientation becomes more ordered compared to the bulk. (*29*) The self-energy of a hydrated ion in low-dielectric-constant nanoconfined water is more than that in high-dielectric-constant bulk water, (*30*) the solvation environment of ions can be significantly distorted (*31*) and in some cases highly stable nanocrystalline-like cation-anion pairs can be formed. (*32*) However, experimental studies on the extent to which the interfacial or nanoconfined water alters the coordination environment of ions in aqueous solutions are an emergent issue, as are efforts to isolate solvent interfacial effects from confinement effects on solute species coordination. (*19, 33-36*)

Having admitted the difficulty of the challenge, we summarize here prior work on confinement effects on ion association. In general, the below studies qualitatively agree on the trend of cation dehydration and ion pairing enhancement under confinement. However, these works are often unable to quantify ion pairing and also present conflicting evidence about the onset of nanoconfinement effects in terms of the pore size.

To begin, both NMR (*19*) and electrochemical (*34*) studies reported partial desolvation of cations during interaction with nanoscale cavities. In addition, the latter study found the extent of cation desolvation to be inversely proportional to the size of the pores. (*34*) Similarly, classical molecular dynamics simulation on aqueous NaCl (*37*) and X-ray absorption spectroscopy experiment on aqueous $CuBr_2$ (*35*) agree about the bulk-like cation-hydration structure in larger pores and the decrease in hydration and enhancement in ion pairing in smaller pores. Moreover, Nelson *et al*., (*36*) used Zn K-edge EXAFS to study aqueous $Zn(NO_3)_2$, and concluded that Zn^{2+} adsorbs in a tetrahedral coordination in nanoporous silica with pores <10 nm whereas the Zn^{2+} ions exists instead as a mixture of tetrahedrally and octahedrally coordinated surface complexes for pore size >10 nm. Another simulation of aqueous Li- bis(trifluoromethane)sulfonimide (Li-TFSI) solutions showed that, in the context of battery performance, the water-in-salt electrolyte (WiSE) effect that is believed to stem from the formation of ion pairs at high concentrations in bulk can be achieved at relatively lower concentrations by using a nanostructured electrode. (*22*)

The question then arises about how to best add to the above literature with complementary (or even initial) characterization of the cation local environment in nanoconfined solutions. While EXAFS is a natural choice for this question, (*35, 36*) it comes with its own difficulties through an undesired sensitivity to the second coordination shell which complicates quantification of ion pairing. (*38-40*) In the present study, we use valence to core X-ray emission spectroscopy (VTC-XES) to quantify the effects of nanoconfinement by nanoporous carbon on the population of Zn^{2+} complexes in aqueous $ZnCl_2$ solution. As the present authors have recently demonstrated and emphasized, the even more extreme locality of VTC-XES compared to EXAFS results in a pure sensitivity to the first-shell coordination and ability to quantify the number of Cl^- ions in the first coordination shell. (*41*) We observe and give numerical estimates for increased ion pairing as a consequence of nanoconfinement and anion activity in a model nanoporous carbon frequently used in battery manufacture. These results are augmented with electrochemical measurements, and we compare the cation solvation structure with the performance of battery in terms of the electrochemical voltage window (EVW) of the electrolyte in the nanoporous carbon and instead when in bulk with a glassy carbon electrode. It is important to note that for bulk electrolytes, studies have attributed the superior performance observed in WiSE to the increased ion pairing and interrupted hydrogen bonding between water molecules in such aqueous systems. (*8-11, 42*) Our study adds valuable quantitative insight on the general topic of enhanced ion association under nanoconfinement and on the positive correlation between the extent of ion pairing and the EVW of aqueous electrolytes. Our work supports the idea of realizing WiSE effects at lower electrolyte concentrations through the use of nanostructured electrodes. (*22*)

7.3: Methods

7.3.1: Sample preparation

Pure and mixed aqueous solution samples containing $Zn(NO_3)_2$, $ZnCl_2$ and LiCl with various concentrations were prepared by dissolving as bought powder $Zn(NO_3)_2$, $ZnCl_2$ and LiCl in HPLC grade DI water in ambient atmosphere. For higher concentration samples, a magnetic stirrer was used for ~30 minutes to generate clear samples without visual sign of undissolved solute. All reagents were purchased from standard vendors (Alfa-Aesar, Sigma Aldrich, Fisher Scientific) in 99.9% purity or higher and in anhydrous state. For bulk XES experiments, the solution samples were then loaded into thin-walled quartz capillaries (Charles Supper Corp.) and then closed with sealing wax. A significant air space was included in the capillary to accommodate possible evolved gas during x-ray irradiation.

Samples with $ZnCl_2$ solution in nanoporous carbon were prepared as follows: first, nanoporous carbon (Sigma Aldrich) with average pore size of 2 nm and specific surface area of 2000 m^2/g, as stated by supplier, was mixed with the given solution in a vial using a magnetic stirrer at low revolution rate for about 12 hours. The ratio of the mass of nanoporous carbon to the volume of solution used was kept constant at 80 mg/ml. Next, the mixture was pushed through a syringe filter with pore size 2 mm leaving a wet paste of nanoporous carbon in aqueous $ZnCl_2$ solution as the residue. This residue was then centrifuged at 5000 rpm for 5 min through the same syringe filter to flush away the remaining bulk solution leaving behind a slightly damp sample that has very minimal remaining bulk-like solution between the particles. Most of the solution is inside the nanopores, where the capillary action is expected to keep the solution from being pulled out during centrifuging. Finally, the damp sample was retrieved from the filter paper and sealed in polyimide film pouch for XES measurements.

7.3.2: X-ray Emission Spectroscopy (XES)

The VTC-XES experiments were performed in a laboratory-based X-ray emission spectrometer, described in detail in Jahrman *et al.* (*43*) This instrument has previously demonstrated good performance for VTC-XES, (*43, 44*) including in a prior study of bulk Zn-halide solutions. (*41*) The X-ray source has a Pd anode and was operated at ~100 W power (35 kV and 2.8 mA). A Ge (555) spherically bent crystal analyzer (SBCA) was used because of the favorable Bragg angles and energy resolution for the required energy range. The samples were placed ~5 mm away from the Be exit window of the x-ray tube. Optimal horizontal placement with respect to the vertical entrance slit of the spectrometer was verified by following the method of Mortensen *et al*. (*44*)

The VTC-XES scans were collected over the energy range 9550 – 9700 eV in steps of 0.25 eV spanning both the main Kβ line and the valence-to-core (VTC) region. A longer, 40 s integration time per point was used in a region spanning the VTC emission (9630 – 9700 eV) and a shorter 4 s integration time per point in a lower-energy region spanning the main Kβ peak (9550 – 9630 eV). The total measurement time for data collection for one sample was typically 18 hrs. Comparison of early and later scans shows no evidence of beam damage or changes in hydration state.

Kβ emission from a metallic Zn reference was used as a check against monochromator drift and for instrumental calibration across multiple experiments. The final energy scale is consistent across all data sets to ~25 meV.

Processing of the XES data followed several steps. First, we subtracted a constant background with value typically <5% of the count rate in the VTC region. This was due to stray scatter of the primary x-ray radiation. Next, the spectra were shifted in Bragg angle until there was energy alignment with the absolute energy value of the $K\beta_{1,3}$ peak from literature. Finally, the spectra were brought to an absolute intensity scale following the methods of Dhakal *et al*. (*41*) In brief, this involved integral normalization of the spectra using the area under the Zn Kβ spectral feature centered around 9572 eV.

Here we use the method introduced in Dhakal *et al*., (*41*) to infer the number of chloride ions in the Zn^{2+} first coordination shell (N_{Cl}) from VTC-XES spectra. Because of the lack of linear independence of the intermediate moieties' spectra on the endpoint spectra, the true distribution of the intermediate moieties cannot be extracted from the VTC-XES data. But it is possible to infer

N_{Cl}. Briefly, the VTC-XES spectra were fitted with a linear combination of endpoint spectra (octahedral and tetrahedral endpoints, explained in detail in the results and discussion section) to obtain the fractional contribution of those endpoints on the given spectrum. These fractional contributions were then combined with the theoretical insights of the intermediate moieties' spectra to get a physically sensible distribution of the possible combinations of species for each spectrum. N_{Cl} values for each of these possible combinations were calculated to get to a distribution of N_{Cl} values for each spectrum and the average of these values were used as the final inferred N_{Cl}. The errors on these inferred N_{Cl} values represent the standard deviation of the distribution of N_{Cl}.

7.3.3: X-ray Absorption Near Edge Structure (XANES)

XANES data were collected in transmission mode at the Advanced Photon Source, sector 10BM. Solutions were suspended in microporous glass filter paper (Whatman GF/F grade) and sealed in plastic washers with rigid polypropylene windows to maintain a constant thickness. NPC samples were prepared in a similar manner, but without the glass fiber separator. XANES data were collected with a downstream Zn metal foil that was later used for energy calibration (9659 eV). Data were measured at least twice to test for beam damage or gradual evaporation, but no changes were found within the duration of the experiment.

7.3.4: Electrochemical measurements

Cyclic voltammetry (CV) and linear sweep voltammetry (LSV) measurements were conducted to learn about the electrochemical voltage window (EVW) of the electrolytes. The EVW is closely linked to the processes occurring in the vicinity of the interface between electrolyte and electrode. We compared the EVW of bulk electrolytes in contact with a standard electrode surface (referred to as the "bulk case") with that of nanoconfined electrolytes in contact with the confining surface (referred to as the "NPC case"). To do this, we utilized glassy carbon working electrodes for the bulk case and nanoporous carbon with 2-nm pores for the NPC case. Glassy carbon was chosen to ensure the electrodes had similar electrochemical properties, making it possible to isolate the differences primarily due to confinement effects.

The LSV measurements for the bulk case were performed in a three-electrode cell with glassy carbon as working electrode, polished platinum sheet as counter electrode and Ag/Ag^+ (saturated KCl) as reference electrode. LSV measurement for a representative sample for the bulk case was also performed in two-electrode configuration, with glassy carbon as working and polished platinum sheet as counter/reference electrodes and compared with the three-electrode setup which showed no difference in the extracted EVW between these two setups. In the case of NPC, two-electrode cells were used with NPC electrode as working electrode and polished platinum sheet as the counter/reference electrode. All measurements were done with a scan rate of 10 mV/sec. The free-standing NPC electrodes, with thickness 0.5 mm, were fabricated using 95 wt. % NPC and 5 wt. % Poly(vinylidene fluoride) (PVDF) as binder. For the EVW extraction, the OER and HER onsets were determined from the point of intersection between the linear extrapolation of signal immediately before and after the sharp rise in current in the CV or LSV curve. The errors in the extracted EVW were estimated by varying the fit range used for the linear extrapolation.

7.4: Results and Discussion

First, we remind the reader that the aqueous zinc chloride system supports, in principle albeit perhaps not in practice, five different local coordinations for the Zn^{2+} ion: one in octahedral symmetry with six water molecules and four in tetrahedral symmetry with n Cl^- ions and $(4 - n)$ water molecules (where $n = 1, 2, 3, 4$), see Figure 1. The Zn^{2+} ion is coordinated to six water molecules in an octahedral coordination geometry in low concentration aqueous $ZnCl_2$ solutions. (*6, 7, 41, 45*) As the ion activity is increased, Cl^- ions penetrate the first coordination shell giving rise to contact ion pairing and, with the presence of even a single Cl^- ion to Zn^{2+} in first shell, a change in overall coordination symmetry to tetrahedral, thereby losing two additional water molecules in the process. At the extreme limit of high anion activity, there is complete contact ion-pairing with four Cl^- ions in a tetrahedral coordination with the Zn^{2+} ion. (*6, 41, 45*)

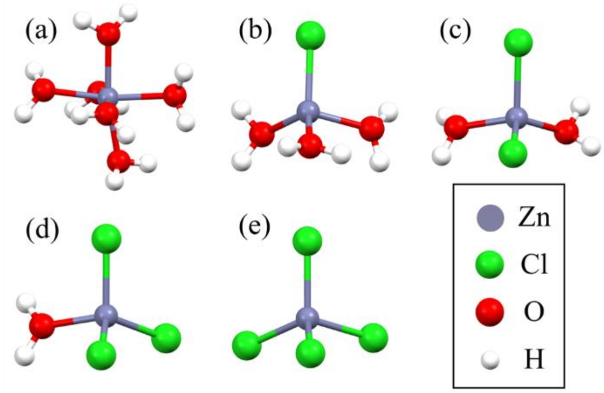

Figure 1: DFT-optimized Zn^{2+} coordination structures for (a) $Zn(H_2O)_6^{2+}$, (b) $ZnCl(H_2O)_3^+$, (c) $ZnCl_2(H_2O)_2$, (d) $ZnCl_3(H_2O)^-$, and (e) $ZnCl_4^{2-}$. (used from Dhakal *et al.* (*41*))

Figure 2 shows a compilation of VTC-XES spectra for both bulk and nanoconfined solutions. Note that the spectra are all on the same absolute intensity scale through normalization to the Zn Kb diagram line. (*41*) First, to establish one endpoint, the low concentration $Zn(NO_3)_2$ solution spectra agree in the bulk and nonconfined environments. This solution in bulk is previously established to have octahedral coordination of Zn^{2+} with six waters, (*46*) and hence we find that the signature of such octahedral coordination is unchanged on nanoconfinement. Note also the perfect agreement between the low concentration $ZnCl_2$ solution (bulk) and the two nitrate spectra: the low Cl^- activity configuration for the zinc chloride system is octahedral with water solvation and no contact ion pairing. Similar results are obtained from the comparison of XANES spectra for the same three samples, see Figure SI-1.

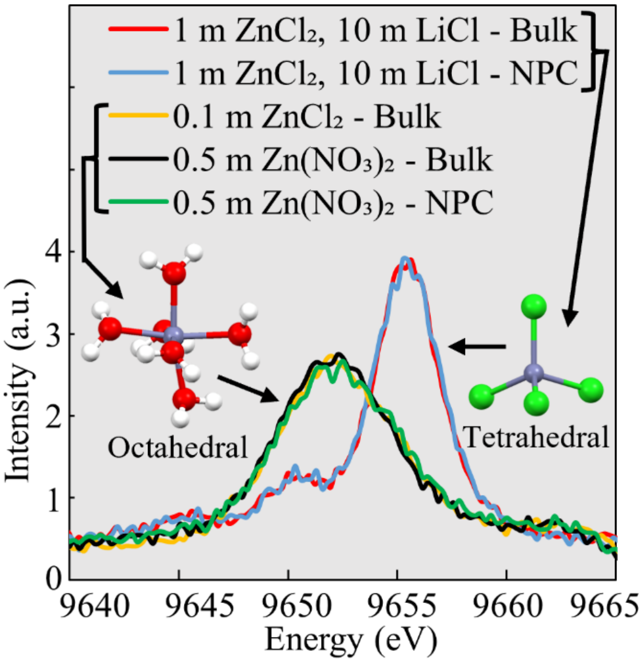

Figure 2: Demonstration of the dependence of Zn VTC-XES on local coordination of the Zn^{2+} ion and its invariance under nanoconfinement for the extreme cases. Zn VTC-XES spectra for aqueous solutions in bulk and in nanoporous carbon (NPC) as indicated in the legend.

At the other extreme in Figure 2, the bulk and nanoconfined samples of 1 m $ZnCl_2$ with added 10 m LiCl represent complete ion pairing in a tetrahedral coordination, i.e., a $ZnCl_4^{2-}$ complex. While the fact of the Cl-saturated tetrahedral coordination is unsurprising in this limit, the actual agreement of the spectra requires some comment. As discussed in detail in Dhakal *et al.*, (*41*) VTC-XES has nearly exclusionary first-shell sensitivity, i.e., the details of hydration or spectator Cl^- ions in the second shell are almost completely irrelevant. Given that the structure and physical properties (e.g., dielectric constant) of nanoconfined water can be very different from the bulk, differences in the second shell between the bulk and nanoconfined cases are possible for all solutions studied here. The predominant first-shell sensitivity of VTC-XES has clear scientific benefit here.

To summarize: the VTC-XES spectral agreement between bulk references and nanoconfined solutions at the extrema of Cl^- ion activity confirms that the spectral features remain invariant. Moreover, the consistency in the spectral characteristics at the endpoints, whether in a bulk or confined setting, strongly supports the notion that any alterations in these spectral attributes observed between bulk and confined samples of intermediate nature are primarily a result of changes *specifically in the first coordination environment*.

We now move to the central question of enhancement of ion pairing in the NPC host. In Figure 3, along with the endpoint reference spectra, we show VTC-XES and XANES for an intermediate case, 1 m $ZnCl_2$ in bulk and in nanoporous carbon (NPC). Both the VTC-XES and the XANES show changes consistent with a general transition from more-octahedrally coordinated Zn^{2+} with water in the first coordination shell to instead favoring a larger fraction of tetrahedral coordination with significant Cl^- ion content in the first shell. Clearly, nanoconfinement results in increased ion pairing. Quantitatively, the bulk case has an N_{Cl} of 0.59 (± 0.07) which dramatically increases to 1.71 (± 0.17) for the nanoconfined solution. This high amount of ion pairing would only occur above 10 m for bulk solutions, and hence represents a truly dramatic increase. The XANES in Figure 3(b) also shows distinctive changes representing an increase in ion pairing. The spectra evolve towards more tetrahedral coordination under nanoconfinement, note how the white line intensity around 9670 eV decreases with a complementary increase in intensity around 9665 eV, consistent with the endpoint spectra for XANES shown in the bottom of Figure 3 (b). Such spectral feature has been shown to be characteristic of lower symmetry tetrahedral coordination between Zn^{2+} and Cl^- in aqueous $ZnCl_2$ solution, (*41, 45*) and in other metal-halide systems in general. (*38-40*) Note, however, that the XANES cannot be used to quantify this effect because of second- and higher-shell contributions.

As a further qualitative demonstration of enhanced ion pairing, see Figure SI-2 for comparisons between both XANES and VTC-XES across different concentrations and Figure SI-3 for comparison of XANES of the same samples for the bulk and nanoconfined cases. This trend persists for solutions where the Cl^- ion activity is increased with added LiCl salt, see Figure SI-4.

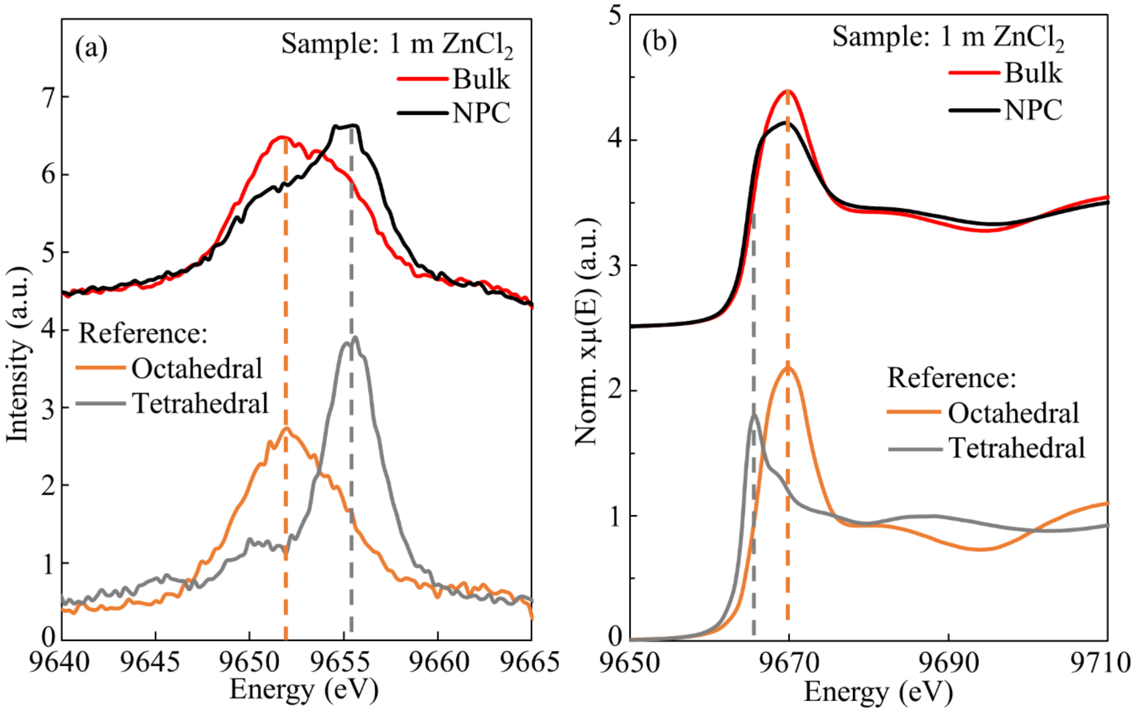

Figure 3: (a) VTC-XES spectra of 1 molal $ZnCl_2$ solution in bulk and in NPC, along with the endpoint reference spectra (octahedral and tetrahedral) from Figure 2, and (b) XANES spectra of 1 molal $ZnCl_2$ solution in bulk and in NPC, along with the endpoint reference spectra (0.1 m $ZnCl_2$ solution (octahedral endpoint) and 0.25 m $ZnCl_2$ + 5 m LiCl (tetrahedral endpoint). XANES for bulk are replotted from Dhakal *et al*. (*41*)

Next, we both quantify the extent of ion pairing and seek to correlated it to electrochemical properties. In the bottom panel of Figure 4 we present the inferred number of Cl^- in the first coordination shell, N_{Cl}, for aqueous $ZnCl_2$ solutions in bulk and inside nanopores.

To begin, note that N_{Cl} is invariant for the nanoconfined solution, with a value only modestly below the theoretical upper limit of 2 due to the 1:2 stoichiometry of $ZnCl_2$. While we delay until later in this section a discussion of mechanisms for the constant high value of N_{Cl} for the nanoconfined case, the numerical value itself requires comment. In sample preparation we aimed to have all the solution inside the nanopores (see Methods section), but it is possible – and perhaps inevitable – that some remnant bulk-like solution still exists between the carbon particles (5-10 mm particle size); this would lower the inferred N_{Cl}. Given the invariance in N_{Cl} with concentration and the considerable likelihood of some remnant bulk liquid, it is fair to speculate the N_{Cl} is likely even closer to the stoichiometric limit of 2.0 in the nanoporous space, i.e., that essentially all Zn^{2+} and Cl^- are incorporated into ion pairing.

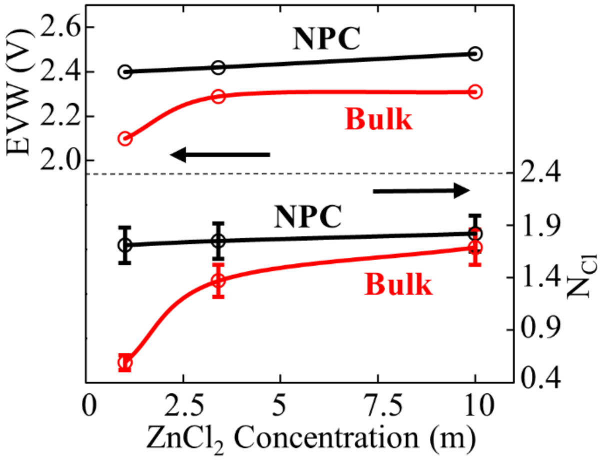

Figure 4: (top) The electrochemical voltage window (EVW) for aqueous $ZnCl_2$ electrolyte as a function of concentration in bulk and in nanoporous carbon (NPC). Error bars are smaller than the symbols. (bottom) Chloride first-shell coordination number, N_{Cl}, for the same solutions.

Next, we shift our attention to the electrochemical portion of our study. As discussed in the introduction, the degree of ion pairing may have significant influence on the electrochemical voltage window (EVW) of electrolytes. (*8-11, 42*) Given the increasing use of nanostructured electrodes in electrochemical applications, any correlational or even causal connection between ion pairing resulting from nanoconfinement and the EVW has both theoretical and practical importance.

To this end, the EVW for nanoconfined (NPC electrode) and bulk (glassy carbon electrode) samples is shown in the top panel of Figure 4. First, for the NPC samples the EVW is, in accordance with the inferred N_{Cl}, effectively invariant. Second, in the bulk case with the glassy carbon electrode, the increasing N_{Cl} with increasing concentration is reflected by qualitatively similar changes in EVW of the electrolyte, again indicating a correlation between the degree of ion pairing and the EVW. Finally, over the present concentration range, the nanoconfined system (i.e., with the NPC electrode) always shows superior EVW over the bulk system (i.e., with the glassy carbon electrode) even when the N_{Cl} values are comparable, i.e., for the 10 m solution. This suggests that while the degree of ion pairing correlates with the EVW, it is not exclusive in that role. This is not surprising; as one example, the same dielectric and structural changes in nanoconfined water that likely encourage ion pairing (discussed in more detail below) can also be expected to change the EVW.

While the situation is surely complex, the results support the idea of EVW enhancement via increased ion pairing and that such enhancement can be realized at much lower electrolyte concentrations (compared to the water-in-salt electrolyte (WiSE) limit) by using nanostructured electrodes. It is worth noting here that a similar conclusion was drawn from a simulation study using boron nitride nanotubes. (*22*) More generally, enhanced ion pairing due to nanoconfinement, if a cause (rather than accidental correlant) of increased EVW's, could be valuable in designing next generation higher-energy-density electrical energy storage employing nanostructured electrodes: the WiSE concept would be effectively extended to lower concentrations because of the enhancement of ion pairing in the electrical double layer for the nanoconfined electrolyte.

We now seek to understand the ensemble of above results in terms of candidate physical models, with the hope of elaborating, if not resolving, the question of whether ion pairing itself is driving the EVW changes or whether it is the effect of confinement on the solvent that both induces ion pairing and also changes the electrochemical properties (with the increased ion pairing a spectator issue).

First, the strong influence of interfaces on the structure of water deserves comment. It has been proposed that water forms a dense ordered layer on the solid – aqueous solution interface and the ordering can extend up to 6 – 7 Å from the wall after which it becomes more diffuse as in the bulk case. (*35, 37*) Such an ordering of water near the interface decreases its dielectric constant and favors ion pairing from an entropic perspective. Further, for NPC with a very large surface area and a very high surface to volume ratio, a large fraction of water molecules in the solution would be consumed in the interfacial layer effectively increasing the concentration of the remaining core solution. As such the Zn^{2+} ions are less hydrated, lowering the free energy barrier for Cl^- ion penetration into the first shell and enhancing contact ion pairing. As Cl^- ions start penetrating the first coordination shell the overall symmetry changes towards more tetrahedral. Having said that, even for the NPC with very high specific surface area (2000 m^2/g) it is less probable for the core solution concentration to reach such high values (≈ 10 m) that are needed to explain the observed change in VTC spectra when compared to the bulk solution. (See SI section 1 for an estimate) Also, nanoporous carbons are in general hydrophobic and formation of layers of water on the interface is less probable. In regard to the electrochemical results, the observed increase in EVW with confinement is counterintuitive considering the formation of water layer at the interface. With water at the interface, the EVW would not be expected to increase owing to the availability of water to be broken down at the interface during charge transfer. (*22*) Thus, this model generally does not support the observed change in the EVW of electrolyte under nanoconfinement.

Second, hydrophobicity or other considerations could favor adsorption of Zn^{2+} ions to the surface of the carbon nanopores. Enhanced Zn^{2+} ion adsorption and changing symmetry towards more tetrahedral coordination has been reported previously with aqueous Zn^{2+} solution in porous silica material. (*36*) The solvation energy of cations is reduced due to the decrease in dielectric constant of water under nanoconfinement. This in turn increases the affinity for cation adsorption to surface sites because of the decrease in the positive contribution of solvation free energy change to the overall adsorption free energy change. (*36*) Similar argument can be made for enhanced ion pairing in those adsorbed cations, in which case, the diminished desolvation barrier of cations effectively amplifies the cation-anion interaction and thus promotes contact ion pairing. Further, the very low dependence of average coordination (N_{Cl}) on the concentration of the confined solution (Figure 4) is nicely consistent with a Zn-adsorption model. Given the large surface area of the NPC material, all of the Zn^{2+} ions could potentially be adsorbed on the pore surface and saturated with Cl^- coordination at all concentrations studied. The surface area density of the NPC does suffice to adsorb all Zn^{2+}, even for 10 m solution, if in fact this is energetically favored, see SI section 2. Further, the presence of a layer of adsorbed Zn^{2+} and coordinated anions and the decreased availability of water near the carbon surface can reasonably be expected to introduce additional overpotential for the hydrogen and oxygen evolution reactions, which in turn increase the EVW of the aqueous electrolyte as observed here for the NPC samples.

Third, fully independent of the details of interfacial effects, we ask about the role of confinement by itself. Under nanoconfinement, water has a reduced degree of freedom and is more ordered, and thus the dielectric constant of water is greatly reduced. (*47-49*) As such, one expects a lowered desolvation barrier and consequently an enhanced affinity for ion pairing between cations and anions. It has been proposed that nanoconfinement effectively shifts the free energy of ion-pair dissociation towards positive values, and massive ion-pairing is favored as a consequence. (*50*) Such a change in the energetics of ion pairing under nanoconfinement could explain the substantial enhancement in ion pairing that is seen for the NPC, especially in the low concentration range. Moreover, while not definitive, this model is broadly consistent with the findings from the EVW measurements. In the case of WiSE electrolytes in bulk, it has been proposed that the EVW of the electrolyte is positively correlated with the extent of ion pairing in the electrolyte. (*8-11, 42*) Therefore, a similar pattern observed in the nanoconfined scenario might be linked to the same underlying phenomenon.

Our study provides valuable quantitative insights into the influence of nanoconfinement on ion pairing behavior in aqueous $ZnCl_2$ electrolytes and reveals several avenues for future exploration. While the precise origin of the enhanced ion pairing in the context of nanoporous carbon (NPC) remains elusive, our findings suggest that a significant portion of this augmentation can be attributed to the interplay of two factors: nanoconfinement-related effects and the mechanisms associated with Zn-ion adsorption at the interface. Future research should delve deeper into these mechanisms, employing advanced techniques to unravel the specific interactions and surface phenomena governing ion pairing within confined spaces.

Following the observation of enhanced ion pairing under nanoconfinement, further studies are warranted to explore the pore-size dependence of ion pairing within the nanopores. Understanding how ion pairing evolves with varying extent of confinement can elucidate size-specific behaviors and provide a comprehensive understanding of ion pairing under confinement for practical applications.

On the other hand, building on the positive correlation observed between ion pairing and the size of the EVW, future work should explore the practical implications of this relationship.

Investigating the impact of enhanced EVW on the performance of nanostructured electrodes in electrochemical storage devices can guide the design of next-generation energy storage technologies.

Moreover, expanding our understanding of nanoconfinement effects to other electrolytes and confining surfaces is imperative. Investigating diverse electrolytes and their respective ion pairing behaviors under nanoconfinement within various confining surfaces can provide a comprehensive view, enabling the development of versatile electrochemical systems.

Thus, our study lays the groundwork for future investigations into the interplay between nanoconfinement, ion pairing, and EVW in aqueous electrolytes. By addressing these research directions, we aim to contribute to the broader understanding of confinement effects on electrolyte behavior and advance the design principles for high-performance energy storage devices.

7.5: Conclusions

We performed X-ray spectroscopy experiments to study the effect of nanoconfinement on the ion pairing behavior of aqueous $ZnCl_2$ electrolytes. Ion pairing was quantified by extracting the average number of Cl^- ions coordinated to each Zn^{2+} ion in the solution (N_{Cl}). Ion pairing was highly enhanced under nanoconfinement compared to bulk in all cases, but interestingly, the extent of ion pairing (N_{Cl}) inside the nanopores is independent of the concentration of the solution used in this study. Finally, we compared the EVW of the electrolytes in contact with NPC electrodes (nanoconfined) and glassy carbon electrodes (bulk) to the corresponding extent of ion pairing expressed as N_{Cl}. A positive correlation was seen between the extent of ion pairing and the size of EVW in each case. Different physical mechanisms were explored to understand the observed enhancement in ion pairing and EVW inside the nanopores. Our data suggested nanoconfinement effects and enhanced Zn adsorption at the interface to be the major contributors for the observed enhancements. These results provide useful insights into the extent of the effects of nanoconfinement on the local structure of cation coordination complexes in aqueous solutions and further demonstrate the value of VTC-XES in the context of coordination chemistry studies. The correlation between N_{Cl} and EVW in both cases aligns with the WiSE concept of enhanced EVW with increased ion pairing and also supports the idea of EVW enhancement in aqueous electrolytes through the use of nanostructured electrodes. Moreover, it may inspire further research in fully understanding the mechanisms responsible for EVW enhancement in aqueous electrolytes and help design next-generation electrochemical storage devices.

7.6: Acknowledgements

This work was supported by the Joint Center for Energy Storage Research (JCESR), an Energy Innovation Hub funded by the U.S. Department of Energy (DOE). This research used resources of the Advanced Photon Source, an Office of Science User Facility operated for the DOE Office of Science by Argonne National Laboratory and was supported by the U.S. DOE under contract no. DE-AC02-06CH11357.

7.7: References

1. G. E. Brown Jr, G. Calas, Mineral-aqueous solution interfaces and their impact on the environment. *Geochemical Perspectives* **1**, 483-484 (2012).
2. M. Tait, F. Franks, Water in biological systems. *Nature* **230**, 91-94 (1971).
3. F. Joó, *Aqueous organometallic catalysis*. (Springer Science & Business Media, 2006), vol. 23.
4. J. O. G. Posada *et al.*, Aqueous batteries as grid scale energy storage solutions. *Renewable and Sustainable Energy Reviews* **68**, 1174-1182 (2017).
5. W. Liu, S. Borg, B. Etschmann, Y. Mei, J. Brugger, An XAS study of speciation and thermodynamic properties of aqueous zinc bromide complexes at 25–150°C. *Chemical Geology* **298-299**, 57-69 (2012).

6. Y. Mei *et al.*, Zinc complexation in chloride-rich hydrothermal fluids (25–600°C): A thermodynamic model derived from ab initio molecular dynamics. *Geochimica et Cosmochimica Acta* **150**, 265-284 (2015).
7. P. Dreier, P. Rabe, EXAFS-Study of the Zn2+ Coordination in Aqueous Halide Solutions. *J. Phys. Colloques* **47**, 809-812 (1986).
8. X. Ji, A perspective of ZnCl2 electrolytes: The physical and electrochemical properties. *eScience* **1**, 99-107 (2021).
9. C. Zhang *et al.*, A ZnCl2 water-in-salt electrolyte for a reversible Zn metal anode. *Chemical Communications* **54**, 14097-14099 (2018).
10. L. Zhang *et al.*, ZnCl2 "Water-in-Salt" Electrolyte Transforms the Performance of Vanadium Oxide as a Zn Battery Cathode. *Advanced Functional Materials* **29**, 1902653 (2019).
11. C. Zhang *et al.*, The electrolyte comprising more robust water and superhalides transforms Zn-metal anode reversibly and dendrite-free. *Carbon Energy* **3**, 339-348 (2021).
12. N. Rampal *et al.*, Local molecular environment drives speciation and reactivity of ion complexes in concentrated salt solution. *Journal of Molecular Liquids* **340**, 116898 (2021).
13. H. W. Wang *et al.*, Countercations Control Local Specific Bonding Interactions and Nucleation Mechanisms in Concentrated Water-in-Salt Solutions. *Journal of Physical Chemistry Letters* **10**, 3318-3325 (2019).
14. H. W. Wang, K. Yuan, N. Rampal, A. G. Stack, Solution and Interface Structure and Dynamics in Geochemistry: Gateway to Link Elementary Processes to Mineral Nucleation and Growth. *Crystal Growth & Design* **22**, 853-870 (2022).
15. J. Brugger *et al.*, Probing ore deposits formation: New insights and challenges from synchrotron and neutron studies. *Radiation Physics and Chemistry* **79**, 151-161 (2010).
16. L. Liu, Y. Qiao, X. Chen, Pressure-driven water infiltration into carbon nanotube: The effect of applied charges. *Applied Physics Letters* **92**, 101927 (2008).
17. M. A. Shannon *et al.*, Science and technology for water purification in the coming decades. *Nature* **452**, 301-310 (2008).
18. J. Livage, Sol–gel synthesis of heterogeneous catalysts from aqueous solutions. *Catalysis Today* **41**, 3-19 (1998).
19. J. C. Luo *et al.*, Distinctive Trend of Metal Binding Affinity via Hydration Shell Breakage in Nanoconfined Cavity. *Journal of Physical Chemistry C* **123**, 14825-14833 (2019).
20. N. Hassan, Catalytic performance of nanostructured materials recently used for developing fuel cells' electrodes. *International Journal of Hydrogen Energy* **46**, 39315-39368 (2021).
21. Z. Shariatinia, in *Nanobatteries and Nanogenerators*. (Elsevier, 2021), pp. 221-292.
22. B. S. Chava, Y. B. Wang, V. S. Sivasankar, S. Das, Water-free Localization of Anion at Anode for Small-Concentration Water-in-Salt Electrolytes Confined in Boron-Nitride Nanotube. *Cell Reports Physical Science* **1**, 100246 (2020).
23. D. Mattia, Y. Gogotsi, Review: static and dynamic behavior of liquids inside carbon nanotubes. *Microfluidics and Nanofluidics* **5**, 289-305 (2008).
24. R. B. Schoch, J. Y. Han, P. Renaud, Transport phenomena in nanofluidics. *Reviews of Modern Physics* **80**, 839-883 (2008).
25. M. Whitby, N. Quirke, Fluid flow in carbon nanotubes and nanopipes. *Nature Nanotechnology* **2**, 87-94 (2007).

26. X. Chen, F. B. Surani, X. G. Kong, V. K. Punyamurtula, Y. Qiao, Energy absorption performance of steel tubes enhanced by a nanoporous material functionalized liquid. *Applied Physics Letters* **89**, 241918 (2006).
27. J. A. Thomas, A. J. H. McGaughey, Density, distribution, and orientation of water molecules inside and outside carbon nanotubes. *Journal of Chemical Physics* **128**, 084715 (2008).
28. M. C. Gordillo, J. Marti, Hydrogen bond structure of liquid water confined in nanotubes. *Chemical Physics Letters* **329**, 341-345 (2000).
29. J. Wang, Y. Zhu, J. Zhou, X. H. Lu, Diameter and helicity effects on static properties of water molecules confined in carbon nanotubes. *Physical Chemistry Chemical Physics* **6**, 829-835 (2004).
30. A. Parsegian, Energy of an ion crossing a low dielectric membrane: solutions to four relevant electrostatic problems. *Nature* **221**, 5183 (1969).
31. Q. Shao *et al.*, Molecular simulation study of temperature effect on ionic hydration in carbon nanotubes. *Physical Chemistry Chemical Physics* **10**, 1896-1906 (2008).
32. L. Liu, X. Chen, T. Kim, A. J. Han, Y. Qiao, Effects of anion size and concentration on electrolyte invasion into molecular-sized nanopores. *New Journal of Physics* **12**, 033021 (2010).
33. T. Ohkubo *et al.*, Restricted hydration structures of Rb and Br ions confined in slit-shaped carbon nanospace. *Journal of the American Chemical Society* **124**, 11860-11861 (2002).
34. W. Y. Tsai, P. L. Taberna, P. Simon, Electrochemical Quartz Crystal Microbalance (EQCM) Study of Ion Dynamics in Nanoporous Carbons. *Journal of the American Chemical Society* **136**, 8722-8728 (2014).
35. Q. Wang *et al.*, Coordination variation of hydrated Cu2+/Br1- ions traversing the interfacial water in mesopores. *AIP Advances* **2**, 022107 (2012).
36. J. Nelson, J. R. Bargar, L. Wasylenki, G. E. Brown, K. Maher, Effects of nano-confinement on Zn(II) adsorption to nanoporous silica. *Geochimica Et Cosmochimica Acta* **240**, 80-97 (2018).
37. M. C. F. Wander, K. L. Shuford, Molecular Dynamics Study of Interfacial Confinement Effects of Aqueous NaCl Brines in Nanoporous Carbon. *Journal of Physical Chemistry C* **114**, 20539-20546 (2010).
38. Y. S. Chen, J. L. Fulton, W. Partenheimer, A XANES and EXAFS study of hydration and ion pairing in ambient aqueous MnBr2 solutions. *Journal of Solution Chemistry* **34**, 993-1007 (2005).
39. J. L. Fulton, S. M. Heald, Y. S. Badyal, J. M. Simonson, Understanding the effects of concentration on the solvation structure of Ca2+ in aqueous solution. I: The perspective on local structure from EXAFS and XANES. *Journal of Physical Chemistry A* **107**, 4688-4696 (2003).
40. M. M. Hoffmann, J. G. Darab, B. J. Palmer, J. L. Fulton, A transition in the Ni2+ complex structure from six- to four-coordinate upon formation of ion pair species in supercritical water: An X-ray absorption fine structure, near-infrared, and molecular dynamics study. *Journal of Physical Chemistry A* **103**, 8471-8482 (1999).
41. D. Dhakal *et al.*, The evolution of solvation symmetry and composition in Zn halide aqueous solutions from dilute to extreme concentrations. *Physical Chemistry Chemical Physics* **25**, 22650-22661 (2023).

42. L. M. Suo *et al.*, "Water-in-salt" electrolyte enables high-voltage aqueous lithium-ion chemistries. *Science* **350**, 938-943 (2015).
43. E. P. Jahrman *et al.*, An improved laboratory-based x-ray absorption fine structure and x-ray emission spectrometer for analytical applications in materials chemistry research. *Review of Scientific Instruments* **90**, 024106 (2019).
44. D. R. Mortensen *et al.*, Benchmark results and theoretical treatments for valence-to-core x-ray emission spectroscopy in transition metal compounds. *Physical Review B* **96**, 125136 (2017).
45. W. Liu, B. Etschmann, G. Foran, M. Shelley, J. Brugger, Deriving formation constants for aqueous metal complexes from XANES spectra: Zn2+ and Fe2+ chloride complexes in hypersaline solutions. *American Mineralogist* **92**, 761-770 (2007).
46. S. P. Dagnall, D. N. Hague, A. D. Towl, X-ray diffraction study of aqueous zinc (II) nitrate. *Journal of the Chemical Society, Faraday Transactions 2: Molecular and Chemical Physics* **78**, 2161-2167 (1982).
47. H. Itoh, H. Sakuma, Dielectric constant of water as a function of separation in a slab geometry: A molecular dynamics study. *Journal of Chemical Physics* **142**, 184703 (2015).
48. C. Zhang, Note: On the dielectric constant of nanoconfined water. *Journal of Chemical Physics* **148**, 156101 (2018).
49. H. C. Zhu *et al.*, Investigation of dielectric constants of water in a nano-confined pore. *RSC Advances* **10**, 8628-8635 (2020).
50. J. Huang, Confinement Induced Dilution: Electrostatic Screening Length Anomaly in Concentrated Electrolytes in Confined Space. *Journal of Physical Chemistry C* **122**, 3428-3433 (2018).

7.8: Supplementary Information

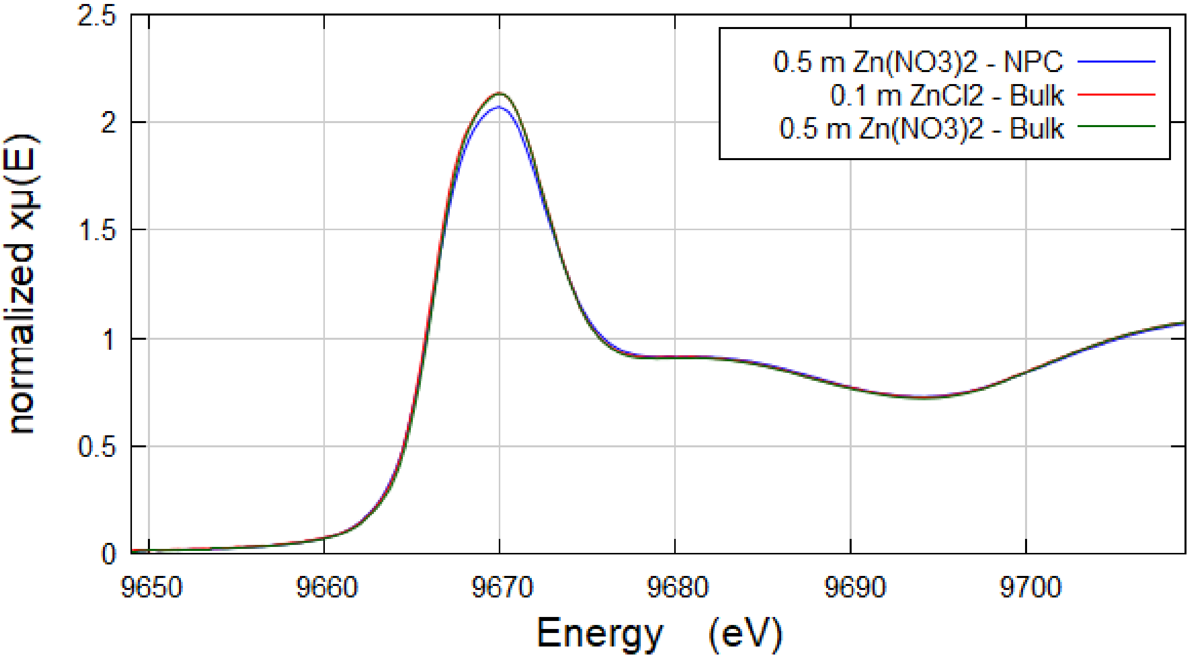

Figure SI-1: Comparison between the XANES spectra for the low concentration Zn solution (octahedral endpoint) in bulk and inside nanopores.

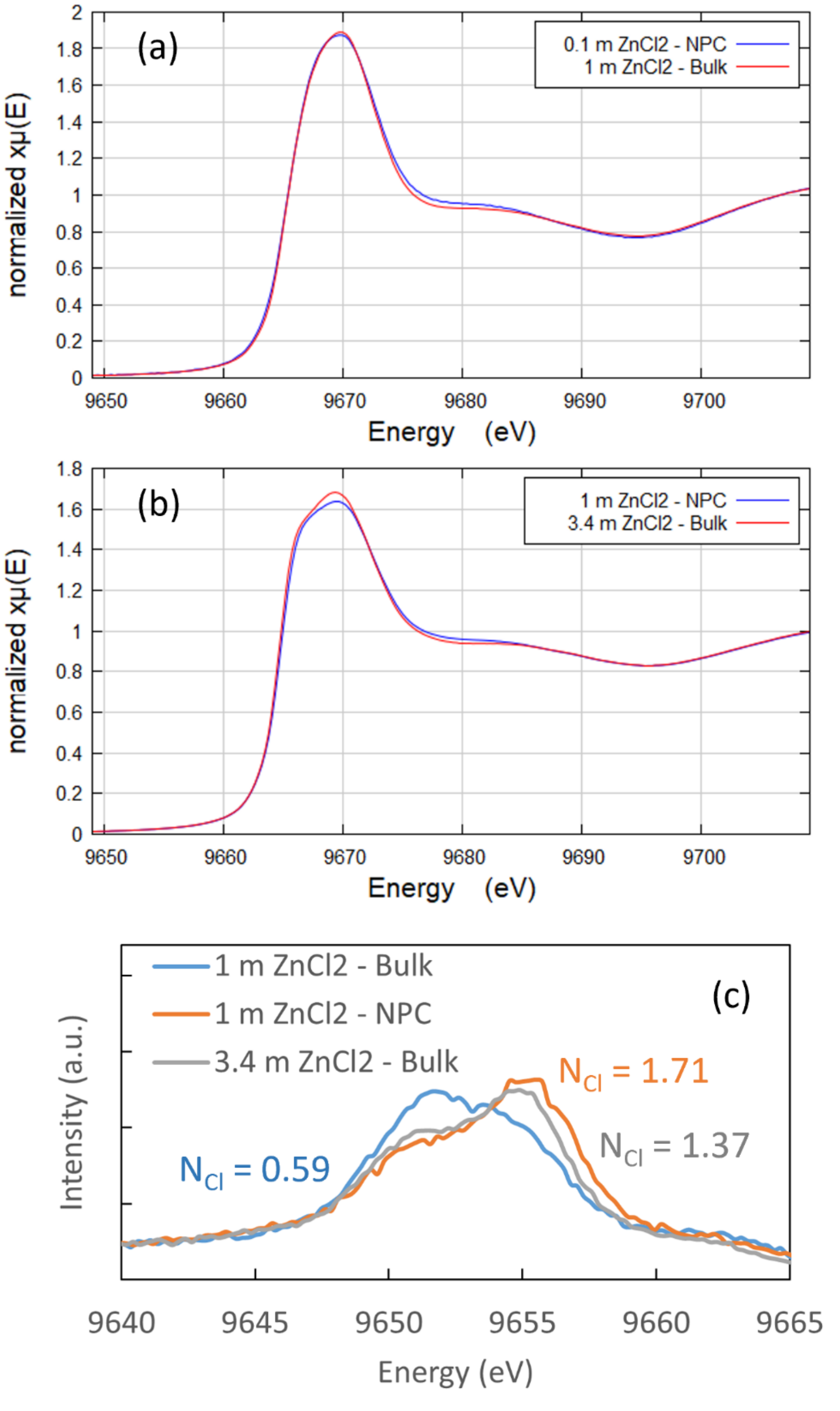

Figure SI-2: Comparison of spectra for lower concentration samples confined in nanopores to those of higher concentration samples in bulk, as indicated in the legends. (a) and (b) XANES and (c) VTC-XES.

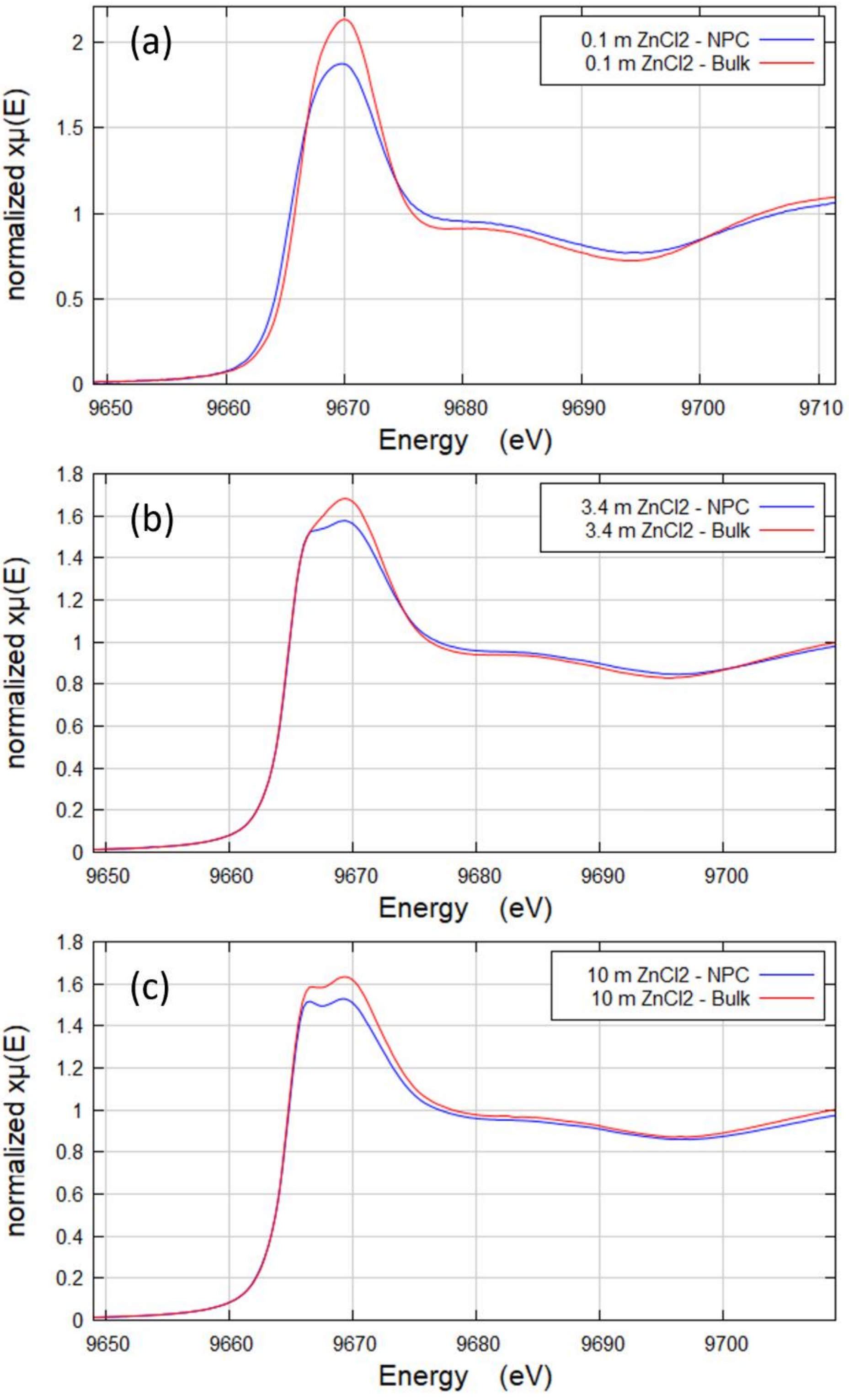

Figure SI-3: Comparison of the XANES spectra between bulk and nanoconfined cases for aqueous solutions with different $ZnCl_2$ concentrations as indicated in the legends.

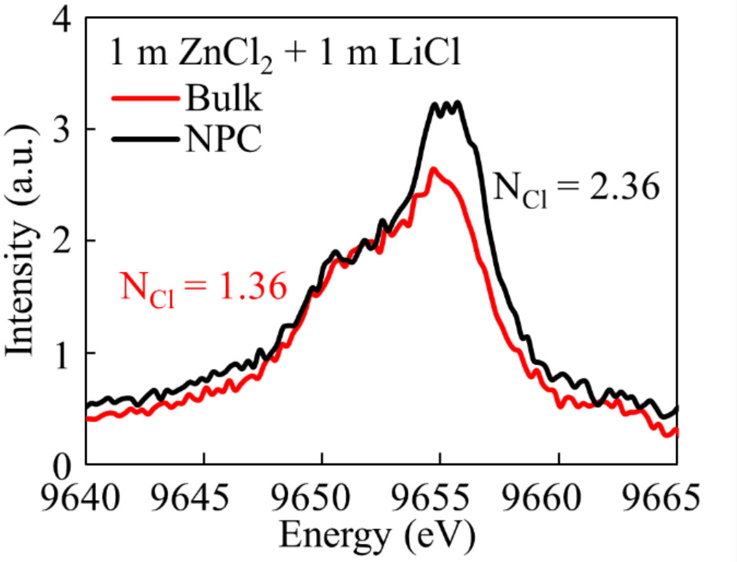

Figure SI-4: VTC spectra of 1m $ZnCl_2$ + 1m LiCl solutions in bulk and inside nanopores (NPC).

Section SI-1: Calculation for the area needed for water adsorption on carbon surface.

Following similar procedure and assumption as for the Zn^{2+} adsorption case (see section SI-2 below), for a 1 molal $ZnCl_2$ solution:

Total number of water molecules in the volume 'V_p' = 9.35×10^{22} g^{-1}

Area needed for adsorption per water molecule = 5.24×10^{-20} m^2

Number of water molecules that can be adsorbed in the available area (i.e., 2000 m^2/g) = 3.82×10^{22} g^{-1}

Which means, about 40% of the total water molecules can be adsorbed in the available surface area (2000 m^2/g). With this much water molecules adsorbed, the concentration of an initially 1 molal $ZnCl_2$ solution becomes about 1.7 molal, much lower than what is needed to explain the changes in VTC XES spectra (≈10 m).

Section SI-2: Calculations for the area needed for Zn^{2+} adsorption on carbon surface.

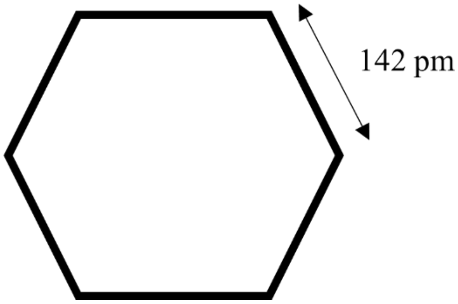

Figure SI-5: Hexagonal unit cell of graphite with sides 142 pm.

Consider a hexagonal unit cell on a graphite surface as shown in Figure SI-5. Each vertices have a carbon atom and each of them are shared by two other neighboring cells in a crystal. Thus, there are 2 carbon atoms per cell.

Assuming that Zn^{2+} ions are not adsorbed to adjacent carbon atoms, there can be a maximum of 1 Zn^{2+} ion adsorbed per cell.

Then the area required to adsorb 1 Zn^{2+} ion is the same as the area of the hexagonal cell.

Area of the hexagonal cell (a) = 5.24×10^{-20} m^2

Packing density (ρ) = 0.3 g/cc (provided by supplier for NPC)

Absolute density (ρ_a) = 2.1 g/cc (for amorphous carbon material)

Porosity (P) = 1 – (0.3/2.1) = 0.85

Total volume/mass (V)= $1/\rho$ = 3.33 cc/g

Total pore-volume/mass (V_p) = P x V = 0.85 x 3.33 cc/g = 2.83 cc/g

For a 'm' molal $ZnCl_2$ solution, the total number of Zn^{2+} ions in a unit volume of the solution is approximately given by:

$n_m = m \times 6.02 \times 10^{23} \times 10^{-3}\ cc^{-1}$

Then, for a 1 molal $ZnCl_2$ solution, the total number of Zn^{2+} ions in a volume 'V_p' of the solution is given by (assuming all the pore volume is filled with solution):

$n_1 = 1 \times 6.02 \times 10^{23} \times 10^{-3}\ cc^{-1} \times V_p$

$= 1.7 \times 10^{21}\ g^{-1}$

Similarly, for a 10 molal $ZnCl_2$ solution, the total number of Zn^{2+} ions in a volume 'V_p' of the solution is given by (assuming all the pore volume is filled with solution):

$n_{10} = 10 \times 6.02 \times 10^{23} \times 10^{-3}\ cc^{-1} \times V_p$

$= 1.7 \times 10^{22}\ g^{-1}$

Total area needed to adsorb 'n_1' number of Zn^{2+} ions is given by:

$A_1 = n_1 \times A_{Zn} = 1.7 \times 10^{21}\ g^{-1} \times 5.24 \times 10^{-20}\ m^2 = 89.1\ m^2/g$

Total area needed to adsorb 'n_{10}' number of Zn^{2+} ions is given by:

$A_{10} = n_{10} \times A_{Zn} = 1.7 \times 10^{22}\ g^{-1} \times 5.24 \times 10^{-20}\ m^2 = 891\ m^2/g$

For NPC, the specific surface area (A_{NPC}) = 2000 m^2/g (provided by supplier)

Since, $A_{NPC} > A_{10}$, all the Zn^{2+} ions can in principle be adsorbed to the surface even for the highest concentration (10 m) solution.

Chapter 8: Quantifying Temperature Effect on the Evolution of Ion Pairing in Aqueous Zn-Cl System Using Valence-to-Core X-ray Emission Spectroscopy

This chapter is based on a manuscript under preparation with the following authors:
Diwash Dhakal, Timothy T. Fister, John L. Fulton, Gerald T. Seidler.

8.1: Abstract

Temperature plays a vital role in the physical and chemical properties of aqueous solutions and bears great importance in the transport of ions and the formation of geological ore deposits from hydrothermal brines. As such, it is imperative to understand the effect of temperature on the properties of aqueous solutions. In this study, we use a recently developed valence-to-core X-ray emission spectroscopy (VTC-XES) method (Dhakal, *et al.*, 2023) to quantify the effect of temperature on the local coordination of Zn^{2+} ions in aqueous Zn-Cl solutions. We study these solutions at fixed 1-m Zn^{2+} ion concentration and varying Cl^- ion concentration up to 12 molal and find that ion pairing is enhanced in elevated-temperature solutions compared to their ambient counterparts. We observe a roughly linear trend in the enhancement of ion pairing with increasing temperature from 25 °C to 135 °C. Comparison of our results to standard theoretical prediction and published work emphasizes the inadequacy of extrapolations based on the dilute limit formation constants. Our results further demonstrate the utility of the VTC-XES method for solution phase ion coordination studies up to the high-concentration region, with much simplified analysis compared to the more commonly used extended x-ray absorption fine structure.

8.2: Introduction

Understanding the physical and chemical properties of aqueous electrolytes is vital to the development of many advanced technologies including energy storage devices, (*1*) advanced filtration systems (*2*) and catalysts (*3*), in addition to the central relevance for ion transport and ore formation in geothermal systems. (*4-6*) The properties of such aqueous electrolytes are defined primarily by the character of dissolved ions and their resulting equilibrium structure in the solution. (*4, 7*) As such, comprehensive knowledge of the atomic-scale structure in solutions aids in the development and optimization of advanced processes pertaining to hydrometallurgy, materials synthesis and corrosion. (*6, 8-10*) The structure of solutions is a complicated problem that is seeing increased contemporary interest. Complete dissociation with at most weak cation-anion coordination at low concentrations and precipitation above the solubility threshold are each generic, but the intermediate states, and especially intermediate high-concentration states, give more varied behavior. (*4, 6, 11, 12*) In the arena of advanced electrolyte systems, such as Water-in-Salt Electrolytes (WiSE) and ionic liquids, the phenomenon of contact ion pairing becomes increasingly prominent, presenting deviations from the behavior observed at low concentrations. (*13-15*) In this context, ionic liquids and WiSE, characterized by their higher concentration regimes, introduce new challenges and opportunities, necessitating a comprehensive understanding of ion pairing and solvation structures. The motivation for this study lies in unraveling the intricacies of these high-concentration states for a comprehensive understanding of such aqueous solutions and providing essential insights for the advancement of electrolyte technologies.

To that end, aqueous Zn-Cl serves as a model system to study the evolution of coordination structures owing to its high solubility and the complicated question of coexistence and relative thermodynamic stability of its several different metal complexes, which are shown in Figure 1. The ion association behavior of this system serves as an important testing ground for numerous theoretical approaches, which often give divergent predictions, while also being immediately relevant to the formation and transport of Zn deposits in hydrothermal brines. (*4, 5, 16*)

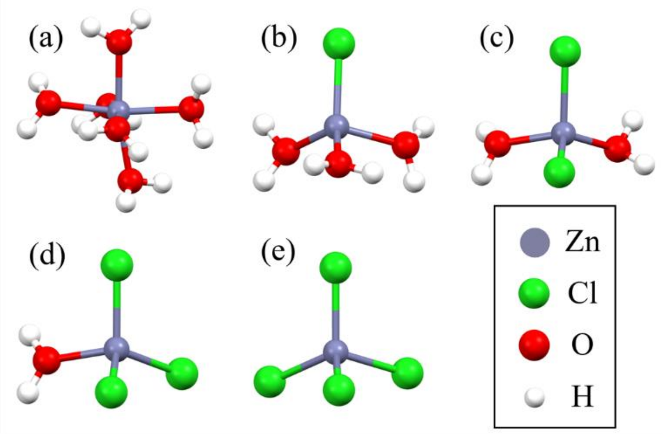

Figure 1: DFT-optimized Zn^{2+} coordination structures for (a) $Zn(H_2O)_6^{2+}$, (b) $ZnCl(H_2O)_3^+$, (c) $ZnCl_2(H_2O)_2$, (d) $ZnCl_3(H_2O)^-$, (e) $ZnCl_4^{2-}$. (used from Dhakal, *et al.* (*17*))

As ion pairing is well outside of the regime where dilute-limit treatments like Debye-Huckel should be applicable, empirical methods have instead seen considerable use in studies of more concentrated aqueous systems. (*5, 18-21*) The widely used solubility-based chemical equilibrium approach relies on fitting of the observed solubilities of salts to a set of coupled equilibrium reactions between the dissolution of salts and the formation of various aqueous metal complexes. However, the difficulty in resolving the contribution of each of the metal complexes to the overall solubility results in large uncertainties in any extracted formation constants. (*4, 22*) Consequently, the speciation results are also skewed. For example, Ruaya and Seward (*18*) provided the formation constants for Zn complexes based on the measured temperature-dependent solubility of AgCl. Their results are thus contingent upon the reliability of the properties of Ag–Cl complexes, which have been revised over time, (*23, 24*) as well as the overall reliability of the extrapolation across different chemistries which can have different ion pairing behavior. The same limitations are true for other, related approaches. For example, Bourcier and Barnes (*5*) measured the solubilities of ZnO and $ZnCO_3$ (100 °C and 350 °C) in 0-5 m NaCl solutions and Wesolowski, *et al*., (*21*) measured the solubility of ZnO in acidic solutions and extracted the formation constants for $ZnCl^+$ and $ZnCl_2$(aq) at 200 °C. These solubility-based studies generally agree on the value of formation constant for the $ZnCl_2$(aq) complex, but the formation constants for other species ($ZnCl^+$, $ZnCl_3^-$ and $ZnCl_4^{2-}$) greatly differ. (*5, 18, 20*) As a result, the speciation distribution predicted from these studies vary in important aspect: some of them predict predominant $ZnCl_4^{2-}$ over a wide range of temperatures in Cl-rich solutions (*18, 20*) while others suggest $ZnCl_3^-$ to be the predominant species at higher temperatures. (*5, 25*)

On the other hand, the structure of metal complexes in solutions can also be interrogated using spectroscopic methods without reference to thermodynamic coefficients. It is interesting that the speciation obtained from such studies differs significantly from that inferred from the solubility studies mentioned earlier. Multiple studies using X-ray absorption spectroscopy (*19, 26-29*) or Raman spectroscopy (*30*) conclude that $ZnCl_4^{2-}$ dominates in highly saline solutions from ambient to high temperatures. Liu, *et al*., (*26*) also confirmed similar results for $ZnBr_2$ solutions up to 150 °C. Moreover, Mei, *et al*., (*4*) combined *ab initio* MD simulations with X-ray absorption fine structure (XAFS) measurement to determine Zn-complexation in Cl rich solutions up to 600 °C and concluded $ZnCl_4^{2-}$ to be the dominant specie over a wide range of temperatures.

More recently, valence-to-core x-ray emission spectroscopy (VTC-XES), combined with TD-DFT calculations, was used by the present authors to again show that $ZnCl_4^{2-}$ (or $ZnBr_4^{2-}$) is the dominant species at high halide concentrations at ambient temperature. (*17*) VTC-XES measures the energy spectrum of the occupied molecular orbitals of the metal complex to fingerprint the local symmetry and, with some limitations, to determine the average Cl^- ion coordination number per Zn^{2+} ion. VTC-XES differs from XAFS in its extreme locality: while second shell effects must be carefully modeled for XAFS analysis in concentrated solutions, the second shell occupation has almost no effect on the VTC-XES spectrum. (*17*)

Here, we extend our prior VTC-XES study (*17*) to explore the effects of temperature up to 135 °C on the evolution of coordination symmetry and composition in 1 m $ZnCl_2$ solution with added LiCl to tune the anion activity. We find that the extent of ion pairing is enhanced in a linear fashion with the increase in temperature of the solution and that the enhancement is more prominent at lower overall concentrations than at higher. We compare our results with the predictions from standard dilute-limit theoretical model and prior work and discuss the implications. This study further demonstrates the potential of VTC-XES method for solution phase ion-coordination studies, exactly because the spectroscopy stands on its own without reference to inferred or calculated formation constants.

8.3: Methods

8.3.1: Sample solutions

Required amounts of powder $Zn(TFMS)_2$, $ZnCl_2$ and LiCl were weighed and dissolved in HPLC grade water to make aqueous solutions with various concentrations. All reagents were purchased from standard vendors (Alfa-Aesar, Fisher Scientific, etc.) in 99.9% purity or higher and were used without further purification. The solutions were degassed by bubbling He gas for about 30 minutes and then immediately loaded into a thin-walled poly ether ether ketone (PEEK) tube cell custom designed for XES measurements (see details in SI). About 10% air space was left to accommodate the volume expansion of water at higher temperatures.

8.3.2: Temperature control

Temperature of the sample cell was controlled using a customized heat-exchange setup. It employs a heat-transfer fluid that is temperature controlled in a heater bath placed outside the spectrometer. Temperature of the sample cell was monitored throughout the experiments with two K-type thermocouples touching the sample cell and remained within +/-1 °C of the set temperature. See SI for further details.

8.3.3: X-ray emission spectroscopy

Zn K-edge XES spectra were collected to include the Kβ and the VTC emission regions. Each scan was collected over the energy range 9550 – 9700 eV in 0.25 eV steps with an integration time of 4 secs around the Kβ peak (9550 – 9620 eV) and 40 secs around the VTC region (9620 – 9700 eV). Multiple scans were collected for each sample and were added to get the final spectrum that has a high signal-to-noise ratio even at the VTC region that has about 100 times less counts compared to the Kβ peak maximum. The energy position and shape of the Kβ emission feature remained invariant in the concentration and temperature range explored in this study. The Kβ emission feature was thus used for normalization between the individual samples to get to mole normalized spectra, which were then compared and analyzed to extract information about Zn-ion coordination geometry, coordination number and identity of the coordinated ligands. In brief, this involves using the end point spectra to perform a linear combination analysis (LCA) of all the other spectra collected as a function of Cl^- ion concentration and temperature. This provides us with the octahedral and tetrahedral contributions in each of the VTC spectra. Then, this fractional contribution is used to arrive at a more quantitative measure of ion pairing, the average number of Cl^- ions coordinated per Zn^{2+} ion (henceforth N_{Cl}). See Dhakal, *et al.*, (*17*) for a detailed description of the analysis procedure and estimation of errors where we have successfully used this approach for similar study under ambient conditions.

8.4: Results and Discussion

Figure 1 shows the DFT-optimized Zn^{2+} coordination structures for various Zn-complexes in a Zn-Cl aqueous system. Zn^{2+} exists in various coordinations in aqueous Zn-Cl solutions ranging from an octahedral coordination with six water molecules (a) to tetrahedral coordination with varying number of Cl^- ions and water molecules (b – e) in Figure 1. The octahedral coordination is generally favored in cases where the ion activity is low, i.e., in the dilute limit. As the anion activity increases, whether due to, e.g., greater anion concentration or higher solution temperature, Cl^- ions start forming contact-ion pairs with Zn^{2+} in the first coordination shell. (*4, 18*) While the chemical progression is complicated, steadily more Cl^- ions coordinate with the Zn^{2+} as the Cl^- ion activity is increased, finally saturating with tetrahedral complex coordinated with four Cl^- ions (Figure 1 (e)). It is important to note that as soon as a single Cl^- ion pairs with Zn^{2+} the overall coordination geometry changes from octahedral to tetrahedral and remains tetrahedral. (*4, 17*)

Our goal is to assess the changing Zn^{2+} coordination as a function of temperature and Cl^- ion concentration. To this end, we first establish endpoint behavior which then allows us to do meaningful spectral analysis following the procedure described in Dhakal, *et al.*, (*17*) for similar solutions in ambient conditions.

In Figure 2 (a) we present the experimental VTC-XES spectra for 1 m $Zn(TFMS)_2$ aqueous solution and for a 1 molal $ZnCl_2$ with 10 m LiCl aqueous solution at 25 °C. Clearly, the two spectra have distinct features with a broad peak centered around 9652 eV for the former in contrast to a more intense peak centered around 9656 eV with a lower – energy shoulder peak around 9650 eV for the latter. In our previous study, (*17*) we have shown that these features can be attributed to Zn^{2+} in octahedral coordination with six water molecules and in tetrahedral coordination with four Cl^- ions, respectively. As such these spectra represent the end points (Figure 1 (a) and (e)) in the series of possible Zn^{2+} complexes in aqueous Zn-Cl system, shown in Figure 1.

Further, in Figure 2 (b) and (c), we present the VTC spectra for these end point complexes as a function of temperature, ranging from 25 °C to 135 °C. It can be noticed that the spectra for both species remains invariant in the given temperature range. It is important to establish this invariance because these spectra will represent the end point species in subsequent spectral analysis of the set of VTC spectra as a function of composition and temperature. Moreover, the invariance of the VTC spectra for the 1 m $ZnCl_2$ + 10 m LiCl sample with temperature further supports the validity of the hypothesis that the tetrahedral coordination is saturated with four Cl^- ions even at 25 °C for this composition.

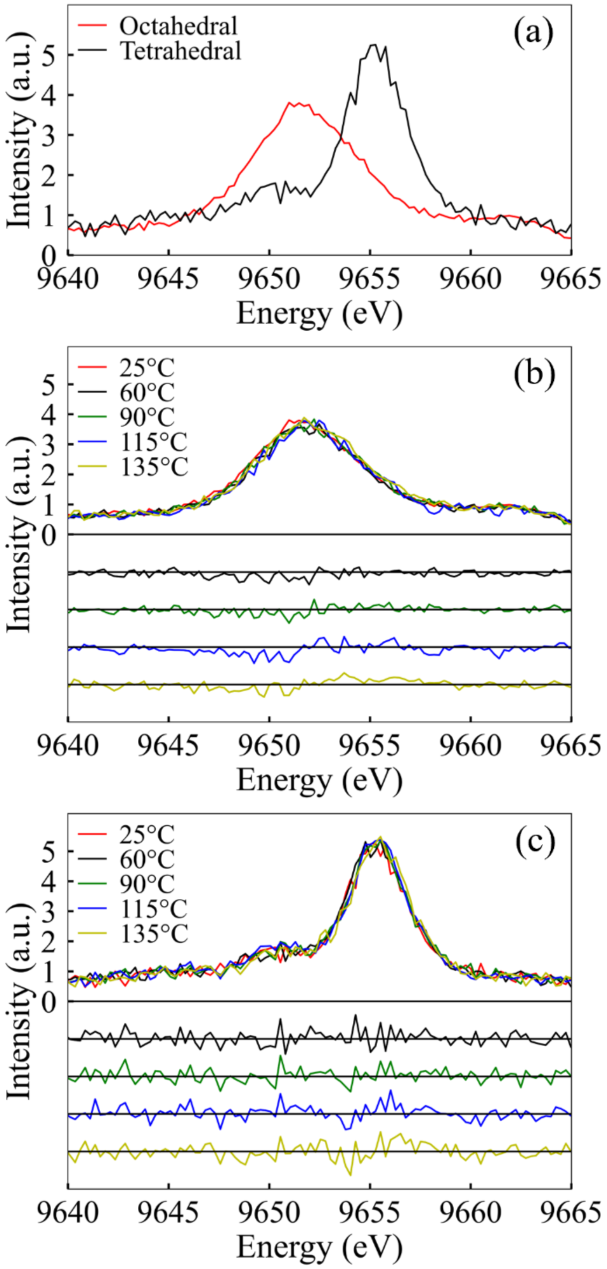

Figure 2: VTC-XES spectra for (a) 1 m Zn(TFMS)$_2$ (octahedral endpoint) and, 1 m ZnCl$_2$ + 10 m LiCl (tetrahedral endpoint) at 25 °C, (b) 1 m Zn(TFMS)$_2$ as a function of temperature and, (c) 1 m ZnCl$_2$ + 10 m LiCl as a function of temperature. The residuals shown in (b) and (c) are the difference between the spectrum at the given temperature and the spectrum at 25 °C and are plotted with arbitrary offset for clear visualization.

Next, in Figure 3 (a) and (b) we present the VTC spectra for 1 m ZnCl$_2$ with various amounts of added LiCl at 25 °C and 135 °C. And Figure 3(c) shows the result of LCA performed on these sets presented as the tetrahedral contribution as a function of total Cl^- concentration. For the 25 °C case, the evolution of spectra with increasing Cl^- concentration is manifested by the decreasing intensity of the peak around 9652 eV along with a complimentary increase in the signal intensity of the peak around 9656 eV. This agrees with our previous observations on similar solutions. (*17*) In contrast, the spectra are consistent with tetrahedral domination even for the lowest Cl^- concentration in the 135 °C dataset. For both temperatures the tetrahedral contribution increases sharply with Cl^- concentration before finally saturating, but the saturation occurs earlier in Cl^- concentration for the higher temperature than for the ambient temperature case. Furthermore, at lower Cl^- concentrations the increase in tetrahedral contribution with increase in temperature is substantially more as compared to the same at higher Cl^- concentrations. Qualitatively, the overall symmetry of Zn^{2+} coordination seems to shift rapidly towards more tetrahedral with increasing Cl^- concentrations at both temperatures.

For a more quantitative picture, let us take the case of 1 m$ZnCl_2$ solution (2 molal total Cl^- concentration) at various temperatures. Figure 4 (a) shows the normalized Zn K-edge VTC-XES spectra for a 1 molal $ZnCl_2$ solution sample at different temperatures from 25 °C to 135 °C. It is easily noticed that the octahedral peak feature at around 9652 eV becomes less intense while the tetrahedral peak around 9656 eV gradually increases in intensity with the increase in temperature of the solution. This behavior mimics the gradual decrease in octahedral coordination with a complimentary increase in tetrahedral coordination observed with increasing concentration at fixed temperature. Further, all of the spectra cross each other at about 9654 eV forming a nominal isosbestic point within permitted errors suggesting that each of the associated spectra could be modelled by a simple mole-weighted linear combination of two endpoint spectra, further supporting our use of LCA.

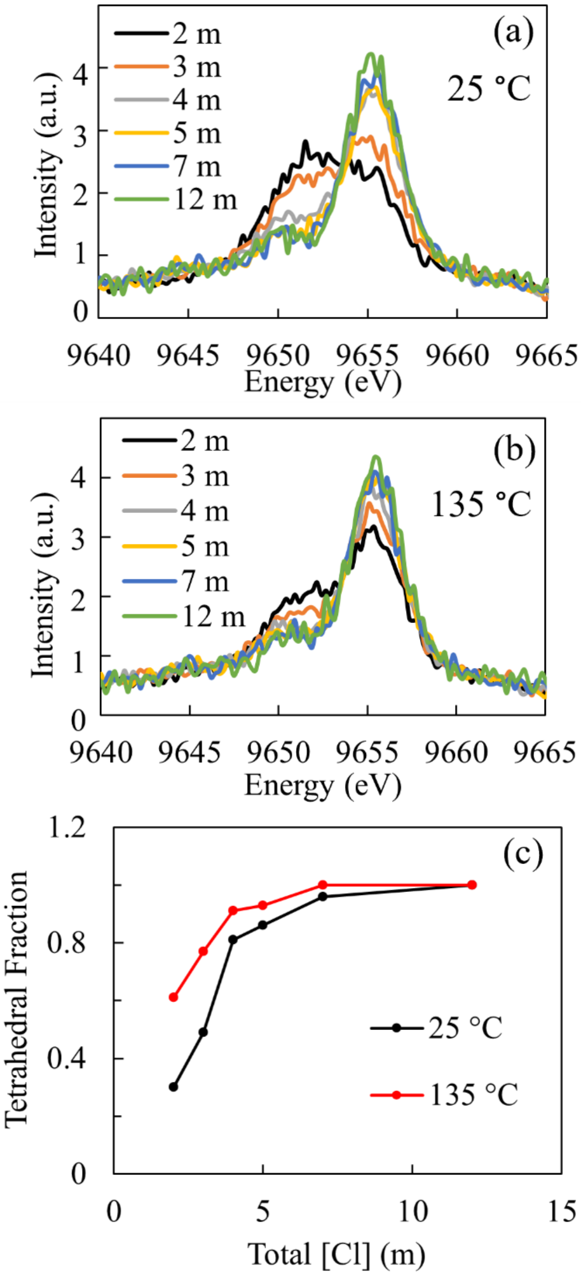

Figure 3: (a) VTC-XES spectra for 1 m $ZnCl_2$ and added LiCl with total Cl^- concentration indicated in legend at 25 °C, (b) VTC-XES spectra for the same samples at 135 °C and (c) results of LCA presented as the tetrahedral fraction at 25 °C and 135 °C.

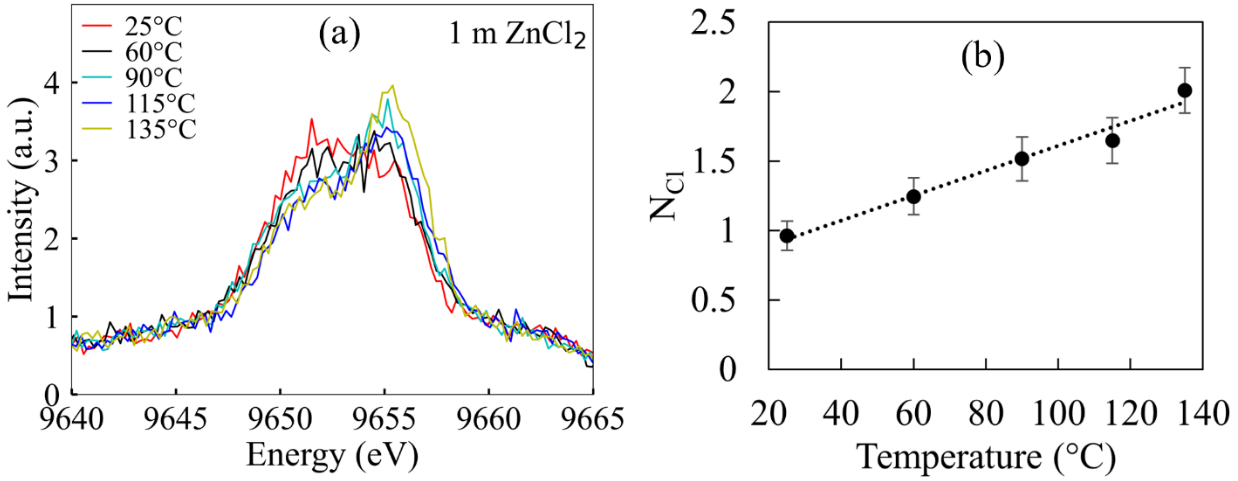

Figure 4: (a) VTC-XES spectra for 1 molal $ZnCl_2$ from 25 °C – 135 °C (b) Number of Cl^- coordinated per Zn^{2+} (N_{Cl}) for the same sample plotted against temperature.

We performed the spectral analysis, as mentioned earlier, on all datasets to extract the average number of Cl^- ions coordinated per Zn^{2+} ion (N_{Cl}) as a quantitative measure of ion pairing in the solution at temperatures up to 135 °C. Figure 4 (b) shows the results of this analysis for the 1 molal $ZnCl_2$ solution sample where N_{Cl} is plotted against the temperature of the sample from 25 °C to 135 °C. The average coordination number increases from about 1 Cl/Zn at 25 °C to about 2 Cl/Zn at 135 °C in a linear fashion. Such a steep increase in N_{Cl} shows a very strong dependence of ion pairing on temperature. Increased ion pairing with increasing temperature has been previously observed in Zn–halide solutions (*4, 26, 27, 29*) and also in other transition metal aqueous solutions. (*31*) This changing coordination environment as a function of temperature may be attributed to the enhanced ion activity due to the decreasing dielectric constant of water with increasing temperature. (*32, 33*) As the dielectric constant of water decreases with increase in temperature of the solution, water becomes less effective in screening the charged ions in the solution, effectively favoring an increase in ion pairing between cations and anions. It is worth noting that for this sample (pure $ZnCl_2$ solution) the stoichiometric limit for the maximum value for N_{Cl} is 2. In fact, even more concentrated pure $ZnCl_2$ solutions saturate around the N_{Cl} value of

2 at ambient temperature. (*17*) But for solutions with added LiCl the coordination number can easily go above two, either because of high Cl^- concentration or because of increased temperature, see Figure 5.

We now present the extracted N_{Cl} values for all the samples as a function of Cl^- concentration and temperature in Figure 5. It can be quickly noticed that the N_{Cl} value, which represents the extent of contact ion pairing, increases with increasing temperature for all samples. Similar trends have been reported in other studies of aqueous Zn-halide systems. (*4, 26, 27, 29*) For the most concentrated samples, there is already a substantial ion pairing and hence N_{Cl} starts at higher values at room temperature. The weak temperature dependence observed in these samples increases N_{Cl} by a small amount at higher temperature. Moving to lower concentration samples, which start at lower N_{Cl} at room temperature, there is an increased tendency for ion pairing enhancement with increasing temperature. In general, the increase in N_{Cl} with temperature is linear for all samples, with the lowest Cl^- concentration having the most pronounced effect. These observations contradict with the predictions from studies using dilute-limit model mentioned earlier (*5, 18, 20*) and also shown in figure 6. For instance, the results reported by Bourcier and Barnes (*5*) (figure 6 (b)) show a decrease in coordination number with increase in temperature at these concentrations which clearly contradicts with our observations.

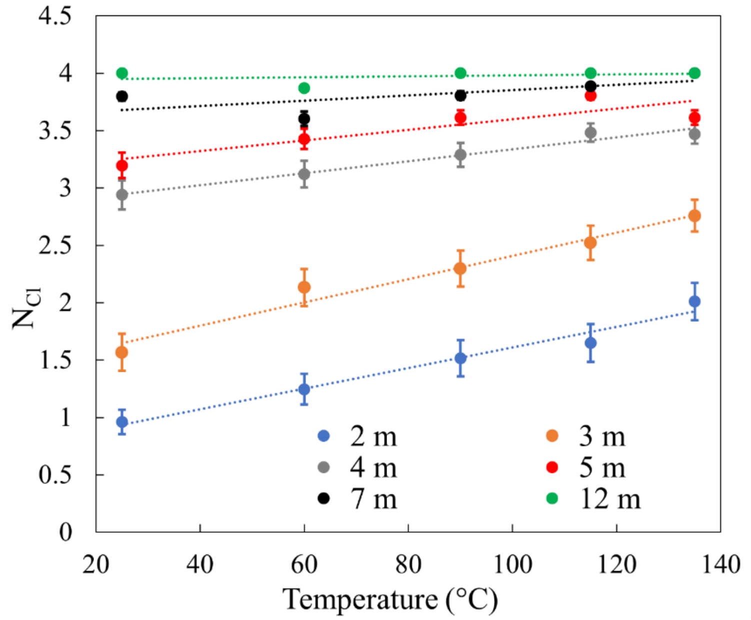

Figure 5: N_{Cl} as a function of temperature for 1 m $ZnCl_2$ samples with added LiCl; the numbers in the legend represent the total Cl^- concentration for the given sample.

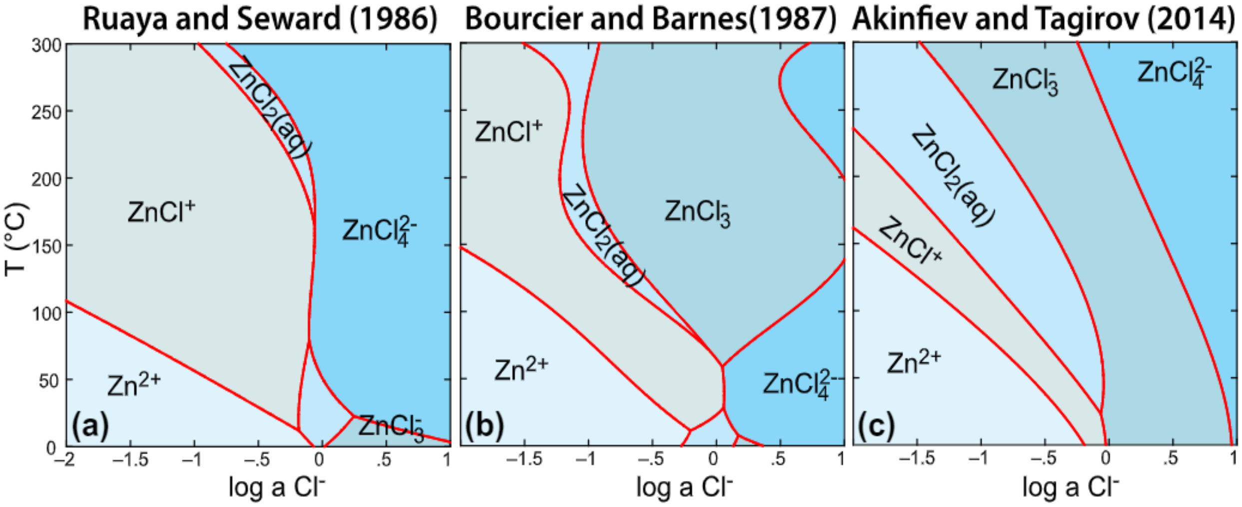

Figure 6: Comparison of Zn-Cl speciation in aqueous solutions as a function of temperature and Cl^- activity from (a) Ruaya and Seward (*18*), (b) Bourcier and Barnes (*5*), and (c) Akinfiev and Tagirov (*20*).

In Figure 7 ((b) and (c)), we compare the results from our study with those obtained using the MINTEQ chemical equilibrium model (M-CEM) that employs the so-called "equilibrium constant method". (*34*) The general trend is common to both approaches: a sharp increase in ion pairing with increase in Cl^- concentration that saturates at higher Cl^- concentrations, and an increase in ion pairing with increasing temperature, especially at lower Cl^- concentrations. But, for all temperatures shown the M-CEM predicts saturation of N_{Cl} at 3.5 whereas results from this study saturate at the full tetrahedral coordination number of 4. This discrepancy mainly stems from a predicted coexistence of $ZnCl_3^-$ and $ZnCl_4^{2-}$ species at higher Cl^- concentrations in the M-CEM, while our study suggests a dominance of $ZnCl_4^{2-}$ species. The M-CEM uses thermodynamic databases of equilibrium constants devised or measured for low concentration solutions and does not account for the effects of change in pressure, which limits our calculations to below 100 °C. Nevertheless, it is important to note that the M-CEM devised for dilute solutions predicts the general trend of more concentrated solutions satisfactorily below 100 °C, except for the value at saturation which is lower than the experimental value at saturation.

In Figure 7 ((a) and (c)), we then compare our results with those obtained using the speciation distribution of Mei, *et al.* (*4*) In that work the authors derived the distribution of ion paired moieties by refining the thermodynamic formation constants on the basis of XAFS fits and MD simulations, improving the quality of the results obtained. Their results are thus among the high-quality published data available for these systems. Consequently, the close similarity between the results from Mei, *et al.*, (panel (a)) and this study (panel (c)) substantiates the robustness and accuracy of VTC-XES method in the study of local structure of Zn^{2+} ions in aqueous solutions without the use of embedded thermodynamic coefficients. This opens avenues for future studies focusing on the application of VTC-XES in similar studies of other Zn-electrolytes and electrolytes involving other metal ions.

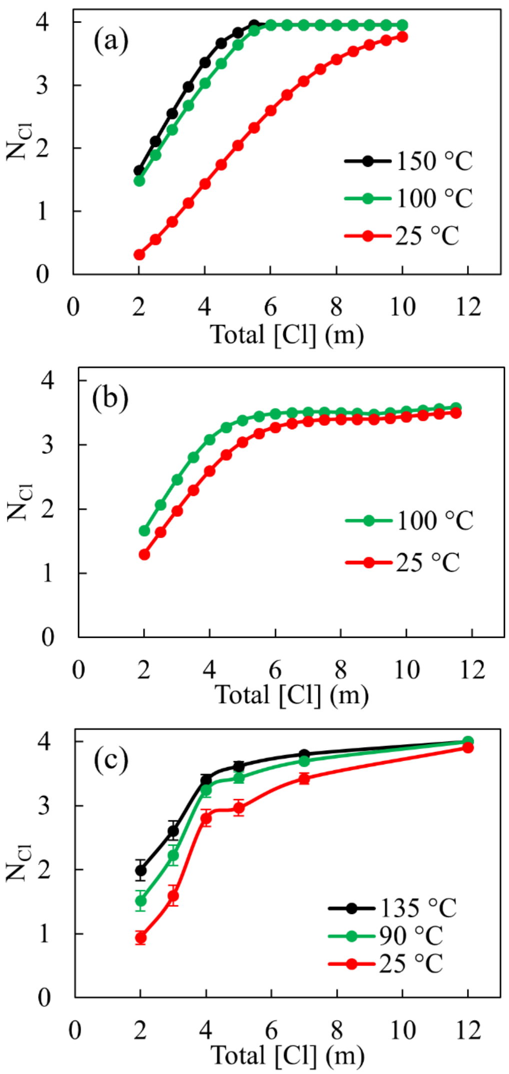

Figure 7: N_{Cl} plotted for different temperatures (as mentioned in legend) as a function of Cl^- concentration at fixed Zn^{2+} concentration of 1 m. (a) Calculated using the values of formation constant at saturated vapor pressure from Table 7 of Mei, *et al*., (*4*) (b) calculated from the speciation distribution obtained from the MINTEQ chemical equilibrium model, and (c) calculated from the fitting results of VTC-XES data from this study.

At present, MD simulation is among the best theoretical approaches to predict the behavior of such high-concentration solutions when the important input parameters of the system, like empirical force fields, are available. MD simulation provides atomistic details and, unlike other computational methods, captures both ion-ion and ion-solvent dynamic interactions. (*35*) But it is computationally expensive which limits the system size and simulation times accessible by this method, seriously discounting its merits. The fact that VTC-XES method does not require the use of thermodynamic coefficients and directly measures the extent of ion pairing should be emphasized because this provides an independent way to compare and validate the thermodynamic properties obtained from other methods and could be valuable in refining the input parameters for theoretical simulation, for example the force fields needed for MD simulation.

8.5: Conclusions

We report an experimental quantification of ion pairing as a function of temperature from 25 °C to 135 °C in Zn-Cl aqueous system over the full range of Cl^- ion activity for 1 m $ZnCl_2$ solutions with added LiCl. Using the recently developed method of ion-pair quantification from VTC-XES, (*17*) we follow the evolution of the Zn^{2+} first shell coordination environment and find that the extent of ion pairing increases with increasing temperature of the solution in a linear fashion for all compositions explored in this study. Furthermore, we find that the temperature effect is most prominent in solutions with lower concentrations and decreases with the increase in overall concentration of the solution. Comparison with theoretical predictions and prior work emphasizes the inadequacy of dilute-limit theory for the study of concentrated solutions and substantiates the robustness and accuracy of the thermodynamic-coefficients-free VTC-XES method for local coordination studies in solution phase.

8.6: References

1. J. O. G. Posada *et al.*, Aqueous batteries as grid scale energy storage solutions. *Renewable and Sustainable Energy Reviews* **68**, 1174-1182 (2017).
2. M. A. Shannon *et al.*, Science and technology for water purification in the coming decades. *Nature* **452**, 301-310 (2008).
3. F. Joó, *Aqueous organometallic catalysis*. (Springer Science & Business Media, 2006), vol. 23.
4. Y. Mei *et al.*, Zinc complexation in chloride-rich hydrothermal fluids (25–600°C): A thermodynamic model derived from ab initio molecular dynamics. *Geochimica et Cosmochimica Acta* **150**, 265-284 (2015).
5. W. L. Bourcier, H. L. Barnes, Ore solution chemistry; VII, stabilities of chloride and bisulfide complexes of Zinc to 350 degrees C. *Economic Geology* **82**, 1839 - 1863 (1987).
6. J. Brugger *et al.*, Probing ore deposits formation: New insights and challenges from synchrotron and neutron studies. *Radiation Physics and Chemistry* **79**, 151-161 (2010).
7. N. Rampal *et al.*, Local molecular environment drives speciation and reactivity of ion complexes in concentrated salt solution. *Journal of Molecular Liquids* **340**, 116898 (2021).
8. J. A. Darr, M. Poliakoff, New directions in inorganic and metal-organic coordination chemistry in supercritical fluids. *Chemical Reviews* **99**, 495-541 (1999).
9. S. E. Ziemniak, M. Hanson, Zinc treatment effects on corrosion behavior of 304 stainless steel in high temperature, hydrogenated water. *Corrosion Science* **48**, 2525-2546 (2006).
10. Y. S. Chen, J. L. Fulton, W. Partenheimer, A XANES and EXAFS study of hydration and ion pairing in ambient aqueous MnBr₂ solutions. *Journal of Solution Chemistry* **34**, 993-1007 (2005).
11. H. W. Wang, K. Yuan, N. Rampal, A. G. Stack, Solution and Interface Structure and Dynamics in Geochemistry: Gateway to Link Elementary Processes to Mineral Nucleation and Growth. *Crystal Growth & Design* **22**, 853-870 (2022).
12. J. L. Fulton, S. M. Heald, Y. S. Badyal, J. M. Simonson, Understanding the effects of concentration on the solvation structure of Ca2+ in aqueous solution. I: The perspective on local structure from EXAFS and XANES. *Journal of Physical Chemistry A* **107**, 4688-4696 (2003).
13. L. M. Suo *et al.*, "Water-in-salt" electrolyte enables high-voltage aqueous lithium-ion chemistries. *Science* **350**, 938-943 (2015).
14. H. W. Wang *et al.*, Countercations Control Local Specific Bonding Interactions and Nucleation Mechanisms in Concentrated Water-in-Salt Solutions. *Journal of Physical Chemistry Letters* **10**, 3318-3325 (2019).
15. Y. F. Hu, X. M. Peng, Effect of the Structures of Ionic Liquids on Their Physical Chemical Properties. *Structures and Interactions of Ionic Liquids* **151**, 141-174 (2014).
16. P. Dreier, P. Rabe, EXAFS-Study of the Zn2+ Coordination in Aqueous Halide Solutions. *J. Phys. Colloques* **47**, 809-812 (1986).
17. D. Dhakal *et al.*, The evolution of solvation symmetry and composition in Zn halide aqueous solutions from dilute to extreme concentrations. *Physical Chemistry Chemical Physics* **25**, 22650-22661 (2023).
18. J. R. Ruaya, T. M. Seward, The stability of chlorozinc(II) complexes in hydrothermal solutions up to 350-degrees-C. *Geochimica Et Cosmochimica Acta* **50**, 651-661 (1986).
19. W. Liu, B. Etschmann, G. Foran, M. Shelley, J. Brugger, Deriving formation constants for aqueous metal complexes from XANES spectra: Zn2+ and Fe2+ chloride complexes in hypersaline solutions. *American Mineralogist* **92**, 761-770 (2007).
20. N. N. Akinfiev, B. R. Tagirov, Zn in hydrothermal systems: Thermodynamic description of hydroxide, chloride, and hydrosulfide complexes. *Geochemistry International* **52**, 197-214 (2014).

21. D. J. Wesolowski, P. Benezeth, D. A. Palmer, ZnO solubility and Zn²⁺ complexation by chloride and sulfate in acidic solutions to 290°C with in-situ pH measurement. *Geochimica Et Cosmochimica Acta* **62**, 971-984 (1998).
22. J. L. Fulton, Y. S. Chen, S. M. Heald, M. Balasubramanian, Hydration and contact ion pairing of Ca2+ with Cl- in supercritical aqueous solution. *Journal of Chemical Physics* **125**, 094507 (2006).
23. G. S. Pokrovski *et al.*, Silver in geological fluids from in situ X-ray absorption spectroscopy and first-principles molecular dynamics. *Geochimica Et Cosmochimica Acta* **106**, 501-523 (2013).
24. A. V. Zotov, A. V. Kudrin, K. A. Levin, N. D. Shikina, L. N. Var'yash, in *Fluids in the Crust: Equilibrium and transport properties,* K. I. Shmulovich, B. W. D. Yardley, G. G. Gonchar, Eds. (Springer Netherlands, Dordrecht, 1995), pp. 95-137.
25. G. L. Cygan, J. J. Hemley, W. M. d'Angelo, An experimental study of zinc chloride speciation from 300 to 600 °C and 0.5 to 2.0 kbar in buffered hydrothermal solutions. *Geochimica et Cosmochimica Acta* **58**, 4841-4855 (1994).
26. W. Liu, S. Borg, B. Etschmann, Y. Mei, J. Brugger, An XAS study of speciation and thermodynamic properties of aqueous zinc bromide complexes at 25–150°C. *Chemical Geology* **298-299**, 57-69 (2012).
27. A. J. Anderson, R. A. Mayanovic, S. Bajt, A microbeam XAFS study of aqueous chlorozinc complexing to 430°c in fluid inclusions from the Knaumuhle granitic pegmatite, Saxonian Granulite Massif, Germany. *Canadian Mineralogist* **36**, 511-524 (1998).
28. W. A. Bassett, A. J. Anderson, R. A. Mayanovic, I. M. Chou, Hydrothermal diamond anvil cell for XAFS studies of first-row transition elements in aqueous solution up to supercritical conditions. *Chemical Geology* **167**, 3-10 (2000).
29. R. A. Mayanovic, A. J. Anderson, W. A. Bassett, I. M. Chou, XAFS measurements on zinc chloride aqueous solutions from ambient to supercritical conditions using the diamond anvil cell. *Journal of Synchrotron Radiation* **6**, 195-197 (1999).
30. M. Buback, in *Proceedings of the First International Symposium on Hydrothermal Reactions.* (Gakuzyutu Bunken Fukyukai, Tokyo, 1983).
31. L. P. M. De Leo, H. L. Bianchi, R. Fernández-Prini, Ion pair formation in copper sulfate aqueous solutions at high temperatures. *Journal of Chemical Thermodynamics* **37**, 499-511 (2005).
32. B. B. Owen, R. C. Miller, C. E. Milner, H. L. Cogan, The dielectric constant of water as a function of temperature and pressure1, 2. *The Journal of Physical Chemistry* **65**, 2065-2070 (1961).
33. Y. Marcus, G. Hefter, Ion pairing. *Chemical Reviews* **106**, 4585-4621 (2006).
34. J. P. Gustafsson, in *KTH, Department of Land and Water Recources, Stockholm, Sweden*. (KTH, Department of Land and Water Recources,, Stockholm, Sweden, 2011), vol. 550.
35. Y. Luo, W. Jiang, H. Yu, A. D. MacKerell, B. Roux, Simulation study of ion pairing in concentrated aqueous salt solutions with a polarizable force field. *Faraday discussions* **160**, 135-149 (2013).

8.7: Supplementary Information

Experiment Setup

Figure SI-1 shows the sample cell and the heating stage setup used for the temperature dependent VTC-XES study of aqueous solutions up to 135 °C and about 5 bar. Note that this setup could potentially be used up to higher temperatures and pressures and for non-aqueous solutions as well. In this setup, a thin-walled PEEK capillary tube (ID 1.4 mm and OD 1.6 mm) (#1) runs through the body of a specially designed aluminum block (#5) used as the heating block and equipped with, among other things, slits for incoming (#3) and outgoing X-rays (#4) (see details in the next section).

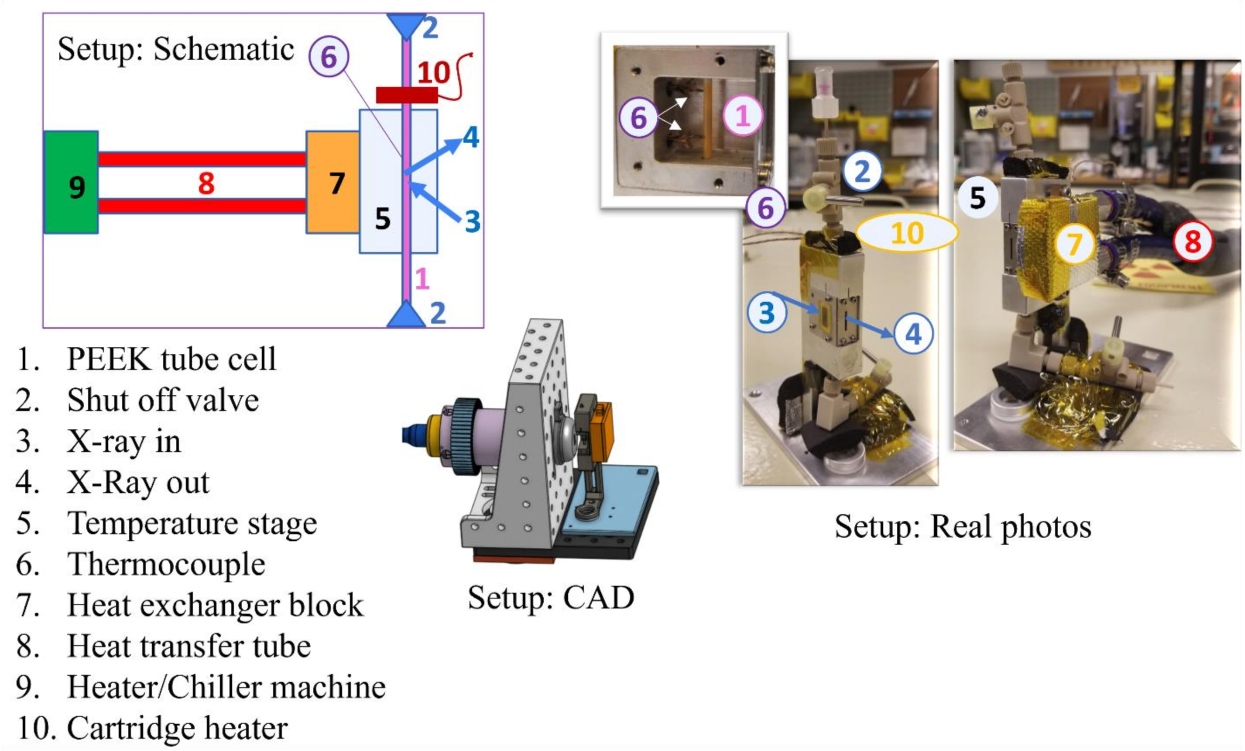

Figure SI-1: (left) Schematic representation of the setup for temperature dependent VTC-XES study. (middle) CAD model of the sample stage and heat exchanger block showing their relative position with the exit window of X-ray tube. (right) Real pictures of the assembled setup showing PEEK cell mounted on the heating stage and other details. The numbers shown in the figures are to be matched with the legend.

Heating stage

The temperature stage (#5) is a machined aluminum block provided with a through hole (diameter = 1.8 mm) for the PEEK tube and two additional holes in the perpendicular direction up to the sample chamber for the thermocouple wires. The sample chamber is a machined space about 10 mm x 15 mm and 15 mm high at the middle of the block in vertical direction and starting from two of the faces; one on the source side and one on the analyzer side. These sides are then covered with 0.8 mm thick stainless-steel sheets containing appropriate size slits for the entrance and exit of the X-rays from the sample. The sample tube sat about 5 mm from the exit slit towards the analyzer with about 10 mm free space behind it. This 10 mm of free space left behind the tube in the sample chamber served to minimize the background from stray scattering from the aluminum block. The sample chamber was designed such that the portion of the sample tube that is illuminated with x rays is in perfect line of sight to the analyzer and that the analyzer does not "see" the aluminum or the thermocouple wires behind the tube. A cross section of the stage at the sample chamber location is shown in figure SI-2.

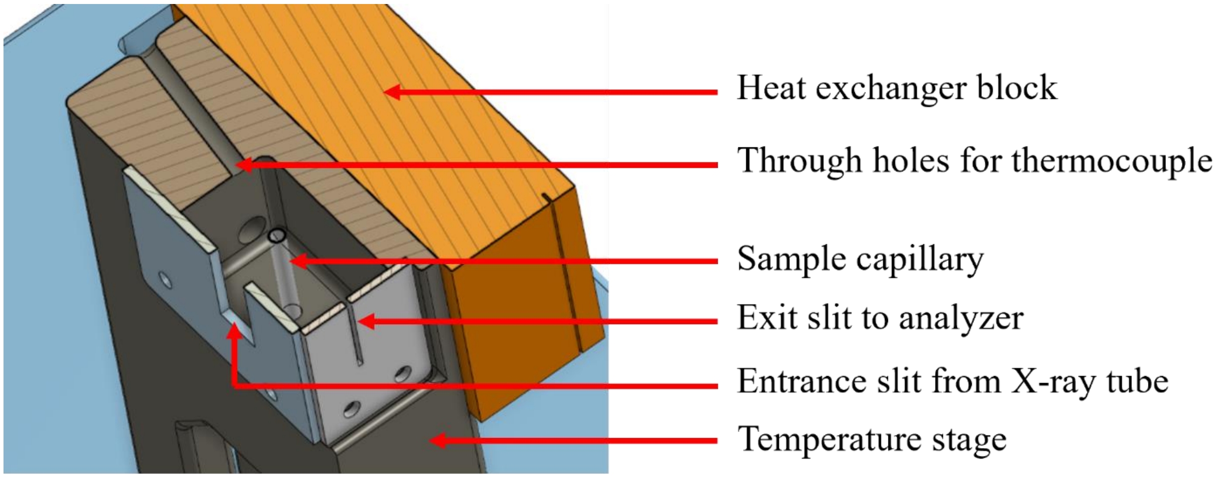

Figure SI-2: Cross section of the heating stage at the location of sample chamber.

In this set up, the sample tube sits about 7 mm from the exit window of the x ray tube and about 5 mm from the slit on the analyzer side. A slit size of 1mm was found suitable to collect most of the emission from the sample and still small enough to give energy resolution of ≈ 1 eV.

PEEK tube and fittings

The cell is composed of a 10 cm long PEEK tube connected at both ends to shut-off valves using suitable fittings. The total sample volume enclosed between the shut-off valves was approximately 1.5 cc. The tube, shut-off valves and fittings used are all rated up to at least 200°C and 10 bar and made from PEEK material which is relatively inert under our experimental conditions. All of these PEEK parts were purchased from a single vendor, IDEX Health Services.

Fixing positions of slit and tube

The PEEK tube is spring loaded on entry and exit points of the block such that the tube does not move during handling and/or measurement and that its position is reproducible. The aluminum block is fixed to the base of the spectrometer's sample platform by a combination of a screw and a slip-fit post such that the X-ray exit slit from the sample sits on the Rowland circle of the spectrometer.

Temperature control

To control the temperature of the aluminum block and hence the sample, a specially machined copper block (#7) was attached to the aluminum block and a heat transfer liquid heated in a bath outside the spectrometer enclosure was flowed through the copper block. The space around the blocks was properly insulated using foam insulation to insure minimum heat loss to the surrounding. In this setup the temperature of the sample was stable within +/-1 °C of the set point during each experiment.

Additionally, two cartridge heaters (≈10 Watts total) were added on the top portion of the cell just outside the aluminum block to keep the temperature at the top of the cell about 10 °C higher than the sample temperature, especially for measurements at temperatures above 100 °C. This was needed to ensure that the vapor bubble formed during X-ray irradiation moved and remained on the top portion of the cell and out of the probed region during measurement. Without the added heat source, it was noticed that the vapor bubble favored being at the hot spot within the cell which unfortunately happened to be at the middle of the tube, exactly where the sample was being probed.

Temperature monitoring

The temperature of the PEEK tube (assumed to be approximately equal to the temperature of the sample inside it) was measured at two points using k-type thermocouples; ≈1 mm above and ≈1 mm below the position where the sample was being probed by X-rays. The temperature was monitored continuously over the whole duration of scans using a thermocouple reader and the associated computer interface (Omega Engineering).

End of Dissertation